TECHNISCHE UNIVERSITÄT MÜNCHEN

Ingenieurfakultät Bau Geo Umwelt

Lehrstuhl für Ingenieurgeologie

Quantifying the Effect of Stress Changes on the Deformation and Cracking Behavior of Solid Rock using Acoustic Emission Techniques

Carola Wieser

Vollständiger Abdruck der von der Ingenieurfakultät Bau Geo Umwelt der Technischen Universität München zur Erlangung des akademischen Grades eines

Doktor-Ingenieurs (Dr.-Ing.)

genehmigten Dissertation.

Vorsitzender:	Univ.-Prof. Dr. rer. nat. Michael Krautblatter
Prüfer der Dissertation:	1. Univ.-Prof. Dr. rer. nat. Kurosch Thuro
	2. Univ.-Prof. Dr.-Ing. Christian Große
	3. Univ.-Prof. Dr. Erik Eberhardt, Ph.D., University of British Columbia, Kanada

Die Dissertation wurde am 29.06.2016 bei der Technischen Universität München eingereicht und durch die Ingenieurfakultät Bau Geo Umwelt am 04.11.2016 angenommen.

Abstract

In recent years, the demand for underground openings has increased steadily and provoked major engineering progress in tunneling technology and modern constructional methods. As tunnel construction progresses to ever-greater depths and the volume and length of underground excavations increase, the challenges for engineers and geologists are subject to constant change. The performance of deep tunneling with tunnel boring machines (TBM) is strongly affected by the primary stress state and the principal stresses in the tunnel face. As the tunnel advances, the primary stresses are redistributed and the stress magnitudes change. Depending on the orientation and the ratio of major to minor principal stresses, increasing stresses and stress relaxation may occur in the tunnel face. Continuous stress changes affect the mechanical rock properties and may affect the TBM performance. Until now, the influence of stress changes on rock properties and on the rock excavation process are not fully understood. Therefore, an experimental approach should provide insight into the effect of stress relaxation and increased stresses on the deformation and cracking behavior of different rock.

In order to assess the stress relaxation behavior of rocks, acoustic emission (AE) monitoring on fresh core material was conducted at the Pyhäsalmi Mine in Finland. The measurements were performed on core material recovered from its primary stress state in order to record the microcrack activity during stress relaxation. The results of AE monitoring and p-wave velocity measurements on metavolcanic rocks revealed that stress-induced microcracking continues for several days or weeks before a new state of equilibrium is reached. The time-dependent change in rock properties must be taken into account when evaluating laboratory rock properties for geotechnical investigations, since they are usually determined on rock samples where stress relaxation has already occurred.

In addition to the field study, the influence of stress changes on laboratory rock properties was investigated. The research included the characterization of rock mechanical and acoustic properties of different rock types using uniaxial compression tests combined with non-destructive testing methods. An extensive analysis of the deformation and cracking behavior of the tested rock types was performed and five groups of rocks with a characteristic failure behavior were established. The results showed that not only truly brittle or ductile material behaviors exist but some rock types showed characteristics of both.

Furthermore, the influence of stress changes on rock properties was assessed using uniaxial constant loading and subsequent standard uniaxial compression tests. Different compressive stress levels in the range between crack initiation and crack damage stress were applied in order to evoke stress-induced damage. The experimental results showed that the induced damage in the form of axial microcracks has a strong influence on p-wave velocity and Young's modulus. A reduction of the uniaxial compressive strength was only observed in samples loaded beyond the crack damage stress. This confirms that the stress level of beginning crack coalescence and major crack formation represents the long-term laboratory strength of rocks. Petrographic analyses of fluorescent thin sections showed that a high number of microcracks already exist in undamaged granite samples, whereas fine-grained basalt did not show any preexisting microcracks or voids. In granite samples loaded beyond the crack damage stress, load-parallel microcracks with a high aspect ratio and length evolved.

In order to transfer the findings from laboratory results to the in-situ rock behavior in the tunnel face, several restrictions need to be considered. Where isotropic, homogeneous and intact rock samples are used for laboratory tests, structural anisotropy, material changes, existing damage and the presence of joints and faults mainly influence the deformation and fracturing behavior of a rock mass in-situ. In a massive, unjointed rock mass, stress changes in the tunnel face are dependent on the ratio of rock mass strength to the stresses at the excavation boundary. In areas of increased stresses, the failure envelope

of the rock mass may be reached so that cracks are initiated. Dependent on the confining stresses, either face instabilities in the form of spalling or rock burst occur, or the generation of microcracks is inhibited by an increased confinement. In the center of the face, the confining stresses are reduced and tensile microcracks may initiate.

Zusammenfassung

In den letzten Jahren sind die Anforderungen an Untertagebauwerke zunehmend gestiegen. Technischer Fortschritt und innovative Konstruktionsmethoden erlauben den Bau von immer tiefer liegenden Tunnels. Durch steigende Ausbruchsvolumina und immer längere Tunnelbauwerke verändern sich die Herausforderungen für Ingenieure und Geologen stetig. Die Leistung von Tunnelvortriebsmaschinen (TVM) in tiefliegenden Tunnelvortrieben wird bedingt durch den Primärspannungszustand im Gebirge und besonders durch den sekundären Spannungszustand im Bereich der Ortsbrust. Beim Tunnelvortrieb werden die Spannungen um den Hohlraum umgelagert so dass sich der Spannungszustand verändert. Abhängig von der Orientierung der Hauptnormalspannungen und dem Verhältnis von Maximal- zu Minimalspannung, können erhöhte Spannungen aber auch eine Entspannung des Gebirges in der Ortsbrust auftreten. Kontinuierliche Spannungsänderungen vor der Ortsbrust können die Gesteinseigenschaften und somit die Vortriebsleistung von TBM beeinflussen. Bis heute ist noch nicht klar, wie sich Spannungsänderungen auf Gesteinseigenschaften und auf die Lösbarkeit auswirken. Deshalb sollten Laborversuche Erkenntnisse zum Einfluss von Entspannung und erhöhten Spannungen auf das Verformungs- und Rissbildungsverhalten verschiedener Gesteinsarten liefern, das durch die zunehmende Schädigung im Gestein bedingt wird.

Um das Verhalten von Gesteinen beim Spannungsabbau zu untersuchen, wurden an frisch entnommenen Bohrkernen aus der Pyhäsalmi Mine in Finnland Schallemissionsmessungen durchgeführt. Dabei konnte die Entspannung des Gesteins an Proben untersucht, die aus ihrem ursprünglichen Gebirgsspannungszustand entnommen wurden. Die Ergebnisse der Schallemissionsmessungen sowie die Änderung der P-Wellengeschwindigkeiten an den untersuchten Metavulkaniten haben gezeigt, dass spannungsbedingte Mikrorissbildung über mehrere Tage oder Wochen andauern kann, bevor ein neuer Gleichgewichtszustand erreicht ist. Die zeitabhängige Veränderung von Gesteinseigenschaften muss bei der Interpretation von Gesteinseigenschaften berücksichtigt werden, da diese meist bestimmt werden, nachdem die Entspannung bereits abgeschlossen ist.

Weiterhin wurden Laborversuche durchgeführt, um den Einfluss von Spannungsänderungen auf die Gesteinseigenschaften zu untersuchen. Dazu wurden mit Hilfe von einaxialen Druckversuchen und zerstörungsfreien Prüfmethoden verschiedene Gesteine nach ihren felsmechanischen und akustischen Eigenschaften charakterisiert. Insbesondere das Verformungs- und Bruchverhalten der Gesteine wurde analysiert und die untersuchten Gesteine wurden nach ihrem Versagensverhalten in fünf Gruppen eingeteilt. Die Ergebnisse zeigen, dass nicht das Materialverhalten nicht nur eindeutig spröde oder duktil sein kann, sondern dass es auch Gesteine gibt, die charakteristische Eigenschaften beider Verhaltenstypen aufweisen.

In einem zweiten Schritt wurde der Einfluss von Spannungsänderungen auf die Gesteinseigenschaften untersucht. Dazu wurden einaxiale Versuche mit konstanter Belastung und anschließend standardisierte einaxiale Druckversuche durchgeführt. Um spannungsbedingte Mikrorissbildung zu verursachen, wurden die Proben mit unterschiedlichen Spannungsniveaus im Bereich im Bereich des stabilen und instabilen Risswachstums belastet. Die Ergebnisse zeigen, dass eine Schädigung vor allem durch axiale Mikrorisse stattfindet und dass eine Vorbelastung einen deutlichen Einfluss auf die P-Wellengeschwindigkeit und den E-Modul hat. Eine Verringerung der einaxialen Druckfestigkeit wurde nur an Proben festgestellt, die über den Schwellwert des irreversiblen Risswachstums belastet wurden. Dies bestätigt, dass das Spannungsniveau, ab dem sich Risse vereinigen und die Bildung von Makrorissen stattfindet, der Langzeitfestigkeit von Laborproben entspricht. Weiterhin hat eine petrographische Analyse von fluoreszierenden Dünnschliffen ergeben, dass in den untersuchten Granitproben eine beträchtliche Anzahl

an Mikrorissen bereits vor der Belastung vorhanden war. In den feinkörnigen Basaltproben waren vor der Belastung keinerlei Mikrorisse vorhanden. In Granit, der bis zum irreversiblen Risswachstum belastet wurde, haben sich lange Mikrorisse parallel zur Belastungsrichtung ausgebildet.

Um die Ergebnisse aus den Laborversuchen auf das Gebirgsverhalten in der Ortsbrust übertragen zu können, müssen einige Einschränkungen berücksichtigt werden. Für Laborversuche wird in der Regel isotropes, homogenes und intaktes Gestein verwendet, wohingegen das Verformungs- und Bruchverhalten des Gebirges durch vorhandene Anisotropie, Materialwechsel, einer Vorschädigung sowie durch Trennflächen und Störungen beeinflusst wird. In einem ungeklüfteten Gebirge sind Auswirkungen von Spannungsänderungen in der Ortsbrust abhängig vom Verhältnis der Gebirgsfestigkeit zu den Spannungen am Ausbruchsrand. In Bereichen mit erhöhten Spannungen kann die Gebirgsfestigkeit überschritten werden so dass sich Risse im Gestein bilden können. Abhängig von der Einspannung im Gebirge kann es zu Abplatzungen oder Gebirgsschlag kommen oder aber die Bildung von Rissen wird durch eine ausreichende Einspannung verhindert. Im Zentrum der Ortsbrust ist die Einspannung am geringsten, so dass sich Zugrisse bilden können.

Acknowledgement

I would like to thank Prof. Kurosch Thuro for the opportunity to write this thesis as well as for the great support and valuable discussions on the topic. Thank you for providing the position at the Chair of Engineering Geology and for the confidence you placed in me throughout the whole period, I really appreciate that.

A special thanks goes to Prof. Christian Große of the Chair of Non-destructive Testing who supported this PhD thesis with his expertise in acoustic emission testing from the beginning. Thanks to his advices and the effort of his team, the AE technique could be set up at the Chair of Engineering Geology and the provided software enabled an advanced data analysis. I cannot thank enough for supporting me as well as for being my second supervisor. Many thanks also go to Manuel Raith, Ronald Richter, Fabian Malm, Franziska Gemander, Robin Groschup, Dorothee Moser and Marina Nahm for their help, whenever I came up with a question. Thank you Manuel for solving my Matlab problems and for spending so much time on helping me!

Thank you Prof. Erik Eberhardt for the co-supervision of this thesis and for coming to Europe for the examination. Your research in the field of rock mechanics inspired me to deal with this subject. Thank you also for your valuable input.

I would also like to thank my mentor Dr. Heiko Käsling for the numerous constructive discussions about laboratory results and especially for supporting all the ideas, I brought forward.

Another thank you to Prof. Derek Martin who kindly established the contact to Rockplan. Thank you for the spontaneous help!

Special thanks goes to Guido Nuijten of Rockplan, who made my in-situ measurements at the Pyhäsalmi Mine possible. Thank you for your support and your interest in the research. Thank you also to the Rockplan team for providing information and rock samples as well as for assisting in the underground tests and sampling.

Here, I would also like to thank Mikko Numminen, the geologist at the Pyhäsalmi Mine, for spending so much time on bringing us underground and up again, for getting us to the drill rig, for translating and for organizing everything. Thank you for your commitment.

I also extend my thanks to all my master and bachelor students as well as the student assistants for contributing to this work. Thank you Matthias Quessel for your assistance in the underground tests and your preliminary tests with the AE technology. Thank you Katrin Schallhammer for putting so much effort in the time-consuming fluorescence microcopy. Thank you also to Greta Meißner and Christian Beck for the commitment on your rock mechanical subjects including huge data sets and Matlab problems. Another thank you to Christian Schneider, Lisa Gigl and Marian Hornung for your contributions to this study. Thank you also to the student assistants who spent many hours on preparing samples or sitting in a dark room for taking images from fluorescent thin sections.

Furthermore, I would like to thank all my colleagues at the Chair of Engineering Geology for their help, their support and discussions. Thank you for the amusing lunch times and coffee breaks. Special thanks goes to Friedrich Ettl and Vladimir Ruttner for the preparation of my samples and for fulfilling all my special and sometimes time-consuming requests. I would also like to thank Ms. Merling for brightening up my late working hours and weekends with her flowers, jelly bears and encouraging words.

Big thanks to Peter Ellecosta and Lisa Wilfing, my favorite office mates! Thank you for all the fun we had, for the intense and constructive discussions and for your encouragement and support. I really enjoyed the time with you!

My greatest thanks goes to my family and friends. Thank you to Andreas, my sister, and Julia for proofreading parts of the thesis. I really appreciate that, since I know very well how valuable your time is. Thank you also to my little nephew for letting his mom proofread some pages.

None of this would have been possible without my family. Thank you for your unlimited trust and support during my whole education. Thank you for listening to my moaning and groaning when writing advanced too slowly or when my motivation reached a low point. Thank you also for encouraging me and for always being there, whenever I need your advice.

My special thanks goes to Andreas. Without your encouragement, I would probably not have started my doctorate and I would not have finished it either. Thank you for your infinite support and motivation.

Contents

Appendix

List of Figures

List of Tables

List of Symbols

$\mathbf{A}$	Area of specimen
$\mathbf{A_R}$	Anisotropy ratio
$\mathbf{A_v}$	Anisotropy coefficient
$\mathbf{D}$	Fatigue damage
$\mathbf{E}$	Young's modulus
$\mathbf{E_r}$	Slope of radial strain curve
$\mathbf{E_A}$	Average Young's modulus
$\mathbf{E_T}$	Tangent Young's modulus
$\mathbf{E_S}$	Secant Young's modulus
$\mathbf{F}$	Force
$\mathbf{K}$	Bulk modulus
$\mathbf{K_I}$	Stress intensity factor (Mode I)
$\mathbf{K_{IC}}$	Critical stress intensity factor
$\mathbf{S}$	Sample
$\mathbf{S_{amp\_max}}$	Maximum amplitude
$\mathbf{Z}$	Acoustic impedance
$\mathbf{b}$	Crack half width
$\mathbf{c}$	Crack half length/sonic velocity
$\mathbf{d}$	Width of test samples
$\mathbf{f}$	frequency
$\mathbf{f_s}$	Sampling rate
$\mathbf{l}$	Length of test samples
$\mathbf{s_a}$	Arrival time
$\mathbf{t}$	Time
$\mathbf{t_R}$	Rise time
$\mathbf{v_p}$	P-wave velocity
$\mathbf{x}$	distance

$\mathbf{\Delta}$	Difference
$\mathbf{\gamma}$	Crack inclination angle
$\mathbf{\varepsilon}$	Strain
$\mathbf{\varepsilon_a, \varepsilon_r, \varepsilon_v}$	Axial, radial, volumetric strain
$\mathbf{\theta}$	Wing crack inclination angle
$\mathbf{\lambda}$	Wave length/Lamé constant
$\mathbf{\mu}$	Coefficient of friction/shear modulus
$\mathbf{\nu}$	Poisson's ratio
$\mathbf{\rho}$	Density
$\mathbf{\sigma}$	Stress
$\mathbf{\sigma_1, \sigma_2, \sigma_3,}$	Principal stresses
$\mathbf{\sigma_{cc}}$	Crack closure stress
$\mathbf{\sigma_{ci}}$	Crack initiation stress
$\mathbf{\sigma_{cd}}$	Crack damage stress
$\mathbf{\sigma_t}$	Tensile stress
$\mathbf{\sigma_u}$	Uniaxial compressive stress
$\mathbf{\tau}$	Shear stress/relaxation time

1 Introduction

In the last decades, engineering progress enabled the construction of large underground openings in ever-greater depth and increasingly difficult geological environments. Major infrastructure projects could be realized in recent years, such as the Base Tunnels of Lötschberg, Gotthard and Brenner in the Alpine region, a number of underground constructions for hydroelectric power plants including the Niagara Tunnel Project as well as deep geological repositories for nuclear waste or underground research laboratories. The advancing depth and the construction of large underground caverns in difficult grounds still pose major challenges for engineers and geologists. As modern tunnels become longer, tunnel boring machines (TBM) are increasingly utilized for construction, since they are supposed to be more efficient than the drilling and blasting method.

1.1 Motivation

In deep tunneling, the major geological influence on construction effort, efficiency and costs are the primary stress conditions. High stresses in the rock mass increase the risk of stress-related instabilities of an underground cavity and several difficulties arise for the rock excavation process. In tunnel excavation in brittle, massive rock, the rock and rock mass conditions in the tunnel face are the main factors, which influence the TBM net performance. Important stress-related difficulties encountered in the tunnel face are

- Face instability due to stress-induced spalling (VILLENEUVE 2008)
- Low penetration rates due to poor chipping (VILLENEUVE 2008)
- Elevated wear of rock cutting tools because of high restraint (ALBER 2008b)

During rock excavation, the previously stressed rock mass is relieved and initially, elastic deformation occurs around the tunnel and ahead of the tunnel face. According to HOEK (1998), the radial deformation of a rock mass begins at about half a tunnel diameter ahead of the advancing tunnel face and it reaches about one third of the final displacement at the position of the tunnel face. The maximum deformation is reached about one and a half tunnel diameters behind the face. Resulting from the excavation of rock, the tunnel face deforms inward with a maximum in the center and a minimum in the outer areas of the face (Figure 1).

Deformation and stresses in the tunnel face are a function of the primary stresses in the rock mass. During the progressive advance of a tunnel, the stresses are redistributed and a secondary stress state establishes, forming an arch around the opening. At the excavation boundary, the radial stress drops to zero and the tangential stress increases. Tunnel excavation in high in-situ stress conditions involves stress rotation, stress relaxation and stress concentrations (MARTIN 1997). When the maximum tangential stress exceeds the rock mass strength, plastic deformation and rock failure occurs. In massive, brittle rock, stress-induced failure is usually violent and results in a spontaneous release of rock fragments from the tunnel wall in the form of spalling (slabbing) or even rock burst. Brittle failure has often been observed in the tunnel walls but also occurs in the tunnel face when the principal stresses at the tunnel boundary exceed the crack initiation stress (MARTIN 1993).

With three-dimensional numerical modelling, EBERHARDT (2001) and DIEDERICHS et al. (2004) analyzed the redistribution of in-situ stresses around the tunnel face. The results showed that the orientation and magnitude of the stresses ahead of the tunnel face change constantly during tunnel advance. The rotation of the principal stress axes is assumed to induce damage ahead of the face due to progressive fracture propagation. The magnitude of the stresses is not uniform over the diameter of the tunnel face. Increased stresses arise in the outer areas of the tunnel face, while reduced stresses or stress relaxation may occur in the center. An increase of the stresses in the outer areas of the tunnel face is illustrated in Figure 2 and the reduced principal stresses in the center of the face are given in Figure 3 (Rocscience Inc. 2014: *RS*^{3}). The efficiency of disc cutting may vary throughout the face, since it is strongly influenced by confining stresses, particularly in homogeneous, unjointed rock.

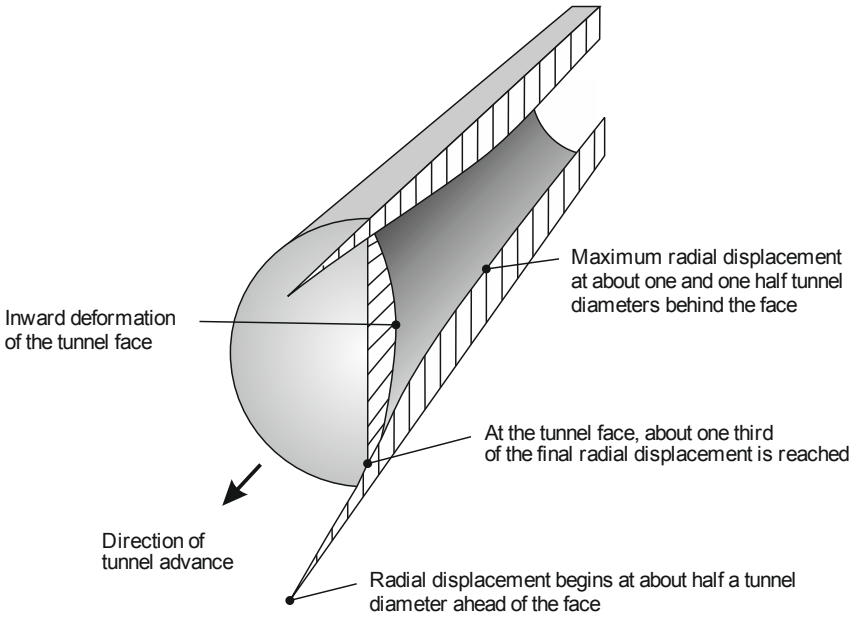

Figure 1: Schematic illustration of deformations around an advancing tunnel (after HOEK 1998).

Numerical modeling of the stress changes due to rock excavation showed that the inward deformation due to the relaxation of highly stressed rock can initiate tensile fractures parallel to the excavation face (VILLENEUVE 2008: 383-396). Stress-induced fractures in the face may improve the chipping process, which is necessary for an efficient TBM performance. Depending on the severity of induced damage in the tunnel face, the advance rate can also be reduced, when spalling or face instabilities occur (KAISER 2005). The time required for clearing the blocks in front of the drill head, the suppression of tensile crack formation under the disc cutters because of spalling and an increased wear can considerably reduce the TBM performance (VILLENEUVE 2015). Additionally, poor fracture propagation under the disc cutters due to a high ratio of rock strength to in-situ stresses in the face has a negative impact on the chipping process (VILLENEUVE 2008: 137).

Ahead of the tunnel face, at distances of at least half a tunnel diameter to several meters, tunnel excavation disturbs the initial stress field. Depending on the primary stress state, the principal stresses progressively change as rock excavation advances (EBERHARDT 2001). The stress path in the rock mass ahead of the face is, in reality, more complex than that achieved in laboratory tests when determining rock strength and deformation parameters. Increasing stresses acting on the rock volume ahead of the face may induce damage and thus affect the subsequent deformation and cracking behavior of the rock at the excavation face. The mechanical properties of the rock under the disc cutters thus differ from the mechanical properties determined in laboratory tests on intact rock.

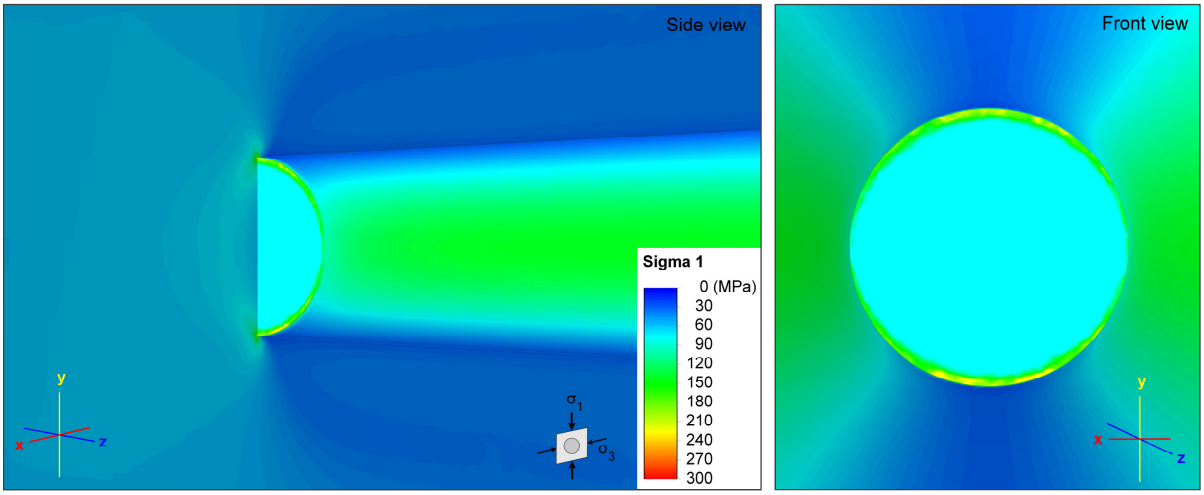

Figure 2: Three-dimensional numerical model (RS³) of an unsupported circular tunnel in a lithostatic stress field. The ratio of maximum to minimum principal stress σ_1/σ_3 is k=2 with σ_1=60 MPa and $\sigma_2 = \sigma_3$ = 30 MPa.

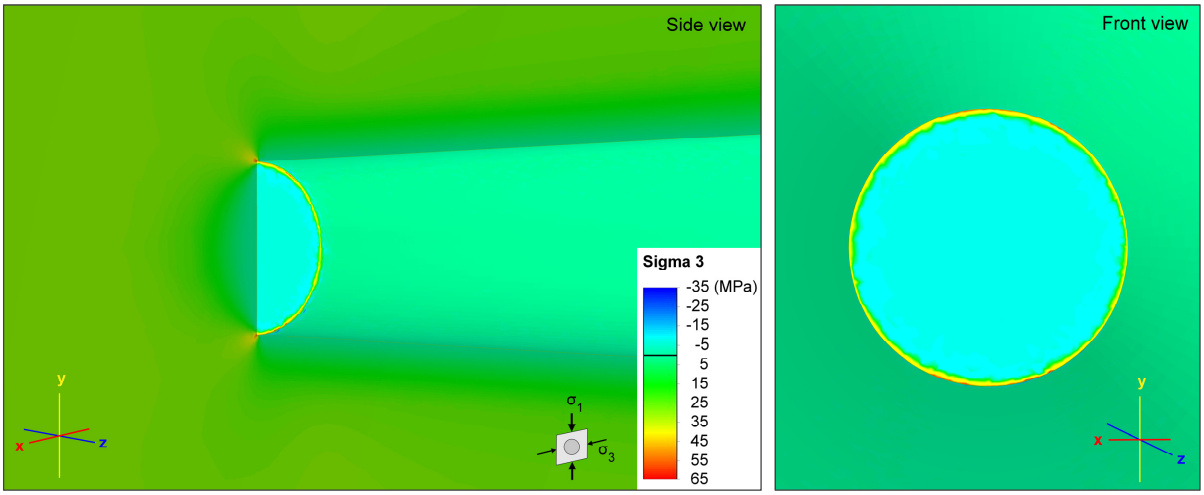

Figure 3: Three-dimensional numerical model (RS³) of an unsupported circular tunnel in a lithostatic stress field. The ratio of maximum to minimum principal stress σ_1/σ_3 is k=2 with σ_1=60 MPa and $\sigma_2 = \sigma_3$ = 30 MPa.

For projects in high-stress environments, laboratory tests for geotechnical investigations are usually conducted on core samples recovered from deep boreholes, but the core material may already have been altered before rock testing is performed. When a rock sample is removed from its initial stress environment, stresses are released, and the rock can expand to a new volume. An instantaneous elastic deformation may be followed by the generation of stress-induced microcracks (MEGLIS et al. 1991). As a drill core is recovered from depth, another possibility of crack formation is drilling-induced damage, which is caused by stress concentrations at the front of the drill bit (STACEY 1982). An extreme form of coring-induced sample disturbance is the phenomenon of core disking, which is observed at a sufficiently high in-situ stress state (MARTIN 1993). Changing temperature and water saturation as well as the sample preparation process may also induce microcracks and reduce the rock quality (HOLT et al. 2000). The question arises of how a previously induced stress damages the rock and how existing microcracks influence the deformation and cracking behavior of solid rock.

1.2 Scope of work and research objectives

In tunneling under high-stress conditions, the laboratory results of the deformation and strength parameters of rock do not represent the mechanical rock properties in the tunnel face. This is because the stress path in the rock volume ahead of the tunnel face is more complex than the standard loading conditions in the laboratory. In this thesis, the effect of stress-induced damage on the deformation and cracking behavior of solid rock is investigated. To evaluate the influence of previously induced cracks on the laboratory properties of rocks, a characterization of the mechanical and acoustic properties of different rock types is performed. A simplified stress path, similar to the stress evolution in an advancing tunnel face is applied to the rock specimens. In order to simulate the processes taking place in the rock mass ahead of the advancing face, changes in the stress magnitude are realized in laboratory tests. In uniaxial constant loading tests, the samples are loaded up to a defined stress level and the stresses are released after several minutes. A second standard uniaxial compression test is performed until the rock fails. Although a uniaxial state of stress cannot fully represent the multiaxial stress conditions in the excavation face, the applied loading procedure can be used to analyze the influence of damage on rock properties. Additional to laboratory investigations, a petrographic analysis of damaged rock samples is performed in order to gain information about the influence of mineralogy, rock fabric and structure on the deformation and cracking behavior of the tested rocks.

Furthermore, the time-dependent behavior of rocks, obtained from high primary stresses, is examined in this thesis. When a rock is recovered from its primary stress state, the stresses within the rock sample are released and strain relaxation takes place (WOLTER & BERCKHEMER 1989). Tensile microcracks are created within the rock so that the rock mechanical properties might change with time without applying a load. It must be noted that the mechanical properties determined in laboratory tests, do not represent the in-situ rock characteristics because of the time-dependent degradation of rock quality (HOLT et al. 2000). Since laboratory tests on rock samples are usually performed after a considerable period of time after drilling, stress relaxation has already occurred when the tests are performed and the in-situ properties can no longer be examined. In order to investigate the time-dependent behavior of core samples and the influence of relaxation-induced damage on the mechanical properties of rock, non-destructive testing techniques were applied to monitor the formation of microcracks in freshly extracted core material from a high in-situ stress environment.

Finally, the findings from laboratory and field tests are transferred to the processes and mechanisms in the tunnel face. Theoretical considerations on the deformation and cracking behavior in the tunnel face are presented, where the results of the mechanisms on the laboratory scale are applied. A conclusion is drawn on the effect of high primary stresses and the resulting stress changes on the net performance of TBM. The aims and objectives of this thesis can be summarized as follows:

1. Investigation of the time-dependent accumulation of rock damage as a result of stress relaxation of rock samples recovered from high primary stresses and the consequences of relaxation-induced damage on rock mechanical and acoustic rock properties.
2. Characterization of the deformation and fracture behavior of different rock types according to their stress-strain behavior and acoustic emission responses with a focus on the differences between brittle and ductile rock behavior.
3. Examination of the influence of stress changes and rock damage on the mechanical and acoustic properties of intact rock and comparison with the microcracking behavior on the microscale using fluorescent thin sections.

The thesis is organized as follows: The introduction gives an overview of the motivation and the research objectives. It is followed by a literature overview on the basics of deformation and fracture of rocks with a focus on the formation of microcracks in rocks. The chapter includes a review on the mechanistic theories about fracture initiation and on the theories on the deformation and fracture behavior of rocks under uniaxial compression. In the methodology, the applied techniques are presented and a detailed description of the data analysis of acoustic emission monitoring tests and fluorescent thin section images is given. The results are provided Chapter 4 to Chapter 6. Chapter 4 presents the results from the field-work conducted underground to monitor the time-dependent accumulation of rock damage during stress relaxation of fresh core material. In Chapter 5, a characterization of the rock mechanical and acoustic properties of several rock types are given and in Chapter 6, the results from preloading tests are presented and the influence of damage and stresses on rock properties are discussed. Chapter 7 gives an interpretation on the transferability of the experimental findings to the in-situ conditions in TBM tunneling in high primary stress environments. Furthermore, it provides the contributions of this work to the current understanding of the processes and mechanisms of deformation and fracture in the tunnel face. Chapter 8 summarizes the conclusions from laboratory tests and fieldwork. The outlook provides recommendations for further research on the mechanisms of deformation and fracture within the tunnel face as well as on the effect of high stresses on the advance rates of TBM. Laboratory tests are proposed to examine the influence of stress rotation on microcrack propagation in rocks.

2 Fundamentals of deformation and fracture

For underground construction and subsurface mining, the knowledge about the deformation and fracture behavior of rock masses and rock is essential. The study of the mechanical behavior of rock is the focus of rock mechanics research and investigations on rock mechanical behavior of rock masses usually begin with the examination of rock samples in the laboratory. For an experimental approach on rock properties, the simplifying assumption of an intact homogeneous rock is made. Although, on the rock mass scale, joints can have a decisive influence on the engineering effort of underground excavation, this simplification is necessary to understand the processes leading to rock failure on a smaller scale.

2.1 The formation of microcracks in rock

The following review of existing research on brittle rock failure thus begins with flaws and cracks on the atomic and microscopic scale. On a macroscopic scale, the state of research on laboratory deformation and cracking behavior of rock specimens under stress is briefly summarized. The deformation and cracking behavior of intact rocks is controlled by its mineral content and structure. To understand the processes involved in rock fracture, a summary of deformations on the atomic scale is given, since the nucleation of fracture begins with the breaking of atomic bonds.

2.1.1 Defects in the crystal lattice

An ideal crystal has a perfectly regular lattice without any impurities or imperfections. In reality, an ideal crystalline lattice does not exist, but all crystalline materials contain crystallographic defects, which are sources of internal stresses (KUNIN 2012: 122). Crystal lattice defects include point or atomic defects like chemical impurities as well as structural defects like vacancy defects or interstitial defects (Figure 4). Line defects imply edge dislocations or screw dislocations (Figure 5) and a third group of lattice defects are planar defects, which include stack errors, twinning or low angle grain boundaries (BORCHARDT-OTT 2009: 299 ff.).

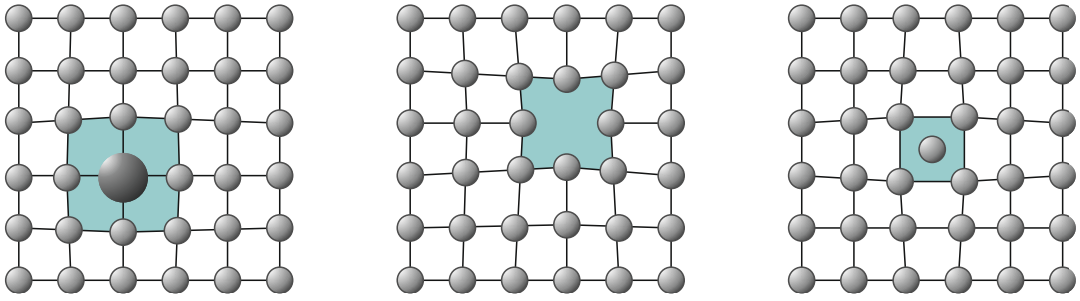

Figure 4: Examples of point defects in crystalline structures. Chemical impurity (left), vacancy defect (middle) and interstitial defect (right) (after BARGEL & SCHULZE 2012: 7).

Every deviation from the ideal periodical lattice structure increases the energy content of a crystal. Atomic defects in the crystal lattice may occur when the thermodynamic equilibrium is disturbed during the formation of the crystal or by an increase in energy caused by mechanical deformation. In an ideal lattice structure, the minimum bonding energy corresponds with the ideal distance between the atoms. When a crystallographic defect disturbs the equilibrium distance, the binding energy between the atoms increases. Interfaces with the highest surface energies are (high-angle) grain boundaries as well as free

surfaces (BARGEL & SCHULZE 2012: 5 f.). Lattice imperfections cause internal stresses and thus have an important influence on mechanical properties of the crystals. For the understanding of the deformation and cracking behavior of rocks, the knowledge about crystallographic defects are essential, since mechanical properties of rocks are ultimately controlled by the atomic structure of its constituents.

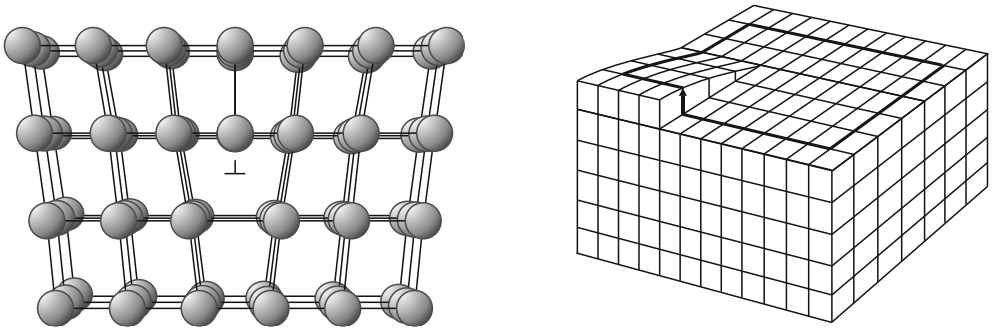

Figure 5: Line defects in crystalline structures. Edge dislocation ⊥ (left) and screw dislocation (right) (after GOTTSTEIN 2013: 80).

2.1.2 Definition of microcracks in rocks

Crystalline rocks contain different types of inherent microcracks, which originate from the formation and the stress history of the rock. SIMMONS & RICHTER (1976) defined microcracks as "an opening that occurs in rocks and has one or two dimensions much smaller than the third." According to their definition, the width to length ratio (crack aspect ratio) of a flat microcrack is less than 10^{-2} and is typically between 10^{-3} and 10^{-5}. The typical length is in the order of 0.1 mm or less but microcracks can also extend up to meters. ENGELDER (1987: 31) define microcracks as planar discontinuities with a length of 0.1 to 1 mm and a width of about 1 µm. SIMMONS & RICHTER (1976) recognized four groups of microcracks. Grain boundary cracks are associated with the boundaries between grains, intragranular cracks lie within one grain and intergranular cracks extend from a grain boundary to the two adjacent grains without reaching a second grain boundary. When intergranular cracks cross more than one grain boundary and more than two grains, they are called multigrain cracks. KRANZ (1983) adds the term "transgranular crack" for cracks extending between two grain boundaries and he separately lists cleavage cracks as a subset of intragranular cracks, which occur along parallel cleavage planes within a mineral. The crack walls of cleavage cracks are usually sharp and are oriented parallel to each other. SPRUNT & BRACE (1974: 144) distinguish between high aspect ratio cracks (HARC) and low aspect ratio cracks (LARC). The LARCs show widths smaller than 1 µm and are typically 1/10 of the grain size. In unstressed rock, they typically show round ends and some are bridged by uncracked material. High aspect ratio cracks are narrow and exhibit sharp crack tips. They are typical for brittle failure and are formed when the rock is stressed. TAPPONNIER & BRACE (1976) observed that stress-induced cracks usually have sharp rims and a nearly constant width.

In general, microcracks nucleate at minor flaws or defects in the crystal lattice as well as on grain boundaries, cleavage planes or healed cracks (TAPPONNIER & BRACE 1976: 105). Stress-induced microcracks in rocks are generated when the local stresses exceed the local strength (SIMMONS & RICHTER 1976). KRANZ (1983) names six mechanisms of mechanical stress, which can nucleate and generate cracks. These are the interaction of twin lamellae with grain boundaries and other twins, the release of stored strain energy of kink bands, deformation lamellae and cleavage planes. Those are the planes in a crystal showing the lowest bond density and strength. Another mechanism are stress concentrations near grain boundaries, cavities and crack tips, where point and line contacts concentrate high stresses. In this case, crack growth results from tensile stresses exceeding the local tensile strength of the minerals. When the

elastic properties of adjacent grains mismatch, extensional cracks may develop in the stiffer mineral. Grain translation and grain rotation may occur under confining pressure in the form of grain boundary sliding in crystalline rocks and especially as motion along grain boundaries in sedimentary rock.

2.2 Introduction to the theories of deformation and fracture

The failure of rock always begins with rock deformation and the generation of microcracks. For investigations on the process of rock failure, theories have been developed in the last century to describe the deformation and cracking behavior of rocks.

2.2.1 The theory of elasticity

The deformation behavior of rock is often approximated with the theory of elasticity. Elasticity is the capability of a deformed isotropic material to return to its original shape after the applied force is removed. The theory of elasticity is valid for small deformations, moderate temperature, pressure and stress conditions (GUÉGUEN & PALCIAUSKAS 1994: 80). At the atomic scale, linear elasticity means that applied shear stress causes stretching of atomic bonds and upon removal of the stresses, the deformations are completely reversed. The linear relation between stress and strain is described by Hooke's law, which states that a force needed to extend or compress a spring is directly proportional to the deformation and is only dependent on the stiffness of the spring. Applying Hooke's law to rock mechanics, the stress-strain-relation can be written as

$$\sigma = E\,\varepsilon \tag{1}$$

where stress σ and strain ε are linearly dependent and are influenced by the modulus of elasticity E (BOURBIÉ et al. 1987, BELTZER 1988). For different deformation modes, various elastic moduli exist, such as the Young's modulus for compression and tension, the shear modulus for shear deformation and the bulk modulus as a measure for uniform compression (GUÉGUEN & PALCIAUSKAS 1994: 84). Elasticity is a simplifying assumption for rock material, which is only valid in the linear segment of a stress-strain relation. Dependent on the physical environment as well as the stress and the strain rate, the deformation behavior of rocks can generally be described by a combination of the models of elasticity, viscosity and plasticity (HAWKES & MELLOR 1970: 195 f.). Most natural materials like rocks show an elastoplastic deformation behavior over a large range of the applied stresses. This means that above a characteristic yield stress, plastic deformation may permanently deform a material in response to an applied force (JAEGER et al. 2007: 252).

2.2.2 The Griffith theory of brittle fracture

Above a characteristic stress threshold, the theory of elasticity is no longer valid. Instead plastic deformation causes fracturing of the solid. The study of crack formation in a material has a long history and a number of mechanistic fracture theories were established. The investigation of crack propagation started with the work of GRIFFITH (1920, 1924), who introduced a theoretical approach for brittle fracture. He postulates that the strength of a brittle material is governed by the presence of a preexisting flaw, the so-called *Griffith flaw*. Griffith established a criterion for an infinite, isotropic plate of glass, containing an isolated elliptical crack (Figure 6). He found that a uniform tensile load applied perpendicular to the major axis of the crack causes large tensile stresses at the crack tip. The Griffith theory of brittle fracture is based on the assumption that crack initiation occurs when the tensile stress at the crack

tip exceeds the theoretical stresses needed to break the atomic bonds. The highest stress concentrations occur at the crack tips of an elliptical flaw and decrease with an increasing distance from the crack tip (LAWN & WILSHAW 1975: 3 f.).

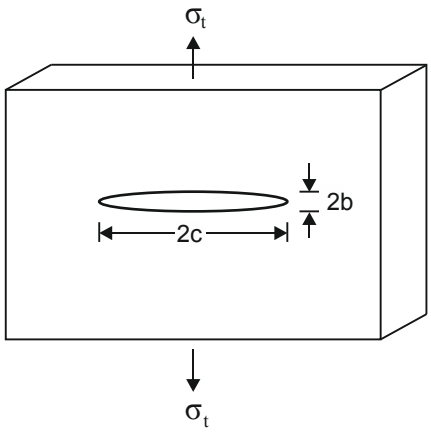

Figure 6: For his theory of brittle fracture, Griffith assumed an isotropic plate containing an isolated elliptical crack with a length 2c and a width 2b, subjected to uniform tensile stresses σ_t (after LAWN & WILSHAW 1975: 2).

Experiments showed that the critical stress required for crack initiation is far below the values for the cohesive strength between the atoms. As a reason, Griffith suggested that naturally existing flaws in a material raise the stresses at the crack tip above the molecular cohesive stress. The basis for his theory is the fact that atoms are in a stable equilibrium when they are arranged in a defined distance to each other. In order to break the atomic bonds, a force needs to be applied to increase the distance between the atoms. The further the atoms are separated, the higher becomes the bond energy (Figure 7: 1–2). As soon as the atoms are separated far enough, the bond energy will decrease and the crack will start to extend (GRIFFITH 1920: 186 f.). The resistance against breaking bonds at the crack tip is known as the fracture toughness (PASSCHIER & TROUW 2005).

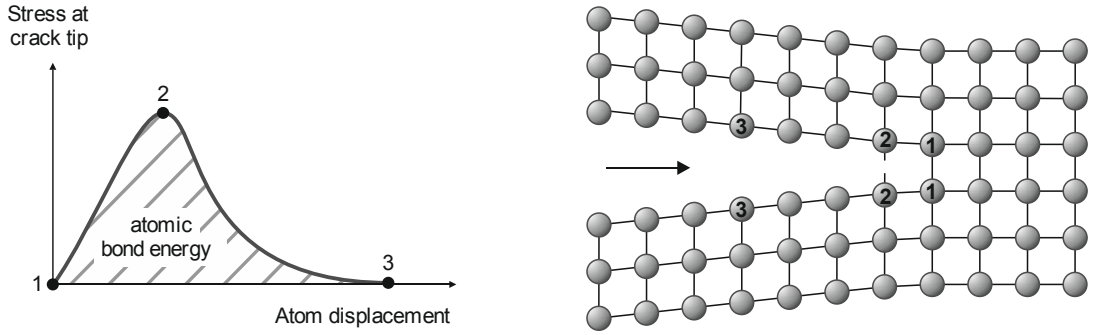

Figure 7: Relationship between tensile stresses at the crack tip and atom displacement. When tensile stresses and thus atom displacement at the crack tip exceed a critical value (2), the atomic bonds break and the crack propagates (after www-1).

The Griffith criterion of fracture is based on an energy balance for crack propagation. The criterion describes that a crack will propagate under a constant stress if an increase in the crack length and thus an increase in the surface area of the crack does not change the total energy of the system. The total energy of the system is the sum of the energy applied by the loading system, the elastic strain energy and the surface energy:

$$E_{total} = E_{loading} + E_{strain} + E_{surface} \quad (2)$$

For crack growth, the cohesive forces of the atoms need to be overcome in order to create two new crack surfaces. An increase in the crack surface area requires additional energy. Following the laws of energy conservation, the increased surface energy due to crack growth must be compensated by a decrease in the elastic strain energy. The elastic strain energy stored in the medium is dependent on the applied load and is released as the crack extends. Under a constant applied stress, the total potential energy of the loading system and the strain energy is equal to the negative elastic strain energy (LAWN & WILSHAW 1975: 5–9):

$$-E_{strain} = -E_{loading} + E_{strain} \tag{3}$$

In Figure 8, the total energy of the system, the surface energy and the released strain energy $-E_{strain}$ are plotted. While the surface energy is a function of the crack length and is constant per unit area, the released strain energy is a function of the squared crack length and is thus parabolic. The critical condition for crack extension is the maximum of the total energy curve. This means that stable crack growth of small cracks requires additional strain energy and at a constant stress, crack propagation will terminate. When the critical crack length c_c for crack extension is reached, the released strain energy becomes higher than the surface energy and the total energy is reduced. From the point of maximum total energy, more energy is released than is consumed by crack propagation. Beyond a critical crack length, unstable crack growth and fracture of the specimen occurs (LAWN & WILSHAW 1975: 5–9, ZANG & STEPHANSSON 2010: 44–47).

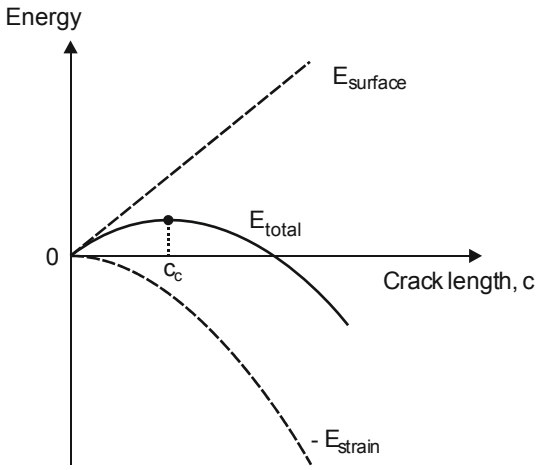

Figure 8: Energy consideration of a Griffith crack under uniform tension related to the crack length (after LAWN & WILSHAW 1975: 8).

Griffith found that the critical tensile stress at the crack tip is dependent on the length of the preexisting microcrack. He states that the tensile stress σ_t, necessary to cause crack growth is dependent on the surface energy per unit area γ_s, the Young's modulus E and the crack length 2c. The following equation results in the tensile stress, required for crack initiation.

$$\sigma_t = \sqrt{\frac{2\,\gamma_s E}{\pi\, c}} \tag{4}$$

The equation indicates that an increasing crack length reduces the critical stress for crack propagation. Whether stable crack growth or unstable crack growth occurs is thus strongly dependent on the crack length (BIENIAWSKI 1967).

The application of the original Griffith theory was limited to tensile stresses applied to an open crack. Therefore, GRIFFITH (1924) extended his theory to compressive stresses. He assumed that crack growth initiates from the largest, most critically oriented crack. For a biaxially stressed solid, the *biaxial Griffith criterion* is expressed as a relation between the principal stresses σ_1 and σ_3 and the tensile strength σ_t:

$$-8\sigma_t = \frac{(\sigma_1 - \sigma_3)^2}{(\sigma_1 + \sigma_3)} \tag{5}$$

For his fracture initiation criterion, Griffith assumed an open elliptical crack. However, under compression, crack closure occurs before crack growth begins so that friction at the crack faces needs to be overcome before (HOEK & BIENIAWSKI 1965: 8). In Griffith's extended theory of cracking, the influence of friction acting on closed cracks was not yet considered. MCCLINTOCK & WALSH (1962) thus developed the *modified Griffith criterion* for crack initiation under compressive stress conditions. They considered frictional slip along closed cracks, which results in tensile stress concentrations at the crack tips. Including the coefficient of friction μ between the crack faces, the McClintock-Walsh criterion is given by

$$\sigma_t = \frac{\sigma_1}{4}\left[\left(\mu^2 + 1\right)^{1/2} - \mu\right] - \frac{\sigma_3}{4}\left[\left(\mu^2 + 1\right)^{1/2} + \mu\right] \tag{6}$$

where σ_t is again the tensile strength and the principal stresses are σ_1 and σ_3.

2.2.3 An introduction to fracture mechanics

With the introduction of Griffith's theory of fracture, an extensive research on fracture propagation processes in rocks started. From the first studies of GRIFFITH (1920, 1924) and IRWIN (1957), the field of fracture mechanics developed, which deals with the study of stress concentrations at crack tips and the conditions for crack propagation (ATKINSON 1987: 2). In linear fracture mechanics, a single, ideal crack with zero thickness, a sharp crack tip and linear elastic conditions are assumed. Three fundamental modes of crack propagation are considered, which are dependent on the orientation of the applied forces (Figure 9). Mode I is the tensile or opening mode, which occurs when tensile stresses are applied normal to the crack plane. Mode II is the in-plane shear or sliding mode, referring to the shear stresses applied in the direction of the crack plane. Mode III is the anti-plane shear or tearing mode, where shear stresses are applied perpendicular to the crack plane or parallel to the orientation of the crack tip line (ATKINSON 1987: 5).

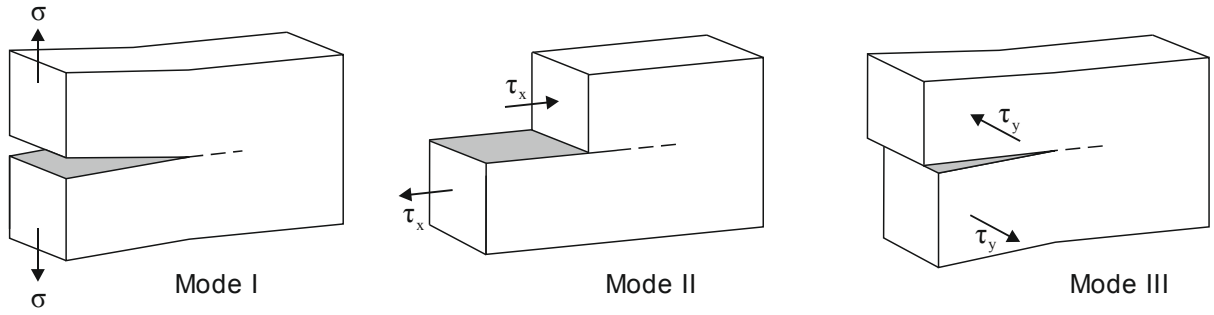

Figure 9: The three basic modes of fracture dependent on the applied forces. Mode I: tensile mode, Mode II: in-plane shear mode, Mode III: anti-plane mode (after ATKINSON 1987: 5).

The most commonly observed type of crack extension is the Mode I type (KRANZ 1983: 462). In crystalline rocks, microcracks can show more complex shapes, especially when the crack tip propagates toward an inhomogeneity or an adjacent crack (PASSCHIER & TROUW 2005: 26). Furthermore, in a natural material with irregularly distributed cracks, the orientation of applied stresses will mainly cause mixed modes of fracture.

In order to determine the critical stress at the crack tip, required to initiate crack growth, the stress intensity is analyzed assuming linear elasticity. For each mode of cracking, the stress distribution near the crack tip in the plane of the crack can be determined using the stress intensity factors K_I, K_{II} and K_{III} (JAEGER et al. 2007). In Mode I for example, the stress component σ_{yy} near the crack tip is written as

$$\sigma_{yy} = \frac{K_I}{\sqrt{2\pi x}} \qquad \text{with} \quad K_I = \sigma \sqrt{(\pi c)} \tag{7}$$

where x is the distance from the crack tip, σ is the applied stress normal to the crack and 2c is the crack length. The stress intensity factor only depends on the applied stress and the crack length. It is a characteristic material property and can be determined experimentally. A crack will propagate when the stress intensity factor reaches a critical stress intensity factor K_{IC}, which is also known as the fracture toughness of a rock (PATERSON & WONG 2005: 241 f.):

$$K_I = K_{IC} \tag{8}$$

In compressive loading, a common model for the description of crack initiation is the *sliding crack model*. BRACE & BOMBOLAKIS (1963) first showed that preexisting cracks, inclined with respect to the major principal stress, propagate by forming axial tension cracks at the tips of the major crack. The sliding crack model generally considers closed and inclined preexisting flaws of length 2c and an angle γ with respect to the major principal stress σ_1 (Figure 10). Under confining pressure, the preexisting cracks are closed and shearing occurs along the crack planes.

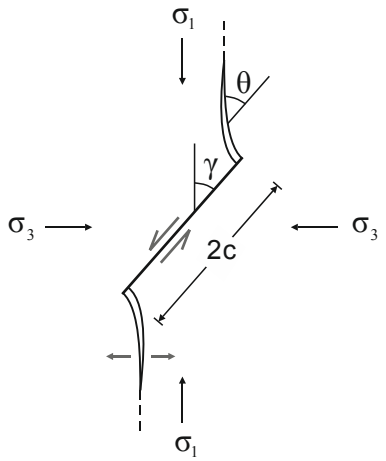

Figure 10: Sliding crack model with a wing crack nucleating from the crack tips of a closed and inclined crack, which is subjected to confining pressure. The preexisting crack of length 2c is inclined at an angle γ and wing cracks propagate from the sliding crack at an angle θ (after PATERSON & WONG 2005: 117).

The sliding motion induces stress concentrations at the edges of the crack. When the critical stress intensity factor is reached, wing cracks nucleate and propagate at the crack tips of the sliding crack at an angle θ with respect to the major stress direction (PATERSON & WONG 2005: 116 f.). With an increasing

length of the wing crack, crack propagation causes a decrease in the stress intensity factor so that stable crack growth occurs. Furthermore, the wing crack gradually aligns to an orientation parallel to the major principal stress until $\theta = \gamma$ (PATERSON & WONG 2005: 120). The sliding crack model is a mixed mode of fracture, since in-plane shear (Mode II) occurs at the major preexisting crack and tensile crack propagation occurs at the wing cracks (Mode I) (ZANG & STEPHANSSON 2010: 49). Crack propagation will also be initiated at further cracks oriented at less optimal angles. When the local stress fields of the extending wing cracks interact, the sliding crack model is no longer applicable but other models need to be applied for studying the processes of crack interaction (PATERSON & WONG 2005).

In rocks, the simplifying assumption of a single, ideal crack and linear elastic behavior is only valid on the microscopic scale. Nonlinear fracture mechanics describes the inelastic processes, occurring in a so-called *process zone* ahead of a propagating microcrack (ZANG & STEPHANSSON 2010: 58). In Figure 11, the assumption of linear elastic fracture mechanics is compared with nonlinear fracture mechanics for Mode I cracks. Assuming nonlinear conditions, instead of creating a pair of new crack surfaces, a process zone develops where isolated microcracks form ahead of a propagating tensile fracture. IRWIN (1957) first described the process zone in metals as a region of large plastic deformation near the crack. The system behavior near the crack tip becomes nonlinear as the number and density of cracks increases during loading. When some of the microcracks of the process zone interact and coalesce, a distinct crack forms and the pre-existing crack propagates (ATKINSON 1987: 12 f.).

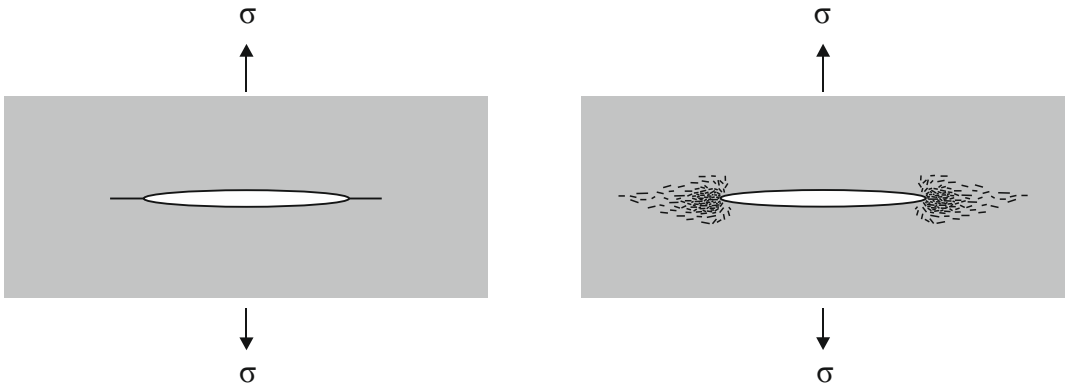

Figure 11: Models of crack propagation in Mode I a) in linear fracture mechanics compared to the assumption of b) nonlinear fracture mechanics, where a process zone ahead of the crack tips is assumed (after BRADY & BROWN 2006: 108).

In general, fracturing means that planes of separation are formed in rock when atomic bonds are broken and new crack surfaces develop. The theories of fracture describe the process of crack initiation on the microscopic scale und thus can contribute to the understanding of the physical processes leading to failure. However, rocks subjected to compression usually do not fail directly at the onset of crack initiation. Instead, the interaction and coalescence of a number of cracks will lead to macroscopic fracture at a considerably higher stress level than the crack initiation stress. Crack interaction occurs if two local stress fields of neighboring cracks overlap. Crack coalescence is the interaction of initially separated cracks, growing together (ZANG & STEPHANSSON 2010: 58).

2.3 Deformation behavior during uniaxial compression

The introduction of the Griffith theory and the subsequent advances in fracture mechanics constitute an important step toward a better understanding of the failure process of rock. The theories of rock fracture, however, mostly deal with the initiation of microcracks but they cannot be transferred to the complete fracturing processes until final rupture of the rock. Therefore, extensive studies have been conducted on the deformation behavior of rocks under compression. BRACE et al. (1966) and BIENIAWSKI (1967) postulated a mechanism of brittle rock fracture, which is generally accepted and has been extended and applied by many authors (MARTIN 1993, EBERHARDT et al. 1998, DIEDERICHS et al. 2004, CAI et al. 2004, AMANN et al. 2011). During unconfined compression of rock samples, axial and radial strain are measured directly, whereas the volume change or volumetric strain $\varepsilon_{volumetric}$ can be calculated from the measured strains (RICHART et al. 1928: 19):

$$\varepsilon_{volumetric} = \varepsilon_{axial} + 2\,\varepsilon_{radial} \tag{9}$$

In the study of rock fracture, COOK (1965) and KNILL et al. (1968) introduced the technique of acoustic emission (AE) testing during the compression of rocks. The method uses the effect that every abrupt deformation in an elastic medium releases stored elastic strain energy and an elastic wave is generated. The elastic stress wave travels through the medium and can be detected as an acoustic emission at the surface of the rock. According to EBERHARDT (1998), AE can originate from dislocations, grain boundary movement and from the propagation of cracks. The shape of an acoustic wave is dependent on the released energy and on the acoustic properties of the wave source (KNILL et al. 1968: 88). In a perfectly elastic, isotropic medium, wave propagation would occur without energy loss or attenuation. Natural materials like rock, however, show a certain degree of inelasticity, meaning that the energy of elastic waves decreases with the distance from the source and the waves are attenuated.

2.3.1 The five phases of rock deformation

From the stress-strain curve, five stages of rock deformation are defined according to BIENIAWSKI (1967). The generation of acoustic emissions demonstrates the process of brittle fracture in the proposed phases (Figure 12).

I. Crack closure

The mechanism of brittle fracture is based on the assumption that microcracks are already present in a rock before the material is stressed. The preexisting flaws like grain boundaries and intracrystalline interfaces are randomly distributed in the rock. In the first stage of uniaxial loading, crack closure takes place. Cracks oriented at a sufficiently large angle to the applied stress close, while cracks parallel to the major principal stress may stay open. In the stage of crack closure, the stress-axial strain curve is non-linear and the slope of the curve increases until the crack closure stress σ_{cc} is reached. The radial strain curve, in contrast, is not affected by crack closure so that it rises steeply without departing from linearity. OHNAKA & MOGI (1982) found that AE activity is low during the first stage, when preexisting microcracks close in the form of a movement along the crack faces. The work of EBERHARDT (1998) suggests that some of the recorded events may also result from the initial coupling of the sample with the loading platens.

II. Linear elastic deformation

In the stage of linear elastic deformation, the stress-strain curves are linear and the modulus of elasticity is constant. Although during this phase, primarily elastic deformation takes place, small displacements in the form of sliding along initial cracks may occur. At irregularities along the crack faces, short crack extensions may develop during this phase. In the stage of linear elastic behavior, the elastic constants, Young's modulus and Poisson's ratio, are determined. After crack closure, the number of AE is lowest in the elastic region when the stress concentrations at the crack tips are too low to induce crack propagation (OHNAKA & MOGI 1982).

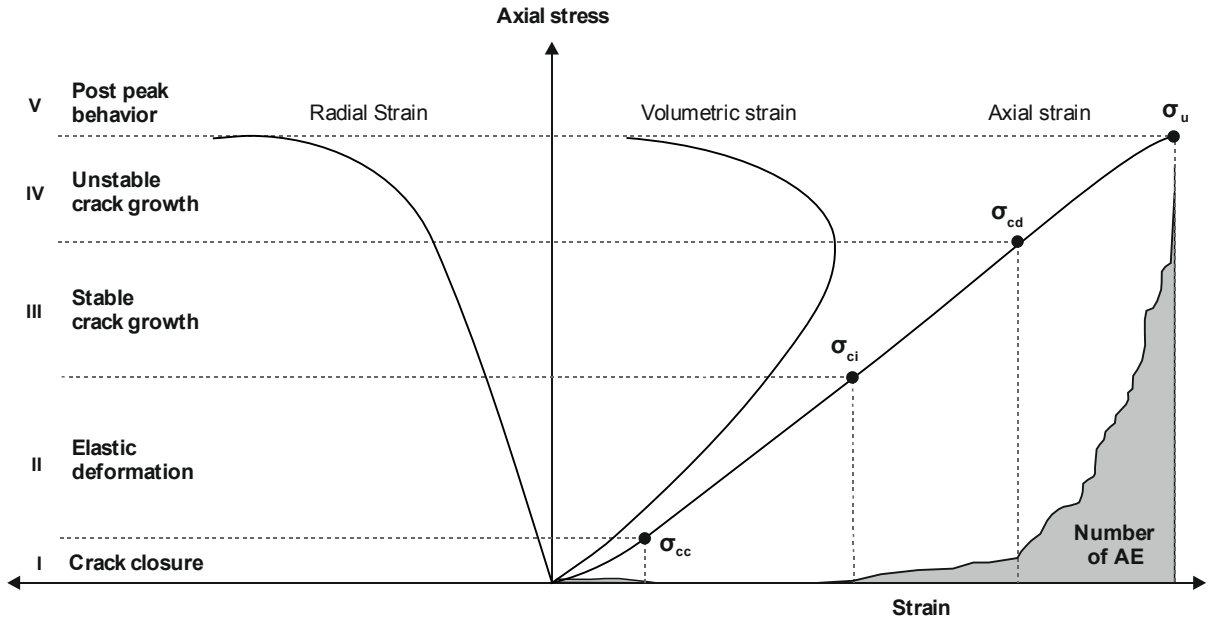

Figure 12: Typical stress-strain curves with the stages of brittle fracture of rock until peak stress and the number of acoustic emissions.

III. Crack initiation and stable crack growth

The stress level when microcracks initiate and propagate from existing defects and flaws is the crack initiation stress σ_{ci}. With the beginning of this phase, short cracks near the crack tip extend and shearing along the closed crack faces occurs. The transition from elastic deformation to the beginning of plasticity is marked by the onset of nonlinearity of the stress-radial strain curve. According to the theory, the axial strain is still linear during the phase of stable crack growth. During this stage, stable fracture propagation takes place and cracks propagate mainly parallel to the principal stress direction. Failure will not occur in that phase even if a constant stress is applied for a long period. In scanning electron microscopy (SEM), FONSEKA et al. (1985) observed only few cracks below the crack initiation stress, whereas above this stress level, small grain boundary and intergranular cracks with lengths of few µm to tens of µm and widths of about 0.1 µm developed. The crack initiation stress can be described with the Griffith criterion of Equation (4) or the McClintock & Walsh criterion of Equation (6) (BIENIAWSKI 1967). The beginning of crack growth coincides with a significant increase in the AE activity. EBERHARDT (1998) found that several AE characteristics like signal energy and event duration increase with the beginning of crack initiation. The crack initiation stress is characteristic for the tested material and is usually given as the percentage of the maximum stress.

Several methods for determining the onset of crack initiation are summarized in Subsection 2.3.2. The results of crack initiation stresses determined for different rock types are given in Table 1. NICKSIAR & MARTIN (2013) tested a number of rock types and found an average crack initiation stress for samples tested under uniaxial compression between 42 and 47 %. Under triaxial compression, they found a crack initiation threshold between 50 to 54 % of the peak stress.

IV. Crack damage and unstable crack growth

When the stress level of critical energy release is exceeded, unstable fracture propagation begins. In this stage, fracture propagation and crack coalescence occur mainly in the direction of the compressive stress. When the stress shadows at crack tips overlap, microcracks begin to interact. Substantial damage takes place within the rock in the form of grain shattering and macroscopic fracture (BIENIAWSKI 1967). In the phase of unstable crack growth, rock failure will occur, if the applied stresses are constant, meaning that fracturing becomes a self-maintaining process. The transition between stable and unstable fracture propagation is also referred to as crack damage stress σ_{cd} (MARTIN 1993: 84). This stress level is a characteristic material property and is considered as the long-term strength of rocks (BIENIAWSKI 1967). It is determined from the reversal of the volumetric strain curve, which is the result of the departure from linearity of the axial strain as well as a considerable increase in the radial strain (Figure 12). EBERHARDT (1998) assumes that the increase in axial strain is due to the coalescence of cracks.

From numerical modelling, DIEDERICHS (2007) presumes that the volumetric strain reversal is dependent on the testing system and is not a reliable indicator for the onset of systematic damage of rocks, since it overestimates the yield threshold. Instead, the yield in rocks is supposed to be better marked by the stress level at which the stress-axial strain curve begins to deviate from linearity. In DIEDERICHS et al. (2004), the authors showed that the thresholds of systematic damage determined from the reversal of the volumetric strain curve and from the nonlinearity of the stress-axial strain curve increasingly diverge with increasing confinement. For uniaxial compression, however, both methods revealed similar stress thresholds. Therefore, the reversal of the volumetric strain as well as the onset of an increasing number of acoustic events are used to determine the crack damage threshold of the tested rocks. The advantage is that the reversal is a parameter that can be easily calculated. A summary of crack initiation and crack damage thresholds for different rock types is given in Table 1. For most rock types, the crack damage stress is between 70 to 85 % (MARTIN 1993: 84).

Table 1: Examples of crack initiation and crack damage for different rock types in percentage of the uniaxial compressive stress.

Rock type	σ_{ci} (%)	σ_{cd} (%)	Authors
Westerly granite	30-60		BRACE et al. (1966)
Marble	45-65		BRACE et al. (1966)
Aplite	40-72		BRACE et al. (1966)
Norite	35	73	BIENIAWSKI (1967)
Grey Lac du Bonnet granite	40	80	MARTIN (1993)
Pink Lac du Bonnet granite	40	76	EBERHARDT et al. (1999a)
Dolomite	52-98	90	HATZOR & PALCHIK (1997)
Opalinus clay	18-36	43-90	AMANN et al. (2011)

V. Failure and post peak behavior

At peak stress, rock failure occurs representing the uniaxial compressive strength σ_u. The maximum strength of rocks is not an inherent material property but is dependent on the loading conditions of the test (MARTIN 1993). If a post-failure phase exists, the stress decreases with increasing strain but a certain strength and cohesion is still apparent until final sample collapse. This stage is characterized by crack coalescence, the formation of macrocracks and it culminates in the rupture of the sample. According to THURO (1998: 60), a post-failure range occurs in rock types with a ductile failure behavior, whereas in rock types with a brittle failure behavior total collapse occurs at peak stress or shortly after. Since the post-failure behavior of rocks is very diverse, it is not represented in the typical stress-strain curve in Figure 12.

2.3.2 Determination of the crack initiation stress

Several methods for the determination of the crack initiation stress have been established and are summarized in NICKSIAR & MARTIN (2012). The most common approach for determining the onset of crack initiation uses the deviation of the radial (lateral) strain curve from linearity (BIENIAWSKI 1967, LAJTAI 1974). The initial curvature of the curve represents the crack closure stress, linear elastic deformation occurs during the linear part of the radial strain and with the deviation from linearity, crack propagation begins (Figure 13a). EBERHARDT (1998), however, observed that the stress-lateral strain curve is never truly linear so that the determination of the crack initiation stress can be very subjective. Another method, developed by BRACE et al. (1966) uses the stress-volumetric strain curve. It is one of the earliest methods, where the deviation from linearity is used similar to the lateral strain method (Figure 13b). Since cracks mainly propagate parallel to the loading direction, no considerable change in the axial strain occurs with the onset of crack initiation but only the lateral strain is affected. Thus, the volumetric strain also changes with crack initiation.

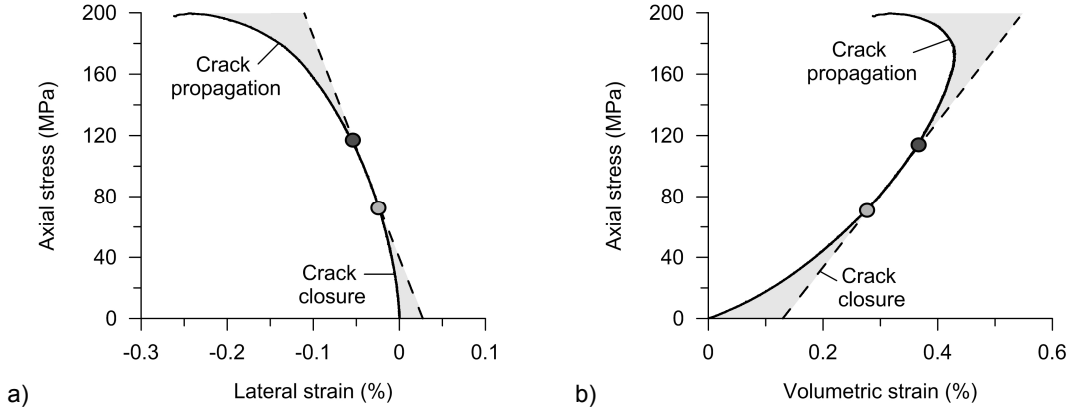

Figure 13: a) Lateral strain method by LAJTAI (1974) and b) volumetric strain method first proposed by BRACE et al. (1966) for the determination of the crack closure stress and the crack initiation stress.

Based on the volumetric strain method, MARTIN (1993) proposed to use the curve of the crack volumetric strain versus axial strain curve (Figure 14). In order to determine the portion of the volumetric strain that is influenced by axial cracking, MARTIN (1993: 79) introduced the crack volumetric strain $(\Delta V/V)_{cr}$. It is defined as the volumetric strain $(\Delta V/V)$ minus the elastic volumetric strain $(\Delta V/V)_{el}$

$$\left(\frac{\Delta V}{V}\right)_{cr} = \frac{\Delta V}{V} - \left(\frac{\Delta V}{V}\right)_{el} \tag{10}$$

In Equation (10), the elastic volumetric strain is calculated from the elastic constants E and ν (MARTIN 1993: 79). This method is strongly dependent on the accuracy of the elastic constants. Since the Poisson's ratio is difficult to determine especially when the lateral strain curve does not show a truly linear segment.

NICKSIAR & MARTIN (2012) proposed the Lateral Strain Response (LSR) Method, which is a mathematical and less subjective approach. The method uses the stress-lateral strain curve and the onset of unstable crack growth (Figure 15). A linear reference line is drawn from the crack damage to zero stress and the difference between loading response and the reference line is calculated. The maximum difference and thus the largest curvature of the lateral strain curve marks the onset of crack initiation.

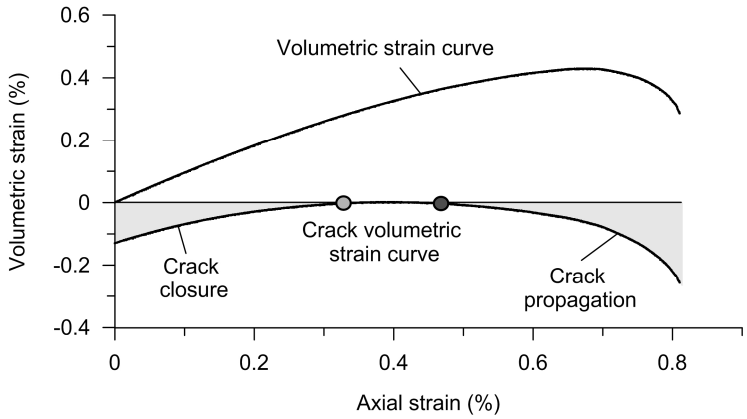

Figure 14: Crack volumetric strain method by MARTIN (1993) as an extension of the volumetric strain method.

Another method for determining the cracking behavior during compression is the acoustic emission technique. Several authors (OHNAKA & MOGI 1982, EBERHARDT et al. 1999a) applied the technique to determine the crack initiation stress. When the stress concentrations at the crack tips exceed a critical value, crack propagation occurs and acoustic signals are emitted. According to the theory, the onset of crack initiation coincides with the onset and increase in the AE rate (OHNAKA & MOGI 1982). The onset of continuous AE activity is illustrated in Figure 12. In order to increase the accuracy for determining the crack initiation stress, EBERHARDT et al. (1999a) suggested a combined approach. They used AE measurements and a moving point regression analysis, which was applied in order to describe the change in the slope of the stress-strain curve by a set of linear regression lines. The result is the average axial, lateral and volumetric stiffness as a function of the increasing axial stress.

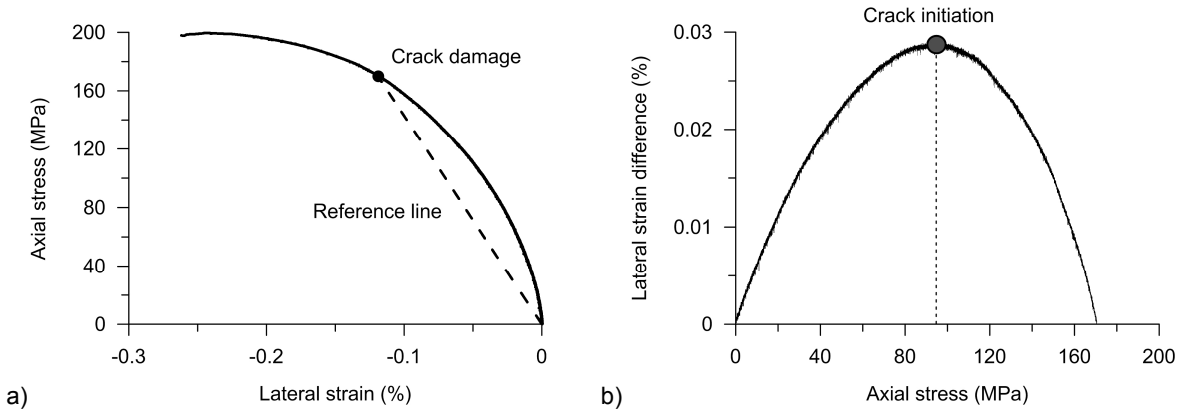

Figure 15: Lateral strain response (LSR) method for the determination of σ_{ci} from the lateral strain curve. The point on the lateral strain curve of maximum curvature is the crack initiation stress (after NICKSIAR & MARTIN 2012).

There are several factors influencing the crack initiation stress including the microstructure of a rock. The Griffith theory of fracture is based on the assumption that the larger the initial flaw length, the smaller is the stress required for crack initiation. The influence of grain size and porosity on the crack initiation stress of dolomite was investigated by HATZOR & PALCHIK (1997), who found an inverse relation between grain size and porosity with the crack initiation stress. In contrast, the studies of NICKSIAR & MARTIN (2014) and EBERHARDT et al. (1999b) showed only a minor effect of the grain size. Instead, the heterogeneity induced by grain size distribution seemed to have a great influence (NICKSIAR & MARTIN 2014). The investigations of EBERHARDT et al. (1999b) revealed that a larger grain size reduces the crack coalescence and crack damage stresses. This effect is attributed to longer grain boundaries and larger intergranular cracks acting as planes of weakness, which enable a more rapid damaging when cracks coalesce and interact.

2.3.3 Modes of rock failure

In uniaxial compression tests, different modes of failure can be observed when testing different rock types. In uniaxial compression, the friction between rock and loading platens causes a radial restraint of the cylindrical specimen so that radial deformations are suppressed. The result is an inhomogeneous stress distribution and a strong variation in the crack density throughout the specimen. HAWKES & MELLOR (1970: 233 f.) calculated the critical value for crack initiation in a cylindrical specimen under increasing load. They used the modified Griffith criterion of Equation (6) with the uniaxial tensile strength representing the McClintock-Walsh parameter C. In a rock specimen, restrained between two loading platens, crack initiation will begin, where C reaches the highest values. The results in Figure 16 show that the most critical stresses occur near the center of the cylinder and around the perimeter of the end surfaces. Almost no cracks initiate in the conical inner areas right below the loading platens. In triaxial compression, end constraints also exist but play a minor role especially in brittle material (PATERSON & WONG 2005: 34).

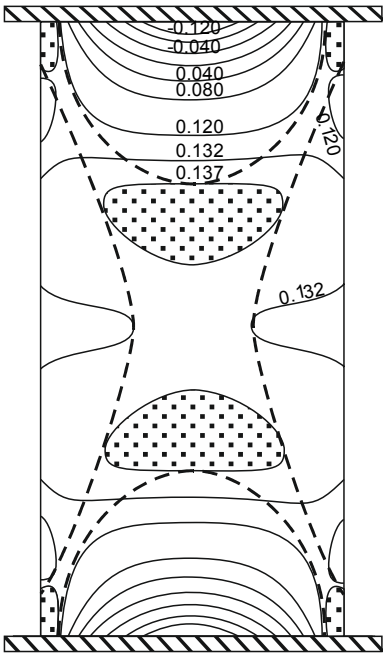

Figure 16: Results of the calculated McClintock-Walsh parameter C or uniaxial tensile strength for a cylindrical specimen under compression. Dotted areas show the most critical stresses for crack initiation and dashed lines indicate a probable failure pattern (after HAWKES & MELLOR 1970: 234).

WAWERSIK & FAIRHURST (1970: 568 f.) distinguished two classes of post failure behavior. Rocks showing class I behavior retain some strength in the post failure region, which means that additional force needs to be applied to destroy the rock. Class II behavior in contrast means that fracture propagation continues without applying additional force because the elastic strain energy stored in the rock is sufficiently high to cause total collapse. This rock failure behavior was observed in homogeneous and fine-grained rocks like basalt and fine-grained limestone. The failure development of class I behavior shows several stages of disintegration. After the maximum stress is exceeded, local crack propagation continues parallel to the loading direction and it becomes more pronounced. In the next stage, boundary faults develop and the load-bearing ability of the peripheral region of the cylindrical specimen is reduced. It is assumed that the axial stress within the sample increases considerably and as a result, shear cracks develop in the center of the specimen. In the last stages of failure development, the interior cracks extend and interact to form a conjugate set of shear fractures.

For uniaxial compression tests of homogeneous, isotropic rock, HAWKES & MELLOR (1970: 218 f.) distinguished three common modes of failure (Figure 17). In the cataclasis-mode, internal cracking occurs and multiple cracks form in the direction of the applied load. Conical or wedge-shaped end fragments as well as elongated fragments form at the outer surface of the specimens develop. Cataclasis is more commonly referred to as failure along two conjugate shear planes. It is the most common mode of failure of most rock types because the influence of the loading plates causing end constraints is reflected by the failure pattern. The axial cleavage or axial splitting failure mode is characterized by the formation of one or more vertical cracks splitting the sample. This failure pattern was observed in fine-grained material of high strength and it is attributed to single cracks propagating through the end planes of the specimen. PATERSON & WONG (2005: 20) attribute that mode of failure to local tensile stresses at flaws or heterogeneities in the rock. Shearing is the third mode of failure and causes the formation of a distinct single shear plane. The failure pattern of rocks may also be a combination of the three failure patterns.

In triaxial compression, shear fracture is the dominant mode of failure at higher confining pressures. The discrete shear plane is usually inclined with an angle between 20° and 30° with respect to the major principal stress direction and the angle may increase with an increasing confinement (PATERSON & WONG 2005: 18).

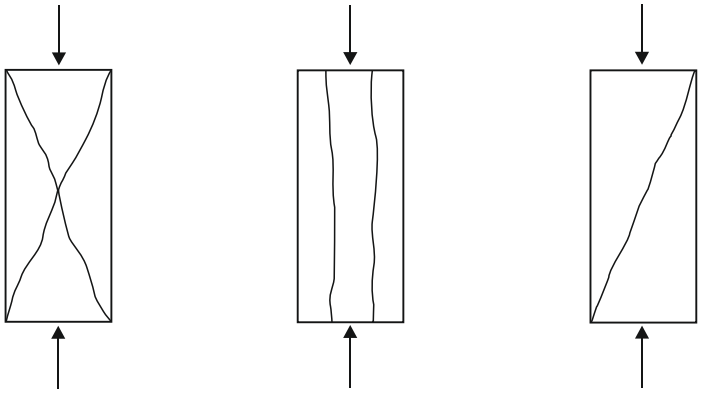

Figure 17: Three modes of failure under uniaxial compression. A set of conjugate shear planes, axial splitting and shear failure.

2.3.4 Time-dependent deformation behavior of rocks

In short-term tests, microcracks propagate when the stress intensity factor at the crack tip exceeds a critical value. Crack propagation may, however, even occur when the stress intensity factor is much lower than the critical stress intensity factor (COSTIN 1987: 168). In this case, stable crack propagation is a time-dependent process that is referred to as subcritical crack growth. In rock, subcritical crack growth is usually the result of stress corrosion, which occurs in a chemically active environment. Other mechanisms like static or cyclic fatigue may also occur but are less common (COSTIN 1987: 179). Still, for rock mechanical problems, fatigue is an important mechanism of time-dependent rock behavior.

During uniaxial cyclic loading, rocks show an inelastic behavior due to the existence of microcracks and shearing along the crack planes. When the stresses are removed, the displacement is not fully recovered and hysteresis is observed in the stress-strain curve (HAWKES & MELLOR 1970: 203). The time-dependent process attributed to cyclic loading is the fatigue crack growth, which means that rocks subjected to compressive cyclic loading are progressively weakened (COSTIN 1987). For a quantification of fatigue damage, XIAO et al. (2010) developed the variable D, which is based on the decrease in ultrasonic wave velocity. It is defined as

$$D = 1 - \frac{v_{p,n}^2}{v_p^2} \tag{11}$$

where $v_{p,n}$ is the p-wave velocity after n circles and v_p is the velocity of the undamaged sample. In general, rocks exhibit a time-dependent fracture and deformation behavior that can be investigated experimentally by strain rate variation, cyclic loading or creep tests. The material behavior of viscoelasticity includes both viscous and elastic deformation. When subjected to a constant stress, viscoelastic materials exhibit a time-dependent increase in strain, which is known from the phenomenon of creep. Creep strain is largely a plastic deformation that is not recoverable when the load is removed (DUSSEAULT & FORDHAM 1993). The creep rate is dependent on the material, temperature, time and the applied stresses (JAEGER et al. 2007).

There are three common phases of creep (Figure 18a), which have originally been developed for metals under constant tensile stress (DUSSEAULT & FORDHAM 1993). In the primary or transient creep phase, elastic deformation occurs with an instantaneous increase in the strain-time-curve. The continuing strain decreases with time, which is known as strain hardening. Primary creep is followed by the phase of secondary or steady state creep where the strain increases continuously (PENG 1973). The creep deformation in this phase is permanent and is not fully recoverable when the stresses are removed. Tertiary or accelerating creep occurs if the applied stresses are sufficiently large for the cracks to grow so that crack coalescence may occur. This phase is characterized by a new increase in the strain rate until failure occurs due to static fatigue (CRUDEN 1971). CRUDEN (1974) suggests that the tertiary creep phase occurs at a critical strain, representing a critical crack density where cracks begin to intersect. Below the critical strain, creep attenuates with time (Figure 18a).

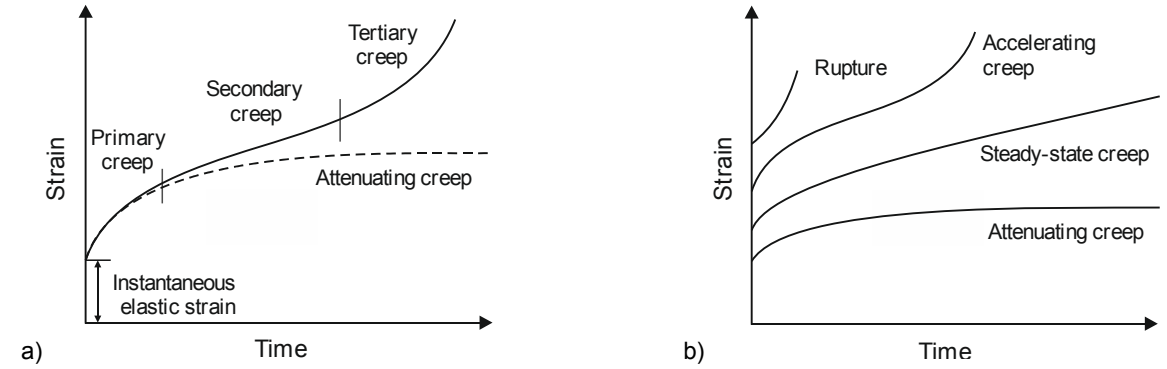

Figure 18: a) The three common phases of creep under tensile load. b) Results of creep tests on rocks under compressive stress showing creep behavior dependent on an increasing damage density (after DUSSEAULT & FORDHAM 1993: 121).

All rocks subjected to stress changes creep, however, for most rocks, creep terminates after several minutes or hours or it is negligibly small. Figure 18b illustrates the results of creep tests performed on rocks under compressive stresses showing attenuating creep and accelerating creep, which occurs at increasing damage density in hard rocks. In low porosity silicates, steady-state creep does not occur under engineering conditions, whereas in ice and some salt rocks, it is the predominant mechanism under constant stress. Tertiary creep leading to rupture may arise in most hard rocks like granite (DUSSEAULT & FORDHAM 1993). LIN et al. (2009) investigated the strength degradation with time using constant loading tests. They found that the evolution of damage in a rock causes a degradation of the elastic properties and thus rock strength is reduced.

If constant stresses below the stress level of beginning plastic deformation are applied to a material, time-dependent deformation may occur as illustrated in Figure 19. At a constant stress, solids show an initial elastic strain ε_1 and after a period, the deformation will stay constant at a maximum value (ε_{max}). If the complete deformation is reversible after stress removal, the deformation is called anelastic (or inelastic) and the time to achieve the anelastic state is called the relaxation time (τ). Upon stress relief, the initial situation ε_0 is established after a similar relaxation time (GOTTSTEIN 2013: 295).

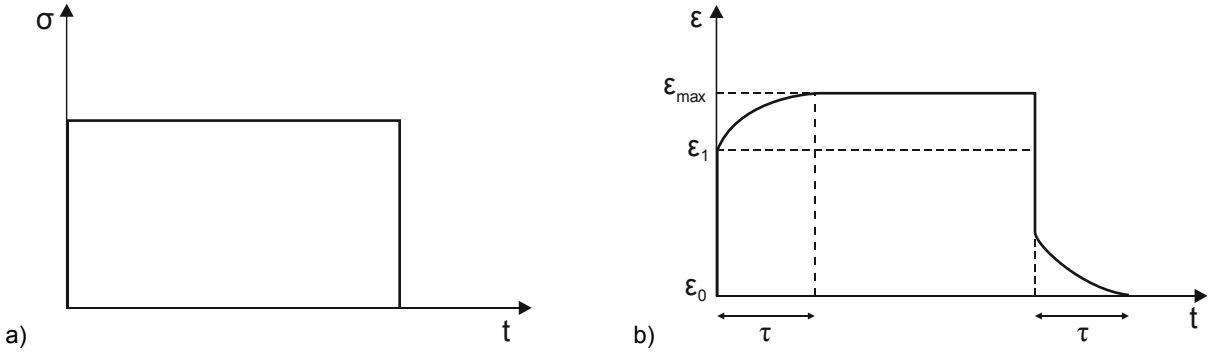

Figure 19: a) Schematic representation of anelastic strain during constant stress. b) Initial elastic deformation (ε_1) followed by anelastic strain, which reaches a maximum value (ε_{max}) after relaxation time (τ). Stress removal reverses the process (after GOTTSTEIN 2013: 296).

2.3.4.1 Stress relaxation

In analogy to the time-dependent process of creep, rocks exhibit a similar deformation behavior when the stresses are removed. The expansion due to stress relaxation includes an instantaneous elastic and a time-dependent inelastic deformation and is called creep recovery or relaxation (ENGELDER 1984). It is assumed that strain relaxation is a result of the formation and opening of microcracks and that the orientation of the cracks might give information about the primary stress state. For in-situ stress measurements, the strain relaxation technique is today commonly used for the calculation of stresses. The doorstopper technique for example uses data from strain gauges that are bonded to the borehole end. When they are overcored, stresses are relieved and strain relaxation occurs. Strain relaxation data together with the elastic moduli are used to calculate the primary stress magnitudes. WARPINSKI et al. (1993) give an overview of the basics of core-based stress measurements. The investigations showed that the basis for the strain relaxation technique is energy that is stored within the rock. According to ZANG & BERCKHEMER (1989), residual stresses in a polycrystalline rock originate from the crystallization of minerals out of the melt, which may have different elastic properties. Furthermore, plastic deformation, recrystallization, phase transitions or diagenetic consolidation as well as different thermal expansion of minerals during cooling may cause residual stresses.

In a rock mass in depth, the internal and external stresses are in equilibrium. When a core is drilled, the external stresses change from a triaxial to a hydrostatic stress field. After extraction from the in-situ stress state, the core adapts to the new conditions until a new equilibrium is established. The stored strain energy and residual stresses of the rock may be balanced by expansion and the formation of microcracks. Upon stress relief, the minerals expand elastically and because of different elastic properties of different minerals and in different directions, tensile stresses arise acting on grain boundaries and existing cracks. The instantaneous component of relaxation already occurs during the drilling process and thus, it can only be measured directly in the borehole. However, not all of the residual stress can be relieved (WARPINSKI et al. 1993).

Acoustic emission monitoring during core relaxation of TEUFEL (1989) and WOLTER & BERCKHEMER (1989) carried out at the German Continental Deep Drilling Project (KTB) revealed that the time-dependent component of strain relaxation is linearly related to the number of AE. Both the number of AE and the strain decrease exponentially with time and may continue for several hours or days. WOLTER & BERCKHEMER (1989) measured relaxation times of 57 hour for a lamprophyre and 28 hours for a gneiss. The mechanism for time-dependent weakening of rock is suggested to be stress corrosion due to existing water at depth and the water introduced with drilling. From strain relaxation experiments performed on cores from high depth, ENGELDER (1984) found that the elastic strain component can be associated with the primary stresses. The direction of the inelastic component showed a different direction, which was ascribed to the opening of healed microcracks present in the rock. Calculations of SAYERS (1990) revealed that strain relaxation largely causes opening of cracks in the direction of the maximum principal stress. WARPINSKI et al. (1993) confirm that microcracks preferentially open normal to direction of the major principal stress, given that rock is isotropic and free of pre-existing cracks. The opening of microcracks in the direction of maximum strain recovery creates an anisotropy within the rock. TEUFEL (1989) notes that the inelastic core relaxation increases with decreasing porosity and grain size because of the increasing number of grain contacts.

2.3.4.2 The Kaiser effect

When stresses are applied to a brittle material, acoustic emissions are emitted when microcracks initiate and propagate. KAISER (1950) was the first to find that there is an influence of the stress history on the onset of AE. The so-called *Kaiser effect* is observable in cyclic loading tests. During the first loading phase up to stresses below the peak strength, microcracking causes AE. When the maximum stress levels of the following cycles exceed the initial stress of the first cycle, AE will not occur until the previous peak stress is reached. As soon as the previous stress level is exceeded, a significant increase in the number of AE occurs (HOLCOMB 1993). The Kaiser effect has often been applied in laboratory uniaxial compressive tests to analyze the previously applied stresses. The results of cyclic loading tests of LI & NORDLUND (1993a) revealed that the degree of damage in rock can be estimated using the stress level of AE onset. They applied the method for a qualitative analysis of blasting induced damage around a tunnel and found that the stress level of beginning AE decreased with decreasing damage.

Many studies tried to use the "stress memory" of rocks for the determination of primary stresses from recovered core samples. Oriented sub-cores taken from the depth have been loaded and AE were measured during the test. Assuming that the in situ Kaiser effect is only dependent on the previous maximum stresses, the approach would be a good alternative to the strain-based in-situ stress measurements. However, HOLCOMB (1993) points out that additional parameters like time-dependence, moisture, coring induced damage and the determination of the AE onset need to be considered before using the in-situ Kaiser effect. Furthermore, it needs to be clear whether the in-situ Kaiser effect must be attributed to the actual primary stresses in the rock mass or to the maximum stresses resulting from drilling.

HOLCOMB also states that the mechanisms for laboratory and in-situ Kaiser effect are not identical. LAVROV (2003) gives an overview of experimental and theoretical results of research on the onset of AE, pointing out the strengths and limitations of stress measurement techniques based on the Kaiser effect. The most important aspects are that the stress memory of rocks disappears after some time and if the preload exceeds the crack damage stress, the AE onset stress is less pronounced and lower than the previously applied load. This confirms the results of RAO & RAMANA (1992), who found that the Kaiser effect is blurred when the loading cycles exceed the crack damage threshold. HOLCOMB (1993) found that the Kaiser effect is dependent on the confining stress in triaxial tests and is thus different in triaxial compared to uniaxial compression. He suggests that the in-situ Kaiser effect might be a result of reclosure of relaxation cracks, which opened during coring. LAVROV (2003) concludes that the uniaxial testing method is not capable of estimating the primary stresses.

3 Methodology

The investigation of the deformation and cracking behavior of hard rock were performed using uniaxial compression testing combined with the non-destructive testing methods of acoustic emission (AE) testing and ultrasonic p-wave velocity measurements. The cracking behavior of ten different rock types has been examined in a first step where standard uniaxial compression tests with axial and radial strain measurements and monitoring of AE were carried out (Figure 20a). In a second step, the influence of existing damage on rock mechanical and acoustic properties of rocks was approached. A uniaxial constant load was applied to the intact rock material in order to generate stress-induced damage within the rocks (Figure 20b-1). Different stress levels within the range of stable and unstable crack growth ensured that the critical stress for crack initiation was exceeded. P-wave velocity measurements before and after constant preloading as well as AE monitoring confirmed that microcracks evolved during compression. The effect of stress-induced microcracks on mechanical and acoustic rock properties were evaluated from subsequent uniaxial compression tests on the preloaded samples (Figure 20b-2).

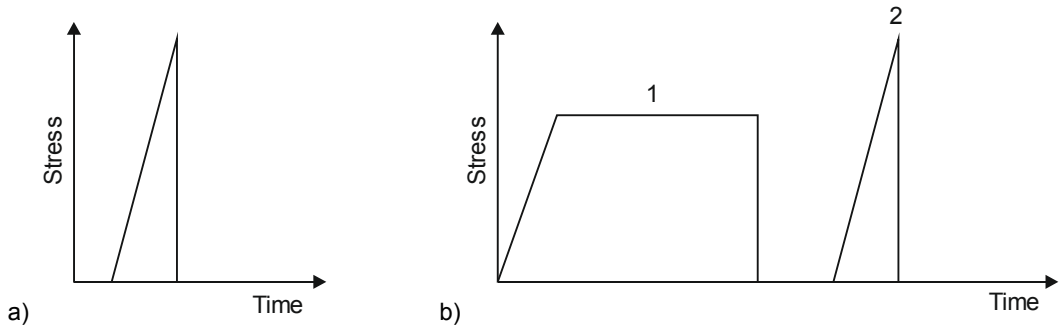

Figure 20: Schematic representation of the loading path during uniaxial compression a) for the characterization of different rock types and b) for investigating the effect of a previously applied load (1) on rock properties determined from uniaxial compression tests (2).

Additionally, petrographic analyses of fluorescent thin sections obtained from untested and tested samples showed the actual influence of mineral composition and rock fabric on the propagation and coalescence of microcracks. Beside the laboratory study on deformation and fracture in hard rocks, the time-dependent behavior of fresh core material recovered from high stress conditions was analyzed. Stress relaxation cracking during strain relief was detected using AE monitoring and p-wave velocity measurements.

3.1 Unconfined compression test

Uniaxial compression tests were performed on cylindrical specimens according to the recommendations of the Commission on Rock Testing (MUTSCHLER 2004). The German recommendations are largely in agreement with the ISRM Suggested Methods (FAIRHURST & HUDSON 1999). For the tests, cylindrical specimens were drilled carefully from blocks of rock using diamond core bits to gain diameters of 50 or 80 mm. With a diamond circular saw, the drill cores were cut to a length of 100 or 160 mm in order to obtain samples with a length to diameter ratio of about 2:1. The end surfaces were grinded parallel to each other with a diamond grinding machine. The unevenness was within the required range of ± 0.1 mm and the parallelism of the end surfaces being ± 3’ met the standards. The applied testing machine *Toni-Norm* by *Zwick/Roell* is a servo-controlled hydraulic machine with two load frames with a nominal load of 2000 kN for uniaxial compression tests and 200 kN for Brazilian tests (Figure 21). For the tests, an

axial force controlled or axial deformation-controlled mode is available. The upper steel platen incorporates a spherical seat and aligns to the upper surface of the specimen in order to compensate nonparallel end surfaces. During the test, a rotation or movement of the platen is prevented. The lower steel platen is movable and applies the load by pressing the specimen against the upper platen. No lubricants or soft materials were placed between specimen and load platens. The control unit *ToniTrol* records the load as well as the strains with a sampling rate of 5 MHz. For data acquisition, the software *TestXpert* was applied.

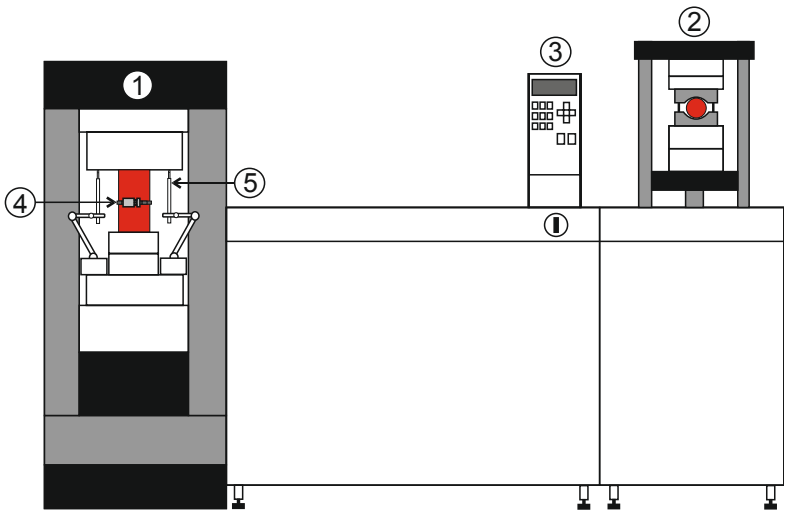

Figure 21: Testing device composed of a load frame of 2000 kN nominal load for uniaxial compression tests (1), a load frame with 200 kN nominal load for Brazilian and point load tests (2), a control unit (3) as well as LVDT for radial (4) and axial strain measurements (5).

Axial strain is measured between the upper and lower platens by three inductive displacement transducers (LVDT = Linear Variable Differential Transformer), mounted evenly distributed around the specimen. The change in the perimeter of the rock due to the application of stress is generally described as radial strain, circumferential strain or lateral strain. In this work, the terms radial or circumferential strain are used, since they describe the actual change in the perimeter best. In literature, the term lateral strain is also common. For recording the radial strain, a measurement chain with an integrated LVDT was installed at mid-height of the rock specimen. With a screw for fine adjustment, the device is fastened around the specimen and a magnetic catch prevents the chain from damage.

3.1.1 Standard uniaxial compression test

Standard uniaxial compression tests were performed in order to gain information about uniaxial compressive strength and the deformation behavior under an increasing load. For the tests, the control mode of the machine is deformation control (Figure 23a) with a constant deformation rate of 0.06 mm/min for 50 mm specimen diameter and 0.1 mm/min for a diameter of 80 mm (MUTSCHLER 2004). The rock is loaded until it collapses and the complete stress-strain curve is recorded during the test. The control system recognizes the rupture by a defined drop in the load. From the stress-strain curve, the uniaxial compressive strength σ_u is determined from the maximum force F, applied on the initial area of the specimen end surfaces A:

$$\sigma_u = \frac{F}{A} \tag{12}$$

The volumetric strain is the sum of radial strain and axial strain according to Equation (9). The crack damage stress was determined from the reversal of the volumetric strain curve and the crack initiation stress was calculated using the lateral strain response (LSR) method. This method was introduced by NICKSIAR & MARTIN (2012) and its application is illustrated in Subsection 2.3.2. It is based on the observation that lateral strain increases significantly when the crack damage stress is reached and unstable crack growth begins. This approach was applied, since it is the only currently available method for a calculation of the stress level instead of a biased determination of the linear portion of a curve. Additional to the determination from the deformation behavior, crack initiation and crack damage were identified from changes in the AE activity from the recorded number of events.

The Young's modulus is determined from the stress-strain curve according to (FAIRHURST & HUDSON 1999). The tangent Young's modulus E_T is the slope of the linear portion of the stress-strain curve at 50 % of the uniaxial compressive strength (Figure 22a). A second employed method defines the secant Young's modulus E_S, which is the slope of a secant from zero to 50 % of σ_u. Since the nonlinear portion at the beginning of the axial strain curve exists due to crack closure, the secant Young's modulus describes the damage already existent in the rock (Figure 22b). As a third method, the average Young's modulus can be determined from the average slopes of the linear portion of the stress-axial strain curve (Figure 22c). In the German recommendations on the uniaxial compression test, the deformation modulus corresponds with the average Young's modulus and is determined in the linear range of the stress-axial strain curve. From a reloading cycle, a modulus of unloading and reloading is determined and the unloading modulus is considered as the modulus of elasticity.

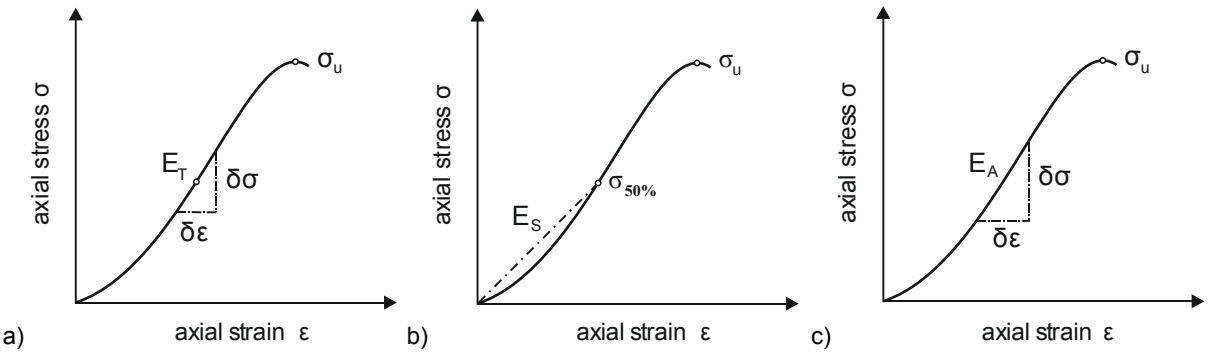

Figure 22: Determination of a) tangent Young's modulus E_T, b) secant Young's modulus E_S and c) average Young's modulus E_A using different segments of the stress-strain curve.

The Poisson's ratio ν describes the elastic constants of a material. It is the ratio of the change in radial to the change in axial strain and can be determined from the slope of the stress-axial strain curve E_T to the slope of the stress-radial strain curve E_r:

$$\nu = -\frac{\Delta\varepsilon_r}{\Delta\varepsilon_a} = -\frac{E_T}{E_r} \tag{13}$$

3.1.2 Constant loading tests

In order to assess the effect of damage on the physical rock parameters, uniaxial constant loading tests were performed to create damage within the rocks. These tests were performed in the force-controlled mode (Figure 23b) until the required stress level was reached after about 8 minutes. Then a constant load was maintained for a period of 30 minutes. It is assumed that the microcracking will mostly have terminated in this time in those samples where the crack damage threshold is not exceeded.

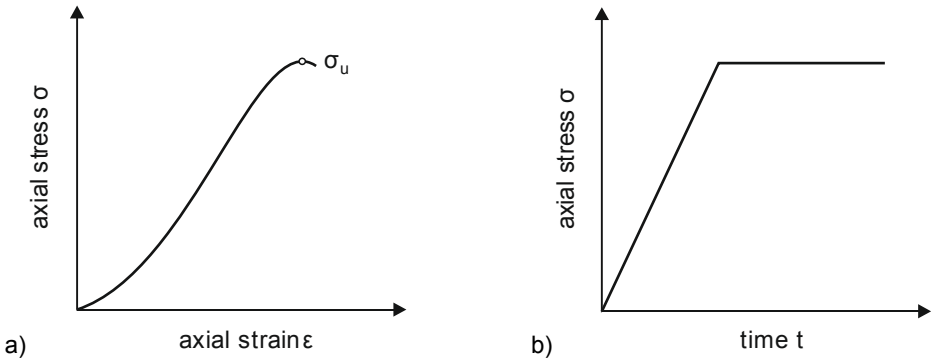

Figure 23: a) Deformation-controlled loading for standard uniaxial compression tests and b) force-controlled mode for constant loading.

3.2 Brazilian Test

The Brazilian test was carried out according to the Recommendations of the Commission on Rock Testing (LEPIQUE 2008) using the small load frame of the ToniNorm testing machine (Figure 21). As there was no clear anisotropy in the tested rocks, the loading direction did not have to be considered. The Brazilian test is a method to determine the indirect tensile strength of a rock by applying a load on the surface line of a cylindrical specimen. The load is applied to the surface line of the specimen using two curved loading jaws. Within the disc-shaped rock, the load results in compressive stresses next to the area where the force is applied and results in tensile stresses over about 70 % of the specimen diameter (LEPIQUE 2008). Inside the specimen, transverse tensile stresses induce the failure of the cylinder by creating a sharp vertical crack (Figure 24). The tensile stress σ_t is calculated from the maximum force F and the specimen dimensions with

$$\sigma_t = \frac{2 \cdot F}{d \cdot l \cdot \pi} \tag{14}$$

For specimen preparation, cylindrical rock specimen were drilled with a diameter of 50 and 80 mm and were cut with a diamond circular saw to a diameter to height ratio of 2:1. For the test, the lateral surface of the cylinder is supposed to be smooth and with minimal irregularities being in the range of ± 0.1 mm.

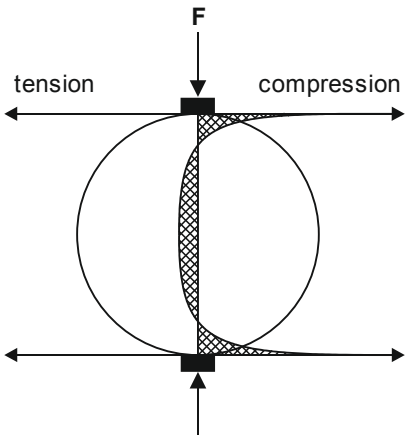

Figure 24: Stress distribution during the Brazilian test. The linear compression induces tensile stresses inside the disc-shaped specimen (after LEPIQUE 2008).

3.3 Ultrasonic testing

Ultrasonic testing is a nondestructive testing (NDT) method, which is applied to detect the sound wave velocity within a material. NDT includes several techniques to examine materials (like integrity, properties and composition) without destroying them. In order to distinguish between NDT methods where the test signals are emitted by an external source and NDT methods where the waves are generated within the material. GROSSE & OHTSU (2010: 3) introduced the terms "active" and "passive" for the two NDT methods. Ultrasonic testing is an active NDT technique with an external source and a receiver, whereas AE testing is a passive NDT technique.

3.3.1 Introduction to wave propagation

Ultrasonic testing uses the phenomenon of an ultrasonic wave propagating through a medium. Generally, a wave is a disturbance that conveys energy through space depending on time and position (WORKMAN et al. 2007). REYNOLDS (2011: 145) describe seismic waves as elastic strain energy that travels away from a seismic source at a velocity determined by the elastic moduli and the densities of the material. A wave can be described as a sinusoidal curve as a function of space x or time t, represented as the equation

$$D(x,t) = A \sin(\omega t - kx) \tag{15}$$

where A is the amplitude of the wave, k is the wave number and ω is the angular frequency (BEATTIE 1983: 98). The propagation speed of the disturbance is the wave velocity. For ultrasonic testing, frequencies above the audible sound from approximately 20 kHz up to several gigahertz are used. A general relation between frequency f, wavelength λ and sonic wave velocity c for all sound waves is

$$c = f \cdot \lambda \tag{16}$$

Basis for the propagation of waves in an infinite, isotropic and linear elastic material is the linear relation between stress and strain. In solids, sound waves or elastic waves propagate as body waves in the form of longitudinal waves (p-waves) and transversal waves (s-waves). For rock testing, the seismic waves most commonly used are longitudinal waves. Those waves are also known as compressional waves, primary waves or p-waves (REYNOLDS 2011: 145). They oscillate parallel to the travel direction and cause compression and dilatation in the direction of propagation (Figure 25). Compressional waves are well known from seismicity, since they are the seismic waves with the highest velocity and thus are the first waves to arrive at a seismograph or receiver.

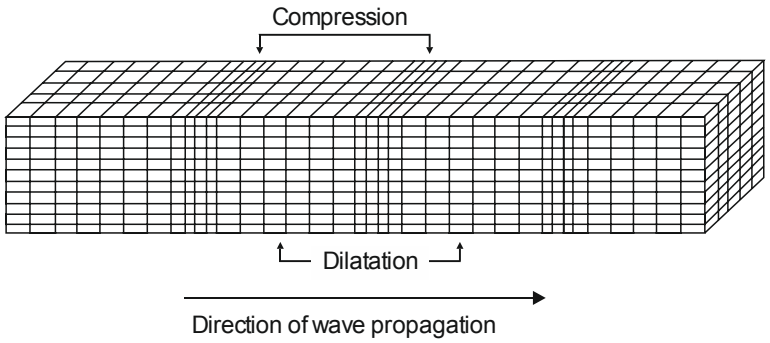

Figure 25: Wave propagation of a compressional or p-wave forming alternating compressions and dilatation (after BOLT 1982: 30).

In general, the p-wave velocity is dependent on the elastic moduli and the density of the medium, the seismic waves travel through. In a homogeneous, isotropic and elastic medium, the p-wave velocity is given by Equation (17), where K is the bulk modulus, μ is the shear modulus, ρ is the density of the material and λ is the Lamé constant.

$$v_p = \sqrt{\frac{K + \frac{4}{3}\mu}{\rho}} = \sqrt{\frac{\lambda + 2\,\mu}{\rho}} \tag{17}$$

Acoustic impedance Z of an elastic medium is the resistance of a medium against a longitudinal wave motion. It is defined as the product of density ρ and sound velocity v_p (BEATTIE 1983: 99, AKI & RICHARDS 2009).

$$Z = \rho \cdot v_p \tag{18}$$

Ultrasonic p-wave velocity detection is a NDT method applied in rock testing to determine the velocity of wave propagation in a rock specimen. An electroacoustic transducer attached to the specimen, generates a longitudinal wave pulse that propagates through the rock and a second transducer on the opposite side of the specimen transforms the wave pulse into an electric signal. Using the determined travel time t and the distance x between pulse transmitter and receiver, the p-wave velocity v_p is calculated.

$$v_p = \frac{x}{t} \tag{19}$$

P-wave velocities of several rock forming minerals are presented in Table 2. Typical velocities and densities of different rock types are given in Table 3.

Table 2: Examples of p-wave velocities and densities of different rock forming minerals (GUÉGUEN & PALCIAUSKAS 1994: 162).

Mineral	v_p	Density	Mineral	v_p	Density
	km/s	g/cm³		km/s	g/cm³
Salt	4.59	2.16	Feldspar (K)	5.59	2.56
Anhydrite	5.63	3.00	Feldspar (Na)	5.94	2.62
Calcite	6.65	2.71	Feldspar (Ca)	7.05	2.73
Dolomite	7.37	2.87	Quartz	6.06	2.65

Table 3: Examples of p-wave velocities and densities for different rock types (REYNOLDS 2011: 147).

Material	v_p	Density	Material	v_p	Density
	km/s	g/cm³		km/s	g/cm³
Air	330	~ 1.20	Rock salt	4.0 – 5.5	2.10 – 2.60
Water	1.45 –1.53	1.00	Granite	4.6 – 6.2	2.50 – 2.81
Sandstone	1.4 – 4.5	1.61 – 2.76	Basalt	5.5 – 6.5	2.70 – 3.30
Limestone	1.7 – 7.0	1.93 – 2.90	Gabbro	6.4 – 7.0	2.70 – 3.50
Dolomite	2.5 – 6.5	2.28 – 2.90	Gneiss	3.5 – 7.6	2.59 – 3.00

3.3.2 Influences on p-wave velocity

The main factor influencing the p-wave velocity is the mineralogy of the rock, but other rock characteristics like porosity and microstructure also play an important role. As described by several authors (WINKLER & MURPHY 1995, SCHÖN 1996), the wave velocity is controlled by the elastic properties of the rock forming minerals, further constituents, the rock composition, mineral contact, cementation or bonding properties as well as pressure and temperature.

WINKLER & MURPHY (1995) describe the effect of an increasing stress on the wave velocity of a porous sandstone. They found that velocities increase in the lower stress range due to the closure of existing pores and nearly stay constant when the stresses are further increased. When the rock approaches failure, the velocities measured perpendicular to the stress axis decrease again because of the opening cracks perpendicular to the loading direction. STANCHITS et al. (2003) found similar results for granite samples. During loading, there was almost no change in axial velocity while the radial velocities were strongly dependent on the dilation due to the opening of microcracks oriented sub-parallel to the stress direction. The cementation in sedimentary rocks causes higher velocities when it consists of silica or carbonate, whereas clay cement causes lower velocities (WINKLER & MURPHY 1995). SCHÖN (1996) gives a correlation between SiO_2 content of igneous rocks and the p-wave velocity. Because of the relatively low velocity of quartz compared to mafic minerals, they found that acidic rocks have lower velocities than basic rocks. SCHÖN (1996) also found that the rock density has a strong influence on the p-wave velocity. He lists several relations of different authors, where, for most rock types, a linear relation was found. Furthermore, wave velocity is dependent on the porosity and fracture content. Lower velocities of porous or disturbed rock are the result of the lower velocities in the pore or fracture filling material. With increasing water saturation, wave velocities increase and furthermore, the grain size seems to have an influence on the velocity. In crystalline rock, temperatures below 100 to 150 °C have only a small effect on the wave speed but the reduction of the velocity increases with increasing temperature.

3.3.3 Attenuation of seismic energy

In a perfectly elastic medium, the total energy of seismic waves is conserved during propagation, whereas in a viscoelastic material, a small amount of seismic energy is dissipated. This means that the amplitude of the seismic signal decreases with distance from the source (LOWRIE 2007, REYNOLDS 2011). The seismic attenuation is partly caused by geometrical spreading effects but also by absorption (anelastic attenuation) and scattering (elastic attenuation). The result of absorption or intrinsic attenuation is a loss of amplitude and energy, meaning that seismic energy is gradually converted into heat due to friction and viscosity on grain boundaries, pores, cracks or fluids (BELTZER 1988: 83, REYNOLDS 2011, MAVKO et al. 2009). Scattering is another mechanism that contributes to seismic attenuation by redistributing wave energy within the medium. When the waves propagate through a non-uniform medium, reflection, refraction and diffraction may occur at heterogeneities like grain boundaries or cracks. BOURBIÉ et al. (1987) give an example of scattering in a porous medium where an incident wave meets a spherical cavity in an otherwise homogeneous matrix. The wave is scattered at the cavity and radiates energy in all directions. This energy is subtracted from the incident wave and the wave is attenuated. The mechanism of scattering is dependent on the number and size of the inhomogeneities as well as on the incident wavelength.

Many properties and conditions influencing the wave velocity also affect the seismic attenuation. TOKSÖZ et al. (1979) investigated the factors influencing the attenuation of compressional and shear waves. According to the authors, attenuation is linear proportional to the frequency in the frequency range of 0.1 to 1.0 MHz. They found that attenuation in saturated rocks is greater than in dry rocks,

whereas it is relatively low in frozen rock. In saturated rocks, the fluid is assumed to act as a lubricant, which increases the attenuation. Furthermore, confining pressure decreases wave attenuation, since crack closure occurs. The suggested mechanism for attenuation is friction on grain boundaries and cracks, which means that confining pressure decreases the number of cracks and thus reduces attenuation due to friction (JOHNSTON et al. 1979).

3.3.4 Velocity anisotropy

Although for many rock mechanical models, an isotropic solid is considered, most rocks show a velocity anisotropy. The presence of an anisotropy in a solid becomes evident from anisotropic wave propagation, where the seismic velocities vary in different measuring directions. Anisotropy may either be transversely isotropic (polar isotropic), meaning that the physical properties are symmetric about an axis normal to a plane of isotropy or anisotropy is orthotropic. Orthotropic materials show three planes of symmetry where material properties differ in three orthogonal directions. A seismic velocity anisotropy can be quantified by the anisotropy ratio A_R, which is defined as the ratio of maximum to minimum wave velocity or by the anisotropy coefficient A_v (SCHÖN 1996: 214):

$$A_R = \frac{v_{max}}{v_{min}} \qquad \text{or} \qquad A_v = \frac{v_{max} - v_{min}}{v_{min}} \tag{20}$$

Several characteristics of minerals and rocks are possible sources of seismic velocity anisotropy. Most of the rock-forming minerals exhibit a velocity anisotropy caused by the structure of the crystal lattice. The anisotropy for several rocks and minerals are given in (Table 4). According to CRAMPIN & LOVELL (1991), a velocity anisotropy is not only attributable to the crystallographic anisotropy of minerals but reasons may also be a lithologic anisotropy due to aligned grains, a structural anisotropy resulting from fine layering in a rock or a stress-induced anisotropy. Stress-related anisotropy may be a direct stress-induced anisotropy or an anisotropy caused by stress-induced cracks with a preferred orientation.

Table 4: Examples of velocity anisotropy given by the anisotropy coefficient A_v (summarized in SCHÖN 1996: 216) and velocity anisotropy of the main rock-forming minerals of the earth's crust (GUÉGUEN & PALCIAUSKAS 1994).

Rock	Anisotropy coefficient A_v	Mineral	Anisotropy in v_p (%)
Granite	0.11	Calcite	0.33
Diabase	0.03	Quartz	0.26
Marble	0.05 - 0.23	Plagioclase	0.31
Limestone	0.11	Alkali feldspar	0.46
Sandstone	0.06	Hornblende	0.27

In an initially isotropic rock, uniaxial compression causes a transversely isotropic anisotropy due to the generation of axial microcracks. According to GUÉGUEN & PALCIAUSKAS (1994: 178), a reduced anisotropy during confined compression gives evidence for the presence of microcracks, since crack closure reduces the anisotropy from preferably oriented cracks.

3.3.5 Experimental setup and testing procedure

Ultrasonic p-wave velocity was measured on the same specimens that were used for uniaxial compression testing. Air-dried rock specimens with diameters of 5 and 8 cm were tested. In order to receive the best possible coupling of the transducers, care was taken to ensure a smooth surface free of dust and loose rock material. Wave speed detection was performed in three to four measurement planes over the height and in 45° distances around the specimen as well as parallel to the axis of the cylinder. In Figure 26, the testing procedure in both measuring directions is illustrated. Coupling is enhanced by using ultrasound gel between sample and sensors.

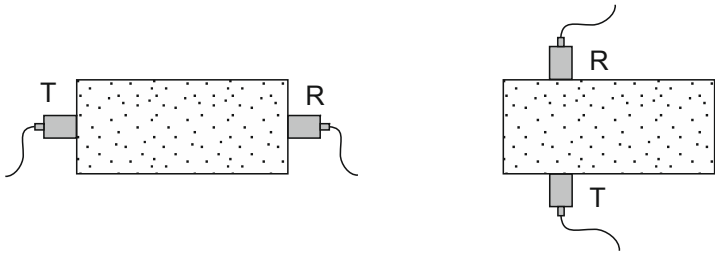

Figure 26: P-wave velocity measurements performed along the axis (left) and around the specimen diameter (right). T: transmitter, R: receiver.

Before every test series, a calibration of the system is required to adapt the system to the temperature and humidity conditions in the laboratory. A ceramic reference sample with well-known acoustic properties was used for calibration. For a better coupling between transducers and rock, a sealing compound or ultrasound gel was applied. The calibration was performed with the same coupling medium as the tests. In order to obtain a body wave (p-wave), the rock specimens need to have an infinite extent compared to the wavelength of the pulse. According to Equation (16), the higher the frequency of the incoming wave is, the smaller is the wavelength, given that the wave velocity of a material is constant. Assuming that the p-wave velocity of a material is up to 7 000 m/s and the pulse frequency is 350 kHz, the wavelength would be 2 cm, which is still smaller than the minimum dimensions of the tested specimens so that the applied sensors were able to detect the p-wave velocities.

For the determination of wave velocity, transmission measurements are performed according to the guidelines of the DIN EN 14579 (2005) for natural stones. The testing device consists of an ultrasonic generator unit with a frequency range of 20 – 350 kHz and an internal continuous trigger or a single trigger for ultrasonic pulses. During the tests, the continuous trigger mode was active and transducers with a frequency of 350 kHz were applied. Both transducers are piezoelectric ceramics using the piezoelectric effect. Piezoelectricity is an electric charge that arises in piezoelectric materials like crystals or ceramics when subjected to mechanical stress (BORCHARDT-OTT 2009: 158 f, OKRUSCH & MATTHES 2014: 18). The displacement of single atoms against each other shifts the charges in an elementary cell so that it becomes a dipole and a measurable electrical charge appears at the surface of the material. An interchange of pressure and tensile stress changes the polarity and leads to an AC voltage (direct piezoelectric effect). The reverse piezoelectric effect is used to transform an alternating electric field into a mechanical vibration like an ultrasonic wave. Piezoelectricity is dependent on the symmetry of the crystal and occurs only in crystals without inversion symmetry. For the generation and measurement of ultrasonic waves in material testing, mainly piezoelectric ceramics like barium titanate, lead zirconate titanate lead titanate are applied (KRAUTKRÄMER & KRAUTKRÄMER 1986). The electric signal obtained from the sensor is amplified with 40 dB and is detected with a sampling frequency of 10 MHz. From the waveform, the first arrival of the p-wave is determined manually from the turn-off point of the curve.

3.4 Acoustic emission testing

In this section, the nondestructive testing technique of acoustic emission testing is introduced and the experimental setup is explained, including the applied equipment. Furthermore, the theory behind the analysis of acoustic signals and the procedure of signal analysis as well as the localization of acoustic events are presented.

3.4.1 Introduction to acoustic emission

Acoustic emissions (AE) are defined in the Standard Terminology of Nondestructive Examinations ASTM E1316-16 (2016) as the phenomenon of transient elastic waves that are generated by a rapid release of energy from localized sources in a material. Other terms for acoustic emission are stress wave emission or microseismic activity. WORKMAN et al. (2007) define AE as stress waves produced by a sudden movement in a stressed material, where the generated stress wave radiates from the source into the material and it is detected by a piezoelectric transducer. Although fracturing of a material und thus the application of a load is necessary for AE testing, it is classified as a passive nondestructive testing (NDT) method. In contrast to most active NDT techniques, AE testing is applied during compression of a solid, making it possible to monitor the entire fracturing process (GROSSE & OHTSU 2010: 3 f.). The nucleation and propagation of cracks releases strain energy, stored within the solid and elastic waves radiate in the material. With AE sensors, the waves are detected at the sample surface and the waves are converted into electrical signals (GROSSE & OHTSU 2010: 16). In contrast to ultrasonic testing, where the elastic waves are generated by a transducer at the surface of the sample, AE implies that the signal is generated by the material itself (BEATTIE 1983: 98). The AE technique is thus a suitable tool for the observation of rock damage and failure of solids. AE signals include all frequencies from audible sound up to high frequencies. In order to avoid low frequency noise from the measuring environment, the ultrasonic frequencies from several kHz up to about 1 to 2 MHz are applied for testing.

3.4.2 Experimental setup

In rocks, cracking occurs either when a load is applied or as relaxation cracks when initial stresses are removed. The experimental setup of the performed tests is shown in Figure 27. Independent of the loading mode, the experimental setup consists of several AE transducers, which are mounted to the specimen surface. The incoming signal is transmitted to a preamplifier, is processed in the data acquisition system, and signal analysis is later performed with a package of MATLAB scripts.

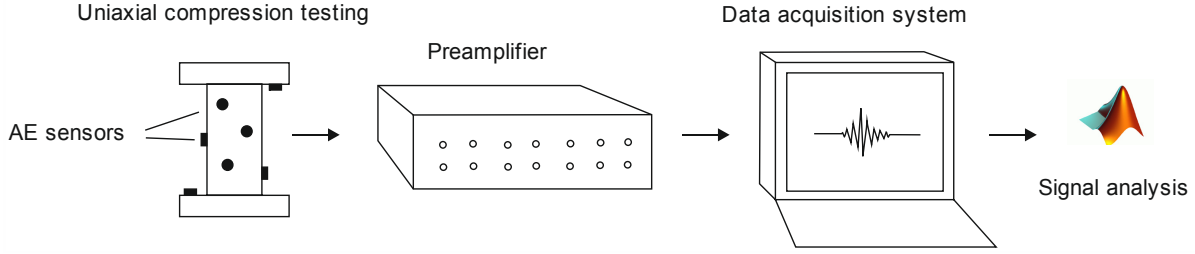

Figure 27: Testing procedure of AE measurements. During uniaxial compression tests, AE sensors detect the emitted signals, which are amplified and transmitted to a data acquisition system. Signal analysis is performed using MATLAB (WIESER et al. 2015b).

3.4.2.1 Transducers, coupling and connection

At the sample surface, AE signals are detected as small displacements, which are converted into electrical signals by piezoelectric sensors. For the tests, signal detection was performed using eight standard contact transducers consisting of a single crystal element acting as receiver. They are broadband transducers with a frequency of 1 MHz and a diameter of 13 mm (OLYMPUS 2015). Because of the low amplitude of AE signals, a good coupling between sensors and rock is required. As coupling and mounting material, a thin layer of hot-melt adhesive is used between transducer and specimen in order to avoid air-filled gaps. Furthermore, irregular surfaces are compensated so that the transmission of the signals is enhanced. The experimental setup for laboratory testing is shown in Figure 28.

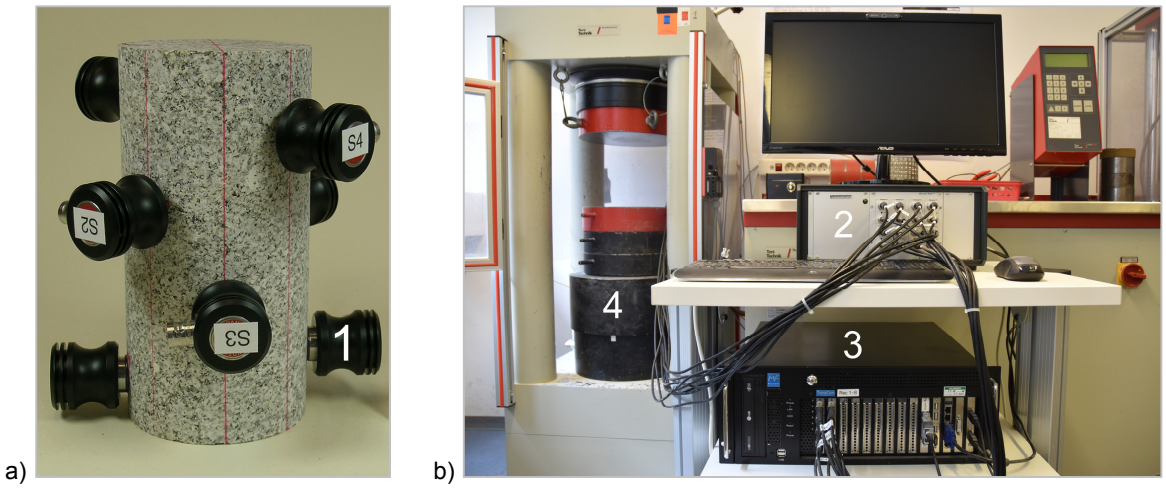

Figure 28: Experimental setup of the AE measuring system. a) AE transducers (1) mounted to a rock specimen with a diameter of 8 cm. b) The channels of the preamplifier (2) are connected with the corresponding channels of the transient recorder for data acquisition (3). In laboratory tests, AE monitoring is performed during uniaxial compression (4).

3.4.2.2 Pre-amplification and data acquisition

For the amplification of the electric signals, preamplifiers with a gain of 60 dB were applied. The system includes a bandpass filter, which allows the filtering of unwanted frequencies of the incoming signals. Using a combination of high-pass and low-pass filter, only frequencies in the range between 10 kHz and 1 MHz were transmitted to the transient recorder. For data acquisition, an 8-channel transient recorder, including a data acquisition software was applied. For the tests, the software TranAx 3 is run in the event-controlled recording (ECR) mode, which allows the controlled acquisition of data (Elsys AG 2014). Instead of a continuous recording of data, only relevant signal data is captured and the acquisition of data only occurs if the defined trigger conditions are met. The advantage of the recording mode is a reduced amount of data and a prevention of data loss. The ECR mode is based on a ring buffer in the form of an onboard memory with a defined time interval. There, the measurement values digitized by the ADC (Analog-to-Digital-Converter) are read and if the trigger conditions are met, the signal is transferred to the hard disk. The sampling rate was set at 2.5 MHz for all tests. In the ring buffer, the oldest data are overwritten by new incoming data as soon as the capacity of the ring buffer is exceeded. Only if the maximum number of events per time unit and thus the maximum possible transfer rate to the hard disk is exceeded, a CPU overload may occur. The applied settings of preamplifier and data acquisition software are listed in Table 5.

The initiation and propagation of a crack is a spontaneous and rapid event that arrives at the sensor. At the same time, a constant background noise is recorded and additional spontaneous noise might be detected. The analysis of AE requires a differentiation of real AE events from noise signals. This is achieved by applying defined trigger conditions, which allow the identification of the signal component. Signals are recorded at all active channels in the ECR multi-channel mode. This implies that as soon as the trigger is released at one channel, signal data is registered at all active channels (Elsys AG 2014). As trigger mode, a slew rate trigger was set with a defined ratio of amplitude versus time. As soon as this slope is recognized within a signal, the trigger is released. With the function Pre- and Post-Trigger, it is possible to set a signal length in order to record a certain period (measurement length) before and after the trigger point.

Table 5: Applied settings for pre-amplification and data acquisition with the software TranAX 3.

Pre-amplification	Unit	Settings	Data acquisition	Unit	Settings
Amplification	dB	60	Operation Mode	-	ECR multi-channel
High-pass filter	kHz	10	Sampling rate	MHz	2.5
Low-pass filter	MHz	1	Pre-Trigger	kS*	1
			Post-Trigger	kS	4
			Holdoff	kS	5
			Trigger Mode	-	Slew rate
			Delta times	S	10
			Delta amplitude	V	0.5 (laboratory tests) 0.05 (stress relaxation monitoring)

*S = samples

3.4.3 Signal analysis

Every formation of a crack causes an elastic wave with characteristic features, which are represented by an electrical signal. Signal parameters are for example the number of events and the signal energy (GROSSE & OHTSU 2010: 38). The procedure for the extraction of event characteristics is outlined in Subsection 3.4.3.3. In order to obtain the p-wave arrival times and the event properties, the signals need to be filtered and conditioned before further analysis. Signal analysis is performed using a software package programmed and kindly provided by the Chair of Non-destructive Testing of the Technical University of Munich. The fundamental background of the software is described in detail in KURZ (2006). The software is based on MATLAB® and consists of the two major components "Squirrel AE" and "Event processing". With Squirrel AE, signal conditioning is performed and the arrival times as well as signal parameters of every event are determined. In Figure 29, a summary of the calculation steps is given. The entire data analysis procedure including the script Event Processing is illustrated in Figure 32.

3.4.3.1 Signal conditioning

After data acquisition, the Squirrel AE is applied for the extraction of signal parameters from the gained TPC5-files. As a first step, the stored binary data from the TPC5-files is converted into voltage values, using given conversion factors. In order to reduce the background noise components of the signal and to increase the signal to noise ratio, the original signal is conditioned. As a first step, a Butterworth high-pass filter with a cutoff frequency of 25 kHz is applied. Low-frequency noise caused by the loading machine or the natural frequency of the specimen are strongly attenuated (RAITH 2013). After filtering the noise components of the signal, a noise reduction is performed using a wavelet transform. With the resulting signal, the arrival times of each event are determined.

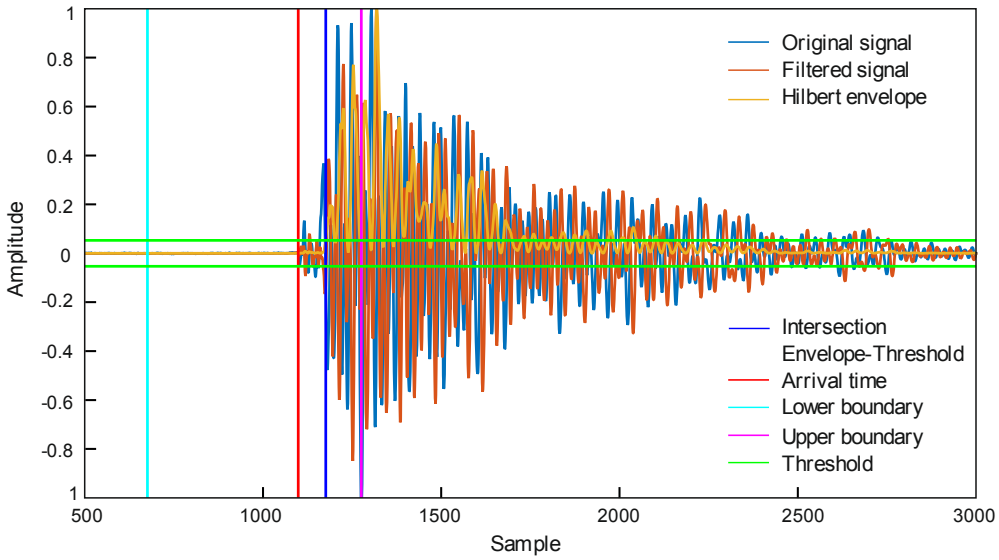

Figure 29: Result from the calculation with Squirrel. From the conditioned signal, the Hilbert envelope is calculated and defined threshold and window boundaries are used for the determination of the p-wave arrival time.

3.4.3.2 P-wave arrival times

In all performed tests, the arrival of the compression wave or p-wave is the first arrival of an elastic wave at the sensor. Where a signal deviates from its small-amplitude noise level around the zero line, the signal arrives at the sensor (Figure 30). The time between an event and the arrival at the sensor is the travel time. The accuracy of onset detection is thus important for the determination of the p-wave velocity, especially for the three-dimensional localization of events. Because of the large number of events occurring during the tests, a manual onset detection is not practicable. Thus, KURZ (2006) developed an autoregressive algorithm (AIC-Picker) for an automated onset determination.

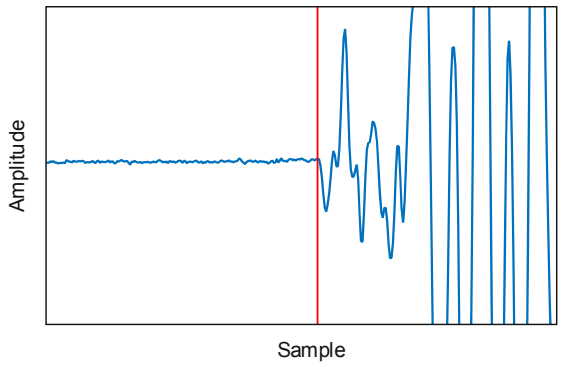

Figure 30: Exemplary illustration of the arrival time detection where the elastic wave arrives at the sensor.

The automated picker is based on an iterative approach, where a section of the signal, containing the p-wave arrival, is selected in advance. For this first approximation of the arrival time, a signal envelope is calculated using the Hilbert transform. The Hilbert transform y(t) of a real, time-dependent function x(u) is defined as follows (BUTTKUS 2000: 38):

$$y(t) = \frac{1}{\pi} \int_{-\infty}^{+\infty} \frac{x(u)}{u - t}\, du \tag{21}$$

The integral is a convolution integral and the resulting function is the original function with a 90-degree phase shift (KURZ 2006). The Hilbert transform is used for the calculation of the Hilbert envelope. For determining a time window, containing the p-wave arrival, the squared and standardized envelope is used. By squaring the envelope, background noise is attenuated and the signal is amplified. As a first approximation of the arrival time, the first intersection between envelope and a predefined amplitude threshold is used. Around this point of intersection, a window is determined, where p-wave arrival times are detected. In KURZ (2006), a detailed description of the AIC-Picker is given. The algorithm is based on the Akaike Information Criterion (AIC), which is a criterion for model selection. The iterative AIC function is (MAEDA 1985):

$$AIC\,(i) = i \cdot \log_{10}(\mathrm{var}(\mathrm{window}\,(i, 1)) + (T_w - i - 1) \cdot \log_{10}(\mathrm{var}(\mathrm{window}\,(1 + i, T_w))) \quad (22)$$

The AIC function is calculated from a defined window with T_w as the upper boundary of the window and i including all values of the window. The term var (window (i, 1)) means that the variance is calculated only from the sample i, whereas var (window (1 + i, T_w) includes all samples from 1 + i to T_w for the calculation. The p-wave arrival time is the global minimum of the AIC function (see Figure 32).

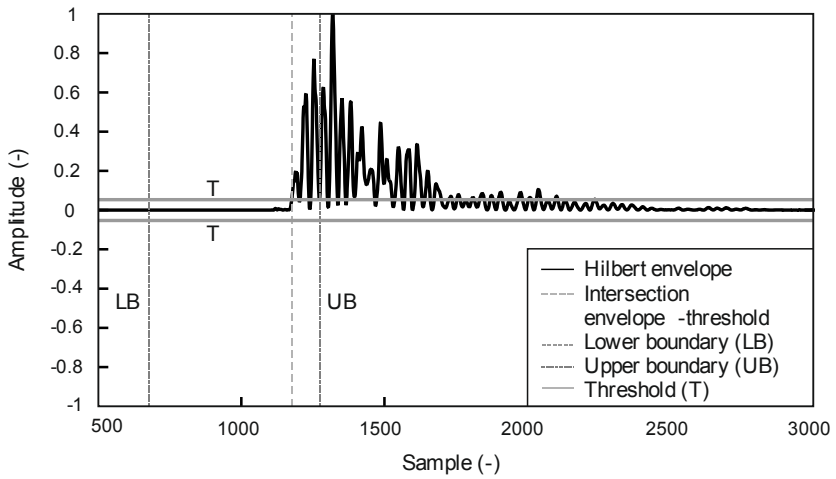

Figure 31: Hilbert envelope for the determination of a data window including the p-wave arrival time. The intersection of envelope with a defined threshold sets the window that is limited by a lower and upper boundary.

3.4.3.3 Acoustic event properties

The determination of the arrival time is followed by the extraction of signal parameters. However, not every signal can be used because some detected events show a high proportion of noise. A reasonable approach is thus to regard only those events with a high signal-to-noise ratio. The signal-to-noise ratio (SNR) is the ratio of signal performance to noise performance and gives information about the quality of the event and the quality of the onset detection. For the calculation of the signal proportion, a section of the signal S of 100 samples after the arrival time t_a is used. The noise is determined from a section of 100 samples before the arrival time (RAITH 2013):

$$SNR = \frac{\sum_{i=t_a}^{t_a+100} \sqrt{S_i^2}}{\sum_{i=t_a-100}^{t_a} \sqrt{S_i^2}} \quad (23)$$

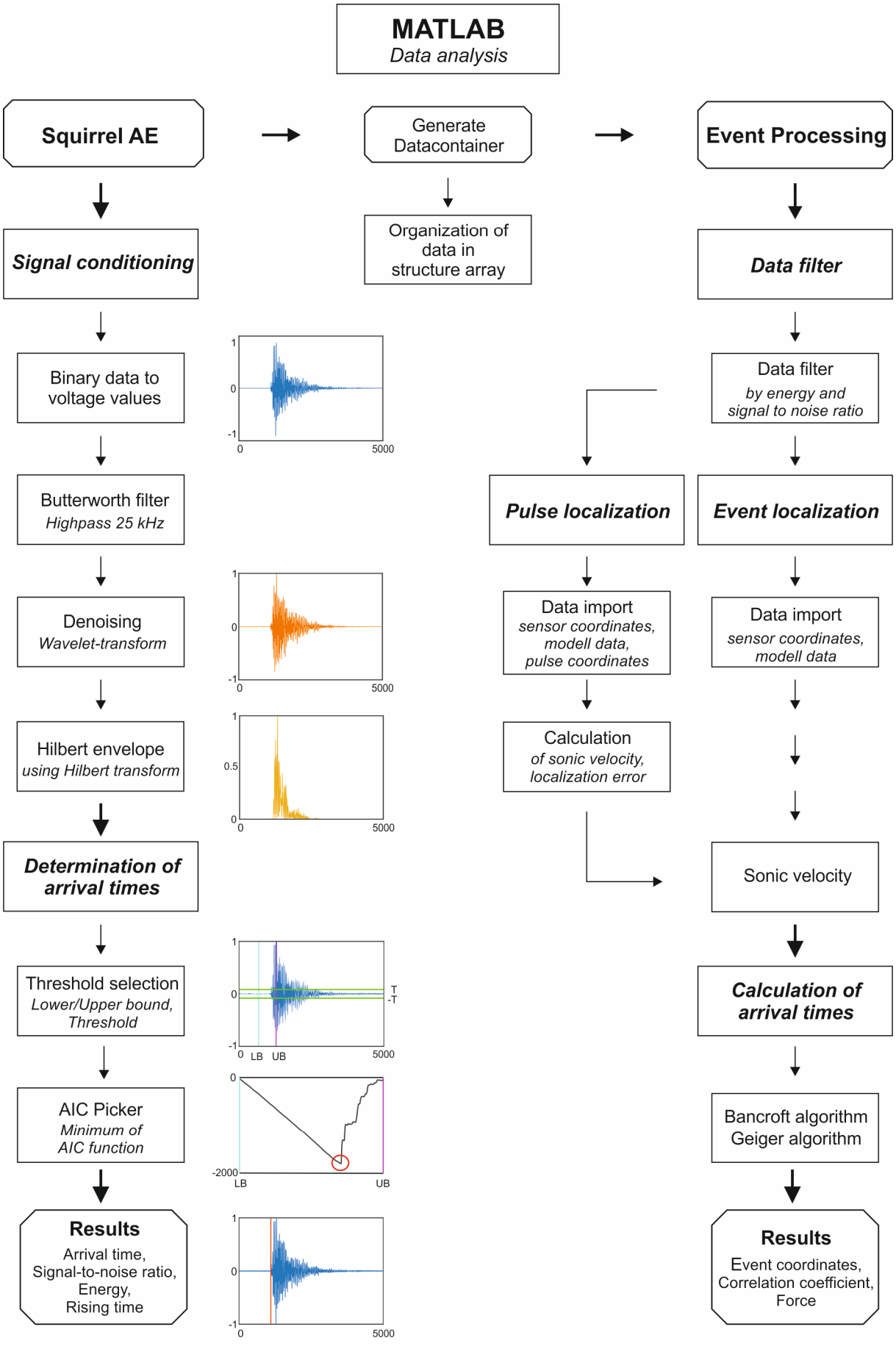

Figure 32: Flow Chart of the signal analysis procedure using a package of MATLAB scripts.

Figure 33 illustrates signals with a high and a low SNR. In signals with a high SNR, the arrival time detection is more reliable.

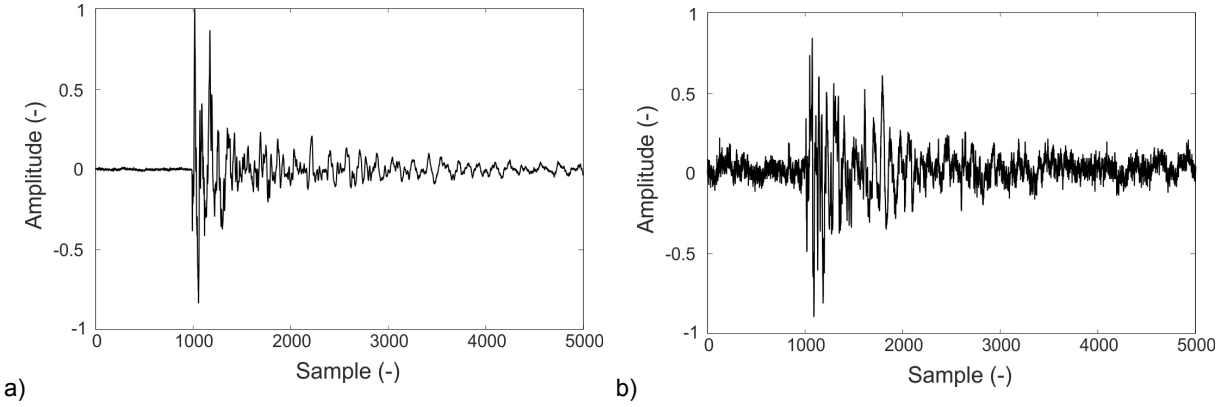

Figure 33: Example of an acoustic signal with a) a high SNR and b) a low SNR.

From the selected AE signals with a high SNR, several signal characteristics can be derived. The parameters are defined in the ASTM E1316-16 (2016) as given in Table 6 and are illustrated in Figure 34.

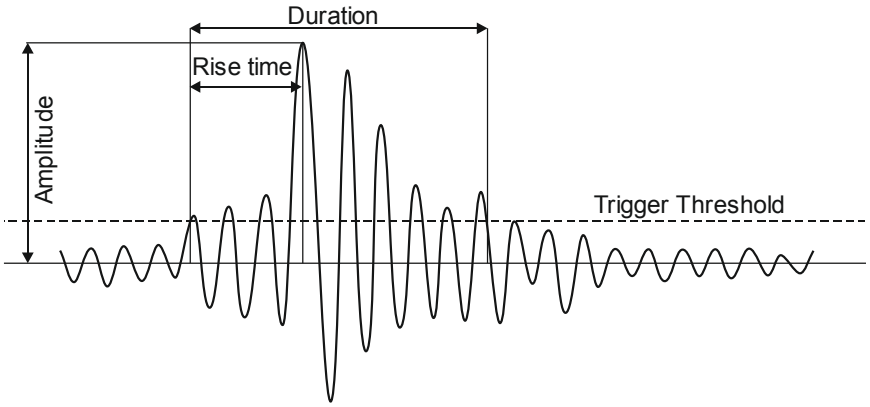

Figure 34: Signal parameters obtained from an AE event (after SHIOTANI 2010: 43).

For the analysis of the recorded AE data, most important are the hit rate, the signal energy and the rise time. The signal energy is the area under the signal envelope, calculated from a defined signal window (RAITH 2013). For the measured AE, the energy window was set between the arrival time and 2000 samples added to the time of maximum signal amplitude (S_{amp_max}). Signal energy is calculated for each channel and an average energy value is determined for every AE event.

$$\text{Energy per channel} = \sum_{i=s_a}^{S_{amp\_max}+2000} \sqrt{S_i^2} \tag{24}$$

The rise time t_R is the time between arrival time s_a and the signal peak or time of maximum amplitude S_{amp_max}. It is calculated using the sampling rate f_s according to

$$\text{Rise time } t_R = \frac{S_{amp\_max} - s_a}{f_s} \tag{25}$$

Table 6: Definitions of AE signal parameters according to international standards (ASTM E1316-16 2016).

Signal Parameter	Definition
Hit	A signal that exceeds the threshold and causes a system channel to accumulate data
Count	Number of times the AE signal exceeds a threshold during any selected portion of a test
Amplitude	Peak voltage of the largest excursion attained by the signal waveform from an emission event
Duration	Time interval between AE signal start and AE signal end
Energy	Total elastic energy released by an emission event
Rise time	Time interval between AE signal start and the peak amplitude of the AE signal

3.4.3.4 Localization of acoustic events

For the investigation of rock failure, the localization of AE events enables the visualization of the cracking process within the rock. The three-dimensional localization is based on the same principles as the techniques applied in seismology for the localization of earthquake hypocenters. In both cases, the arrival times recorded at a number of seismometers are necessary for localization (GROSSE & LINZER 2010: 68). Two localization methods, the Geiger method and the Bancroft method, were applied in this work and they will be presented in this section. For most applications, it is assumed that the material is homogeneous and isotropic and the origin of the elastic wave is regarded as a point source (KURZ et al. 2010: 102 f.). The three-dimensional localization of a point source using arrival time differences is a nonlinear system

Geiger's method

GEIGER (1910) originally introduced an iterative localization method for earthquakes. In earthquake localization, originally, the arrival times of both p-wave and s-wave were required. The arrival of the shear wave is often difficult to determine, since it may be hidden in the coda of the p-wave, especially at a small measuring distance. Geiger solved this problem by using only the first arrival times of the p-wave at a number of sensors (GROSSE 1996: 107). Geiger's method is the standard approach for the three-dimensional localization in seismology and in the analysis of AE. The method uses a linearization of an originally non-linear problem. A first approximation of the solution is calculated from a first guess signal source, which is located near the real source coordinate (KURZ 2006: 66). For the localization of the source coordinates (x, y, z) and the origin time t_0, the coordinates of at least four sensors are required. The arrival time of the p-wave is calculated for every sensor, using the first-guess signal source and the ultrasonic wave velocity of the material. For homogeneous and isotropic materials, the theoretical arrival times t_i between source and sensor are calculated as

$$t_i = \frac{\sqrt{(x - x_i)^2 + \left(y - y_i\right)^2 + (z - z_i)^2}}{c} + t_0 \tag{26}$$

where (x, y, z) are the coordinates of the first-guess signal source, (x_i, y_i, z_i) are the coordinates of the sensors (i = 1,…, N for N sensors). c is the measured p-wave velocity of the material and t_0 is the guessed origin time, which is proposed by KURZ (2006) and KURZ et al. (2010) as the center of the specimen. If more than four sensors are applied, the system is overdetermined and the equation system can be solved iteratively, using the least squares method. Arrival time residuals are calculated from the theoretical arrival times and the guessed origin time. In order to minimize the arrival time residuals at all sensors, the first-guess signal source is corrected for the subsequent iterations (FINCK 2005: 48).

The Bancroft method

Another location method was originally developed for the application in GPS positioning by BANCROFT (1985), who introduced an algebraic solution of the GPS equations for overdetermined systems. The Bancroft algorithm is a direct solution for the non-linear problem, and like the iterative method of Geiger, it uses travel time differences. The background of the Bancroft localization method is illustrated in Figure 35 and it is described extensively in KURZ (2006: 69–80). GPS localization is also based on travel time differences of at least four satellites. The position of a receiver R with the unknown coordinates (x, y, z) is calculated, using the satellite positions S_i of satellites with the known coordinates (x_i, y_i, z_i). The pseudo distance between each satellite and a receiver is the pseudorange p_i. It is the sum of the speed of light c and the arrival times t_i.

$$p_i = c \cdot t_i \tag{27}$$

The receiver position is determined using the pseudorange of each satellite and the satellite coordinates. Applying the method to AE localization, p_i is the distance from the signal source to the AE sensors with the known coordinates (x_i, y_i, z_i). Rearranging Equation (26) and implementing Equation (27) results in the pseudoranges as

$$p_i = \sqrt{(x - x_i)^2 + \left(y - y_i\right)^2 + (z - z_i)^2} + c \cdot t_0 \tag{28}$$

where c is now the wave velocity in the material and t_0 is the origin time. With more than four sensors, the system is overdetermined, meaning that more than four equations exist for the determination of four unknown quantities. The Bancroft algorithm results in two possible solutions for the quadratic equation but the searched solution is unambiguous from the data. From the correct solution, the four source parameters (x, y, z, t_0) can be calculated. The advantage of this location method is that it is numerically more stable than the iterative approach. A first guess of the location is not required and there are reliable results, even if the sensor covering is poor (KURZ 2006: 69–80).

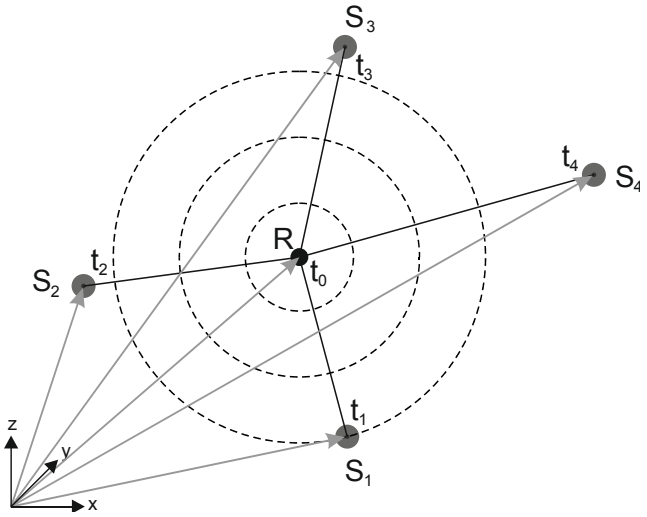

Figure 35: Localization of the position R of the receiver with the unknown coordinates (x, y, z) and the unknown origin time t_0 is based on travel time differences from a number of sensors S_i with known coordinates (x_i, y_i, z_i) and arrival times t_i.

Localization accuracy

The accuracy and reliability of the localization is dependent on different sources of error. One of the most important reasons for an inaccuracy are errors in the arrival time detection, which is influenced by the quality of the data and the clarity of the signal onset (KURZ et al. 2010: 124). A high signal to noise ratio and a high signal amplitude contribute to better results. From experiments, FINCK (2005: 157) identified several influences on the signal quality, which have to be considered: A good sensor covering and an optimal distance between source and sensor of about 10–30 cm increases the accuracy of the location as well as an ideal angle of wave incidence. The minimization of noise and an optimized experimental setup, including sensor coupling, cable length, and experimental settings also play an important role. Furthermore, a larger number of sensors increases the localization accuracy.

In general, a homogeneous p-wave velocity is assumed throughout the specimen and during the tests. It is clear from the representation of the cracking behavior under compressive stress in Subsection 2.3.1 that the p-wave velocity will change during the loading process of the rock specimen. Perfectly homogeneous rock samples are an exception and not very common. Instead, the rock fabric, inhomogeneities, and the stress history of the rock sample will mostly cause at least a slight inhomogeneous p-wave velocity. KURZ et al. (2010: 133) found that the location accuracy decreases with increasing damage of a specimen, since wave propagation cannot occur when open cracks exist. The elastic waves are scattered and reflected in the damaged regions. Besides, SCHECHINGER (2005: 75) mentions the influence of the sensor diameter, which is sensitive over a large proportion of the surface as well as an inaccurate determination of the sensor coordinates. If the coordinates of the signal source are known, an absolute localization error can be determined. Thus, in advance of all tests, external ultrasonic pulses with known coordinates have been set and localized. An average p-wave velocity for the whole rock specimen was assumed. In order to obtain the best possible localization results, the data was filtered and only the data fulfilling the requirements of a high SNR and signal energy were selected for localization.

3.4.4 Testing procedure

Acoustic emission testing was performed during uniaxial compression testing and during stress relaxation of rock samples. The testing procedure was identical for both applications. Before every test, ultrasonic pulses were set at the surface of the cylindrical rock surface at defined coordinates. The instantaneous examination of the waveform enabled the control of the sensor coupling. It revealed errors in the experimental settings, irregularities in the data transmission or technical defects in the system. An average p-wave velocity was calculated for the specimens from the different arrival times at the sensors. The p-wave velocity was used for the back-localization of the external events and an average localization error was determined for every pulse. If necessary, events with an extraordinary high error were excluded from the calculation of the p-wave velocity. After the placement of the ultrasonic pulses, AE monitoring was started. In uniaxial compression tests, AE were recorded during loading, whereas stress relaxation of fresh core material was continuously monitored for several days.

3.5 Thin section analysis

Thin section analysis was carried out on thin sections impregnated with fluorescent resin so that open microcracks were made visible under ultraviolet (UV) light. A qualitative analysis was performed to reveal whether microcracks preferably occurred at existing cracks or flaws, whether their occurrence is limited to specific minerals or structural features, and whether the cracks are intragranular, intergranular or transgranular. With a quantitative analysis, the crack density and orientation of existing microcracks was examined.

3.5.1 Thin section preparation

Cracks in a specimen can be made visible by coloring the rock with fluorescent dye. For this method, the desired part of the rock is carefully cut and grinded to a plain surface. The rock cube is impregnated with a mixture of Araldite, epoxy resin and green fluorescent dye. The permeation of the liquid is enhanced leaving the rock in a vacuum oven for about 24 hours so that the liquid intrudes the open cracks. After that, the remnants of the hardened mixture are grinded off until only the rock with the fluorescent cracks remains. Thin sections have been manufactured from the rock cubes in a second step, leaving the cover glass away for a free view of the fluorescent cracks under UV light.

3.5.2 Microscope image acquisition and processing

Thin section analysis was performed using the system microscope Leica DM LM with an integrated mercury-vapor lamp as light source for fluorescence microscopy. For digitization, a microscope camera together with an image acquisition software was used. A cross table was mounted on the object table for an exact positioning of the thin section. With a micrometer screw at the cross table, the sample can be moved in x- and y-direction. In order to obtain a representative section of the sample, a defined part of the thin section with a size of about 1 cm² was digitized. The same section of the sample was captured three times using plane-polarized light (P-pol), crossed polarizers (X-pol) and incident light for fluorescence microscopy with UV light. In order to obtain a high-resolution image, a 5-times magnification was used and 169 single images were taken from every thin section. The images overlapped by about 55 % in horizontal direction and by about 40 % in vertical direction. For the fluorescent images, it was important to use the same settings for all images, to be able to compare the images without any differences in exposure time, light sensitivity or resolution. The free software Microsoft Image Composite Editor (ICE) was used for processing the single microscope images. ICE is an advanced panoramic image-stitching program, which is able to create a high-resolution panorama picture by combining the original images in a user-defined structure.

3.5.3 Qualitative and quantitative image analysis

For the qualitative image analysis, a composed image was created with the fluorescence image overlying a composed image, which was taken with crossed polarizers. With the overlying images, open, fluorescent microcracks could be assigned to minerals and grain boundaries. The focus of the qualitative image analysis was the cracking behavior of different minerals and the occurrence of intragranular, intergranular or transgranular microcracks.

The quantitative crack analysis was performed using the open source software ImageJ (Fiji) (SCHNEIDER et al. 2012, SCHINDELIN et al. 2012), including the BioVoxxel Toolbox (BROCHER 2014). ImageJ is an image-processing program based on Java, which was developed at the National Institutes of Health. A

quantitative analysis with ImageJ should provide information about the area, the orientation and the length of microcracks. Image analysis of natural microcracks in rocks poses several difficulties. SIMMONS & RICHTER (1976) defined that a microcrack is a void with one or two dimensions smaller than the third. They also defined that the crack aspect ratio, or width to length ratio, must be less than 0.01 and the length should be smaller than 100 µm. Fluorescence images show that a large amount of existing cracks do not meet these crack definitions. In most cases, cracks do not form a defined geometry of a typical crack being straight, without branches and interactions with other cracks. Instead, there is a crack network of multiple branching cracks interacting with each other and only a few single microcracks exist. Thus, a fast analysis of the whole crack network in an image is limited by several factors.

- Especially in feldspar, natural microcracks may already be present, which are sometimes better referred to as flaws than real microcracks. They follow twin lamellae or alteration products of feldspar and thus penetrate the whole mineral (Figure 36a). The flaws are diffusely distributed within the feldspar minerals and they form a dense network of fluorescent flaws, where the color was able to intrude. The crack networks do not give any information about stress-related crack orientations or the extent of cracks. Still, the crack networks contribute to the rock damage and they are thus considered in the total crack area.
- When analyzing the extent of microcracks, it must be considered that some cracks are slant cut and appear broader than they actually are (Figure 36b). In contrast, cracks cut at an exact right angle appear clearly and thin. The width of microcracks can therefore not be determined with a two-dimensional analysis.
- Some cracks are not dyed completely or the color is not intense enough to be recognized in the image (Figure 36c). This is because the fluorescent color did not penetrate all cracks entirely or because the crack is unfavorably cut. Furthermore, the appearance of the fluorescent color is strongly dependent on the exposure time when the images are taken.
- Particularly in granite specimens, many natural microcracks are present and only few cracks are separated from the total crack network. Usually, cracks cross each other (Figure 36d: i), cracks meet at one point (ii) or split up in two cracks (branching) (ii). The identification of the orientation and the length of one single crack is thus not possible with a fast image analysis.

According to the actual appearance of dyed cracks, new limitations for the definition of cracks have to be defined. Separating all single cracks from the crack network is difficult and almost impossible for the analysis of a whole image. A procedure has been developed to analyze as many cracks as possible and at the same time obtain representative results for the preferential orientation of cracks. The developed flow diagram for digital image analysis with ImageJ is shown in Figure 37. Image analysis requires the following steps: After opening the stitched fluorescent image, a scale needs to be set with the help of the existing scale in the image. Preprocessing of an image includes a color threshold, binarization and denoising. A defined color threshold is set for the initial RGB color image in order to consider only those colored pixels, which correspond to a crack. The selection is converted into a binary image and outlying white pixels in a radius of two pixels are removed in order to remove noise pixels.

The crack area is calculated as the percentage of crack pixels with respect to the total pixels of the whole image. This is a fast method to compare the crack area from intact samples with the samples loaded with different stress levels. For the analysis of the crack orientation, a preselection of considered areas is made because of the numerous limitations mentioned above. The operation “Extended Particle Analysis” in the BioVoxxel Toolbox is an additional tool for selecting areas with required parameter specifications. A selection is made using the defined restrictions for Area, Circularity and Aspect Ratio, given

in Figure 37. After applying that filter, only elongated shapes with a defined minimal area, maximum circularity and minimal aspect ratio are analyzed. The most significant parameters of the analyzed cracks are illustrated in Figure 37. Those parameters are used on the one hand to filter crack networks and to consider only single microcracks with an elongated shape. On the other hand, the Feret diameter gives the maximum extension of the crack. The orientation of the cracks with respect to the horizontal are given by the Feret angle.

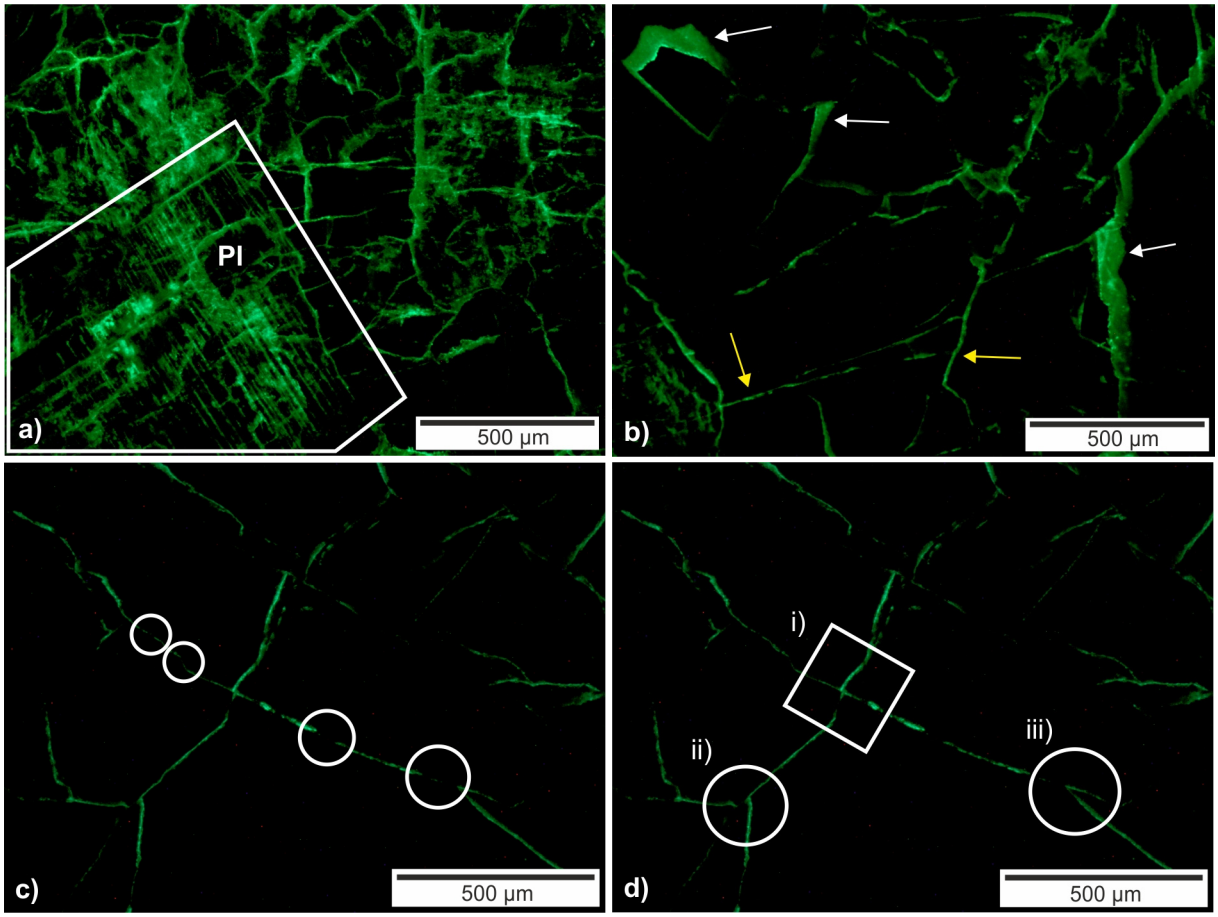

Figure 36: a) Plagioclase mineral with colored twin lamellae and diffusely distributed color inside further feldspar minerals. b) Broad slant cut cracks (white) next to thin cracks cut at a high angle (yellow). c) Incompletely colored cracks. d) Interaction and branching of cracks where (i) two cracks cross each other, (ii) three cracks meet in one point and (iii) cracks branch.

The procedure for crack analysis is given in Figure 38 as a sequence illustrating the initial fluorescent image, the binary image, and the image with only those cracks used for the analysis of the crack orientations. From the original image, the mainly vertical and horizontal cracks are only partly suitable for the analysis of the crack orientation, since the shape of the connected crack network does not meet the requirements. Although most of the crack area had to be filtered, the general trend of mainly vertical and horizontal microcracks becomes clear from the cracks remaining for the analysis (Figure 38c).

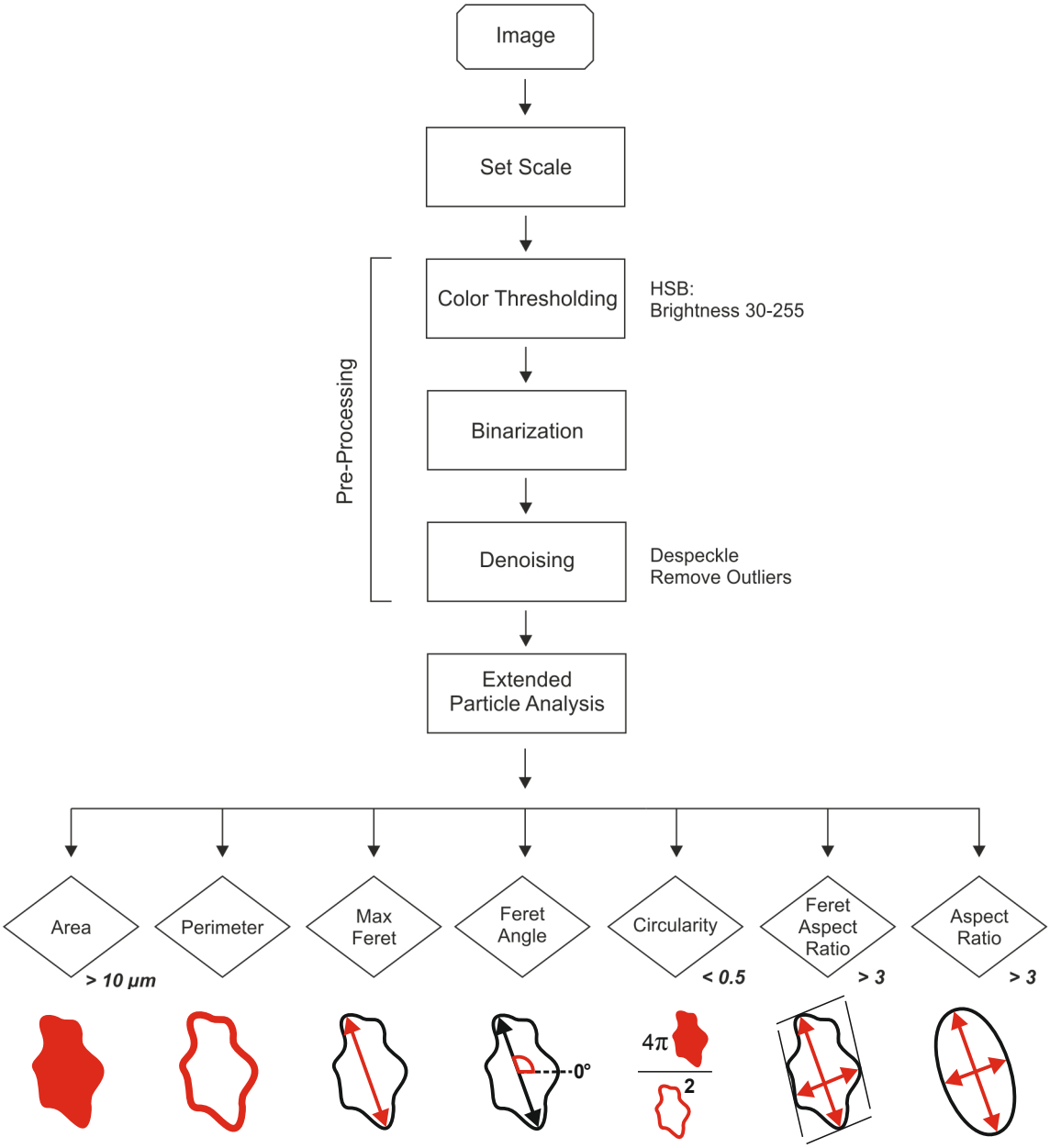

Figure 37: Flow diagram for digital image processing and crack analysis of fluorescence images using ImageJ (after www-2).

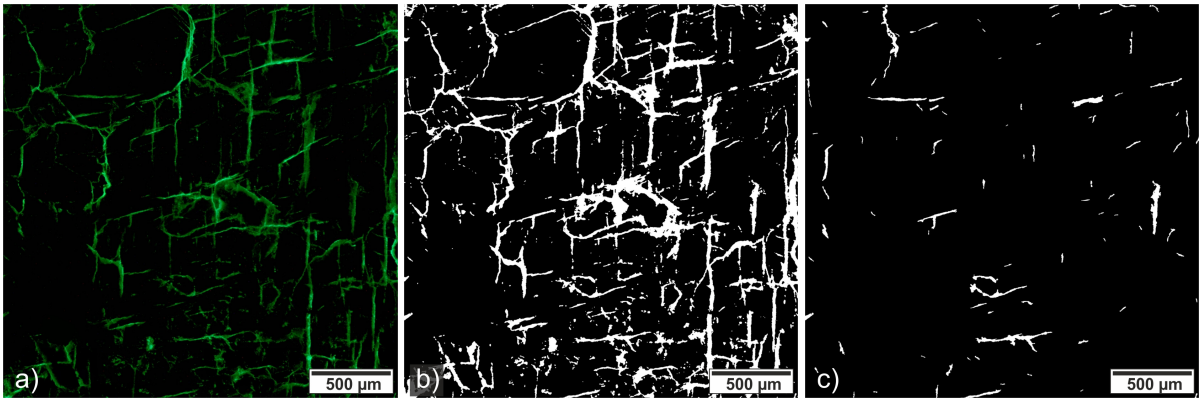

Figure 38: Illustration of the procedure for filtering single cracks with a suitable elongated shape. A) The original image is preprocessed with a color threshold and b) a binary image is created. c) Further preprocessing steps are required to analyze the suitable microcracks.

4 Time-dependent accumulation of rock damage

In this chapter, the results of field investigations on core material recovered from a high in-situ stress environment are presented. Additional laboratory tests were performed in order to examine the deformation and cracking behavior of the analyzed metavolcanic rocks. The time-dependent accumulation of rock damage was investigated on fresh core samples recovered from the primary stress field. When the confining stresses are removed, strain relaxation takes place and microcracks may initiate. Deformation and cracking of core specimens from the depth is a time-dependent process and is characteristic for different types of rocks. Acoustic emission monitoring and p-wave velocity measurements were performed on fresh metavolcanic core samples and stress relaxation was monitored within about one hour after core recovery.

4.1 The Pyhäsalmi Mine

Investigations on stress relaxation were conducted at the Pyhäsalmi Mine in central Finland (Figure 39). The Pyhäsalmi Mine is a copper and zinc mine located in the Pyhäjärvi municipality. Production commenced in 1962 as an open pit mine by Outokumpu Corporation. It is the oldest operating metal mine in Finland and is today one of the deepest metal mines in Europe with a depth of 1 444 m below the surface (First Quantum Minerals LTD. n.d.). Beginning in 1967, exploitation of the drop-shaped ore body proceeded underground and since then, the mine has been deepened gradually. A ramp and a new shaft go down to the level +1 441 (meters below surface). The Pyhäsalmi Mine is owned by the Canadian mining corporation First Quantum Minerals Ltd. and is operated by the Pyhäsalmi Mine Oy. According to current estimations, mining of the ore deposit will continue until the year 2019 (RUBBIA 2013a). As a future use of the mine facilities, the Pyhäsalmi Mine is a candidate location for LAGUNA (Large Apparatus studying Grand Unification and Neutrino Astrophysics), which is a European project of scientists working on particle and astroparticle physics.

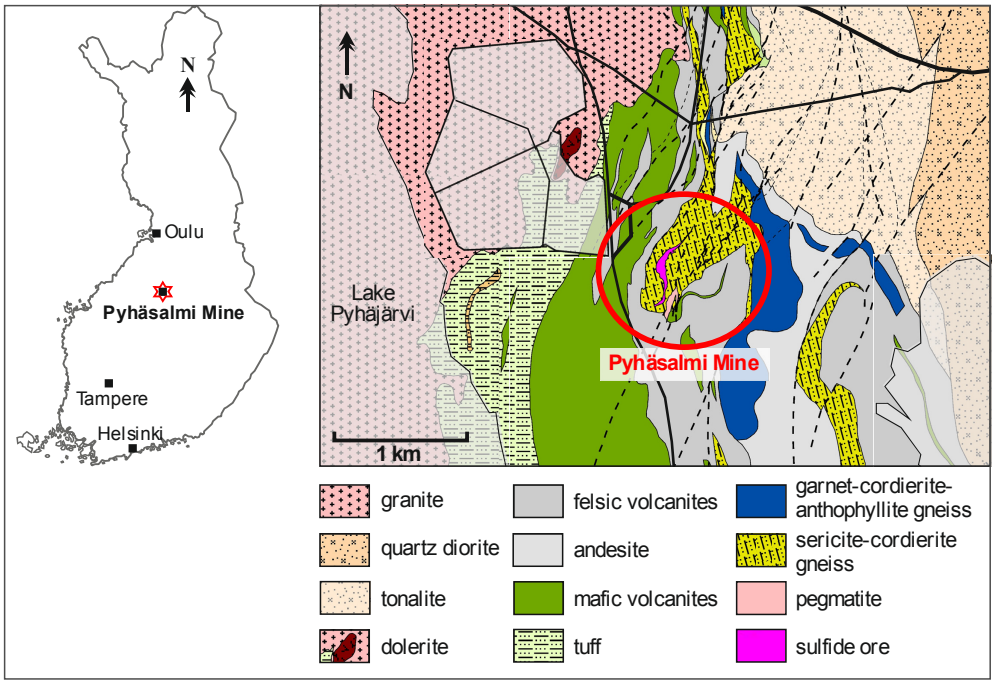

Figure 39: Location and geology of the Pyhäsalmi Mine (geological map after Geological Survey of Finland (2012).

The aim of the project is to establish a large-scale underground observatory in Europe for proton decay, low-energy neutrino astrophysics and long-baseline experiments. It is planned to send long baseline beams from the particle physics laboratory of CERN to the selected underground observatory (RUBBIA 2013b). For the experiments, large liquid-target detectors are planned to be built up in an underground observatory. Seven potential sites in Europe have been investigated in the first phase. The new design study LAGUNA-LBNO focuses on two of the preselected sites, where the Pyhäsalmi Mine is considered as one of the most promising sites. The current layout of the planned LAGUNA-LBNO underground laboratory at the Pyhäsalmi Mine is illustrated in Figure 40.

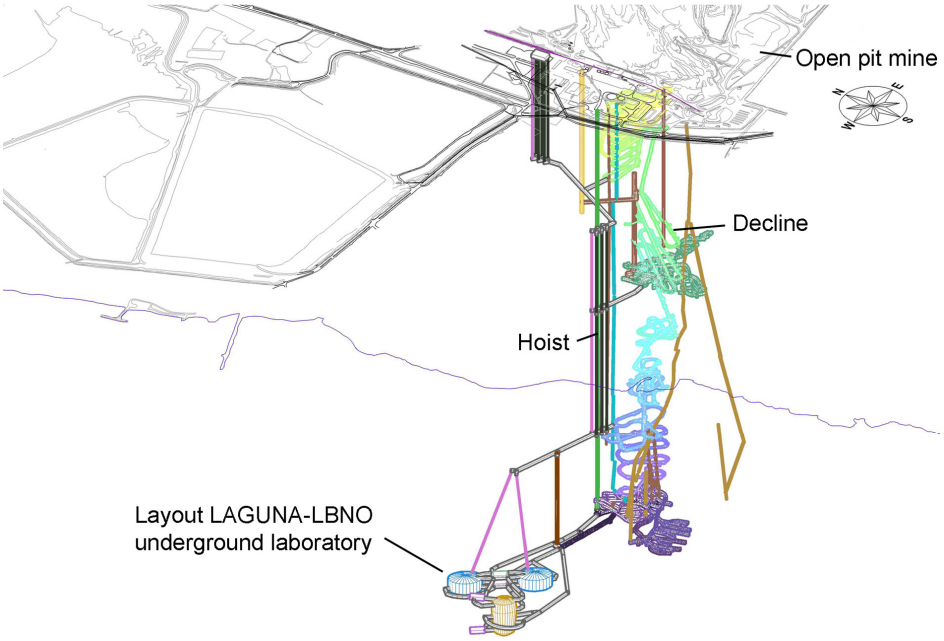

Figure 40: Underground infrastructure of the Pyhäsalmi Mine with the layout of the planned LAGUNA-LBNO underground laboratory (Rockplan: NUIJTEN & ZITO 2012).

Three possible detector technologies are considered, which are based on large volumes of liquids. The planned detector types GLACIER, MEMPHYS and LENA all use the emission of light pulses when neutrino particles interact with the liquid inside the detector (RUBBIA 2013b). For the three underground experiments, caverns with a span of up to 100 m and a minimum overburden of 1100 m are required (TRZASKA 2012). A total excavation volume of about 880 000 m³ is expected at the Pyhäsalmi Mine (RUBBIA 2013a). In order to investigate the geological and geotechnical conditions at the planned location of the detectors, deep exploratory core drillings were sunk in the surroundings of the Pyhäsalmi Mine. Rock samples from those drill cores were used in this field study. They were used to investigate the time-dependent relaxation behavior of rocks recovered from high primary stresses.

4.1.1 Sampling and rock description

The study on stress relaxation and stress-induced microcracking was carried out during an investigation period of two weeks in April 2014. For the study, fresh core samples were recovered from an exploratory drilling. The drilling site of the borehole PH105 was on the level +1 080 (Figure 41a). The borehole was drilled with an inclination angle of 30° in northwest direction, with an azimuth of 330°. The drilling diameter was 50 mm and the drill cores were all oriented. Core samples were selected at the drill rig upon retrieval from the borehole (Figure 41b). Mainly dark mafic volcanic rocks alternating with felsic volcanic rock and irregularly traversed by dykes of pegmatite were retrieved.

Figure 41: a) Drill rig at borehole PH105 at the level +1080 with an azimuth of 330° and an inclination angle of 30°. b) Samples of the mafic volcanic rock were selected from the drill core immediately after core recovery.

Samples were taken from the mafic volcanic rocks and the most homogeneous and isotropic samples were selected. Still, a slight foliation was present in all samples. After sampling, the rocks were immediately brought to the level +1 430, where the measurement device was set up in an underground office. The time between drilling and core recovery took about 30 minutes. The time for transporting the sample to the level +1 430 and the instrumentation of the rock samples took another 30 to 40 minutes. In total, the AE monitoring and the p-wave velocity measurements could be started about one hour after the core was drilled. The advantages of the measurements underground were stable temperature and humidity conditions and a relatively quiet environment. For AE monitoring, it is essential to minimize noise signals in the recorded frequency domain, which can be generated by electric devices or human disturbance. Most of the samples were amphibolite, consisting mainly of light plagioclase and green to brown amphiboles, showing a distinct foliation (Figure 42a). In most rocks, biotite occurs and enhances the foliation. In some rocks, dark green chlorite was present (Figure 42b).

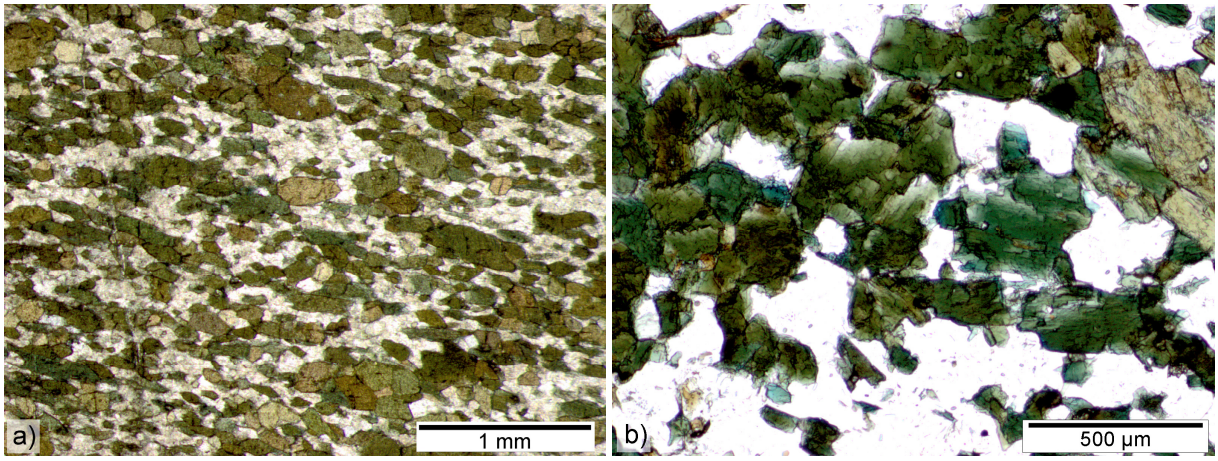

Figure 42: Samples from drill cores at the Pyhäsalmi Mine. a) Amphibolite consisting mainly of green and brown amphiboles and light plagioclase, showing a distinct foliation on the microscopic scale. b) Some analyzed rock contained chlorite instead of amphiboles.

4.1.2 Stress state at the Pyhäsalmi Mine

On the European section of the world stress map, stress measurement data indicate an orientation of the major principal stress in NW-SE direction for the central part of Finland (Figure 43a, see HEIDBACH et al. 2008). At the Pyhäsalmi Mine, in-situ stress measurements were performed at different levels of the mine. Measurements at level +1 125 and level +1 350 showed that the major and intermediate principal stresses are almost horizontal and the minor principal stress is vertical. According to the stress measurements, the major horizontal stress is oriented in NW-SE direction (280–310°) with a mean magnitude of 54 MPa. The ratio of major to minor principal stress is 1.8 to 2.0 (HAKALA et al. 2002: 63, HAKALA 2014). The mean and upper values of the principal stresses are given in Table 7.

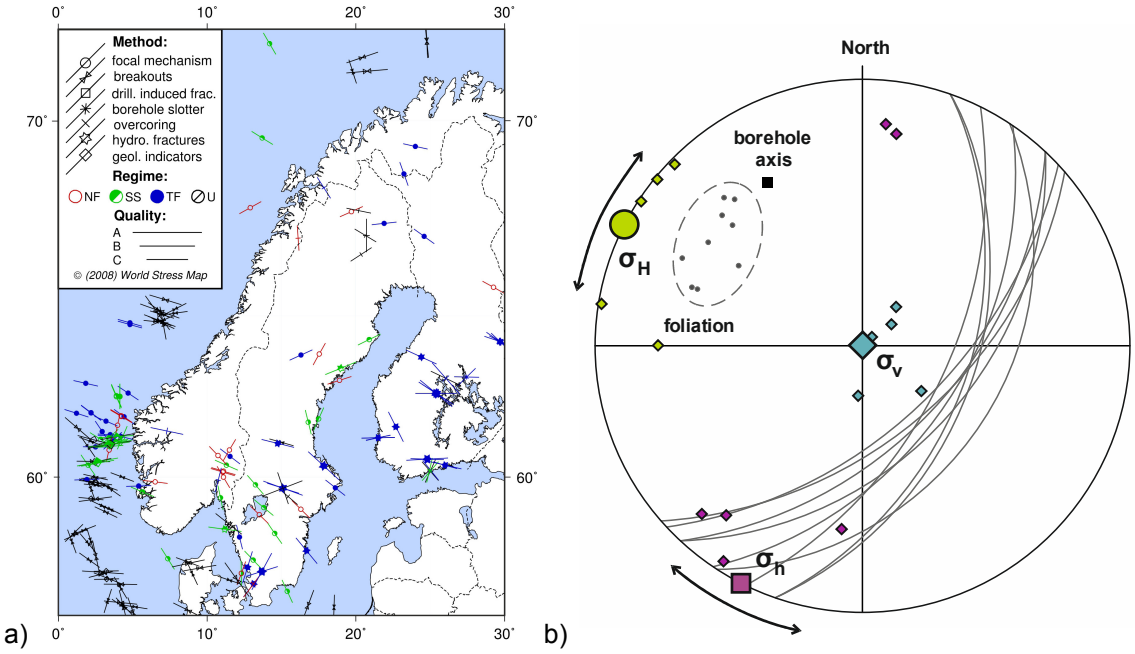

Figure 43: a) World stress map of Scandinavia (HEIDBACH et al. 2008) and b) pole plot diagram with principal stresses (big markers are average values, small markers are single values), the orientation of the borehole axis and the foliation planes at level +1125 (stress data from HAKALA 2014).

In the analyzed areas of the rock mass, the foliation dips on average with an angle of about 60° to the southeast. With an inclination angle of about 10 to 30°, it is oriented almost perpendicular to the core axis. In Figure 43b, the average and single values of the major horizontal stress σ_H, the minor horizontal stress σ_h and the vertical stress σ_v are illustrated, together with the orientation of the foliation planes and the borehole axis of drilling PH 105. The azimuth of the drilling is 330° with an inclination of 30°. The mean orientation of the foliation is 304/57 in the area of the tested rock samples. In the drilling, the normal of the foliation is oriented almost parallel to the borehole axis and parallel to the major principal stress component.

Table 7: Suggested in-situ stresses at the Pyhäsalmi Mine (from HAKALA 2014). Stresses were determined from stress measurements at the levels +1 125, +1 375 and +1 430. Upper values are 95 % confidence limits.

Principal stress	**Stress magnitude**		**Orientation**	
	Mean (MPa)	Upper (MPa)	Trend	Plunge
Major horizontal stress, σ_H	54	72	280° – 310°	5°
Minor horizontal stress, σ_h	39	44		
Vertical stress, σ_v	39	43		

4.2 Monitoring of stress relaxation

Stress relaxation of core material recovered from the primary stress environment was measured over a period of several days. Two nondestructive testing methods, acoustic emission monitoring and p-wave velocity measurements were used to measure the increasing accumulation of damage due to the relaxation of the rock samples.

4.2.1 Acoustic emission monitoring

The acoustic emission technique enables monitoring of the cracking process within crystalline rocks, using elastic waves generated by dislocations inside the rock. When relieved from the in-situ stress environment, core samples adapt to the altered, unconfined conditions until a new stress equilibrium is reached. Upon removal, stored residual stresses inside the core are released by the opening of preexisting cracks and by the generation of new cracks. Several studies have been conducted in order to investigate the correlation between primary stress state and strain or p-wave velocities (ENGELDER 1984, LIM et al. 2012, ZANG et al. 1996). Further researchers dealt with the time dependency of stress relaxation for different rock types (TEUFEL 1989, WOLTER & BERCKHEMER 1989, MEGLIS et al. 1991, ZANG & BERCKHEMER 1993).

In order to approach the time-dependent process of rock damage, AE monitoring of rock specimen recovered from a high primary stress environment were carried out. Within one hour after coring, the specimens were prepared for AE monitoring. Eight piezoelectric transducers were mounted to the core by hot glue and the specimens were installed on foamed material in order to avoid noise signals being transmitted to the transducers. A slew rate trigger combined with a ring buffer was applied in order to save only those events exceeding the trigger conditions. AE monitoring was carried out on two fresh core samples (see Table 8) with a measurement duration of 146 hours for sample L77-2 and 66 hours for sample L82-2. Both metavolcanic rock samples showed a slight foliation almost perpendicular to the core axis. In general, the rocks appeared dark grey to black but areas of lighter bands were apparent. The AE transducers were mounted in the dark and most homogeneous areas of the core (Figure 44).

The results of AE monitoring of two core samples are given in Figure 45. In the first hours, a high number of AE were recorded in sample L77-2 and about 22 hours after starting the measurement, the AE activity decreased steadily. Until the end of the monitoring period, the gradient of the curve is almost constant with only few recorded events. Several distinct jumps in the curve might be attributed to a higher cracking activity or to the occurrence of larger cracks. WOLTER & BERCKHEMER (1989) also detected such “bursts” in the AE curve during the relaxation of a lamprophyre sample and they assume that this might reflect avalanche-like microcrack interactions.

Table 8: Core samples applied for AE monitoring and ultrasonic p-wave velocity measurements (US).

Sample	Test	Depth	Rock description	Foliation*	Relaxation time (h)
L70-1	US	1238 m	Massive to foliated grey metavolcanic rock	15°	47 / 56
L77-1	US	1253 m	Massive, fine-grained, dark grey metavolcanic rock	15°	65 / 97
L77-2	AE	1253 m		15°	38
L82-2	AE	1265 m	Massive to foliated grey metavolcanic rock	5°	6

*Angle between core axis and the normal of the foliation planes

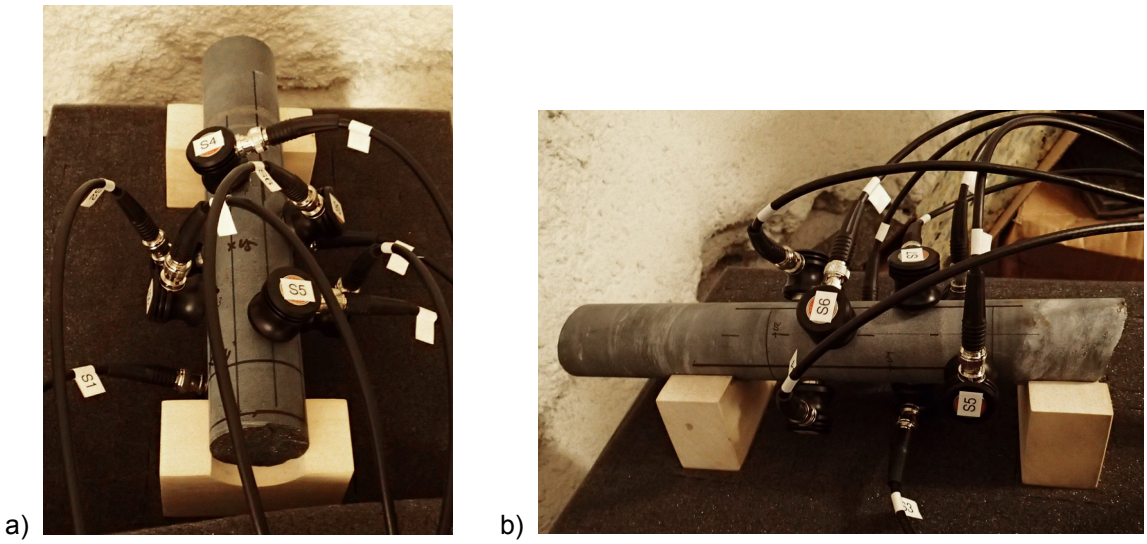

Figure 44: Core samples instrumented with sensors for AE monitoring a) Sample L77-2 from a depth of 1 257 m and b) sample L82-2 from a depth of 1 270 m. Both cores have a diameter of 5 cm.

In sample L82-2, a considerably larger number of events occurred, especially in the first hours. The curve of the AE rate is smoother compared to sample L77-2 and shows only minor bursts. After about 10 hours, the gradient of the curve decreases and stays almost constant until the end of the measuring period. Same as in sample L77-2, there were still events occurring when the monitoring period had to be stopped. In general, both curves show a similar, almost logarithmic shape with many cracks occurring in the first hours of measuring. Even after several days of measuring, the AE activity did not fully cease. In both samples, a true state of equilibrium was not reached within the measuring period. The number of acoustic events approximately follows an exponential decay and can be described with the relaxation law by WOLTER & BERCKHEMER (1989):

$$A(t) = A_{\infty}\left(1 - \exp^{\left(-\frac{t}{\tau}\right)}\right) \tag{29}$$

where A(t) is the number of AE at time t, A_{∞} is the asymptotic value for $t \rightarrow \infty$ or the maximum number of cumulated events. The relaxation time τ is defined as the time when $t = \tau$, which is achieved when A(t) is about 63 % of the ultimate number of events A_{∞}. For sample L77-2, the relaxation time is 38 hours and in sample L82-2, the relaxation time was reached after 6 hours.

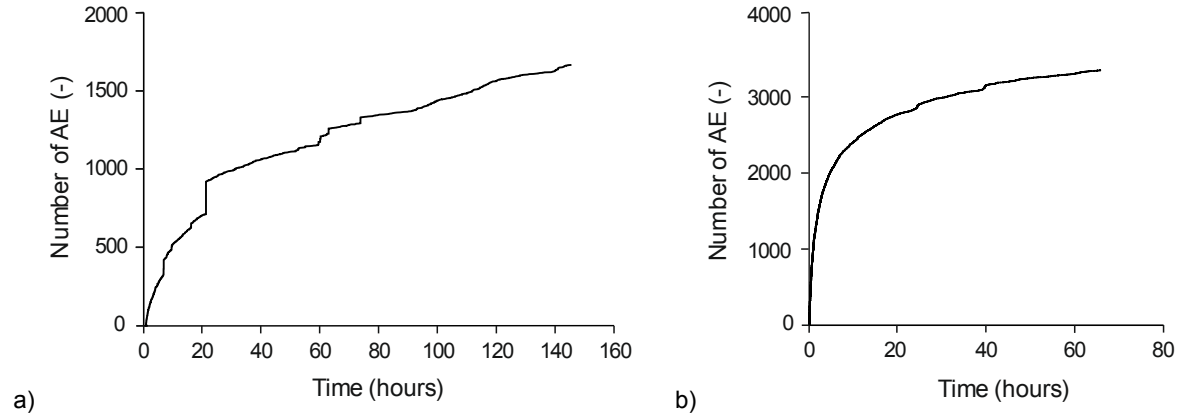

Figure 45: AE monitoring results of two core samples showing the number of AE of sample a) L77-2 and b) L82-2. (WIESER et al. 2015a).

The results of AE and strain recovery of WOLTER & BERCKHEMER (1989) on a lamprophyre and a paragneiss sample showed that the relaxation time determined from the number of AE is almost similar to the relaxation time calculated from strain recovery. ZANG & BERCKHEMER (1993) determined the time constant τ from strain relaxation data of samples from the KTB. From seven amphibolite samples with different mineral compositions, which were obtained from depths between 3 590 m and 3 858 m, they determined time constants between 1 and 42 hours. Before the monitoring of AE was started, ultrasonic pulses were set at six defined coordinates on the surface of the core before and after the monitoring. With the arrival time differences at the eight sensors, a theoretical p-wave velocity was calculated for every event according to Equation (26). From the results, an average p-wave velocity was determined for the whole sample. With the average velocity, a back-calculation of the pulse coordinates was performed. The deviation of the back-calculated pulse coordinates from the known coordinates resulted in a mean localization error for every event.

A two-dimensional projection of the localization results of sample L77-2 with the error vectors is illustrated in Figure 46. At the beginning of the measurement, an average p-wave velocity of 5.6 km/s was determined, which resulted in a localization error between 8.1 and 18.1 mm. After six days of relaxation, the average p-wave velocity decreased to 3.7 km/s and a considerably higher localization error between 20.4 and 42.3 mm was obtained. The reason for the poor localization accuracy can be attributed to multiple causes: For the localization, an average p-wave velocity is assumed for the whole sample, but in fact, the p-wave velocity varies strongly within the samples. The initial velocities calculated for the pulses range from 5.2 to 5.9 km/s, with a standard deviation of 0.2 km/s. After the monitoring period, the p-wave velocities resulted in values between 3.0 km/s to 4.5 km/s, with a standard deviation of 0.5 km/s. Accordingly, the variation of the velocity increases with increasing core relaxation. Furthermore, p-wave velocity measurements of a second sample, conducted parallel to AE monitoring, revealed an anisotropic velocity distribution within the sample. P-wave velocity measurements will be discussed in the next subsection.

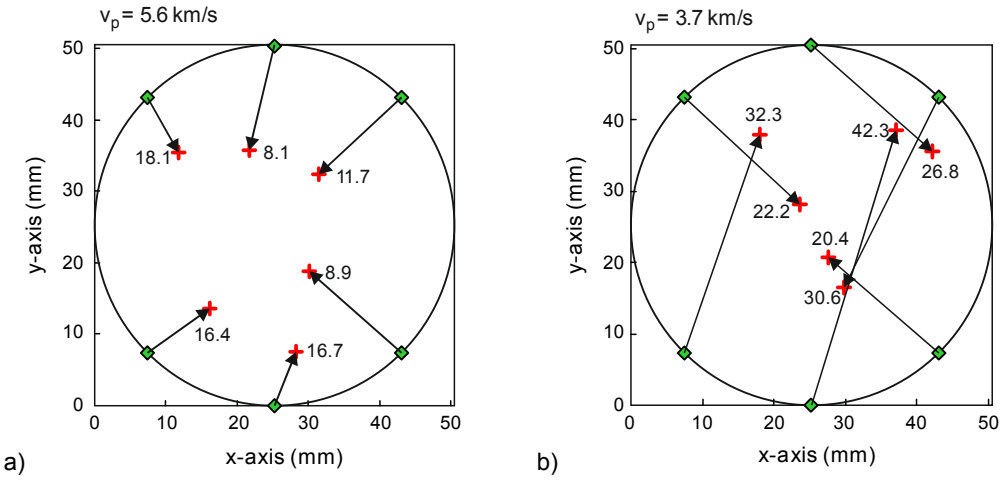

Figure 46: 2D projection of ultrasonic pulse localization of sample L77-2, a) about one hour after drilling and b) after 6 days of core relaxation. Green: pulse coordinates, red: back-calculated pulses, arrows: error vectors.

When the first pulse detection was performed, the instantaneous relaxation and part of the time-dependent, anelastic relaxation has already occurred. The existent cracks in the first measurement will thus also have an influence on the localization accuracy of the first pulses. The increasing inaccuracy of the calculation after relaxation can be ascribed to an increasing damage within the sample, which is caused by

the formation and propagation of microcracks during anelastic stress relaxation. In addition to an increasing crack density, an increase in the anisotropy due to a preferred opening of cracks in the direction of the previous maximum stress might also contribute to the high and increasing localization error.

4.2.2 P-wave velocity measurements

Simultaneously to AE monitoring, p-wave velocity measurements were carried out using similar core material from the same depth. Velocities were measured parallel to the core axis and in distances of 45° in three or four measurement profiles normal to the core axis (Figure 47). The first measurements were performed about 1 hour after drilling and measurements were repeated in irregular intervals, since the mine was not accessible during nights and weekends. After the investigation period, additional measurements were conducted days and weeks later in the rock mechanics laboratory at the Technical University of Munich. P-wave velocities were determined on two rock samples (see Table 8) with measurements until 37 and 45 days after drilling.

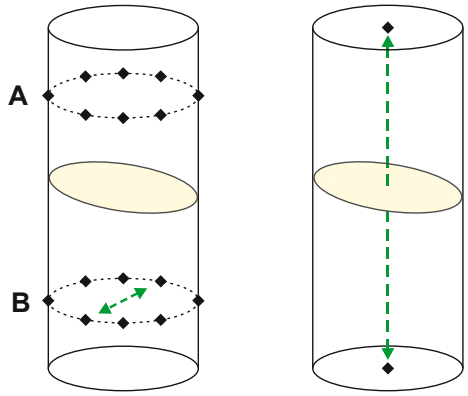

Figure 47: Procedure of p-wave velocity measurements in radial direction in 45° distances and in several measurement planes (A, B) perpendicular to the core axis and in axial direction parallel to the core axis. Yellow planes illustrate the orientation of the foliation.

In the polar plots of Figure 48a and Figure 48c, the mean values of the radial p-wave velocities are given, which are averaged over the measurement planes. The velocities determined after 1 hour (black) and the velocities of the last measurement (grey) are illustrated. Both samples show a clear anisotropic p-wave velocity distribution throughout the specimen diameter. The ratio of maximum to minimum value is 1.11 for sample L70-1 and 1.06 for sample L77-1. In both samples, the inclination of the foliation has an influence on the velocities, since the highest values were measured along the foliation and the lowest values occurred where the ultrasonic waves had to cross the schistosity planes.

The data also shows a distinct decrease of v_p from the first to the last measurement. In total, velocities of L70-1 decreased from 6.4 km/s to 5.4 km/s, which is a reduction of 15.5 %. In specimen L77-1, velocities are reduced by 10 % from 6.7 km/s to 6.0 km/s. The diagrams of Figure 48b and Figure 48d illustrate the average decrease in radial and axial velocity during stress relaxation, beginning with the first data about one1 hour after drilling. The strongest decrease of the radial velocity occurred in the first hours after core recovery until an almost constant value is reached after several days. The first axial velocities of both samples revealed an almost identical value of 5.4 km/s. The axial v_p also decreased rapidly within few hours until a threshold value was reached. Specimen L70-1 reaches a minimum value of 3.6 km/s and exhibits the greatest reduction of 33 %. In specimen L77-1, velocities are reduced by 22 % to a value of about 4.2 km/s. Like the radial velocities, the axial velocities showed and exponential decay (Figure 48b, d).

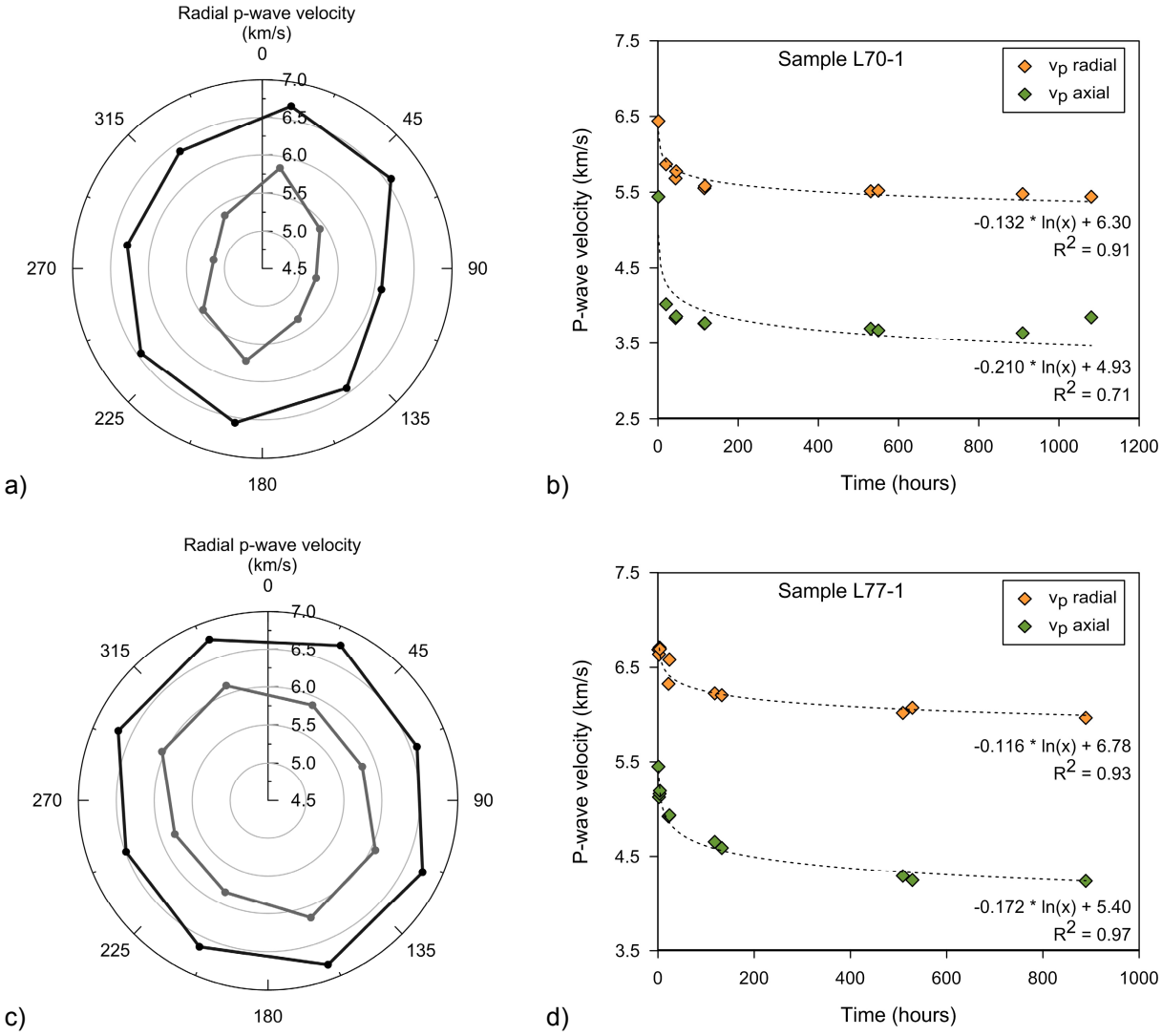

Figure 48: Results of radial and axial p-wave velocity measurements of sample L70-1 (a, b) and L77-1 (c, d). a, c) Pole plot diagrams show average radial v_p 1 hour (black) after drilling and the last measurement (grey) after several weeks. b, d) Average radial v_p and axial v_p both show an exponential decrease with time.

Within all specimens, the lowest velocities were measured parallel to the core axis and perpendicular to the foliation. Highest values were detected in radial direction, where the ultrasonic waves travel along the foliation planes and do not cross them. The velocity anisotropy ratio ($v_{p,radial}/v_{p,axial}$) is illustrated in Figure 49. During core relaxation, the ratio of radial to axial p-wave velocity showed a strong increase during the first hours. The reason is a considerably stronger decrease of the axial compared to the radial velocity. After several hours, the ratio reached an almost constant value. The velocity in specimen L70-1 increased to a ratio of 1.51 and in L77-1, it reached a maximum of 1.43. The exponential fit of sample L70-1 shows a relatively low coefficient of determination, mostly because of the last data point, which has to be considered as an invalid value due to a possible measuring error. The relaxation time of the p-wave velocity is determined according to Equation (29). In contrast to the analysis of the AE data, the measuring values could not be used directly for the calculation because of the small number of data points. Instead, the exponential functions describing the data were used. The relaxation time of sample L70-1 are 56 hours for radial v_p and 47 hours for axial v_p, while the relaxation time of sample L77-1 are 97 hours determined from radial v_p and 65 hours from axial v_p (see Table 8).

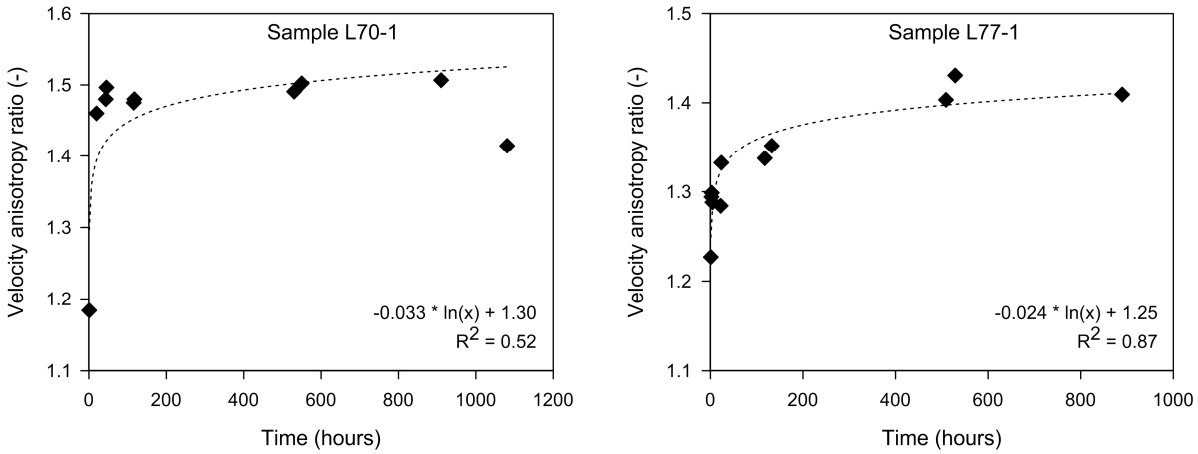

Figure 49: The velocity anisotropy ratio of samples L70-1 and L77-1 shows a distinct increase in the first hours after core recovery and reaches an almost constant value after the measuring period.

4.2.3 Petrographic analysis

From some samples, fluorescent thin sections were prepared in order to visualize possible relaxation cracks. A sample taken from the horizontal drilling PH107 at the level +1430 showed a number of cracks all oriented parallel with a regular spacing of about 2 mm (Figure 50a). The length of the open cracks filled with fluorescent resin is up to 1.5 mm. The formation of these cracks occurred along the foliation where aligned amphibole and plagioclase enable crack opening along their grain boundaries. Those stress-induced microcracks are interpreted as a beginning stage of core disking that only occurred on the microscopic scale and did not propagate further. In Figure 50b, the same sample shows a set of preexisting fractures crossing the foliation. Since the cracks are healed and the fluorescent resin could not penetrate them, it is clear that they were not reactivated during the drilling process. The fractures are parallel to the core axis and thus, core disking did not activate the cracks although they represent favorable planes of weakness.

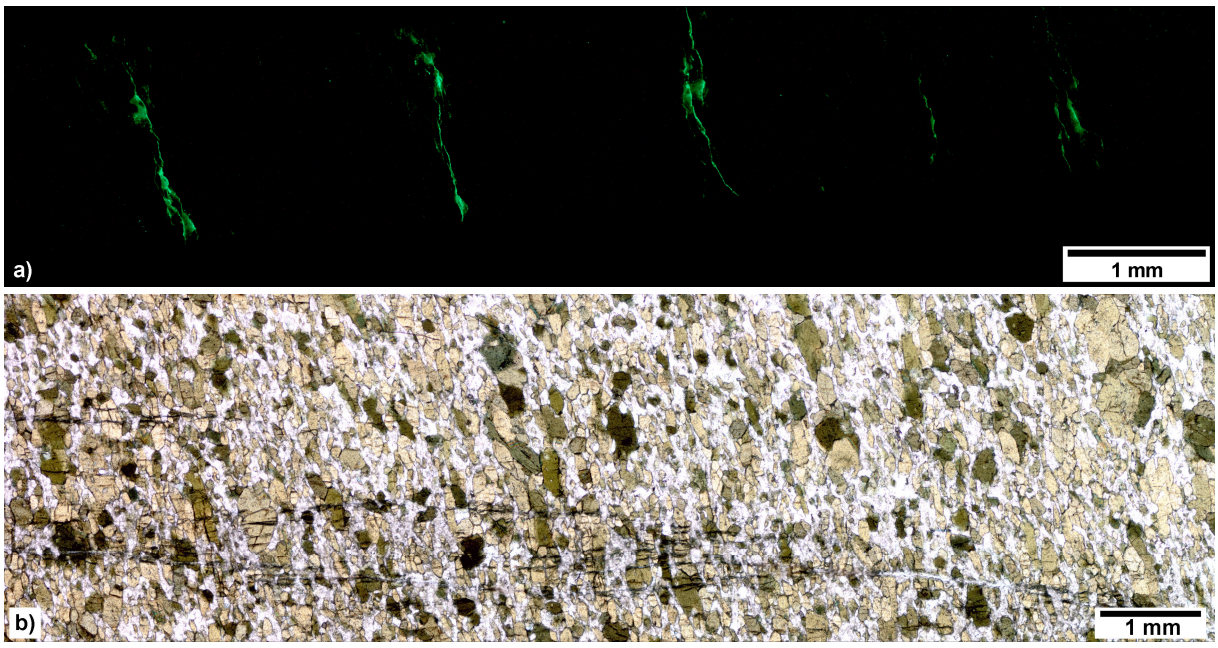

Figure 50: a) Fluorescent thin section of sample 107-3 showing parallel relaxation cracks with a regular spacing. The cracks opened along the foliation and in the direction of the previous maximum stress. b) The foliation is crossed by healed cracks (plane-polarized light). Orientation of both sections is parallel to the horizontal core axis.

Stress-induced tensile microcracks are generated in cores recovered from a high primary stress state. When stress concentrations at the drill bit exceed the crack initiation stress of the rock material, fractures perpendicular to the core axis develop. Although macroscopically core disking was not observed in the tested samples, thin section analysis revealed that the crack initiation stress was exceeded in the analyzed part of the core. It is suggested that the core material can be damaged by core disking if the crack initiations stress is exceeded in the weakest areas of the rock. The phenomenon of core disking was also observed in a different section of the same drilling. Figure 51 shows discs of about 1.5 cm thickness that evolved perpendicular to the core axis. Core disking developed near a zone of strongly disturbed rock, which might also be the result of a reduced crack initiation strength in a weaker material. With an azimuth of 280° and an inclination of –1°, the drilling is oriented parallel to the maximum horizontal stress and the foliation is almost perpendicular to the core axis. The opening of microcracks thus not only follows the foliation but also occurs in the direction of the major stress component.

Figure 51: Core disking observed in a section of the drilling with weaker core material where stress concentrations at the drill bit exceeded the crack initiation stress.

4.3 Laboratory rock properties

In order to analyze the geotechnical laboratory parameters of the amphibolite, samples were taken from the same drilling and a similar depth. From uniaxial compression tests with AE, the deformation and cracking behavior was investigated and fluorescent thin sections were prepared to analyze the stress relaxation microcracks. With the oriented thin sections, the orientation of the induced microcracks due to stress relaxation could be derived.

4.3.1 P-wave velocity measurements

P-wave velocities of samples taken from the drilling few meters above or below the monitored samples were measured in axial and radial direction. The measurements were carried out several weeks after drilling so that relaxation was finished by then. In Table 9, the mean values of axial and radial velocities are given.

Table 9: P-wave velocities and velocity anisotropy ratio of metavolcanic rock samples from drilling PH105.

Sample	**Depth**	**Mean $v_{p,axial}$**	**Std. dev.**	**Mean $v_{p,radial}$**	**Std. dev.**	**$v_{p,axial}/v_{p,radial}$**
ID	m	km/s	km/s	km/s	km/s	-
L68	1,233	5.4	0.3	6.9	0.5	1.28
L72	1,243	6.5	0.2	7.1	0.1	1.10
L74	1,245	5.9	0.2	6.9	0.1	1.17
L78	1,255	5.0	0.5	5.7	0.8	1.14

In all tested samples, the axial velocity was smaller than the radial velocities, which results in a velocity anisotropy ratio ($v_{p,radial}/v_{p,axial}$) between 1.10 and 1.28. Within 22 m of core material, the high data variation of 1.4 and 1.5 km/s must be attributed to small differences in the mineralogical composition or fabric of the rock. This becomes clear from the radial measurements in different planes of the rock. In some cases, the velocity strongly varied over the length of the specimen. A significant difference in the velocity of one plane compared to other measurement planes was apparent in several specimens. An example for velocity anisotropy is given in Figure 52. Although the different velocities were not clear from the outward appearance of the sample, the anisotropy must be attributed to differences in the mineralogical composition.

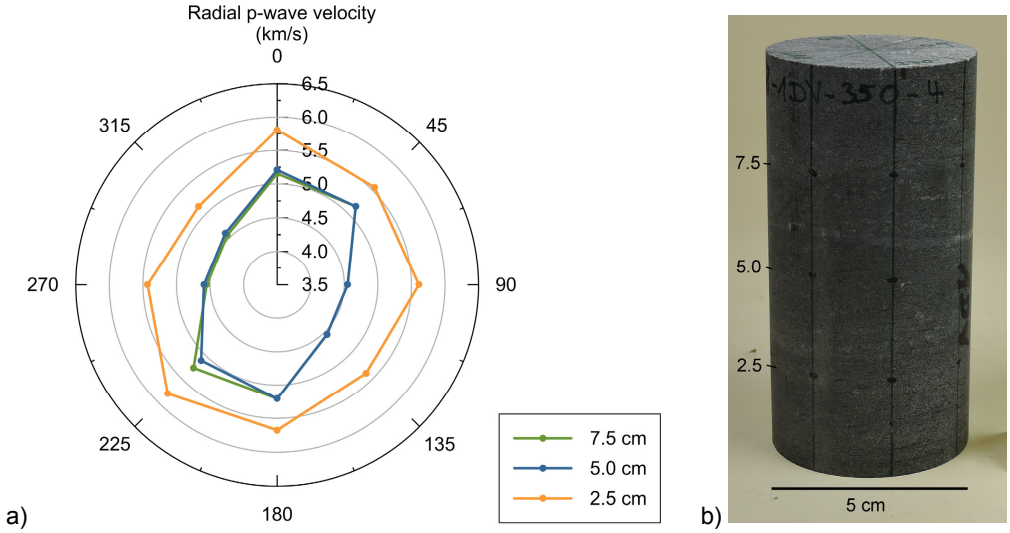

Figure 52: a) P-wave velocity of sample L78-4 with significantly higher velocities in the measurement plane at 2.5 cm. b) The appearance of the sample does not clearly indicate the different properties in that plane.

4.3.2 Uniaxial compression tests

Uniaxial compression tests were carried out on six fine-grained metavolcanic rock specimens from a similar depth like the monitored samples. Crack damage and crack initiation stress level could not be calculated from the stress-strain curves, since the brittle rocks did not show a reversal of the volumetric strain curve. Instead, the stress levels were determined from the AE activity. The absence of a reversal in the volumetric strain curve is the result of a low radial strain until failure. Table 10 summarizes the results of the uniaxial compression tests. The tested samples of L72 resulted in a mean uniaxial compressive strength of 296 MPa and the samples of L78 revealed a mean strength of 270 MPa. According to the ISRM (1978: 348), both rock types can be classified as extremely strong rock. High values for the Young's modulus show the high stiffness of the rocks. A low radial strain in the linear portion of the curves results in low values for the Poisson's ratio of 0.06 to 0.08 for L72 and 0.12 to 0.16 for L78.

The crack initiation threshold determined from the number of events is between 65 and 85 % of σ_u and the crack damage threshold is between 93 and 99 % of σ_u. It must be taken into account that the visual determination of the stress level might be subject to a certain error. An example of a uniaxial compression test is given in Figure 53. The stress-strain curves of all samples showed a similar appearance with a very low radial strain, a straight, almost linear stress-axial strain curve with a short phase of plastic deformation and without a post-failure phase. With a mean of about 3400 events until peak strength, the number of AE is comparatively low in the brittle rock types.

Table 10: Results of uniaxial compression tests of metavolcanic rock samples from borehole PH105 with simultaneous monitoring of acoustic events. The number of AE until failure is given as $N_{AE,u}$.

Sample	Depth	σ_u	E_T	v	$\varepsilon_{l,u}$	$\varepsilon_{q,u}$	$\sigma_{ci,AE}$	$\sigma_{cd,AE}$	$N_{AE,u}$
ID	m	MPa	GPa	-	%	%	%	%	-
L72-1	1 243	318	70	0.06	0.49	0.03	69	99	5 291
L72-2	1 243	321	73	0.06	0.51	-	66	93	1 426
L72-3	1 243	250	69	0.08	0.40	0.02	85	99	2 642
L78-1	1 255	273	59	0.16	0.52	0.08	77	99	5 161
L78-2	1 255	271	61	0.13	0.49	0.06	85	97	2 728
L78-4	1 255	267	59	0.12	0.51	0.05	65	97	3 054

In the crack closure phase, a small number of events was emitted in all tested rock samples. This indicates a preexisting rock damage and the cracks closed as a compressive load was applied. The existing microcracks can be stress relaxation cracks, which opened after the rock was removed from its primary stress environment. Fluorescence microscopy showed an opening of cracks in the direction of the previous maximum stress, which is almost parallel to the core axis. Reloading of the samples perpendicular to the cracks again closed the stress-relief cracks. During elastic deformation, AE activity largely ceased apart from single events. During this phase, the stress-axial strain curve is linear over a long proportion of the curve and a high amount of energy is stored within the rock without the generation of stress-induced microcracks. With the onset of crack initiation and stable crack growth, stored strain energy is partly released by the generations of microcracks. The beginning of crack interaction and crack coalescence is marked by a distinct increase in the cracking activity. Unlike the described phases of rock deformation, the tested rocks did not show a distinct increase in the radial strain during unstable crack growth. The phase of unstable crack growth is followed by an explosive collapse of the specimen, when the rock broke into pieces, thin rock fragments split off the external areas. In several specimens, major fractures even crossed the end surfaces of the rock. The fine-grained metavolcanic rock showed a brittle failure behavior, where the applied strain energy is released by microcracking only shortly before final rupture.

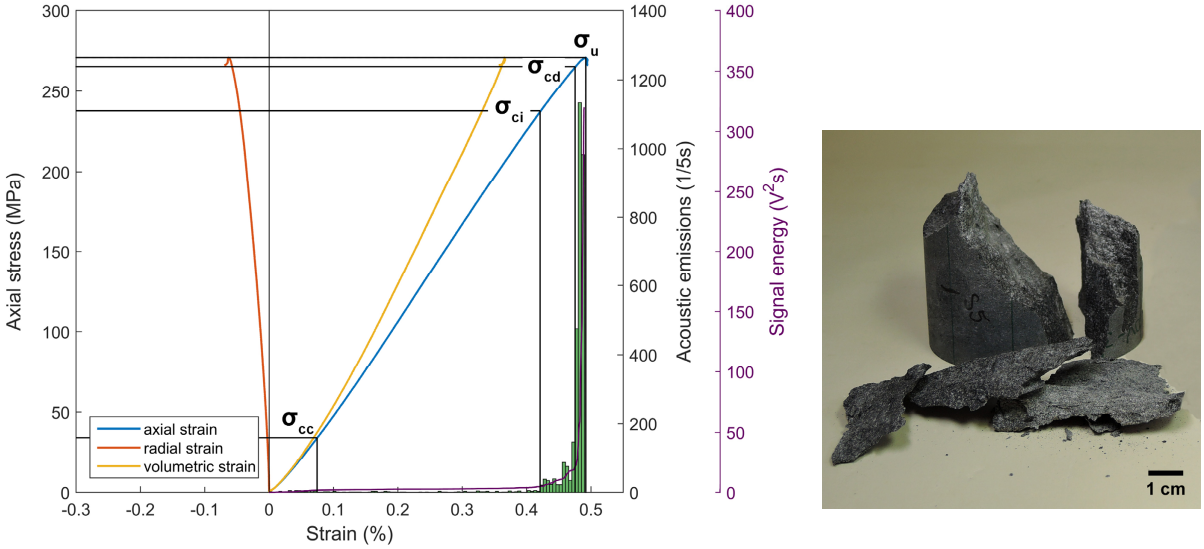

Figure 53: Stress-strain curve of sample L78-4 with crack closure σ_{cc}, crack initiation σ_{ci} and crack damage σ_{cd}, determined from the number of AE. Small pieces and thin rock fragments developed during failure, and only few bigger parts remained.

4.4 Discussion of field and laboratory results

In this section, the results of the field and laboratory tests on investigating the time-dependent accumulation of rock damage are interpreted. Mechanisms and processes leading to rock damage related to stress changes are proposed and the influence of stress-induced damage on rock properties is discussed.

4.4.1 Experimental results

When a core is recovered from its primary stress field, it adapts to the changed stress condition by the release of stored strain energy and residual stresses. The instantaneous component of relaxation occurs during the drilling process, whereas the time-dependent, anelastic strain relaxation continues for several hours and days. At the Pyhäsalmi Mine, monitoring of the anelastic relaxation was started within about one hour after drilling. The results of AE monitoring and p-wave velocity measurements during core relaxation both revealed an increase in rock damage. In the tested metavolcanic rocks, the main cracking activity occurred in the first hours and days after drilling, until it became increasingly less and ceased after several days. The occurrence of acoustic events gave evidence that permanent damage accumulated in the rock during stress relaxation. This is in agreement with the assumption that relaxation does not only occur as elastic strain but is also a result of the opening and growth of microcracks (ZANG et al. 1996). In addition, the increasing crack density and the propagation of existing cracks strongly affect the p-wave velocity. A more pronounced decrease in the axial compared to the radial velocity indicates that microcracks preferentially opened in the direction of the core axis and thus in the direction of the previous maximum stress. The field data revealed that the generation of stress-induced microcracks increases the velocity anisotropy of the recovered rock material.

Microscopic analyses furthermore revealed that the stress-relief cracks occurred along the existing foliation, where the opening of microcracks was facilitated by the grain boundaries of aligned minerals. Both, the results from p-wave velocity measurements as well as fluorescence microscopy showed that stress relaxation cracks mainly open in the direction of the previous maximum stress direction. The observations indicate that the previous maximum stress is the dominant cause for the orientation of the stress-relief cracks but the favorable orientation of the foliation is supposed to intensify the process of crack opening and crack propagation. Laboratory data showed that the mineralogical composition and fabric of the analyzed rocks strongly influence the p-wave velocities. As soon as the foliation is traversed by the ultrasonic waves, the velocity is clearly reduced. In the tested samples, a slight inclination of the foliation with regard to the core axis caused an additional velocity anisotropy in the radial measuring planes. Considerable velocity variations were also observed between single measuring planes because of suspected heterogeneities in the tested cross sections. The anisotropy of radial compared to the axial velocity is the result of two mechanisms: On the one hand, the axial wave velocity is reduced because the travel path needs to cross a number of foliation planes. On the other hand, an increased relaxation in the direction of the highest principal stress and a resulting opening of cracks reduces the p-wave velocity. The formation and opening of microcracks under compression could also be observed in uniaxial compression tests. According to the theory of BIENIAWSKI (1967) and others, existent microcracks will close when the rock specimen is loaded. In uniaxial compression tests performed on previously relaxed rock specimens, the stress-axial strain curve shows a non-linear axial strain behavior in the first phase of loading. In this phase, the recorded AE activity provided evidence for an existent damage in the rock samples.

4.4.2 Stress-induced damage

MARTIN & STIMPSON (1994) introduced a sample disturbance index D_i for samples recovered from the primary stresses. D_i is the ratio of the major principal stress to the undamaged compressive strength. According to the proposed classification of MARTIN & STIMPSON (1994) obtained for Lac du Bonnet granite, damaging begins when the major principal stress is greater than 10 % of the uniaxial compressive strength. For the tested rocks from the Pyhäsalmi Mine, the sample disturbance is between 0.22 and 0.27, when applying the maximum value for the major principal stress of 72 MPa. According to the authors, minor damage begins at an index D_i of 0.13 and significant damage occurs when D_i is about 0.28. Hence, the sample disturbance index confirms that microcracks can occur in the given stress environment at the Pyhäsalmi Mine.

Sample disturbance is the result of two mechanisms acting on the extracted core material. First, stress-induced damage may occur during the drilling process because of stress concentrations at the drill bit (STACEY 1982, LI & SCHMITT 1998, LIM & MARTIN 2010). The complex stress path at the face of an advancing drill bit leads to stress changes so that the magnitude and orientation of the stresses change. When the stresses at the drill bit exceed the core disking initiation stress of the rock material, coring-induced damage occurs. From investigations on Lac du Bonnet granite, LIM & MARTIN (2010) found that the initiation of core disking is dependent on the ratio of maximum principal stress to the Brazilian tensile strength of intact rock. They observed that core disking is mainly controlled by tensile stresses at the drill bit. The phenomenon of core disking is considered to occur when the core axis is oriented similar to the minimum principal stress (KANG et al. 2006). In the recovered samples from the Pyhäsalmi Mine, beginning core disking was observed on the microscale. Petrographic analysis showed parallel microcracks with a constant spacing, which developed along the foliation and perpendicular to the core axis. The phenomenon of core disking was also noticed at different core localities in the mine. This suggests that core disking occurs at planes of weakness where the tensile strength of the rock is lower than in adjacent areas.

The second mechanism inducing stress-related damage is the release of stresses stored within the core material. Core recovery from an initial stress state reduces the externally applied stress magnitude to zero stress so that strain relaxation takes place (ZANG & BERCKHEMER 1989). Where the external areas may expand instantaneously, within the rock, the release of residual stresses and strains is a time-dependent process. The initial stress state changes so that the stresses are redistributed and the stress magnitude changes. Dependent on the elastic properties of the constituent minerals and the interlocking forces between the minerals, microcracks may be initiated as a result of local stress concentrations at grain boundaries or heterogeneities in the rock (GORBATSEVICH 2003).

4.4.3 Influence of damage on rock properties

The results from p-wave velocity measurements and petrographic analyses showed that the relief of stresses causes microcracks to open normal to the foliation and in the direction of the previous maximum stress. The preferred opening of crack normal to the core axis is illustrated in Figure 54 (left, middle). When recovered from the primary stress field, elastic and anelastic strain occurs. In the phase of elastic strain, the stored strain energy is released by small expansions of the mineral grains. In the present case of a high ratio of major to minor principal stress and an anisotropy of the elastic properties of the aligned minerals, stress relaxation is assumed highest parallel to the core axis. GORBATSEVICH (2003) calculated the values of linear compressibility in the three crystallographic axes for several minerals. He found that minerals like amphibole, plagioclase, and particularly biotite show a marked anisotropy. According to

the author, stress relaxation thus results in high internal stresses, which may cause fracturing or a separation along the existing cleavage planes. During elastic relaxation, the different elastic properties of the constituent minerals, which are mainly plagioclase, amphibole, biotite or chlorite, may cause internal stresses at grain boundaries between adjacent minerals. When the stress concentrations at grain boundaries, flaws and existing microcracks locally exceed the critical tensile stress, crack initiation occurs. The findings of GORBATSEVICH (2003) revealed that the occurrence of mica strongly promotes the process of microcracking in rocks.

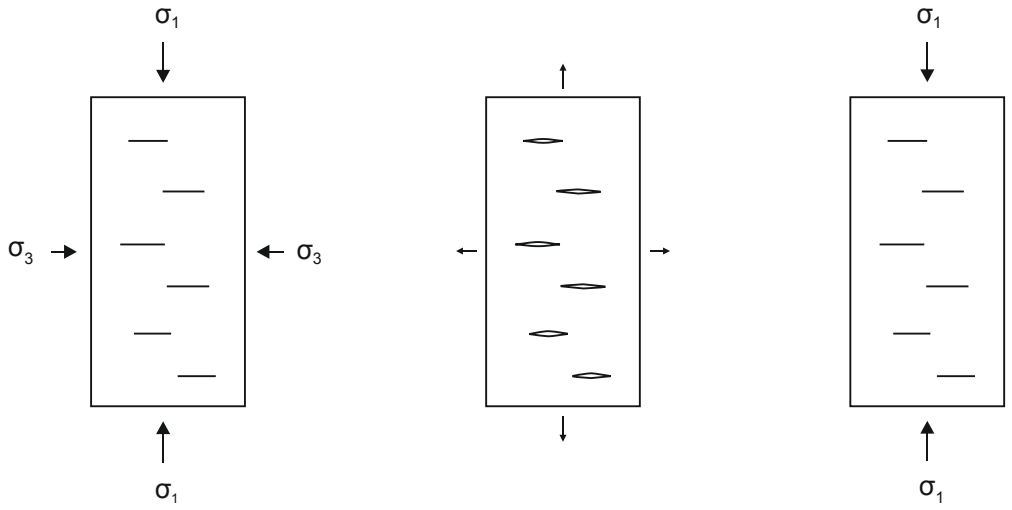

Figure 54: Schematic of principal stresses and their influence on existing microcracks in cores recovered from their primary stress state. An influence of open stress-relief cracks on laboratory properties is minimal because the second compression was applied in the same direction as the previous maximum stress.

For an investigation of the influence of relaxation cracks on rock properties, the cores were loaded in the same direction as the previous maximum stress (Figure 54, right). The application of compressional forces initially closes the open microcracks. The existence of damage was apparent from the AE activity and a non-linear behavior of the stress-strain curve. A significant influence of the stress-induced damage on laboratory properties, however, was not apparent, although a comparison of pre-damaged rocks with undisturbed samples from a location near the surface was not possible. Still, the influence of existing microcracks on the cracking behavior during uniaxial compression is supposed to be minimal. In general, microcracks originate at grain boundaries and preexisting intra- or transgranular cracks. Under uniaxial compression, crack growth will preferentially occur parallel to the loading direction and cracks will mainly initiate at cracks or flaws aligned parallel or at a small angle to the core axis. In the tested rocks, however, the main planes of weakness are represented by the stress-induced microcracks, which are oriented perpendicular to the loading direction. Consequently, those horizontal microcracks cannot cause crack initiation by shearing along closed crack planes. Although stress-relief damage is present in the rocks, the existent microcracks do not facilitate crack initiation during loading because the cracks are not oriented in a preferential direction. Instead, high stresses are required to initiate crack growth in the fine-grained structure of the brittle rocks. Although the stress-relief cracks do not promote the initiation of microcracks, they can facilitate the coalescence of cracks as soon as the crack damage stress is exceeded.

5 Characterization of rock properties

In this chapter, the results of laboratory investigations on ten different rock types are presented. The focus was on the mechanical and acoustic rock characteristics in order to achieve a thorough understanding of the characteristic material behavior of all tested rocks. Nondestructive testing techniques like ultrasonic testing and acoustic emission testing were applied to monitor the development of microcracks under uniaxial compression. The stress-strain curves, the located acoustic events, the mechanical and the acoustic parameters were used to determine the differences in the deformation and cracking behavior of the rocks.

5.1 Description of tested rocks

Laboratory investigations were mostly carried out on rock samples from different localities in Germany. Blocks of rock were obtained from quarries in the crystalline basement of the Bavarian Forest region, from the Mesozoic South German Scarplands and the Elbe sandstone highlands. Some samples were taken from Alpine regions in Austria and Italy (Figure 55) and diabase samples from an unknown locality in South Africa were used.

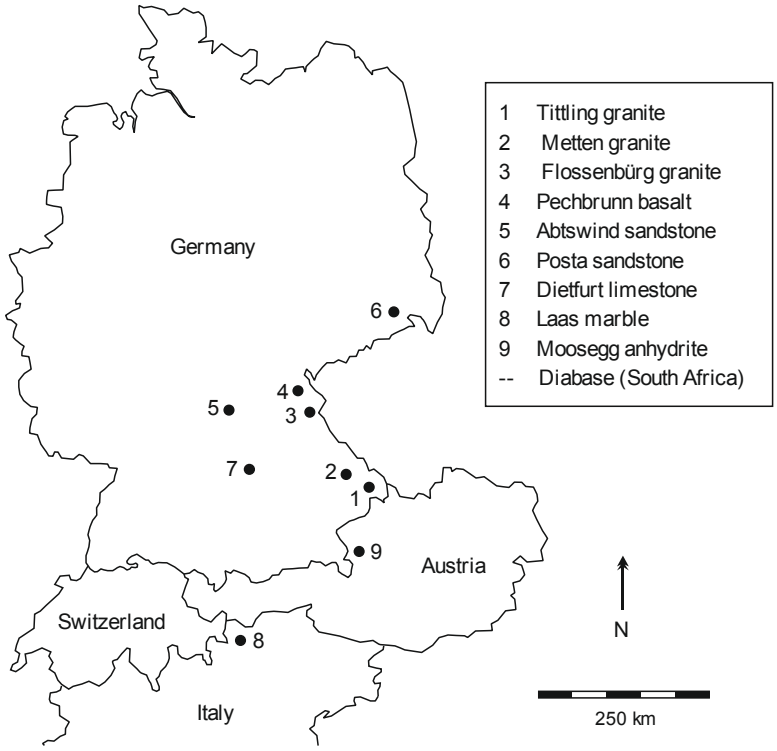

Figure 55: Localities of the tested samples in Germany, Austria and Italy.

5.1.1 Pechbrunn basalt

The Pechbrunn basalt is quarried in an open cast mine at the „Großer Teichelberg“, in northeastern Bavaria. The basalt was formed during the volcanic activity of the Miocene in the Fichtel Mountains forming a sequence of basalt sheets that emerged from fissures and volcanic vents in the center of the quarried hill. The Basalt AG exploits the deposit mainly for the production of railway ballast. The Pechbrunn basalt is a dense, dark grey to black, massive rock showing conchoidal fracture. The texture is aphanitic containing macroscopically visible minerals of mainly yellowish-green olivine (Figure 56). On a microscopic scale, a porphyric texture is visible with phenocrysts of olivine and pyroxene minerals of up to 0.5 mm in a fine matrix. The olivine is idiomorphic or shows corroded grain boundaries. It is often irregularly crossed by cleavage cracks. The dense fine-grained matrix shows dark and light minerals irregularly distributed. According to (KAIM 1990), the matrix consists mainly of idiomorphic, lath-shaped titanaugite and nepheline crystals with abnormal greyish-blue interference colors. Accessory constituents are opaque magnetite, plagioclase and biotite. A chemical analysis by (NÄHER 1989) resulted in the classification of the rock as plagioclase-bearing olivine nephelinite.

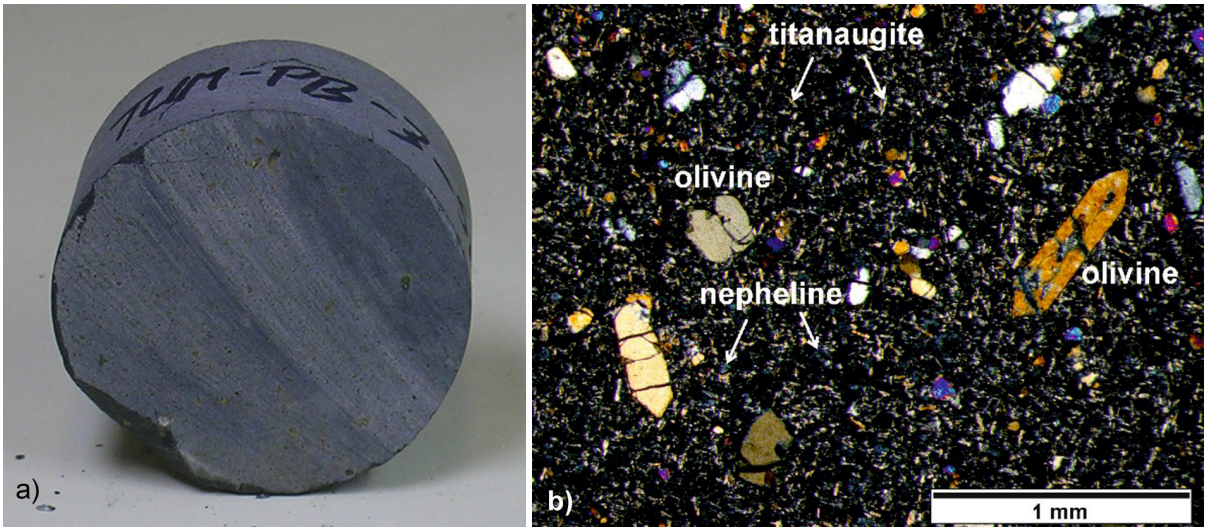

Figure 56: a) Dark fine-grained Pechbrunn basalt. b) The aphanitic porphyric texture consists of idiomorphic and corroded olivine phenocrysts. The matrix consists of fine-grained titanaugite, nepheline and plagioclase (X-pol).

5.1.2 Tittling granite

The Tittling granite is a grey homogeneous, equigranular, medium-grained rock. It belongs to the intrusive district of Fürstenstein-Tittling located in the northeastern Bavarian bedrock area (Moldanube) north of Passau (Figure 57). The pluton intruded in the Upper Carboniferous between 312 and 323 million years in the southwestern part of the Bohemian Massif (HELM 2013: 42). The granite is mined at the quarry Höhenberg in the northern part of the intrusive area of the Tittling granite. It is mainly composed of quartz, feldspar and biotite. For the quarry, TROLL (1964) gives a mineral composition of plagioclase 37.5 %, alkali feldspar 27.4 %, quartz 23.8 %, biotite 10.3 % and accessory minerals. Plagioclase is subhedral or anhedral, showing polysynthetic twinning. Some plagioclase minerals are zoned and most of them are partly or completely altered. The xenomorphic alkali feldspars show the lattice structure of microcline and they are generally less altered than the plagioclase minerals. The transparent grey quartz is xenomorphic with irregular grain boundaries.

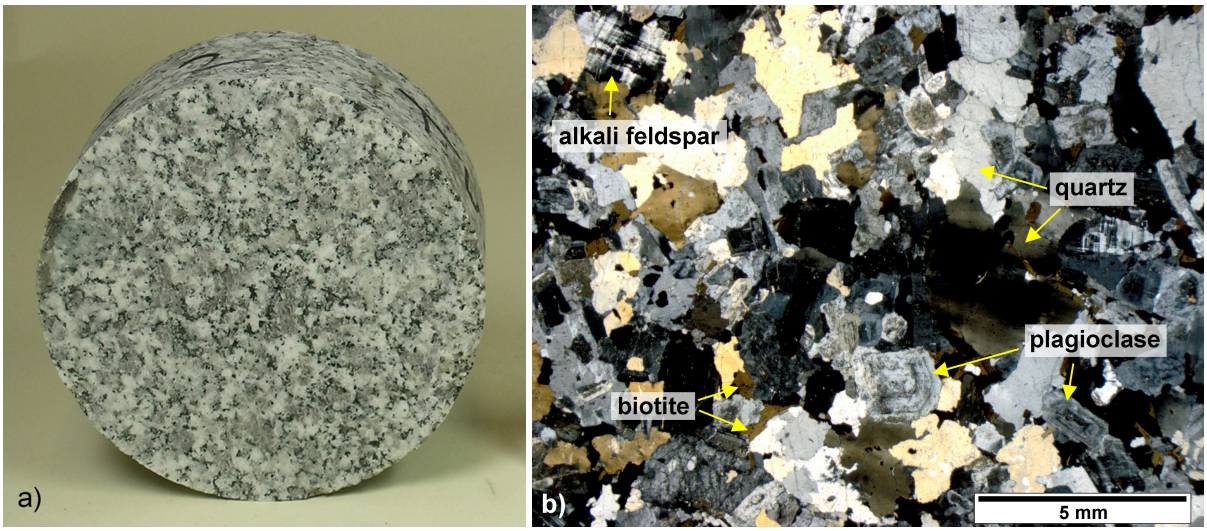

Figure 57: a) Medium-grained Tittling granite, b) with quartz, biotite, zoned plagioclase and alkali feldspar with microcline structure (X-pol).

5.1.3 Diabase

The diabase from an unknown locality in South Africa is a dark grey, dense and homogeneous rock. The texture is fine-grained and is traversed by some thin joints healed with quartz. The diabase consists of fine lath-shaped plagioclase crystals in the groundmass with xenomorphic phenocrysts of pyroxene in the intergranular areas. The formation of chlorite from pyroxene shows a beginning alteration (Figure 58). Furthermore, opaque ore minerals are distributed in the rock matrix.

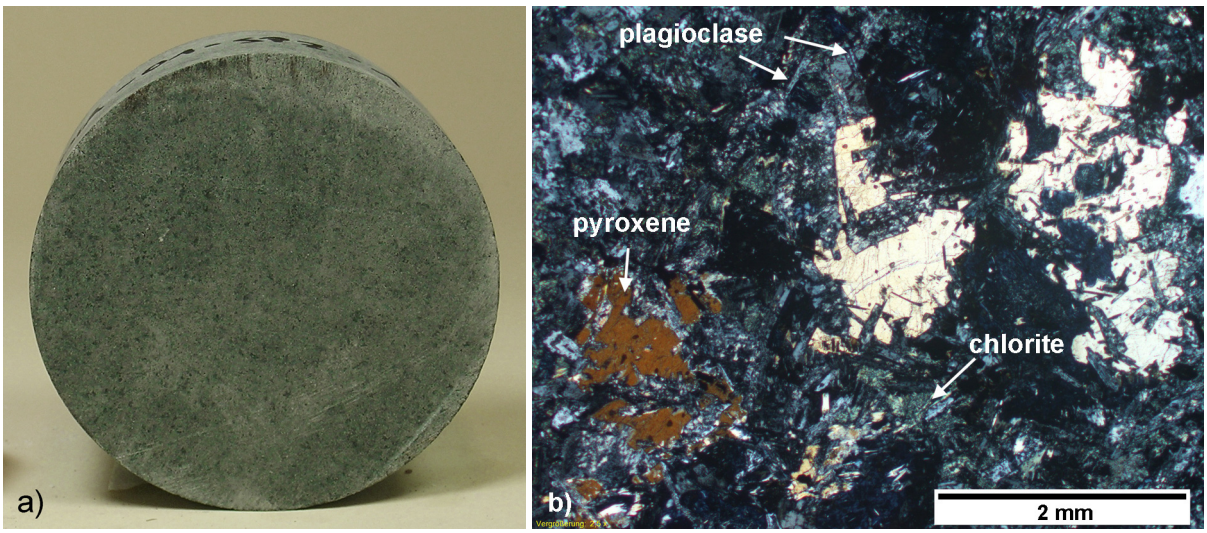

Figure 58: a) Homogeneous structure of a dark grey diabase sample (diameter 8 cm). b) Ophitic texture sample with plagioclase laths surrounding xenomorphic pyroxene crystals, which occur in the intergranular areas (X-pol).

5.1.4 Dietfurt limestone

The Dietfurt limestone is mined in the village Dietfurt, south of Treuchtlingen, in Middle Franconia (Germany) by the Frankenschotter GmbH. The rock was sedimented during the Upper Jurassic period (Malm), in the Kimmeridgian, in a shallow ocean basin (MEYER & SCHMIDT-KALER 1983). The rock is a popular natural and building stone in Germany and is known as “Jura Marmor” or “Treuchtlinger

Marmor" (Treuchtlingen Marble). It is a light beige, micritic and particle-rich limestone with irregular spots of grey and beige color. The limestone contains few veins of manganese oxides and some pyritic inclusions, which can be altered. Where the pyritic inclusions are missing, there are open pores in the otherwise dense fine-grained material. It is composed of more than 95 % of calcium carbonate in the form of biogenic material like calcareous microfossils, fossil remains and lithoclasts.

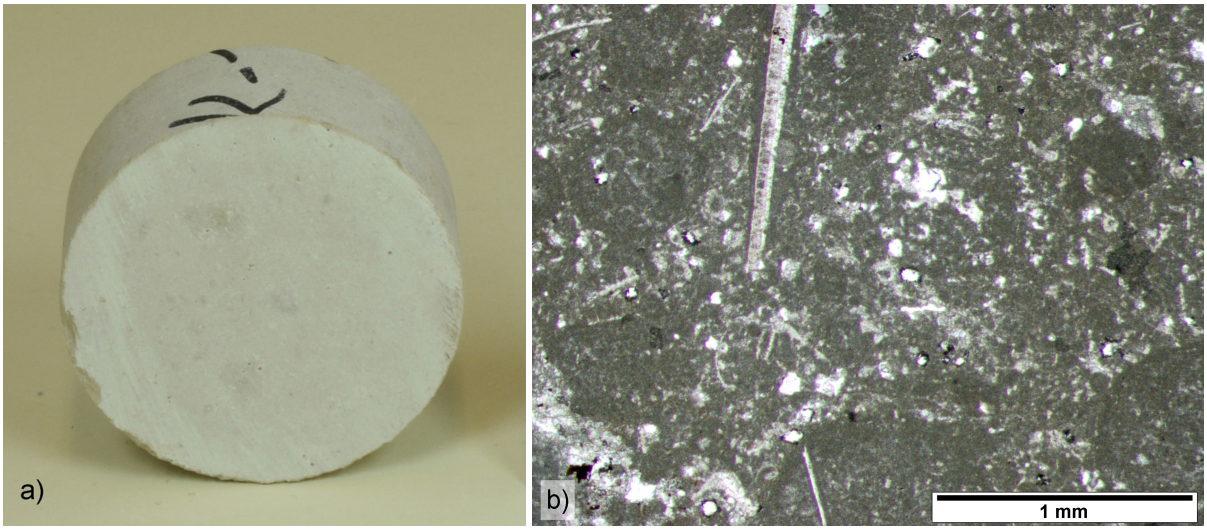

Figure 59: a) Light beige, micritic Dietfurt limestone with microfossils, fossil remains, calcareous lithoclasts and black pyritic inclusions (diameter 5 cm). The dark grey areas may be sponge or algal structures (P-pol).

5.1.5 Moosegg anhydrite

The Moosegg anhydrite was obtained from a gypsum quarry south of Salzburg, near the village Golling in the Salzkammergut Mountains. The anhydrite is part of the Mesozoic sedimentary rock sequence of the Northern Calcareous Alps in the Austroalpine units. The grey, dense anhydrite is fine to medium-grained and shows an equigranular texture. A change of color from light to dark grey generates an irregular lamination and several white joints healed with calcite traverse the rock. Microscopic analysis showed a preferred orientation of the anhydrite minerals, which show well-defined orthogonal cleavage planes. The minerals exhibit third order interference colors and sometimes twins are apparent.

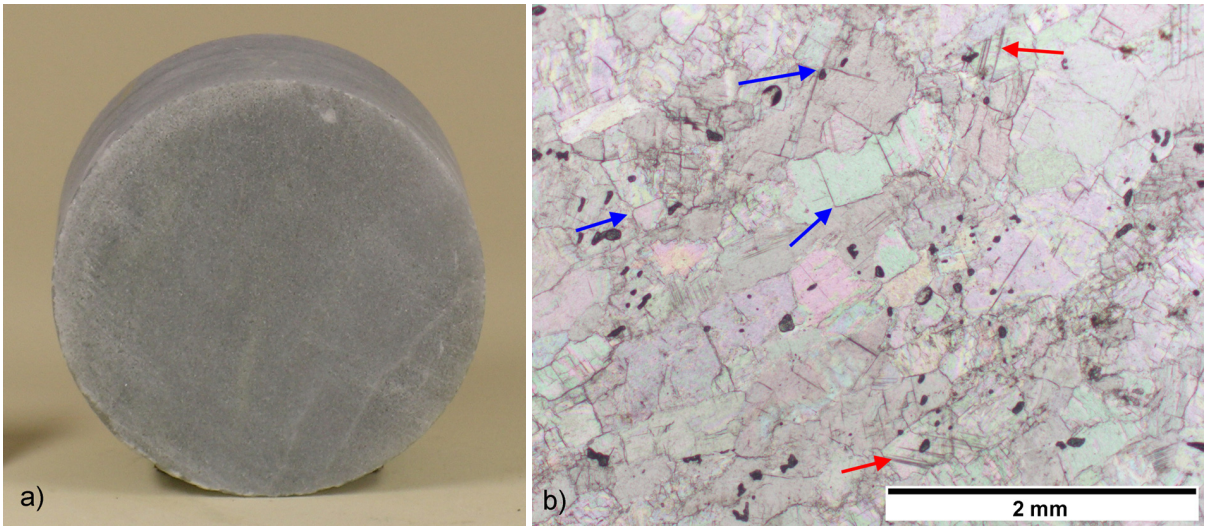

Figure 60: a) Grey, fine to medium-grained Moosegg anhydrite (diameter 5 cm). b) Anhydrite minerals show orthogonal cleavage planes (blue) and twins (red) (P-pol).

5.1.6 Laas marble

The Laas marble is a homogeneous, white, fine-grained calcite marble, which is a popular building stone in Central Europe. The marble is mined near the village of Laas in South Tyrol, Northern Italy. It belongs to the Laas unit of the Ortler-Campo-Crystalline. It is an almost pure white marble with more than 95 % of calcite. Accessory minerals can be dolomite, quartz, mica and feldspar as well as pyrite and graphite (UNTERWURZACHER & OBOJES 2012). The occurrence of dark inclusions and occasional bands of muscovite indicate a slight foliation in some samples. The marble shows a polygonal granoblastic texture with equal grain sizes between 0.2 and a maximum of 1 mm. Hypidiomorphic to xenomorphic calcite minerals showing high interference colors as well as calcite twins occur (Figure 61).

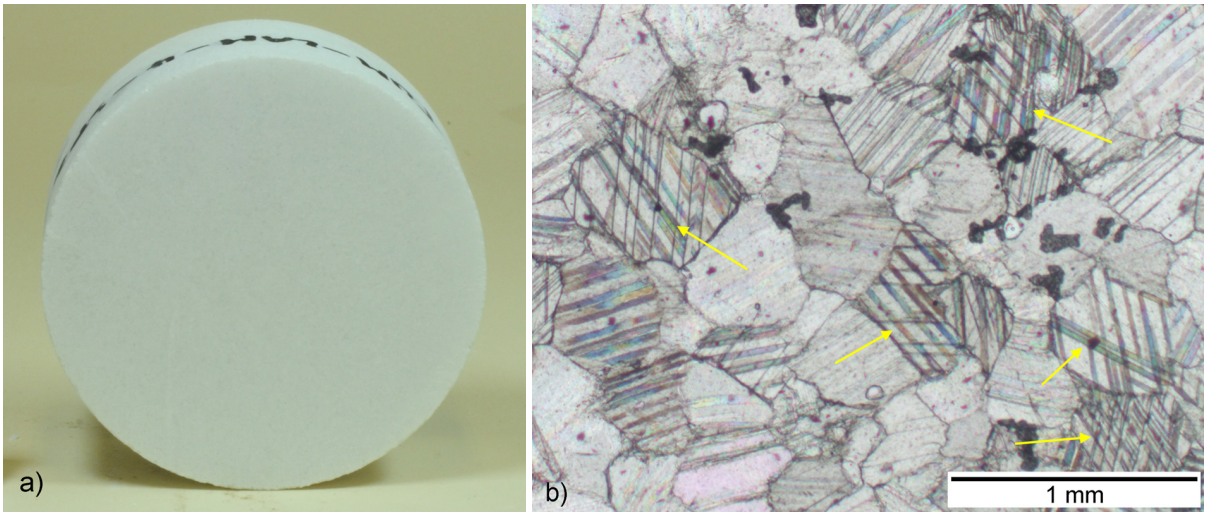

Figure 61: a) Plane white, homogeneous Laas marble (diameter 8 cm). b) Granoblastic texture of calcite crystals showing calcite twinning (P-pol).

5.1.7 Flossenbürg granite

The Flossenbürg granite is mined at a quarry in Flossenbürg, in eastern Bavaria, Germany. It is a yellowish grey, homogeneous granite (Figure 62), which intruded in the Upper Carboniferous. It belongs to the granite massif of Flossenbürg in the Upper Palatinate Forest.

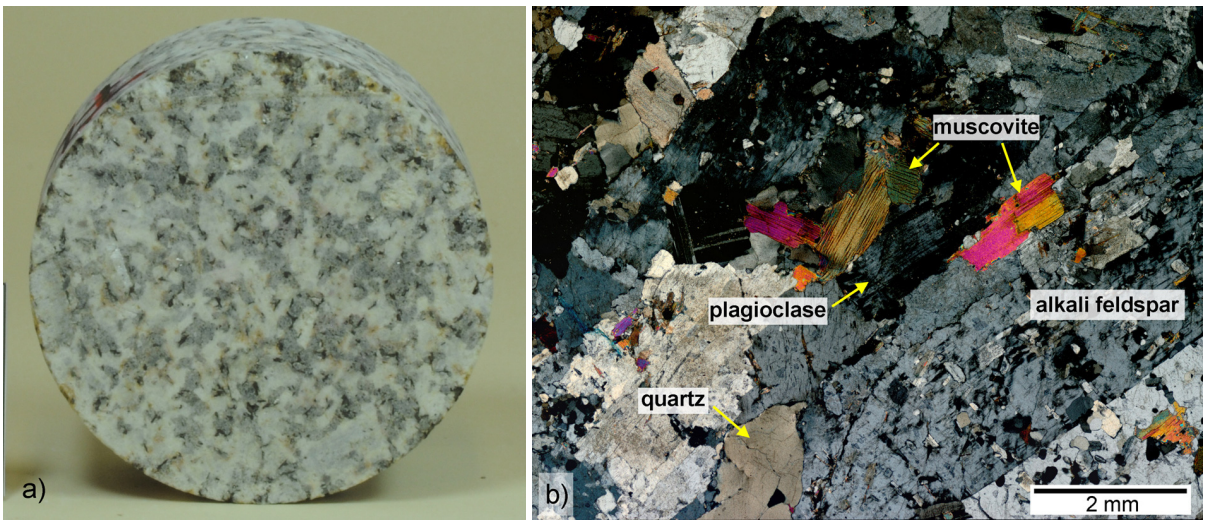

Figure 62: a) Porphyric texture of Flossenbürg granite (diameter 8 cm), b) consisting of quartz, plagioclase and big alkali feldspar minerals with Carlsbad twinning as well as biotite and muscovite (X-pol).

The rock is a medium- to coarse-grained two-mica granite with a porphyric texture. It is composed of alkali feldspar, plagioclase, quartz, biotite and muscovite. The large alkali feldspar minerals can reach a size of up to 25 mm, which often show Carlsbad twinning. In the smaller plagioclase, polysynthetic twinning is present and they show beginning alteration in the center of the minerals. The beginning weathering of biotite is macroscopically visible as a yellowish-brown coloration of the neighboring minerals caused by limonite.

5.1.8 Metten granite

The Metten granite is a light, brownish-grey, fine to medium-grained granite from the granite massif of Metten. The intrusive body is located in the Bavarian Forest northwest of Deggendorf and belongs to the western Bohemian Massif. The granite shows an equigranular texture and consists of plagioclase, alkali feldspar, quartz, biotite and muscovite (Figure 63). Alkali feldspar often shows exsolution lamellae and Carlsbad twinning, whereas plagioclase usually exhibits polysynthetic twinning. Both feldspars are sericitized and the biotite minerals show a beginning alteration to limonite.

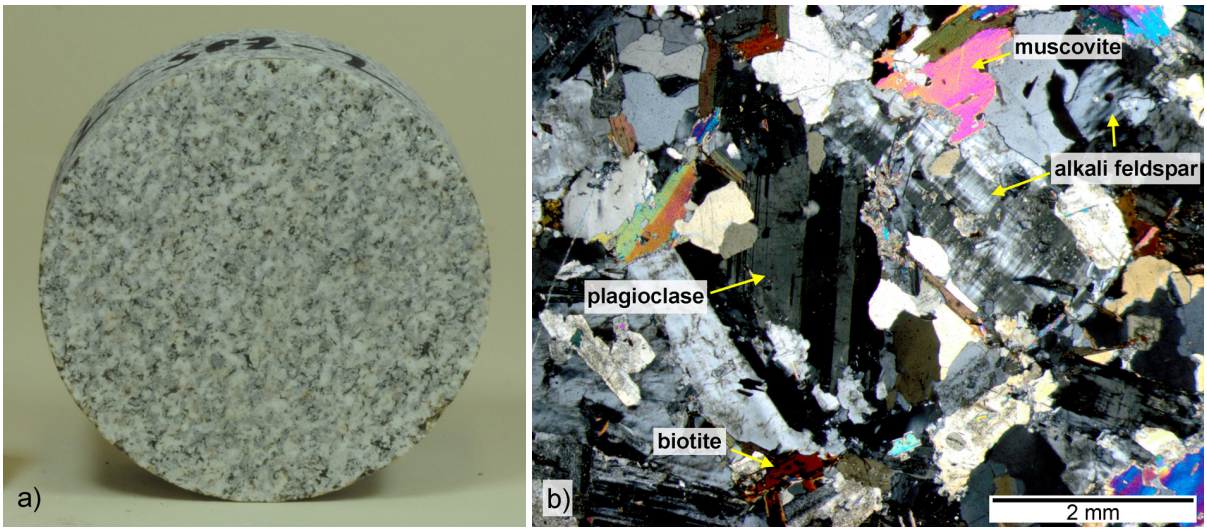

Figure 63: a) Equigranular texture of Metten granite (diameter 8 cm). b) The main components are quartz, plagioclase, alkali feldspar, biotite and muscovite (X-pol).

5.1.9 Posta sandstone

The Posta sandstone or Wehlen sandstone is a medium-grained, beige-yellow sandstone and was sedimented during the Late Cretaceous (Figure 64). It is also known as “Over Ashlar” (German: Überquader) and belongs to the Elbe Sandstones. The rock is a popular natural and building stone in Germany. SKOČEK & VALEČKA (1983) assumed a deposition in a marine environment in a shallow shelf sea in the Bohemian Basin. Today, the sandstone is mined on the right bank of the Elbe River, next to the town of Pirna in Saxonia, Germany. It is a mature siliceous sandstone with grain sizes between 0.2 and 1 mm. The rock is well graded and the grains are mainly angular to sub-round. A real bedding does not exist in the Posta sandstone, but brown streaks, resulting from an increased limonitic coating of the grains, cross the material. The rock fabric is clast-supported and the pore spaces are largely open. GRUNERT (2007) measured a porosity of 22 % and additional measurements by SCHALLHAMMER (2014) confirmed the value. With more than 95 % of quartz grains, the rock is a mature quartz sandstone. Besides quartz, dark brown iron hydroxide concretions or inclusions are irregularly distributed.

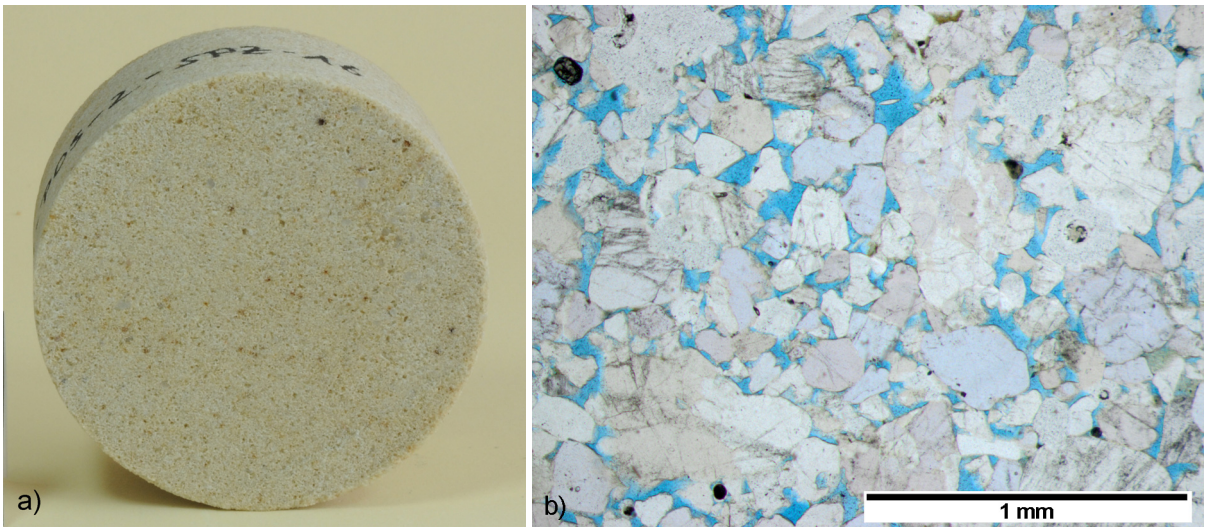

Figure 64: a) Homogeneous texture of yellowish Posta sandstone with inclusions of limonite (diameter 8 cm) b) Irregularly arranged quartz grains with open pore space in blue color (P-pol).

5.1.10 Abtswind sandstone

The Abtswind sandstone is a homogeneous, fine-grained, yellowish brown sandstone of the Stuttgart-Formation, known as "Schilfsandstein" (Figure 65). The fine clastic rock was sedimented during the Upper Triassic, in the Middle Keuper. The Abtswind sandstone is quarried at the western margins of the Steigerwald in Lower Franconia, east of the village Abtswind. The sandy facies of the Abtswind sandstone is mined in the quarry "Castell" on the western mountain slopes of the Friedrichsberg. It is a popular building stone, known as "Abtswind Sandstone Castell" or "Abtswinder Grün-Gelb" (www-3). The sandstone is largely unstratified and shows an equigranular texture. It consists mainly of quartz with grains of feldspar and mica. The grain sizes are mostly in the range between 0.1 and 0.3 mm. According to INSK n.d.), the quartz content is 53 %, feldspar and rock fragments are around 20 %. As accessory minerals muscovite, biotite, chlorite and few heavy minerals are present. The clayey cement material fills the pore space and the porosity of the sandstone is on average 15.5 % (QUEISSER 1988).

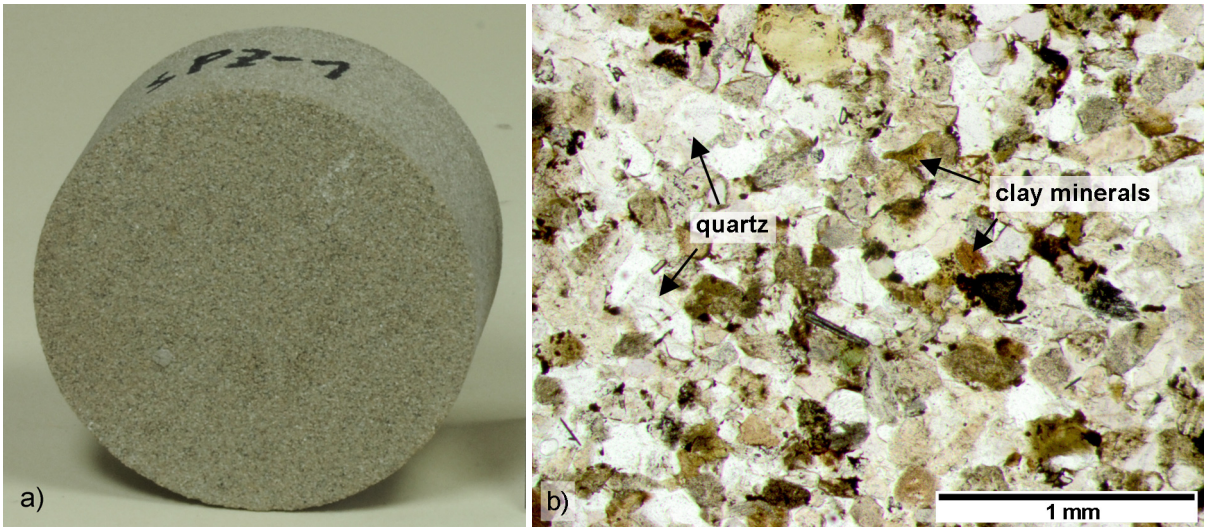

Figure 65: a) Homogeneous, fine-grained texture of Abtswind Sandstone 'Castell' (diameter 5 cm). b) The rock consists mainly of quartz and few feldspar grains with a clayey cement (P-pol).

5.2 Deformation and cracking behavior of different rock types

This section presents the results of the deformation and cracking behavior, the rock mechanical properties and the acoustic characteristics of the analyzed rocks. Laboratory tests were carried out in the rock mechanics laboratory at the Technical University of Munich. The tests were performed according to the methods described in Chapter 3 and a list of the tests is given in Table 11. In the following diagrams and descriptions, all results are sorted by the uniaxial compression strength.

Table 11: Performed tests and summary of the number of tests carried out on ten different types of rock.

Rock type		Uniaxial compression test		Brazilian tensile test	P-wave velocity measurements	
		total	with AE		axial	radial
Pechbrunn basalt	PB	22	9	14	10	10
Tittling granite	TIT	17	4	16	19	19
Diabase	DIA	6	3	10	4	4
Dietfurt limestone	DK	7	4	8	9	9
Moosegg anhydrite	MO	21	2	6	7	7
Laas marble	LAM	10	4	11	14	14
Flossenbürg granite	FLB	12	4	12	9	9
Metten granite	MET	19	3	15	12	8
Posta sandstone	POS	19	3	14	9	8
Abtswind sandstone	ABC	8	5	6	6	6

5.2.1 Stress-strain relationship and cracking activity

Under compression, each type of rock reveals a characteristic stress-strain curve and a characteristic emission of acoustic events. Since the occurrence of acoustic emissions (AE) is directly associated with the formation of cracks, the event rate provides information about the deformation and cracking behavior of the rock. In this subsection, representative examples of stress-strain curves and acoustic event rates are given for the tested rock types. In the stress-strain curves, the axial strain is represented in blue, radial strain is orange and volumetric strain is yellow. The number of AE is illustrated as green bars and is given per 5 seconds, calculated from the applied loading rate, which depends on the sample size. The cumulative signal energy is given in purple as the signal energy normalized by the uniaxial compressive strength. In this thesis, the terms ‘brittle’ and ‘ductile’ (or tough) are used to classify the material behavior of rock. Rock classification according to the deformation and failure behavior is discussed in detail in WILFING (2016), where the existence of a phase of plastic deformation after peak strength is proposed as an important characteristic for the classification of rock. The results of WILFING showed that brittle rocks exhibit a minor plastic deformation in the pre-failure phase and a minor or non-existent post-failure phase. Ductile rocks, in contrast, are characterized either by a high plastic deformation in the pre-failure phase and the lack of a post-failure phase (e.g. calcareous mica schist), by a minor plastic deformation in the pre-failure phase with a pronounced post-failure phase (e.g. anhydrite), or by a combination of a high plastic deformation in the pre-failure phase and a distinct post-failure phase (e.g. weathered granite).

5.2.1.1 Pechbrunn basalt (PB)

A representative stress-strain curve of the fine-grained Pechbrunn basalt is presented in Figure 66. The deformation behavior of basalt is characterized by a very low radial strain at failure. All stress-strain curves are almost linear over a great range of applied stress and the volumetric strain curve does not reverse because the radial strain shows only a minor increase during the phase of unstable crack growth. Although the typical stages of cracking are indicated by the AE activity, the deformation phases cannot be identified from the stress-strain curves. Since the volumetric strain curve did not reverse, the stress thresholds could only be determined from the number of events. The presented example of a tested basalt shows some events at the beginning, which mark the phase of crack closure. In the second phase of linear elastic deformation, only single events were recorded. An increase in the number of AE and an increase in the signal energy mark the crack initiation stress and the onset of stable crack growth. The release of high-energy signals begins with the onset of cracking and rises gradually until the rock collapses. At the maximum stress, all tested specimens showed an abrupt collapse where the rock burst into pieces. The total number of acoustic events is low showing a maximum of 100 events per 5 seconds shortly before failure.

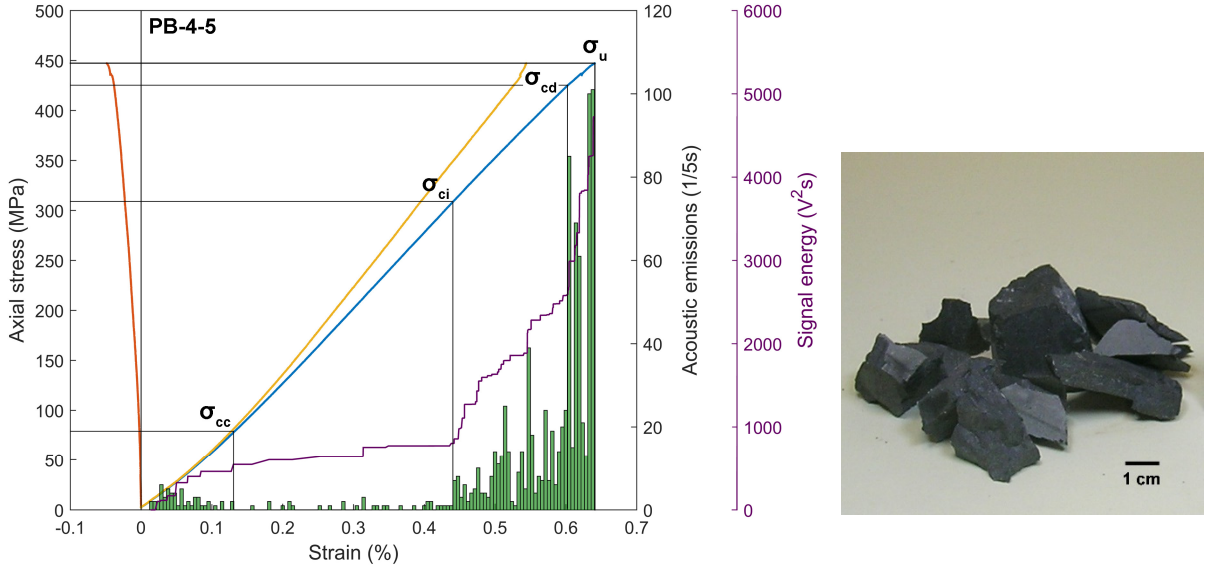

Figure 66: Stress-strain curves of the fine-grained Pechbrunn basalt and an example of its typical failure pattern.

5.2.1.2 Tittling granite (TIT)

The stress-strain curves of Tittling granite begin with a short period of crack closure where a non-linear deformation and a small number of events occur (Figure 67). During elastic deformation, only few events were recorded and signal energies remained at a constantly low level. Because of a low radial strain, most stress-volumetric strain curves did not show a reversal of the curve. The onset of stable crack growth was therefore determined from the onset of AE, which occurred at about 50 % of the uniaxial compressive strength. In the phase of stable crack growth, the number of events increased steadily so that a clear transition to unstable crack growth was not always clear. For the determination of the crack damage stress, the number of AE and the curve of the cumulative signal energies were used. Signal energies showed an increase when the crack damage stress was exceeded and a distinct increase in high-energy signals occurred right at failure when major cracks developed. After failure, most of the tested samples showed a distinct set of conjugate shear planes as illustrated in Figure 67.

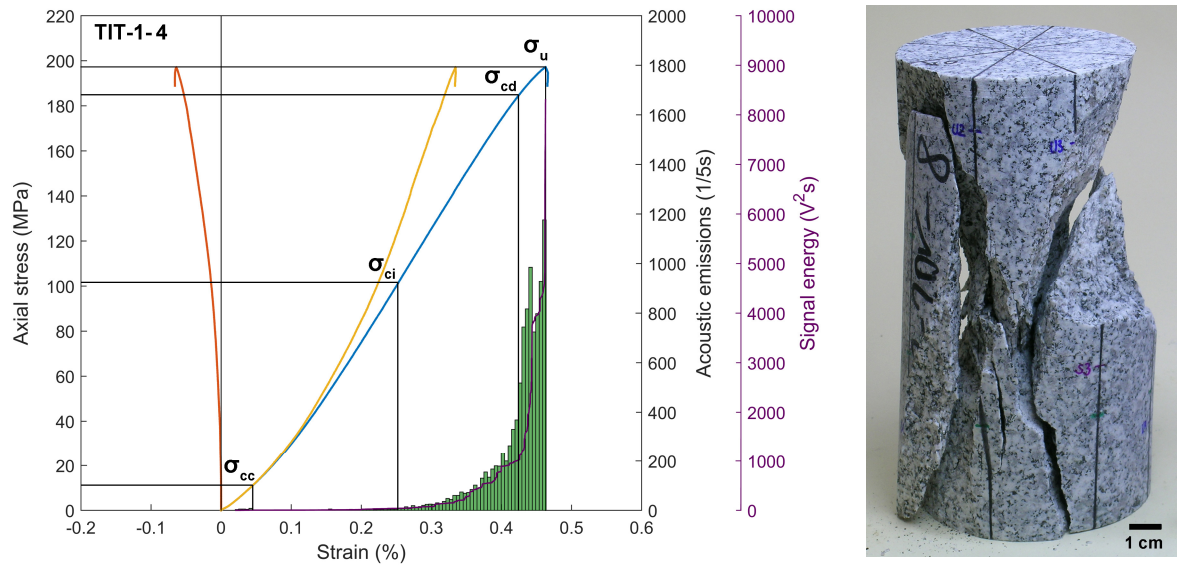

Figure 67: Stress-strain curves of Tittling granite including AE and cumulative signal energies as well as a representative example of the failure pattern showing a set of conjugate shear planes.

5.2.1.3 Diabase (DIA)

The stress-strain behavior of the tested diabase samples is similar to the stress-strain curve of basalt. The axial strain curve shows a pronounced linear proportion of the curve and a post-failure phase is missing (Figure 68). The phase of crack closure is very unclear with a negligible number of events, similar to the AE activity in the phase of elastic deformation. Crack growth begins at a late stage of deformation and it is indicated by the onset of the AE activity. The stress-strain curves do not show a clear deviation from linearity so that the volumetric strain curve does not reverse. Instead, a considerable increase in the number of events shortly before peak stress marks the beginning of unstable crack growth. The stress thresholds for crack initiation and crack propagation could, therefore, only be determined from the onset of a considerable number of events. Rock failure occurred right after the onset of crack damage and is associated with a distinct increase in the signal energy. All samples burst spontaneously and showed an indistinct shear fracture combined with axial splitting through the end surfaces.

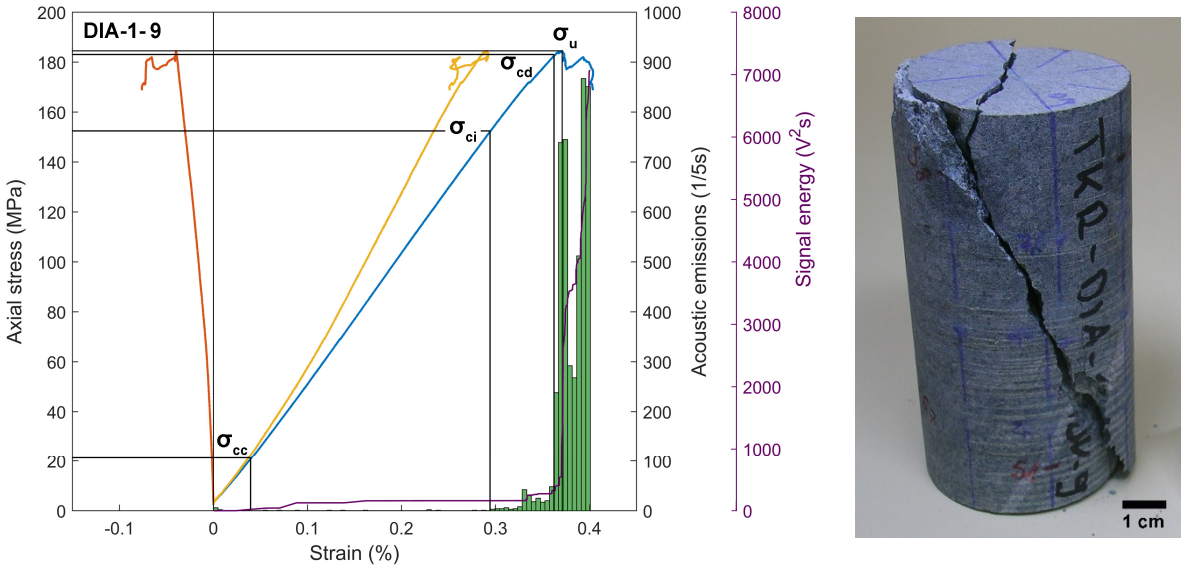

Figure 68: Stress-strain curves of diabase including AE and the cumulative signal energy as well as an example of its brittle failure pattern with a distinct shear fracture combined with axial splitting.

5.2.1.4 Dietfurt limestone (DK)

Similar to the brittle failure behavior of the rocks described before, the fine-grained Dietfurt limestone showed almost linear stress-strain curves with a short and indistinct phase of crack closure (Figure 69). The stress-strain curves are characterized by an almost linear axial strain curve so that volumetric strain reversal does not occur. The onset of cracking is marked by a small increase in the AE rate and an increase in the signal energy. A considerable increase in the number of events shortly before rock failure marks the onset of unstable crack growth and an increase in high-energy signals occurs when the peak stress is reached. The total number of AE was low and only single events occurred for a large proportion of loading. At the maximum stress, the rock collapsed so that a post-failure phase does not exist. The failure pattern shows a set of conjugate shear planes combined with axial fragments splitting off the lateral areas of the specimens and small rock chips spalling from the edges of the cylinders.

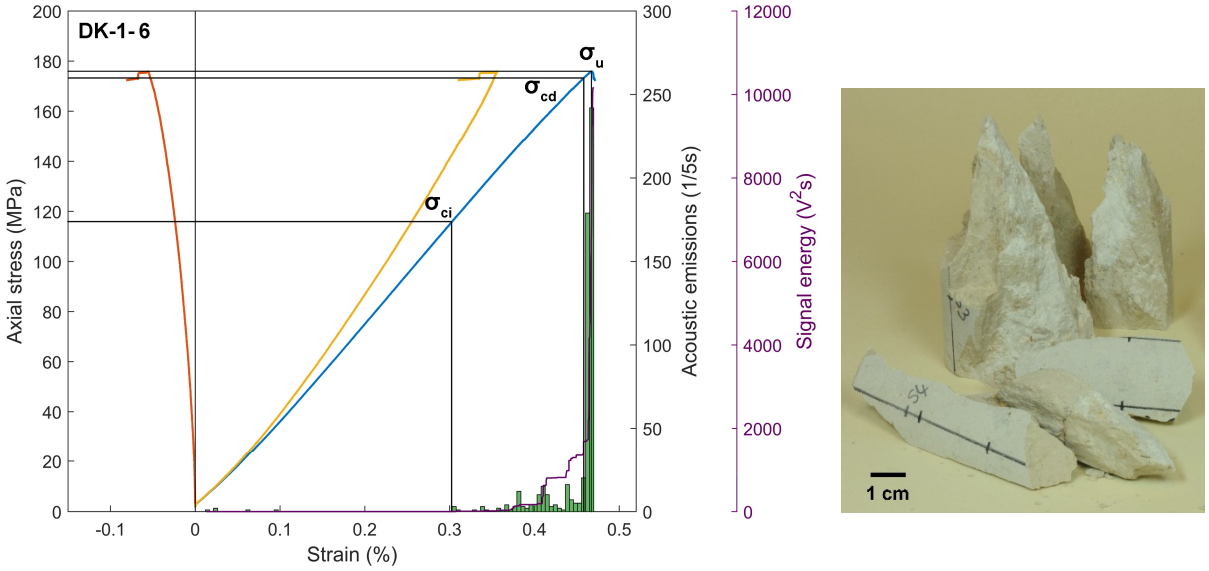

Figure 69: Stress-strain curves of fine-grained Dietfurt limestone and an example of its failure pattern with axial splitting and an indistinct set of conjugate shear planes.

5.2.1.5 Moosegg anhydrite (MO)

The deformation behavior of Moosegg anhydrite is characterized by a very low radial strain that first increases when failure is approached (Figure 70). Both radial and axial strain at failure resulted in very small total values. The axial strain curve shows a large linear proportion starting almost from the beginning of compression so that a nonlinear stage of crack closure does not exist. The crack initiation stress illustrated in Figure 70 was calculated using the LSR method but from the number of events, it is clear that cracking begins much earlier, almost with the beginning of loading. After a distinct increase in the number of events, the AE activity stays at an almost constant high value. The onset of unstable crack growth is marked by the reversal of the volumetric strain curve and the stress level coincides with a second increase in the number of events. The AE activity reaches a maximum during the formation of major fractures in the post-failure phase. All tested anhydrite samples showed a distinct post-failure phase, where pronounced radial deformation and intense cracking occurred. During loading, the signal energy increases steadily and shows a noticeable increase in the post-failure phase, when major fractures developed. The anhydrite specimens did not show a uniform failure pattern but in most samples, conjugate shear planes were indicated and axial splitting occurred. The sample in Figure 70 additionally shows a major axial fracture through the upper surface plane.

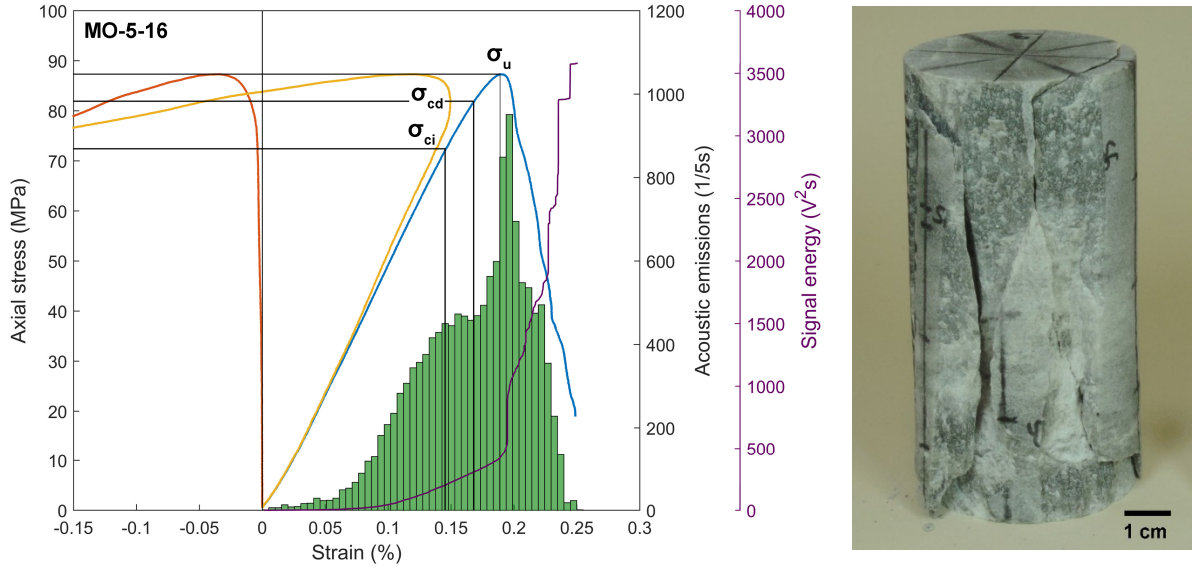

Figure 70: Stress-strain curves of Moosegg anhydrite including AE and signal energy and an example of a failure pattern showing mainly axial fractures.

5.2.1.6 Laas marble (LAM)

The stress-strain curve and the AE rate of Laas marble exhibit an exceptional deformation and cracking behavior. All tested samples showed a uniform failure behavior and a similar fracture pattern. The deformation of marble is similar to the deformation behavior in anhydrite. It is characterized by a low strain at the beginning and a significant increase in both radial and axial strain when the peak strength is approached (Figure 71). Therefore, the crack damage stress was determined from the maximum of the volumetric strain curve. In all tested samples, the number of AE did not reveal the typical phases of crack formation. Instead, a considerable increase in the number of events first occurred after the peak strength was exceeded and after the stress had already dropped to a lower stress level. Up to the increase in the AE activity, only a minor number of events was recorded. The crack damage stress in Figure 71 represents the maximum of volumetric strain but not an increase in the AE activity. Until the maximum of the volumetric strain, only few events were emitted and at the peak stress, the AE rate even decreased. A considerable increase in events and in the signal energy did not occur before the post-failure phase. After final rupture, all tested marble specimens showed a single shear fracture crossing the specimen from the upper to the lower end surface.

The characteristic deformation behavior of the calcite minerals is assumed as the reason for the exceptional behavior of the rock. In Laas marble, natural twin lamellae exist in almost every calcite crystal and often two sets of twins are present (see Figure 61b). It is assumed that the low number of events in the pre-failure region is due to an accumulation of damage on the atomic scale. Instead of brittle cracking along grain boundaries and along the cleavage, deformation is supposed to occur within the crystal lattice without the emission of acoustic events. In the crystal lattice, most of the strain energy is taken up by twin gliding, which means that deformation twins are generated as a result of small shear displacements within the crystal lattice. Obviously, lattice gliding does not emit acoustic events with a sufficiently high amplitude to allow a detection with the applied AE system. A considerable number of events is only recorded when the major failure plane develops.

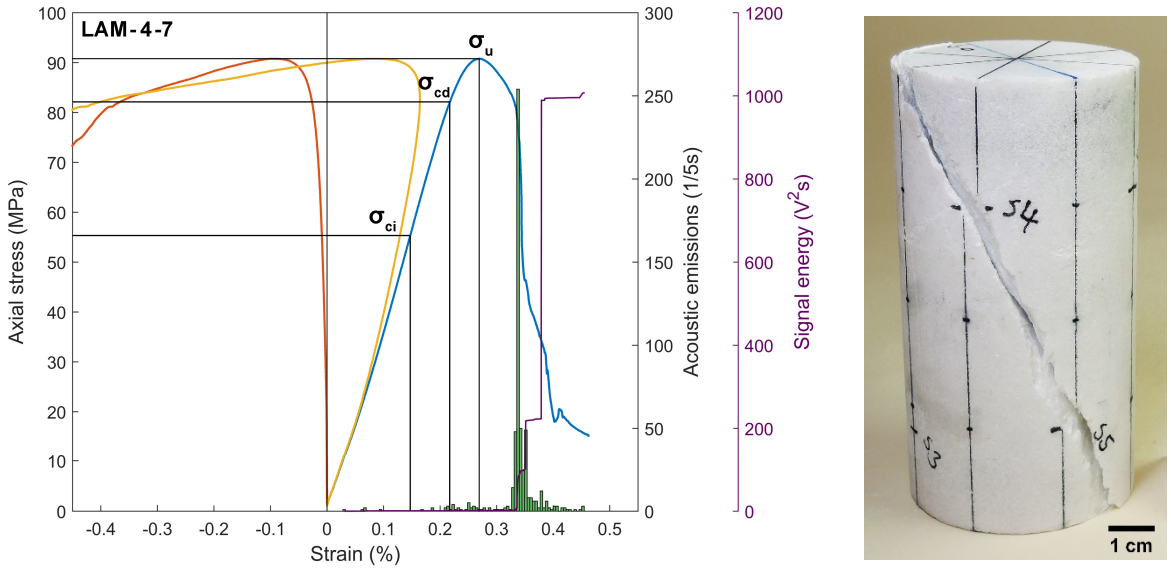

Figure 71: Stress-strain curves of Laas marble and the typical failure pattern as a single shear fracture.

Twinning is a characteristic intracrystalline deformation mechanism in calcite, which already occurs at low temperatures and little deformation (BURKHARD 1993). OLSSON & PENG (1976) found that shear stresses are released by displacements along the twin lamellae so that stresses concentrate at the edges of the lamellae. The stresses may be relieved by gliding along a plane near the twin tip if the shear stresses exceed a critical value. Otherwise, a new microcrack may nucleate in a neighboring grain because of local stress concentrations at grain boundaries acting as an obstacle to the glide. The microcrack nucleation mechanisms observed by OLSSON & PENG (1976) in Tennessee marble are illustrated in Figure 72. Similar plastic deformation at glide lamellae is expected to induce microcracking in Laas marble.

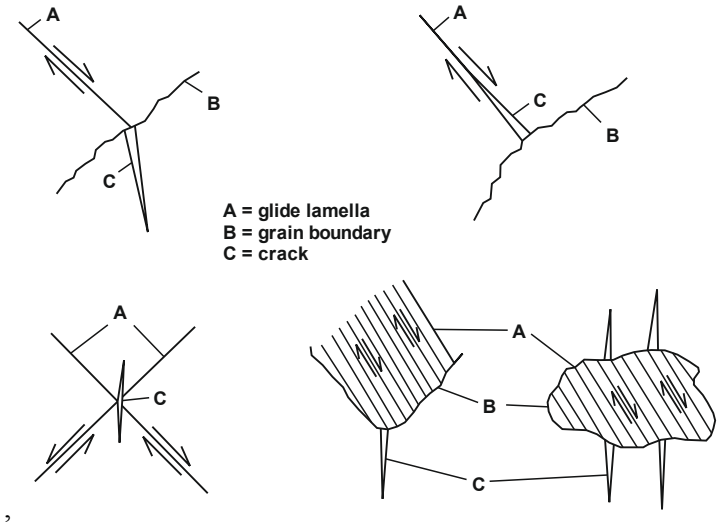

Figure 72: Schematic illustration of the principal microcrack nucleation mechanisms observed in Tennessee marble. The maximum compression is vertical (after OLSSON & PENG 1976: 54).

5.2.1.7 Flossenbürg granite (FLB)

The medium to coarse-grained Flossenbürg granite shows a clearly different stress-strain curve than the unweathered samples of Tittling granite. All tested specimens of FLB showed a distinct post-failure phase and a distinct reversal of the volumetric strain curve (Figure 73). Because of a strong increase in the radial strain, the reversal occurred already at a relatively low stress level. In many of the tests, a radial strain measurement was not possible throughout the whole test, because the safety closure of the measurement device opened before the maximum stress was reached. Therefore, the crack damage stress could not be determined from the maximum volumetric strain in most specimens. In the illustrated stress-strain curve (Figure 73), the crack damage stress could be determined from the volumetric strain and the crack initiation stress was calculated using the LSR method after NICKSIAR & MARTIN (2012).

In contrast to the stress-strain curve, the number of acoustic events do not reveal the typical cracking behavior of brittle rocks. Instead, a continuous increase in the number of AE occurred until the peak stress so that a reliable definition of the five deformation stages was not possible. In total, the granite emitted a large number of AE and the maximum number of workable events was exceeded in several tests. In the weathered granite, cracking started with the beginning of loading and a continuous increase in the number of events shows that crack propagation occurred during the whole test. Therefore, the AE activity indicates a considerably lower crack initiation level than the calculated value determined with the LSR method. A region of linear elastic deformation without microcracking is not apparent from the AE activity. In Flossenbürg granite, rock failure did not occur as a single violent event but evolved gradually. After failure, elongated fragments developed in the external areas and a largely intact core with an hourglass shape remained. The gradual disintegration of the rock fabric must be ascribed to the beginning alteration of the rock and a disintegration of the rock structure. Furthermore, failure often occurred along the cleavage planes of favorably oriented feldspar minerals, where particularly the coarse grains of alkali feldspar enable crack propagation along cleavage planes, grain boundaries or the suture of Karlsbad twins.

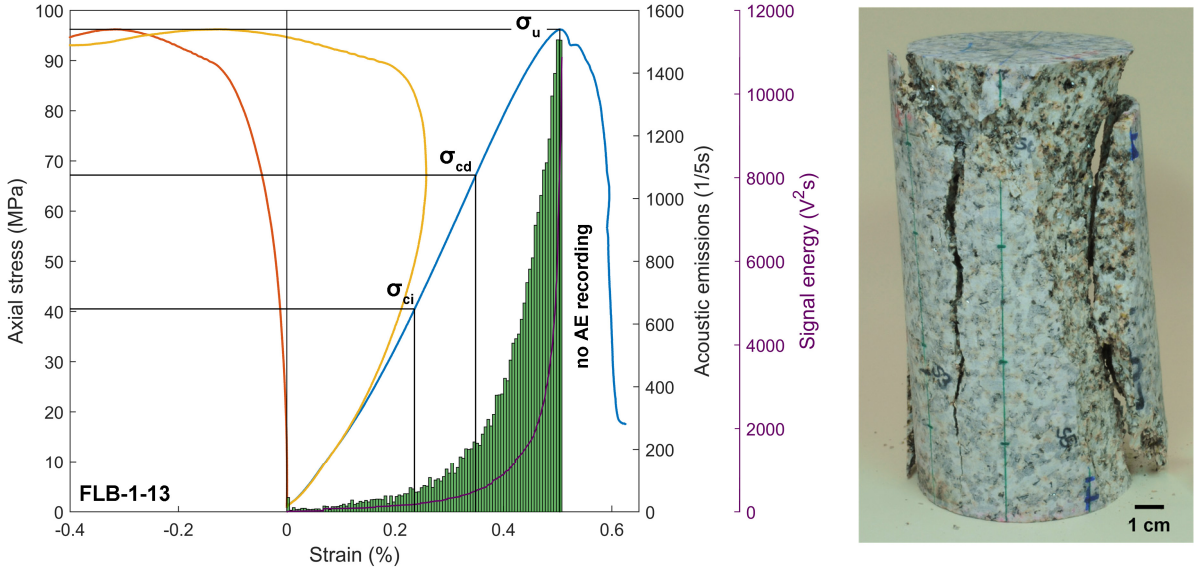

Figure 73: Stress-strain curves of weathered Flossenbürg granite and a typical failure pattern showing a core with an hourglass shape and axial fractures splitting off externally.

5.2.1.8 Metten granite (MET)

Metten granite shows a largely similar deformation behavior to that of Flossenbürg granite. The radial strain curves show a distinct increase and thus causes a clear reversal of the volumetric strain curve at a comparatively low stress level. In contrast to FLB, the stages of crack closure, elastic deformation, and the onset of crack propagation are clearly represented by the number of AE. The phase of crack closure is marked by a considerable number of events, which decreases when linear elastic deformation begins. An increase in the AE activity marks the beginning of crack initiation and a continuous increase in the number of events was emitted until failure. For the specimen in Figure 74, the crack initiation threshold calculated with the LSR method coincides well with the onset of AE. A clear transition from stable to unstable crack growth is not apparent from the number of AE so that the crack damage stress could only be determined from the reversal of the volumetric strain curve. The failure pattern is similar to that of FLB. It showed an hourglass-shaped core and long fragments that split off the the sample surface along axial fractures. The formation of major fractures first occurred in the post-failure phase. The deformation and cracking characteristics of Metten granite are influenced by the beginning alteration so that the degradation of rock quality facilitates the initiation of microcracks.

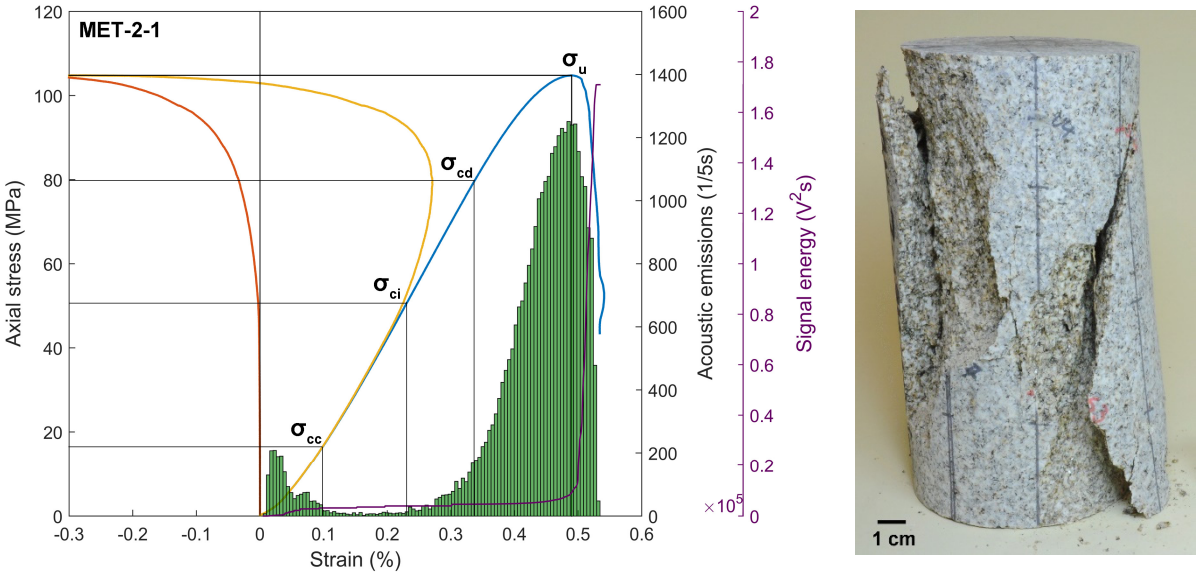

Figure 74: Stress-strain curves of fine-grained Metten granite with the crack damage threshold determined from the number of AE, and a typical failure pattern.

5.2.1.9 Posta sandstone (POS)

Posta sandstone emitted the largest number of events of all tested rocks and showed a clearly different cracking behavior. In the sandstone, a large number of AE occurred from the beginning of compression and during the entire loading phase (Figure 75). A large number of AE occurred right after the test started and the number of AE increased until the AE activity remained at a high level. The high AE activity can be attributed to the high porosity of about 22 % because the open pore spaces allow relatively large displacements of poorly compacted grains against each other. During the entire loading phase, the tendency of the grains for close packing and the associated displacements along grain contacts as well as breaking of the cement are reasons for a high AE activity. After an almost constant number of events, a new increase in the AE activity occurred and the number of events increased until the peak stress was reached.

Considering the differences in the structure of clastic sedimentary compared to crystalline rocks, the mechanism of deformation and cracking, described by BIENIAWSKI (1967), cannot be easily applied to porous rocks with a granular structure. In the tested sandstone, the emitted events and the deformation behavior indicate the following phases of deformation and fracture. In the first stage of loading, loosely bonded quartz grains are rearranged and open pore cavities are reduced. Uniaxial compression causes a compaction of grains and the associated breaking of the quartz cement causes a high AE activity and a high event energy during the entire loading phase. In the stage of almost constant AE activity, many grains are already closely packed and forces act directly on the grain contacts. The consistently high number of events must be ascribed to further displacements caused by compaction and shearing along grain boundaries.

When the AE activity increases again, the forces acting on grain contacts may be exceeded in some areas of the rock and microcracking occurs along preexisting flaws or within the grains. The crack initiation threshold determined with the LSR method (Figure 75) coincides with a distinct increase in the AE activity, whereas the stage of unstable crack growth is not marked by an increase in the number of events. Instead, it can only be determined from the maximum of the volumetric strain. In this phase, an interaction and coalescence of pores and cracks and the formation of major fracture planes begin. The Posta sandstone shows a distinct post-failure phase, where a disintegration of the rock structure takes place. The mode of failure of all tested specimens was shearing along a diagonal plane with axial fractures showing a beginning formation of a set of conjugate shear planes. In the failure plane, the rock was disintegrated in loose sand grains and the specimen split up along several axial and surface parallel fractures (Figure 75).

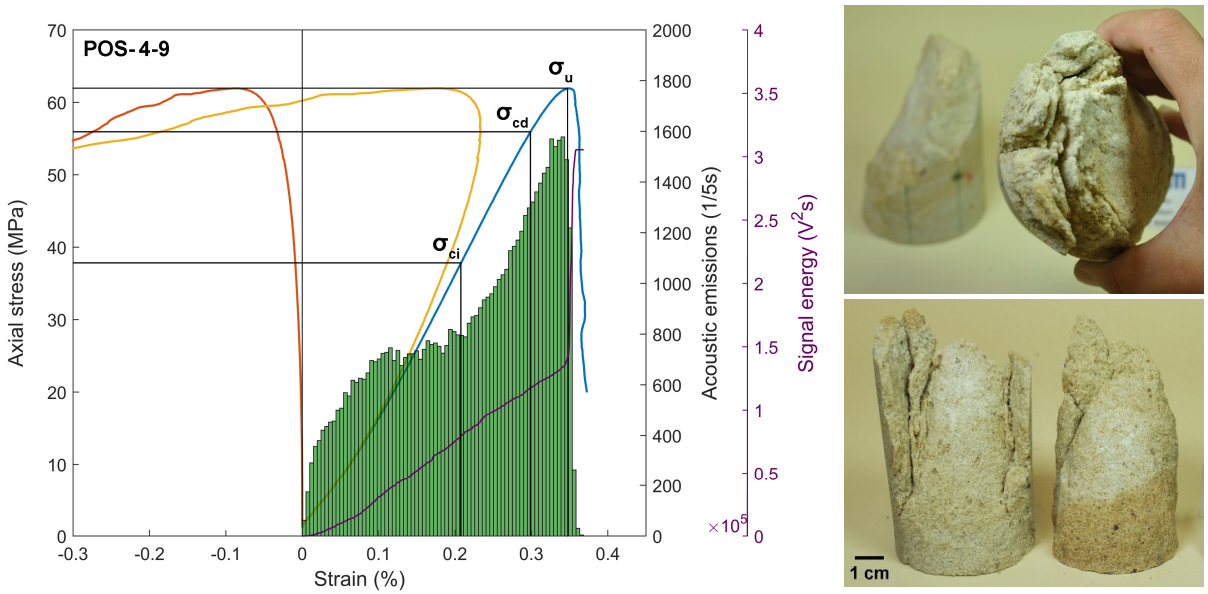

Figure 75: Stress-strain curves of the porous Posta sandstone and typical failure pattern of two representative samples showing a set of beginning conjugate shear planes and surface parallel axial fractures.

5.2.1.10 Abtswind sandstone (ABC)

The fine-grained Abtswind sandstone (porosity ~15.5 %) shows a different cracking behavior than the Posta sandstone (porosity ~ 22 %). From the beginning of loading until peak stress, only a few events occurred so that a considerably lower number of AE was recorded. Until the maximum strength, the number of AE increased continuously but at a very low level (Figure 76). Compared to other rock types, axial and radial strain are exceptionally high with respect to the low uniaxial compressive strength of

about 28 MPa. The discrepancy between a very high deformation and an absence of events is attributed to the structure of the sandstone. In contrast to the siliceous Posta sandstone, the fine-grained components of Abtswind sandstone are bonded by a clayey cement material. During compression, the weak bonding forces between the grains can easily be exceeded. This is confirmed by the low uniaxial compressive strength. The low number of AE indicates that the displacements and the breaking of the weak clay cement do obviously not emit acoustic signals. The cracking activity only begins to increase shortly before or directly at the maximum stress. This low AE activity also results from the fabric of the sandstone, where the clay minerals in the pores are much weaker than the strong quartz grains. When compressive stresses are applied, the clay minerals may deform elastically without being broken. The low number of events can also be the result of intracrystalline displacements along the weakly bonded crystal layers.

In the post-failure phase, a discrete failure plane evolves as a result of the coalescence of pores and cracks. The formation of cracks crossing single quartz grains and shearing along grain boundaries causes a high number of AE. Since almost no signals are emitted before peak stress, it is not possible to determine the stress level of crack initiation and crack damage from the number of AE, whereas the crack damage threshold is clear from the maximum volumetric strain. In the post-failure phase, the stress-strain curve indicates a stepwise fracturing of the rock. The failed specimens showed a distinct shear plane with the beginning formation of two conjugate shear planes.

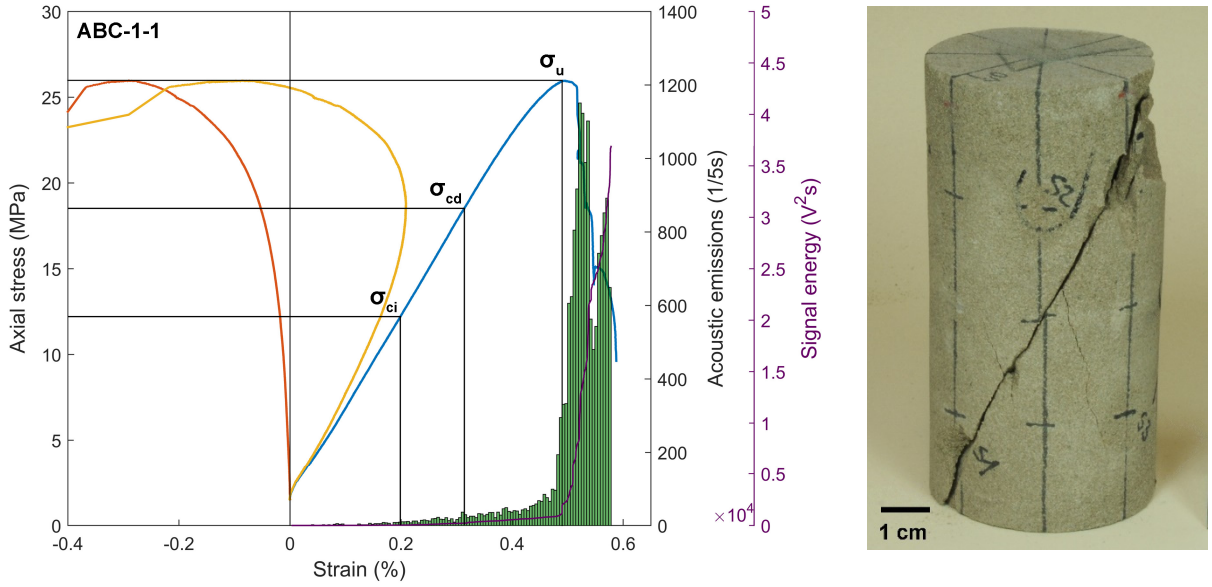

Figure 76: Stress-strain curves of the fine-grained, clayey Abtswind sandstone and a representative example of the failure pattern showing a distinct shear plane with the beginning formation of conjugate shear planes.

5.2.2 Acoustic emission localization

As shown in the section above, the localization of acoustic events is an important tool for the understanding of the cracking behavior of rocks. In this section, the results of acoustic event localization in the tested rock types are discussed. Although both, the Geiger method and the Bancroft localization algorithm were applied, only the results of the Bancroft method are presented, since they generally revealed more reliable results. Before the events were localized, those events with a low signal-to-noise ratio and an extremely high signal energy were filtered. Only high-quality signals, recorded at all sensors with a high signal-to-noise ratio and thus a distinct arrival time of the sonic wave were used.

The accuracy of event localization is determined from sonic pulse tests before every uniaxial compression test. Sonic pulses set at known coordinates and with a known origin time were used for a back-calculation of the pulse coordinates. From the difference between calculated pulse coordinates and real pulse coordinates, an error vector was calculated for every localized pulse. The mean and maximum errors determined from pulse localization are given in Table 12. For a more precise analysis of the localization accuracy, KURZ et al. (2010: 124) recommends the determination of a three-dimensional error ellipsoid to visualize the spatial localization errors. For the events from uniaxial compression tests, a simplified mean error is considered to correspond with the mean error determined from sonic pulse localization. Damage accumulation with increasing stress, however, might reduce the localization accuracy towards the end of the test, because the p-wave velocity of the rock material changes continuously. In addition, an increasing number of low-quality events is recorded when approaching rock failure so that the number of events available for localization decreases.

Table 12: Localization errors of the tested rock types determined from sonic pulse localization.

Rock	Sample diameter	Mean error		Maximum error	
	mm	mm	%	mm	%
PB	50	8.6	17	20.0	40
TIT	80	13.2	17	29.6	37
DIA	50	5.8	12	15.7	31
DK	50	6.8	14	25.2	50
MO	50	8.1	16	22.6	45
LAM	80	8.4	11	37.6	47
FLB	80	13.7	17	41.8	52
MET	80	7.7	10	16.5	21
POS	80	16.3	20	43.6	55
ABC	50	8.5	17	27.7	35

According to the fabric and composition, the mean error strongly varies between the tested rocks. The highest error was calculated for Posta sandstone because of its porous structure, where the sonic waves are attenuated. High mean errors above 10 mm were also determined for Flossenbürg granite and Tittling granite. In Flossenbürg granite, the beginning weathering caused a disintegration of the rock structure so that a similar effect like in Posta sandstone was present. The maximum errors in percentage of the sample diameter are between 21 % for Metten granite and 55 % for Posta sandstone. In the following illustrations, the localized event coordinates are displayed in a Cartesian coordinate system, where only those events located within the rock specimen and with a correlation coefficient above 0.8 are plotted.

The colors of the displayed symbols show high (light red) and lower correlation coefficients (black) between 1.0 and 0.8. The size of the symbols indicates the signal energy, where larger symbols represent high signal energies and small symbols represent low energies. From every rock type, the results of a representative rock specimen are presented in the following subsections.

5.2.2.1 Pechbrunn basalt

The results of AE localization of Pechbrunn basalt show that until crack damage, most events occurred at the bottom and some in the upper part of the specimen (Figure 77). Some of those events might be caused by friction at the loading plates. Until failure, additional events are located at the edges of the lower end surface and more events occurred in the middle and upper part. This corresponds with the final fracture pattern, where major cracks formed in the lower part of the specimen and along axial fractures, especially at one side of the cylinder. Furthermore, major fractures through the end surfaces of the specimen developed. In contrast to most other tested basalt specimens, the illustrated specimen did not burst into many fragments but a large part of the sample remained intact. From all recorded events, 24 % could be used for localization but none of the last 280 events fulfilled the requirements for localization so that localization results are not available for the last five seconds before failure. The illustrated event locations, thus, represent the developing cracks before final failure occurred. Several high-energy events (large symbols) especially in the upper and lower areas of the rock are an evidence for the rapid release of stored energy in brittle rocks.

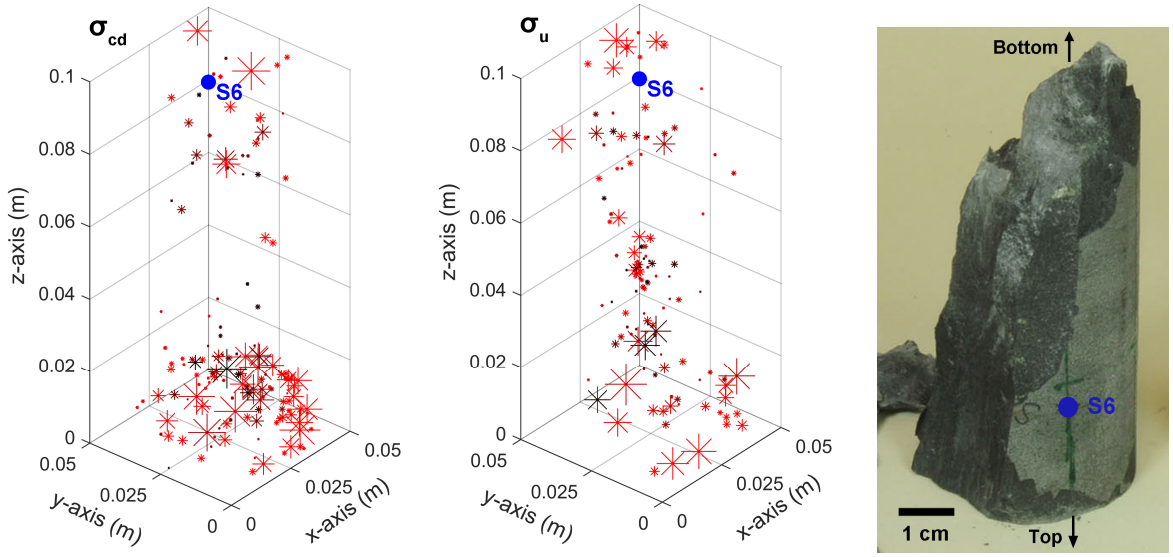

Figure 77: Results of AE localization of Pechbrunn basalt (PB-4-5) until crack damage (σ_{cd}) and during the phase of unstable crack growth until failure (σ_u). The localized events display the final fracture pattern, where fractures developed mainly at the bottom of the cylinder (right, upside down and rotated).

5.2.2.2 Tittling granite

In Tittling granite, the localized events are presented until the crack initiation stress, the crack damage stress and until failure of the rock (Figure 78). Until crack initiation, the few emitted events were only located in the lower part of the specimen and may have been caused by a small irregularity between end planes and loading plates or by a heterogeneity within the rock. In the phase of stable crack growth, many events occurred throughout the whole specimen. In the lower part of the specimen, near the radial position of sensor S2, a small accumulation of events marks the beginning formation of a major crack. When failure is approached, the number of events strongly increased throughout the whole specimen

and particularly in this area. A second accumulation of events is located in the upper part but on the same side of the specimen. The strong accumulation of events is also visible in the top view in Figure 78. From all events, 19 % could be used for localization, whereas no events could be localized in the last 10 seconds before failure. The quality of the signals strongly decreased toward the maximum stress because rock damage increased and the sonic waves were impeded by open cracks. Furthermore, one sensor was directly located on the final failure plane so that it fell off when the fracture developed. The presented specimen of Tittling granite did not fail completely but a major axial crack developed in the lower surface area of the specimen, where a lateral fragment began to split off the specimen. The location of the final fracture coincides with the accumulation of events in the lower area of the specimen.

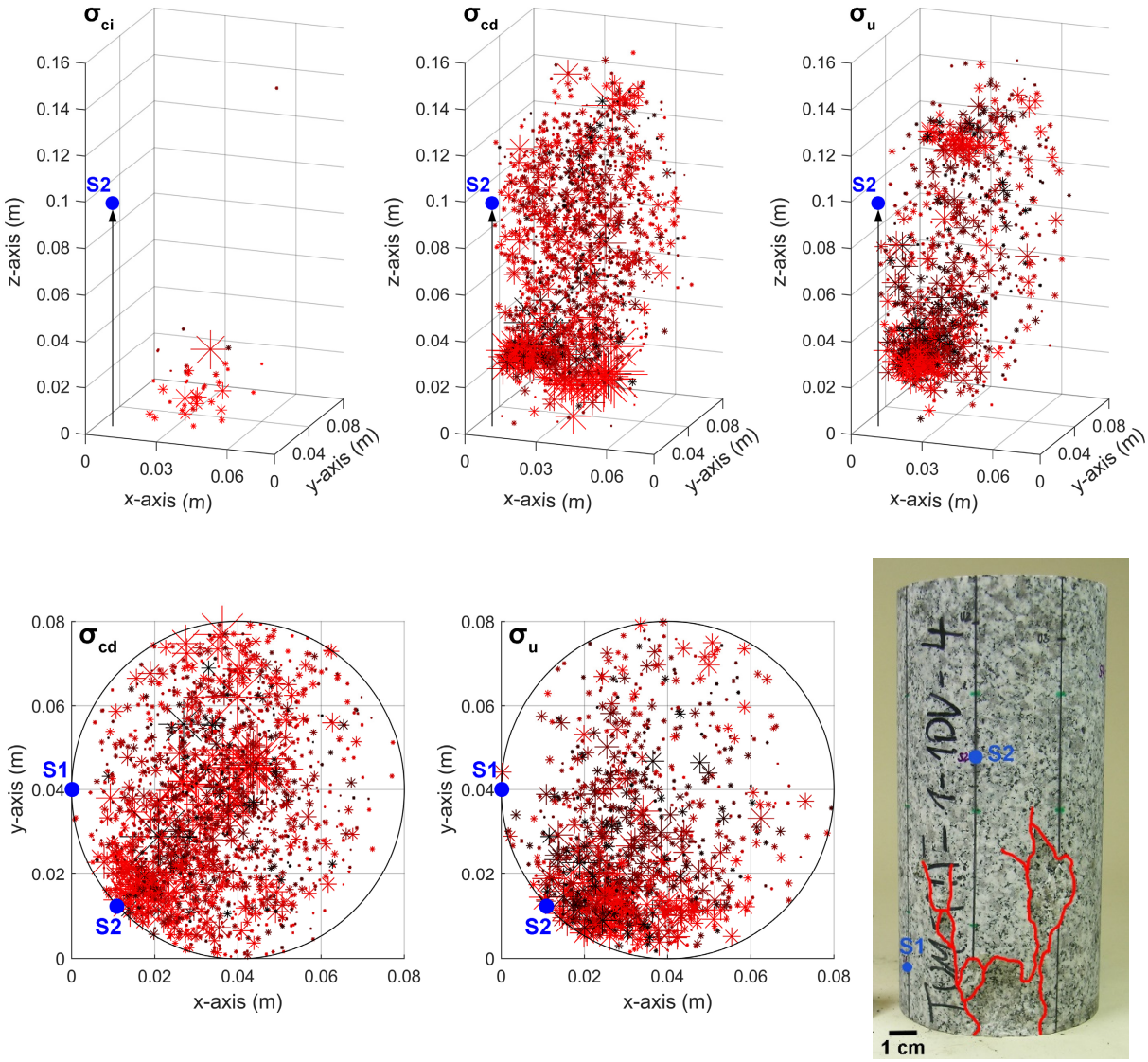

Figure 78: Results of AE localization of Tittling granite (TIT-1-4) until crack initiation (σ_{ci}), during stable crack growth (σ_{cd}) and during unstable crack growth until failure (σ_u). Failure occurred as an axial rock fragment spalling off from the lower area of the specimen.

5.2.2.3 Diabase

The localization results of diabase are presented in Figure 79. Since the crack damage threshold of the diabase almost coincides with the peak stress, the illustrated results include all events until failure. The located events indicate two distinct fracture planes, which are inclined at an angle of about 50°. When comparing the results with the final failure pattern, the two fracture planes are less clearly visible than in the localized events. The failed rock shows a number of fractures indicating two indistinct and uneven conjugate shear planes. The cracks partly cross the end surfaces and the shear planes are irregular shaped with a number of branching cracks. The failure pattern in Figure 79 is oriented similar to the coordinate system of AE localization (left). The failed rock shows that the localized events follow in parts the upper light band of a healed joint, which traverses the specimen (upper red arrow). The localized AE from the lower plane largely coincide with the lower quartz vein, although no major crack developed there. The axial fracture in Figure 79 (Front view) is not represented by the localized events because it developed in the post-failure phase.

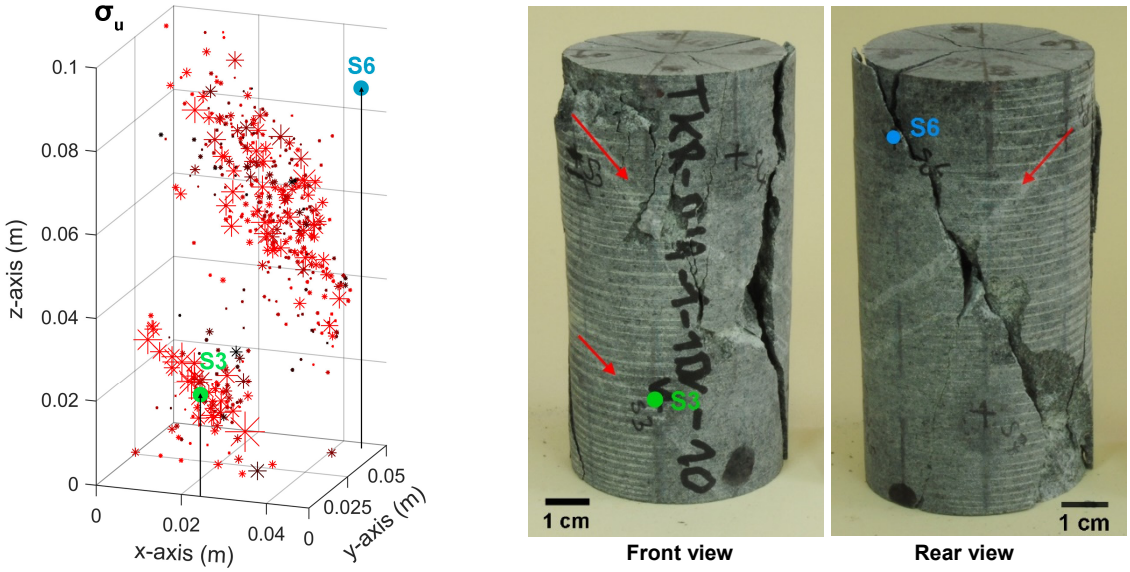

Figure 79: Results of AE localization at failure of diabase (DIA-1-10). The events indicate two almost parallel fracture planes. The failure pattern shows that the events do not mark final fracture but they mainly follow the healed joints traversing the sample.

When comparing the event coordinates with the rear view of the specimen (Figure 79), it becomes clear that failure did not occur along the healed joints but a major crack evolved almost perpendicular to the healed joint plane. The main reason is certainly the fact that a large number of events recorded towards the end of the test could not be used for localization. Many of the late events were high-energy events, where a determination of the arrival time was not possible because the signal-to-noise ratio of at least one sensor was too small. Therefore, none of the last 155 events fulfilled the requirements for accurate localization. Consequently, the illustrated event coordinates do not include the events from the moment when failure occurred. The diabase sample failed abruptly and most of the energy was violently released in the moment of failure. In total, about 50 % of all recorded events could be localized reliably, which is a very high number compared to other analyzed rock types. From the results of the diabase sample, it becomes clear that the localization of AE in extremely brittle rocks might not represent the final fracture planes, since only few events are available for localization particularly in the moment of failure. Instead, the evolution of microcracks during loading showed the weakest areas of the specimen, where cracks could develop first.

5.2.2.4 Dietfurt limestone

The results in Figure 80 show that cracking of Dietfurt limestone preferably occurred in the upper and lower areas of the specimen and the large size of the symbols reveals that mostly high-energy events were emitted. From the AE recorded in limestone, only 3.5 % of all events could be localized and in the last 14 seconds before failure, no reliable results were obtained. Since most of the events occurred when the maximum stress was reached, the main quantity of events is missing in the represented results. The failure pattern shows sharp axial fractures in the external areas and cracks crossing the upper end surface. Several inclined cracks are also present and slightly indicate a set of conjugate shear planes. The fracture through the upper end surface is already observable in the localized events until crack damage. With progressive compression, further cracking occurred there. Owing to the late beginning of major cracking and the small number of events, an interpretation of microcrack evolution is difficult. The example of Dietfurt limestone showed that AE monitoring, including the localization of acoustic events, is difficult in fine-grained, brittle rock types, because the rock collapses violently. As the rapid formation of cracks is associated with the emission of extremely high-energy signals as well as a number of signals where the determination of the arrival time is not possible, the generation of fractures during failure cannot be examined with the AE localization method.

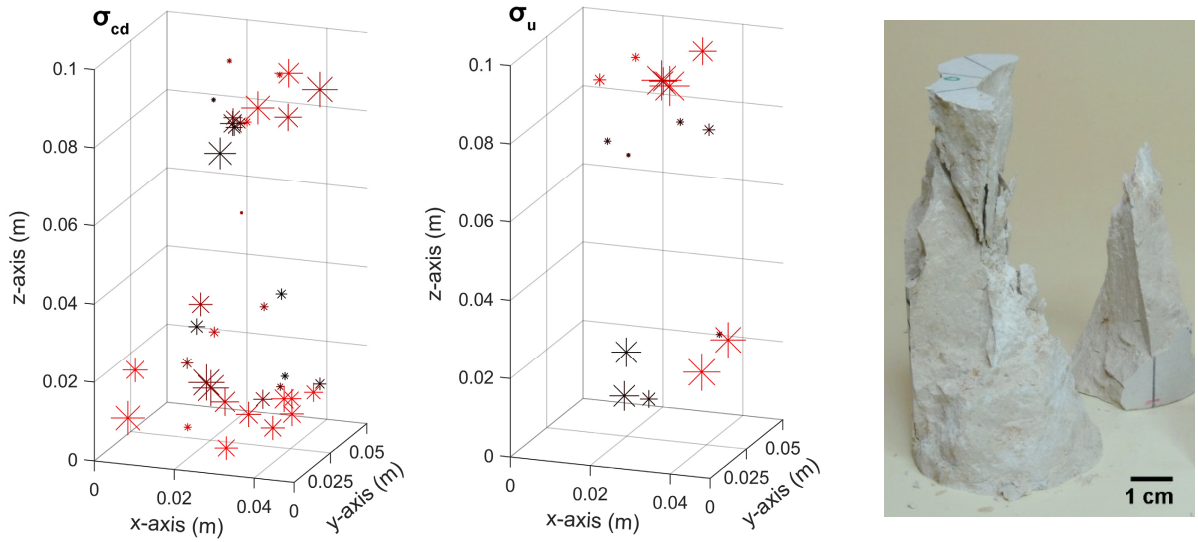

Figure 80: Results of AE localization in Dietfurt limestone (DK-1-4) until crack damage (σ_{cd}) and during the phase of unstable crack growth until failure (σ_u). The orientation of the failed specimen (right) is similar to the given coordinate systems (left, middle).

5.2.2.5 Moosegg anhydrite

The localization results of Moosegg anhydrite are given in Figure 81 until crack initiation, until crack damage, until the maximum stress and until final rupture of the specimen. Until crack initiation, some events were localized in the lower area of the specimen. With increasing compression, a high number of events occurred in the lower area and several small-energy events in the upper part of the specimen. After the maximum stress was exceeded, major cracks developed and a high number of events occurred throughout the specimen. The accumulation of events in the lower part of the specimen coincides with an area where the rock exhibits a more pronounced lamination than in the upper area. The variable composition and structure in this part of the specimen is assumed to facilitate the formation of cracks so that major fractures could nucleate there. Originating from the lower area, distinct axial fragments de-

veloped and finally split off the cylinder. One major fracture crossed the upper end surface but in general, a conjugate shear system is indicated. From the total number of events, about 6 % could be used for localization but in the last 27 seconds, only one event was suitable for localization. The development of the final fracture planes is thus not visible in the localized events.

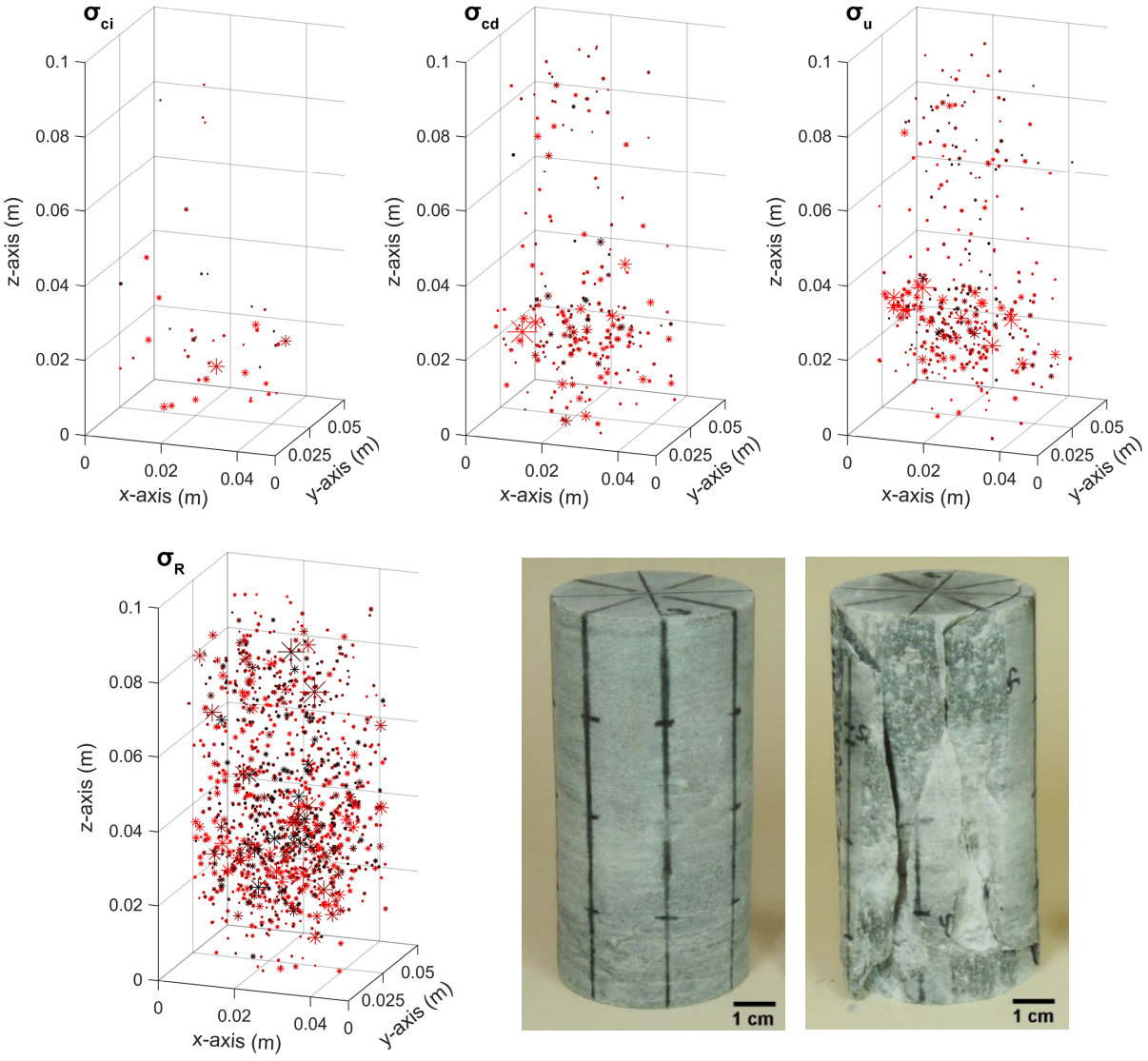

Figure 81: Results of AE localization in Moosegg anhydrite (MO-5-13) until crack initiation, crack damage, failure and until final rupture (R). Major fractures developed preferably in the lower area, where a more pronounced lamination was present.

5.2.2.6 Laas marble

For Laas marble, event localization is illustrated until the peak stress and until final rupture (Figure 82). Until the maximum stress, only very few events occurred and few events were suitable for localization. The failure pattern in Figure 82 shows the final major shear plane crossing the specimen and several smaller branching cracks. A similar failure pattern with a major shear plane was observed in all tested marble specimens. From the event coordinates until maximum stress, however, the final shear plane is not yet indicated. Only during the post-failure phase, a higher number of events occurred. Event localization showed an accumulation of events in the upper part of the specimen, whereas in the lower part, less cracks evolved. The final shear plane of the given specimen corresponds with the accumulation of events in the upper part of the sample where the main fracture started to develop. The extension to the

lower part of the specimen obviously evolved in the pronounced post-failure phase. Until the end of the test, only 6 % of the recorded events could be used for localization. Particularly toward final rupture, the accuracy of event localization decreased because of an increasing rock damage. No reliable results could be obtained for the last two minutes of the post-failure phase.

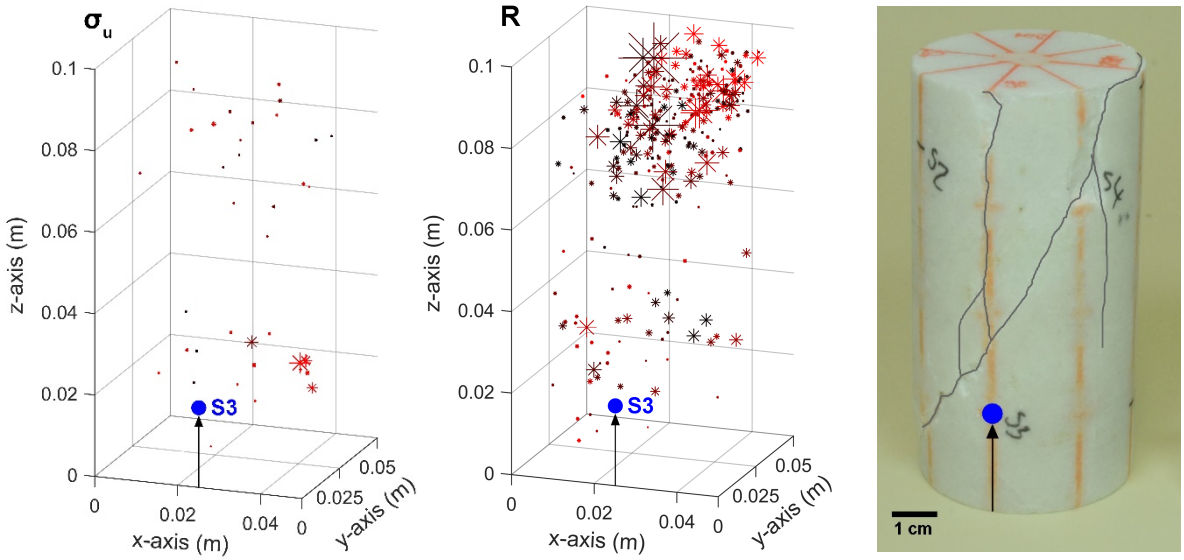

Figure 82: Results of AE localization in Laas marble (LAM-2-4). Only few events occurred until peak strength and the final shear plane started to form in the post failure phase (R).

5.2.2.7 Flossenbürg granite

In Flossenbürg granite, a high total number of events occurred and 15 % of the events could be used for localization. Since crack initiation and crack damage could not be determined from the number of AE, the localized events are given for a time interval after the test started and until final rupture (Figure 83). At the beginning of compression, cracks developed in the upper and lower part of the specimen and only few events were localized in the center. With progressive loading, intensive cracking took place and the diffusely distributed event coordinates show that cracks developed within the whole specimen.

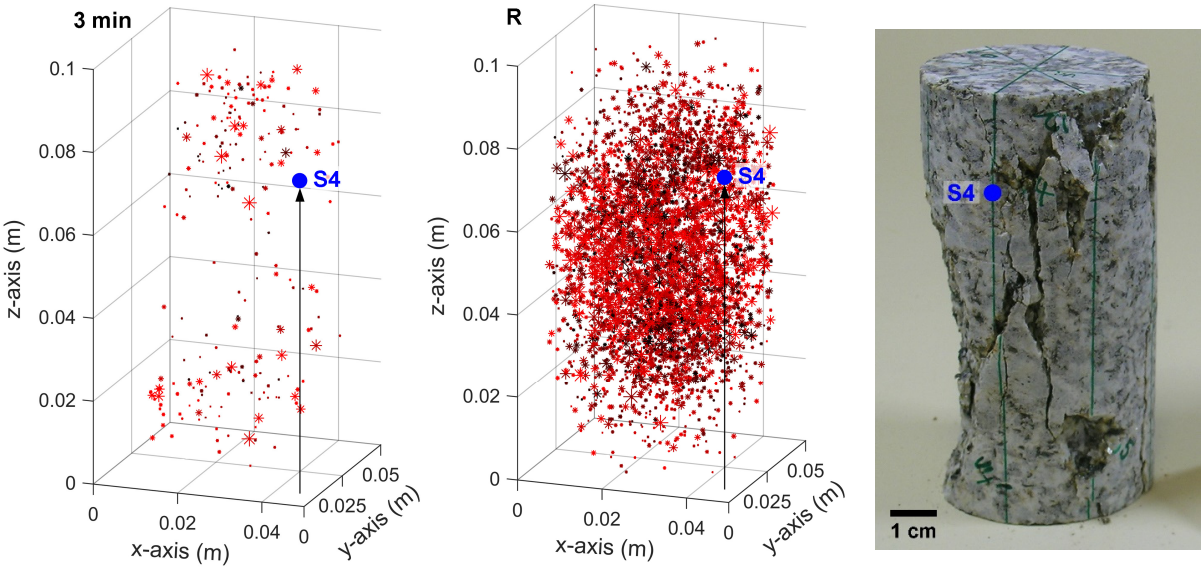

Figure 83: Results of AE localization in Flossenbürg granite (FLB-1-17) after 3 minutes and when final rupture (R) occurred.

The localized cracks, however, did not indicate a major fracture plane in advance of rock failure. The high number of events in the center of the specimen can be attributed to the composition and fabric of the granite. In the medium- to coarse-grained rock, many long grain boundaries and intragranular cracks at cleavage and twin planes exist and may act as stress concentrators where cracks are initiated. Furthermore, the weathering of feldspar and mica caused a disintegration of the rock structure so that cracking is facilitated.

5.2.2.8 Metten granite

In Metten granite, the phases of rock deformation could be determined from the number of events and from the stress-strain curve. Figure 84 shows the localization results for the five phases of rock deformation and the final fracture pattern. In the granite, a pronounced crack closure phase is present, where events mostly occurred in the upper part near the end surface of the specimen and in the center of the lower part. Crack closure is thus limited to the areas near the loading plates and does not occur in the center of the specimen. It is possible that friction at the loading plates caused some of the events, because of small irregularities at the end surfaces.

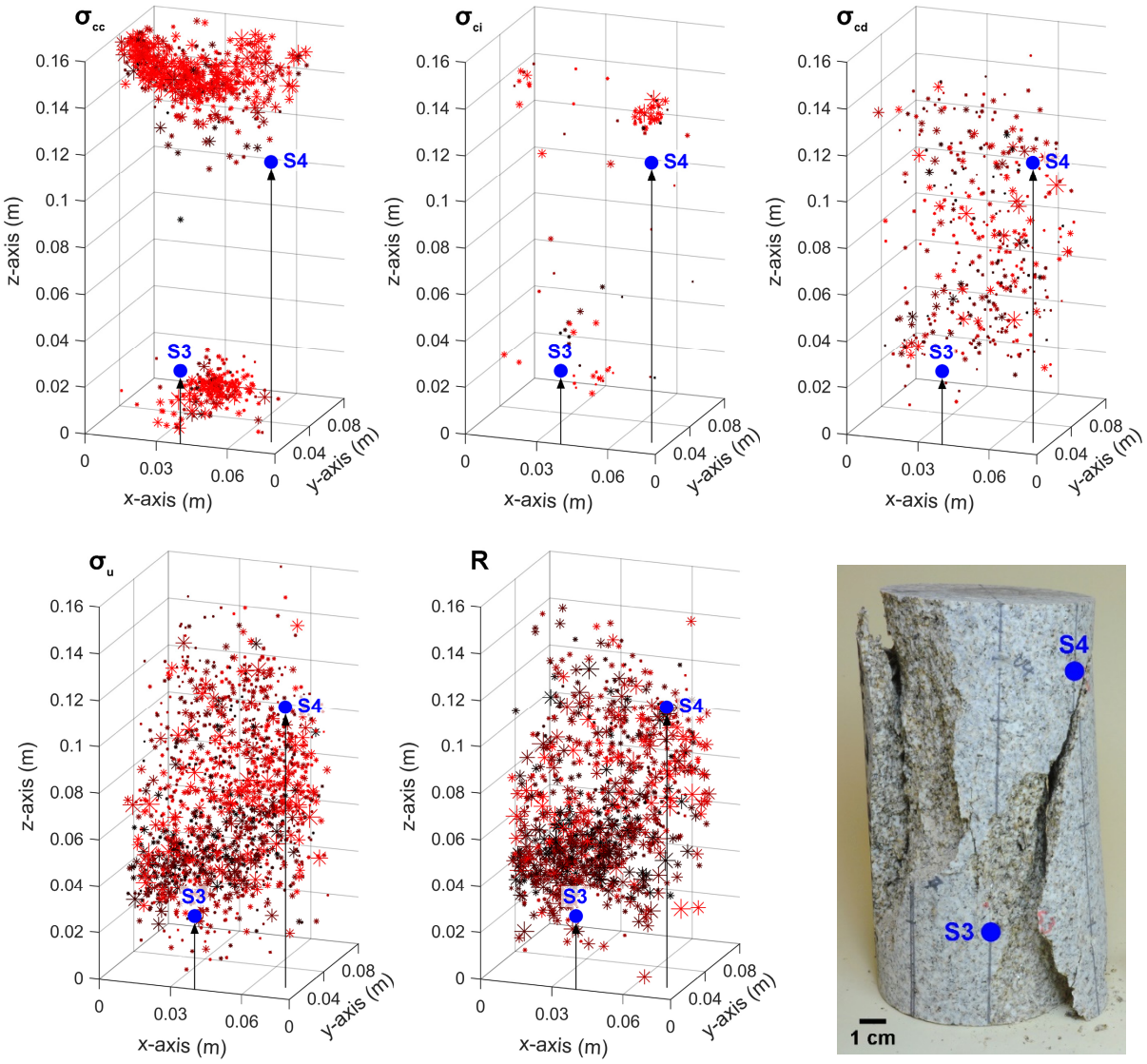

Figure 84: Results of AE localization in Metten granite (MET-2-1) during crack closure, linear elastic deformation, stable crack growth, unstable crack growth and in the post-failure phase.

In the second stage during linear elastic deformation, only few events occurred, which are distributed over the whole specimen. At a spot near sensor S4, a small accumulation of events shows that crack growth has already occurred in the stage of linear elastic deformation. In the stage of stable crack growth, events were mainly emitted in the central part and no longer at the ends of the specimen. During unstable crack growth, the number of events increased and an accumulation of events with a lower correlation coefficient (black to dark red) can be observed in the lower third of the specimen. The events emitted in the crack closure stage revealed the highest correlation coefficients, shown by the light red colors. With an increasing rock damage, the correlation coefficient decreased. Metten granite shows a typical failure pattern with a set of conjugate shear planes in the form of an hourglass and lateral axial fragments.

5.2.2.9 Posta sandstone

For AE localization in Posta sandstone, events with a correlation coefficient above 0.95 were used in order to reduce the large number of events. For the calculation, the p-wave velocity determined from the sonic pulses could not be used, because the variation in the velocities was extremely high. Therefore, the calculation resulted in much smaller velocities than the values measured with the ultrasound transmission method. Consequently, the highest value of the measured p-wave velocity was applied, since it provided the best possible localization results. Still, the event coordinates of Posta sandstone showed the highest localization errors of the tested rocks (Table 12), which is certainly the result of the high porosity and the anisotropy of the sandstone.

In Posta sandstone, the located events indicate a clearly different cracking behavior than the previously described low-porosity rocks. The typical phases of deformation and fracture are not clearly present in the sandstone but the localization results indicate a multiphase spatial evolution of damage in the pre-failure range (Figure 85). From the beginning of compression, many events occurred in two parallel planes at a distance of about 1 to 2 cm from the lower and upper end surfaces of the specimen. In this stress phase, no events were located in the middle of the specimen and the correlation coefficient was high. Since the events were limited to two distinct planes without considerable variations, a systematic localization error is excluded. The phase was divided into two phases, which are equivalent to crack closure and linear elastic deformation in low-porosity rocks (Figure 85: σ_{cc} and σ_{ci}). In the first phase, the number of events increased considerably, whereas an almost constant number of events characterizes the second phase.

In the third phase, events additionally occurred in the center of the cylinder and many events were still located in the two planes near the end surfaces. With increasing compression, the events in the two planes occur closer to the middle of the rock. The onset of AE activity in the central part of the specimen coincides with a distinct increase in the number of events (see Figure 75). With the beginning of this phase, the correlation coefficient and the number of events, which fulfilled the requirements for localization, decreased. The increase in the AE activity is defined as the crack initiation threshold because final failure is not directly associated with the parallel planes but only with the induced damage in the middle of the rock. In a fourth phase, microcracks mostly occurred in the middle of the specimen and only very few events were detected in the two planes. This phase correlates with the phase of unstable crack growth, which was determined from the reversal of the volumetric strain curve because it is not reflected in the number of events.

The failed sandstone shows a clearly developed set of conjugate shear planes with two cone-shaped ends of the cylinder as well as axial fragments in the lateral areas of the specimen. During failure, loose sand grains crumbled from the center of the specimen because the grain bonding totally sheared off. The

failed specimen (Figure 85, right) shows a limonitized band in the upper part of the specimen. The upper plane of localized AE coincides with the transition between the limonite-rich band and the area below, without limonite. The lower area of the specimen, however, does not show any occurrence of an accumulation of iron hydroxides. It is thus concluded that the limonitic band might contribute to the localized AE activity but it is not the main cause.

A high number of events near the ends of sandstone specimens was also observed by FORTIN et al. (2009), who investigated porous sandstones at different confining pressures. The results from their study revealed that the localized events resulted from the formation of compaction bands at a distance from the end planes. According to the authors, stress concentrations in this plane induced the formation of compactions bands, where cement bonds are broken and grain compaction occurs. Deformation bands were first described by AYDIN & JOHNSON (1978), who observed that compaction bands are characterized by pore collapse, grain fracturing, volume change and highly localized shearing. Investigations of MOLLEMA & ANTONELLINI (1996) revealed that the narrow planar bands form perpendicular to the largest compressive stresses.

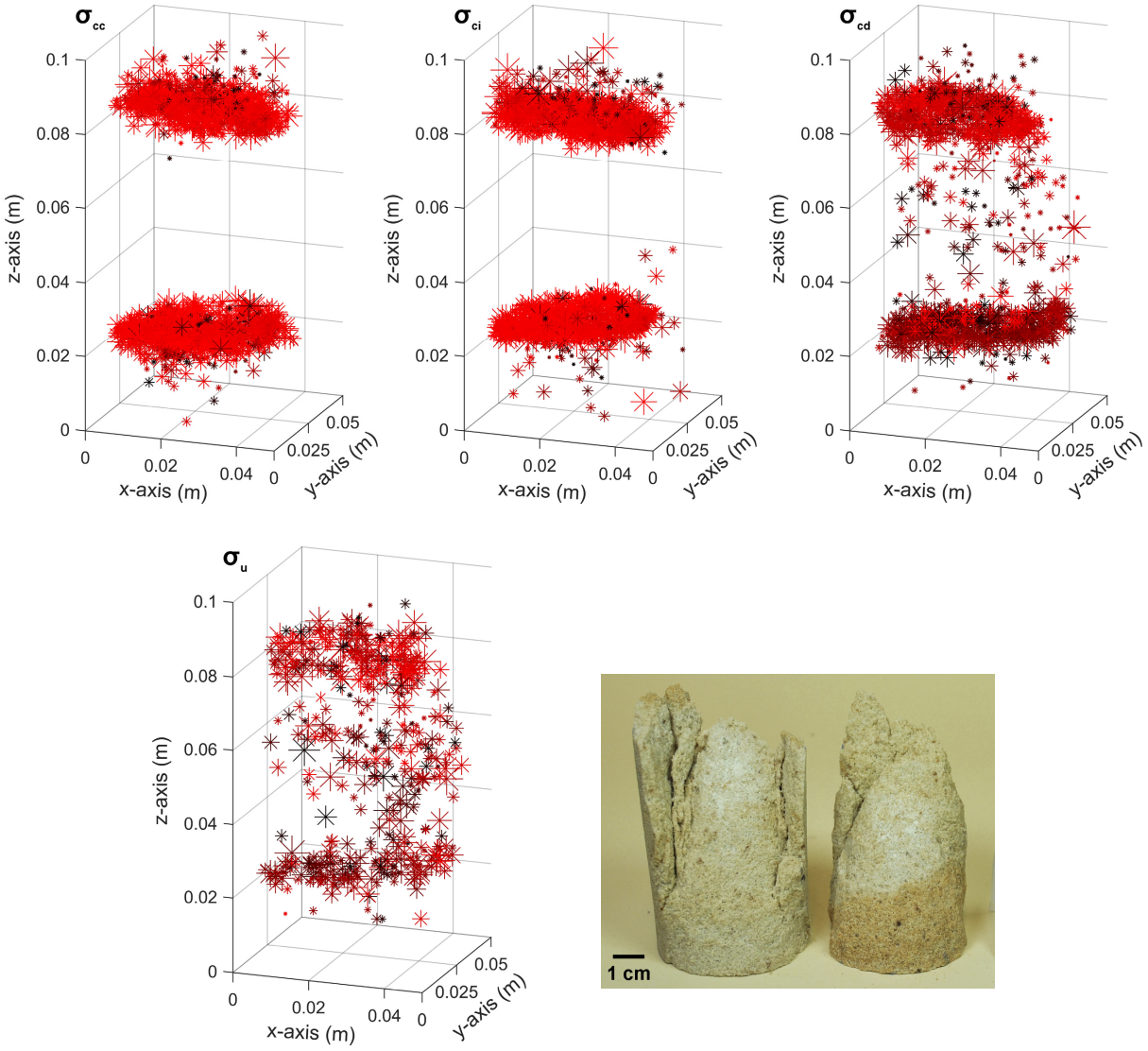

Figure 85: Results of AE localization in Posta sandstone (POS-4-9). In the first two phases (until σ_{cc} and σ_{ci}), localized compaction occurs in planes near the sample ends. In phase 3 (until σ_{cd}), additional cracking takes place in the middle. In phase 4 (until σ_u), cracking predominantly occurs in the middle of the specimen.

Assuming the formation of compaction bands in Posta sandstone, the emission of a large number of events is supposed to be caused by shearing along grain boundaries and fracturing of the siliceous cement material. A localized initiation of microcracks in the quartz grains is also possible. During the first phase, compaction occurs in localized compaction bands, where loosely bonded grains are rearranged and open pore cavities are reduced. The high AE activity and a high signal energy result from the breaking of the siliceous cement material. In the phase of constantly high AE activity, further compaction occurs in the compaction planes. Besides that, many grains are already closely packed and forces act directly on the grain contacts where elastic deformation occurs. The high number of events must be ascribed to further displacements caused by compaction and shearing along grain boundaries. In the third phase, when the AE activity increases again, the forces acting on grain contacts may exceed the tensile strength of the grains so that microcrack initiation takes place. A high number of events, which is distributed over the middle part of the specimen indicates that in this phase, stress concentrations also arise in the middle of the specimen so that pore and crack coalescence can occur. This phase is considered equivalent to the phase of stable crack growth in low-porosity rocks. The crack initiation threshold calculated with the LSR method (Figure 75) coincides with the onset of those events. In the phase of unstable crack growth, only few AE occurred in the compaction bands but most events are located in the middle part, where pore and crack coalescence occurs and major failure planes evolve.

5.2.2.10 Abtswind sandstone

During loading of Abtswind sandstone, only a small number of events occurred until shortly before failure. Most of the events in the pre-failure phase developed in two parallel planes about 2 cm away from the end surfaces, where the events occurred mainly near the edges of the specimen (Figure 86). Although the event rate is different, AE localization shows that the cracking behavior is similar to that of Posta sandstone. It is assumed that the two distinct planes of localized AE represent compaction bands where shearing along grain boundaries and cracking of grains take place. In the first phase of compression, AE only occurred in the two compaction bands and no events were located in the middle of the specimen. In this phase, the ductile clay minerals in the space between the strong quartz and feldspar grains are deformed without an emission of events. Only the breaking of quartz-quartz contacts or quartz-feldspar contacts as well as shearing along the grain boundaries is expected to emit acoustic signals. After the reversal of the volumetric strain curve until maximum stress, some cracks also occurred in the middle of the specimen, in addition to the events in the compaction bands. In this phase, stresses also concentrate in the central part and irregularly distributed cracks evolve.

Final failure of the clay-cemented sandstone occurred in the post-failure phase after the maximum stress was exceeded. The events in the post-failure phase did no longer occur in the compaction bands but they clearly mark the final shear plane. Compared to the events in the pre-failure phase, a number of high-energy events occurred especially in the upper part of the specimen and localization resulted in an accumulation of events in the lower left and the upper right part of the rock. In the post-failure phase, the correlation coefficient is considerably lower than in the pre-failure phase because of the accumulation of rock damage. The failure pattern represents the inclined shear plane, which is also visible in the AE coordinates. A second major shear plane developed in the lower part of the rock but it is not displayed by the event coordinates because it developed in the last seconds of the post-failure phase, when the events could no longer be used for localization. Since sensor S2 was located directly on the final shear plane, a reliable calculation of the event coordinates could not be performed after the sensor fell off. Since most events were emitted in the post-failure phase, only about 6 % of all recorded events fulfilled the requirements for localization.

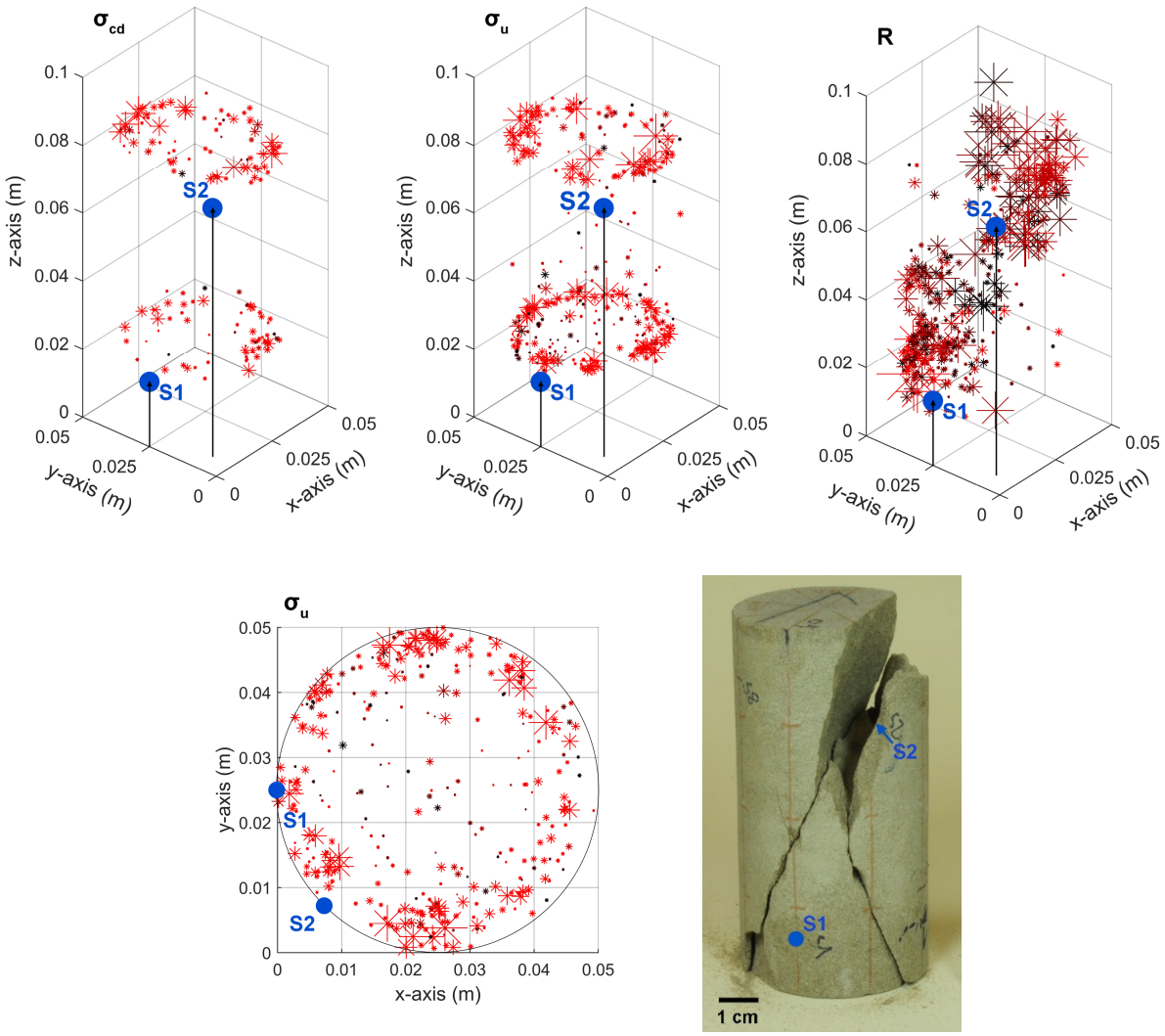

Figure 86: Results of AE localization in Abtswind sandstone (ABC-1-1). Above: AE coordinates until σ_{cd}, until maximum stress (σ_u) and in the post-failure phase until final rupture (R). Below: View along the z-axis, illustrating the events from σ_{cd} until σ_u and final failure pattern.

5.2.3 Rock mechanical properties

For a characterization of the different rock types, several rock mechanical parameters were obtained from uniaxial compression tests and nondestructive testing techniques. A selection of the mean values of selected rock mechanical parameters is summarized in Table 13 and the detailed laboratory data is given in Appendix I. The majority of the tests was performed within the scope of this dissertation project. Some additional data was collected in the course of the master theses of QUESSEL (2014), SCHALLHAMMER (2014), MEIßNER (2015), and BECK (2015), as well as in the course of bachelor theses of ZAEGE (2012), SCHNEIDER (2014), GIGL (2015), HORNUNG (2015), and GRUBER (2015). Single results were also obtained within concurrent dissertation projects of WILFING (2016) and ELLECOSTA (in prep.). The investigations were conducted on the ten rock types described in Section 5.1. From several rock types, the rock specimens had to be obtained from different blocks of rock.

Table 13: Summary of rock mechanical parameters of all tested rocks. For several rock types, specimens from different blocks of rock were used. A detailed summary of laboratory data is given in Appendix I.

Rock type	σ_u	E_T	ν	$\varepsilon_{a,u}$	$\varepsilon_{r,u}$	$\sigma_{ci,AE}$	σ_{ci}	$\sigma_{cd,AE}$	σ_{cd}	σ_t
	MPa	GPa	-	%	%	%	%	%	%	MPa
Pechbrunn basalt	408	75	0.05	0.57	0.04	64	53	95	99	18
Tittling granite	199	46	0.13	0.49	0.07	46	63	96	99	9.5
Diabase	190	53	0.12	0.39	0.05	75	50	99	100	17
Dietfurt limestone	162	37	0.10	0.49	0.05	70	59	98	100	9.5
Moosegg anhydrite	96	57	0.08	0.23	0.05	17	66	99	91	8.8
Laas marble	87	44	0.10	0.27	0.06	66	64	-	94	7.2
Flossenbürg granite	88	23	0.19	0.49	0.35	2	43	-	72	6.0
Metten granite	80	21	0.28	0.48	0.35	45	42	-	71	6.8
Posta sandstone	60	22	0.09	0.32	0.08	56	60	-	91	4.1
Abtswind sandstone	28	5.5	0.27	0.56	0.31	12	39	99	70	2.1

σ_u: uniaxial compressive strength, E_T: tangent Young's modulus, ν: Poisson's ratio,
$\varepsilon_{a,u}$, $\varepsilon_{r,u}$: axial and radial strain until failure,
σ_{ci}, σ_{cd}: crack initiation level and crack damage level determined from the stress-strain curve,
$\sigma_{ci,AE}$, $\sigma_{cd,AE}$: crack initiation level and crack damage level determined from the number of AE,
σ_t: Brazilian tensile strength

5.2.3.1 Uniaxial compressive strength

The uniaxial compressive strength, illustrated in Figure 87, shows mean values for all rocks ranging from 28 MPa for the clayey Abtswind sandstone to 410 MPa for basalt. Overall, rocks with a medium to extremely high strength, according to the ISRM (1978), were tested. In some cases, the different blocks of rock exhibited a high strength variation. Especially the strength values of anhydrite and basalt varied strongly between the different blocks so that the uniaxial compressive strength of anhydrite is between the classification of high and very high strength. The three tested types of granite (Tittling, Flossenbürg and Metten granite) showed that the uniaxial compressive strength is affected by the degree of weathering. The data shows that the laboratory rock strength of the unaltered Tittling granite is considerably higher than the strength of the weathered Flossenbürg and Metten granite.

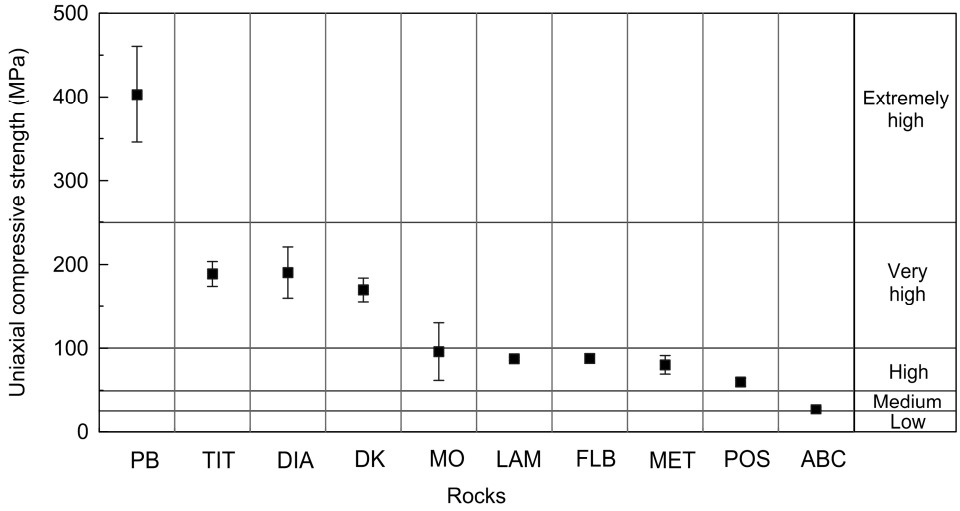

Figure 87: Mean values for the uniaxial compressive strength of all tested rocks, classified according to ISRM (1978).

5.2.3.2 Tangent Young's modulus

The tangent Young's modulus was determined from the stress-axial strain curve at 50 % of the uniaxial compressive strength. The obtained results range from the lowest mean value of 5.5 GPa for Abtswind sandstone to the highest mean value of 76 GPa for basalt (Table 13). The low Young's modulus for Abtswind sandstone is caused by the clay minerals, which build up the matrix and the cement of the rock. Since clay minerals have a higher compressibility than quartz grains, the clay content determines the deformation behavior of rocks (SCHÖN 1996: 176). In Figure 88, the relation between tangent Young's modulus and uniaxial compressive strength is illustrated according to the classification system of DEERE & MILLER (1966) for intact rocks. By combining Young's modulus and uniaxial compressive strength, the authors introduced the modulus ratio M_R. The modulus ratio is defined as the ratio of tangent Young's modulus to the uniaxial compressive strength.

$$M_R = \frac{E_t}{\sigma_u} \tag{30}$$

The modulus ratio is a measure for axial deformation with regard to the strength of the rock. A low modulus ratio indicates that high axial strain occurred until failure, whereas a high modulus ratio characterizes rocks with a less pronounced axial deformation. According to Deere's classification system, basalt and Abtswind sandstone result in a low to average modulus ratio, whereas anhydrite and marble revealed an average to high modulus ratio. Despite a very low axial strain, those rock types revealed a relatively low uniaxial compressive strength and they showed a rather ductile failure behavior with a distinct post-failure phase. All other tested rock types resulted in an average modulus ratio (Figure 88). The results are largely in agreement with the findings of DEERE & MILLER (1966), who also tested basalt, diabase, granite, marble and sandstone samples. Their results revealed an average modulus ratio for granites, basalt and diabase, an average to high ratio for limestone, a high modulus ratio for marble and a low to average ratio for sandstone.

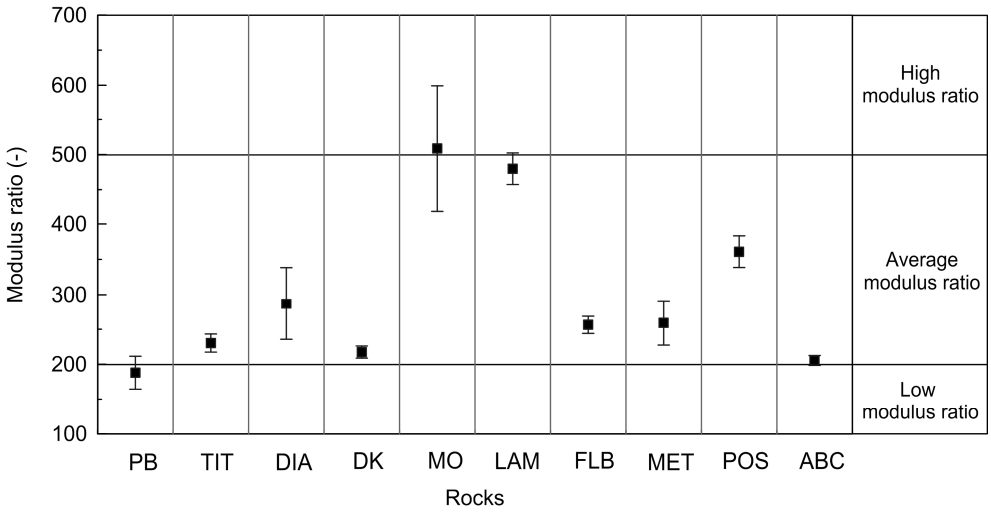

Figure 88: Classification system for intact rocks after DEERE & MILLER (1966), using the ratio of tangent Young's modulus versus uniaxial compressive strength.

5.2.3.3 Strain at failure

Similar to the Young's modulus, the total deformation at maximum stress provides information about the deformability of the rock. In Figure 89, the results of the total axial and radial strain of all tested rock types are given. The results show that there is a strong difference in axial strain compared to radial strain. This is particularly because the radial strain was very low in many rocks, whereas the axial strain shows a high variability. Of all tested rocks, only the weathered granites and Abtswind sandstone revealed a significant radial strain. When comparing axial strain and modulus ratio, it becomes clear that the modulus ratio is a strong measure for the axial deformability of rocks. A low modulus ratio thus coincides with a high axial strain and a high modulus describes a low axial strain at failure. The modulus ratio, however, does not fully describe the deformation and cracking behavior of rocks, because additionally to axial strain, the rock behavior under uniaxial compression is strongly dependent on the radial deformation.

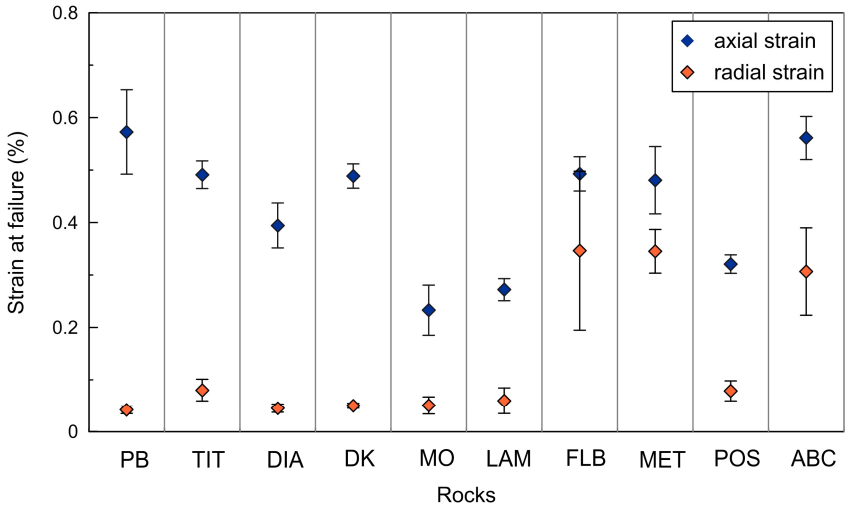

Figure 89: Results of axial and radial strain at failure for the tested rock types. Only FLB, MET and ABC show a significant radial strain at failure.

Figure 90 shows the difference between axial strain and radial strain and it is makes clear that the four rock types with a brittle failure behavior (PB, TIT, DIA, DK) revealed the largest disparity in axial and

radial strain. The brittle rock types are mainly deformed in axial direction but the deformation is not reflected by a radial expansion. During loading, the generated strain energy is not released by the initiation of microcracks but the energy is stored within the specimen. Shortly before or directly at peak stress, a rapid formation of major cracks and an instantaneous release of the previously stored energy occurs. Rock types showing a more ductile failure behavior resulted in a smaller difference in axial compared to radial strain at failure. This was also clear from the stress-strain curves, where brittle rock types do not show a yield in the radial strain curve, whereas the more ductile rock types show a distinct increase in the radial strain when unstable crack growth begins. The strain difference is thus a valuable measure for the brittleness of rocks.

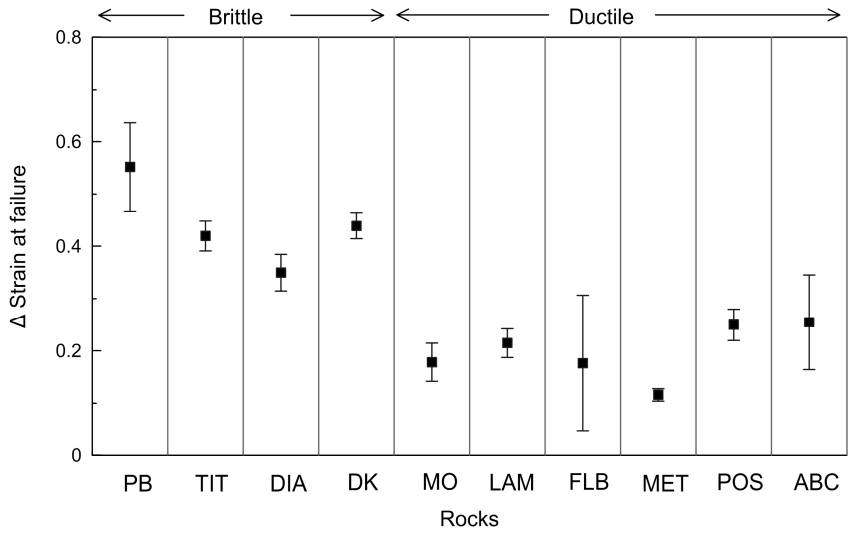

Figure 90: Difference between axial and radial strain at failure. Brittle rock types generally revealed a more pronounced difference in the strains than more ductile rock types.

In Figure 91, radial and axial strains are given as mean normalized values of the uniaxial compressive strength. The four rock types with a brittle failure behavior showed the lowest total values for radial and axial strain. Anhydrite, marble and Posta sandstone also revealed low values, whereas the weathered granites were deformed more intense in radial and axial direction. Abtswind sandstone showed an extremely high deformation in both, radial and axial direction. With relatively low strains, Posta sandstone shows an exceptional behavior. The difference between the two types of sandstone is supposed to be the result of their sedimentary fabric. Where the Posta sandstone consists of a framework of quartz grains bonded by siliceous cement, the structure of Abtswind sandstone is more influenced by the clayey matrix. This indicates that the grains in Posta sandstone are more densely packed and deformation occurs by breaking the cement bonding. In contrast, the grains of Abtswind sandstone are embedded in a clayey matrix and deformation is facilitated, since the strong quartz grains can easily deform the weak clay minerals.

From the axial strain behavior of rocks, WILFING (2016) proposed a classification system for the brittleness of rocks, where the ratio of axial strain at failure versus axial strain at the crack damage threshold is used. A strain index of 1.1 is suggested as the transition between rock types showing a brittle and ductile (or tough) failure behavior. The strain index quantifies the phase of plastic deformation, which is represented by a yield in the stress-axial strain curve. Brittle rock types generally show a straight axial strain curve without a distinct increase in the strain toward the peak stress, whereas ductile rock types are characterized by a high proportion of plastic deformation.

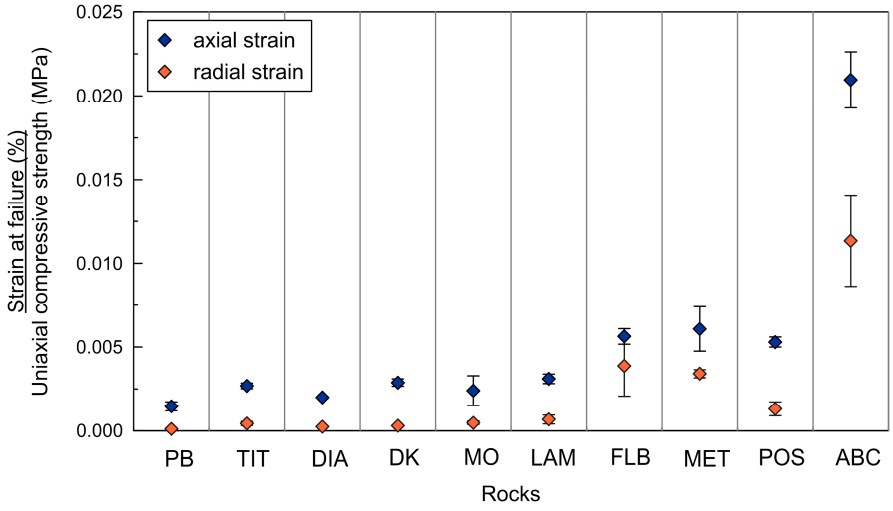

Figure 91: Strain at failure normalized by the uniaxial compressive strength. Rocks are arranged according to their mean strengths.

The classification method proposed by WILFING (2016) was applied to the tested rock types and the strain index is given in Figure 92. The axial strain until crack damage was determined using σ_{cd} from AE testing (PB, TIT, DIA, DK) and only where the AE method could not be applied reliably, the reversal of the volumetric strain curve was used (MO, LAM, FLB, MET, POS, ABC). Figure 92 shows that the fine-grained rocks like limestone, and diabase revealed a strain index of almost 1.0, whereas basalt and Tittling granite resulted in a mean strain index of about 1.05. According to this method, basalt, Tittling granite, diabase, and Dietfurt limestone can be classified as brittle. The rock types with a distinct deviation from linearity in the axial strain curve showed a mean value above the threshold of 1.1 but with a high variation in the data. Anhydrite, marble and Posta sandstone revealed medium values because of a late yield in the volumetric strain curve. The stress-strain curves of the weathered granites and Abtswind sandstone showed an early yield and thus resulted in higher values above 1.4. According to this classification system, the mono-mineral crystallized rocks, the weathered granites and the sandstones are classified as ductile and is generally in agreement with the observations in this study.

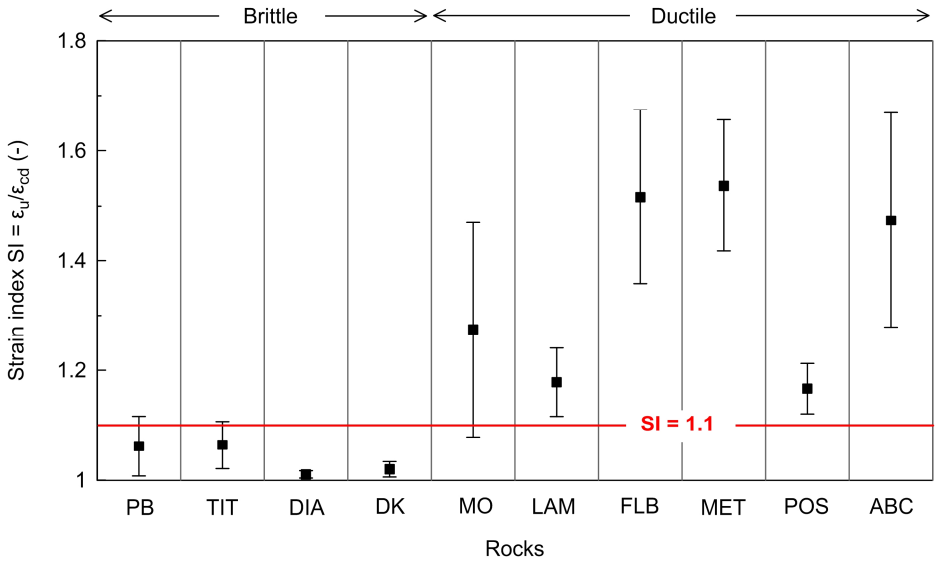

Figure 92: Strain index SI as a classification method for the brittleness of rocks after WILFING (2016). A strain index of 1.1 is defined as the transition between brittle and ductile rock types.

5.2.3.4 Deformation stages under uniaxial compression

The crack damage and crack initiation stress levels were determined with two different methods, the volumetric strain method combined with the Lateral strain response (LSR) method and the acoustic emission method. Applying the volumetric strain method, the crack damage stress is defined as the maximum volumetric strain or the reversal point of the stress-volumetric strain curve. With the AE method, the crack damage stress is determined from a distinct increase in the number of AE. In Figure 93, the crack damage thresholds from both methods are given as percentage of the uniaxial compressive strength. Many of the analyzed rock types did not show the characteristic deformation and cracking behavior as would be expected according to the theory of deformation and fracture. From the tested rock types, not a single rock showed at the same time the typical deformation behavior and the expected phases of cracking. In the brittle rock types, the AE activity revealed the typical phases of cracking but the crack damage threshold is not displayed by the stress-strain response. Several stress-strain curves of brittle rocks did not exhibit a reversal of the curve so that the crack damage stress was equal to the peak strength. AE testing of the brittle rocks, however, confirmed the high crack damage levels, which almost coincided with the uniaxial compressive strength. The tested samples of basalt, Tittling granite, diabase and limestone showed a crack damage threshold between 0.95 and 1.0 σ_u and both methods revealed almost similar results. It is thus concluded that in brittle rock types, the phase of unstable crack growth is comparably short, whereas ductile rocks show a more pronounced phase of unstable crack growth.

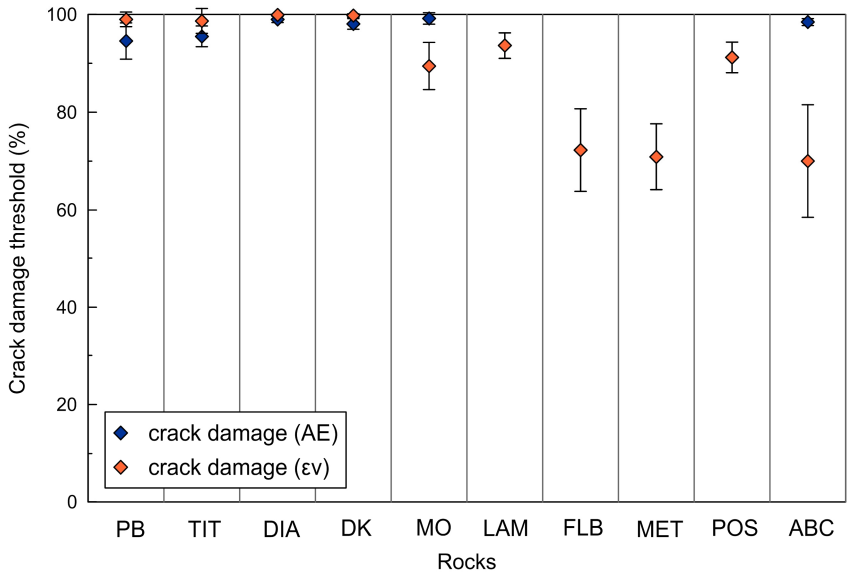

Figure 93: Comparison of the calculated crack damage threshold determined from the number of AE and the maximum of volumetric strain. For LAM, FLB, MET and POS, the AE method was not applicable.

The stress-strain curves of the ductile rock types showed the typical deformation phases but in most rocks, the cracking activity was different from the expected behavior. A clear reversal of the volumetric strain curve was present in all ductile rocks but most of the rocks did not show a noticeable increase in the number of events so that the crack damage stress could only be determined from the volumetric strain curve. In anhydrite, a distinct reversal of the volumetric strain curve occurred at a stress level of about 0.9 σ_u, but a considerable increase in the number of events only occurred shortly before failure. Marble showed an exceptional cracking behavior with only single events in the pre-failure phase so that a crack damage stress could not be determined from the number of events. Intense cracking first started in the post-failure phase after the peak stress was exceeded. It is assumed that in marble, the signal amplitudes of intracrystalline cracks were too low to be detected with the applied detection threshold.

The applied trigger was set at a level just above the noise amplitude so that as many events as possible could be detected. The low-amplitude signals might thus have disappeared in the background noise. The crack damage levels of the weathered Flossenbürg and Metten granite revealed low values with a mean of about 0.7 %. The cracking activity, however, increased gradually but without a marked increase in AE that would indicate major crack coalescence. The discrepancy between deformation behavior and cracking activity is assumed to result from the beginning alteration of the granites and a reduced interlocking strength of the minerals.

The AE activity in Posta sandstone does not indicate a true crack damage threshold, although the volumetric strain curve shows a clear reversal. The reason for an exceptional cracking behavior is the porous, granular structure of the sandstone so that a true initiation and propagation of microcracks does not occur. Instead, most of the deformation takes place at the grain boundaries so that cracking primarily means breaking of the quartz cement between the grains and not fracturing of the grains. In Abtswind sandstone, the volumetric strain curve reversed at a low stress level of about 0.7 σ_u but a high number of events first occurred right before failure. Only few events occurred in the pre-failure phase before the number of events increased significantly. It is assumed that the deformation mainly concentrates on the clay minerals between the solid quartz grains because the clay minerals can deform elastically without emitting acoustic signals. Therefore, the high rock deformations are not accompanied by a high cracking activity during a large proportion of compression.

In Figure 94, the single values of the crack damage stresses are plotted against the uniaxial compressive strength. For the brittle rock types as well as for anhydrite, the results of the AE method were used, whereas for the ductile rock types, the stresses determined from the volumetric strain method are given. Averaged over all rock types, the mean crack damage threshold is 0.95 σ_u. This high value results from the very high stress levels in the brittle rock types, which almost coincide with the uniaxial compressive strength. In addition, also the mono-mineral rocks and Posta sandstone revealed high crack damage thresholds above 0.9 σ_u. Only the clearly ductile rock types like the weathered granites and Abtswind sandstone showed lower crack damage thresholds.

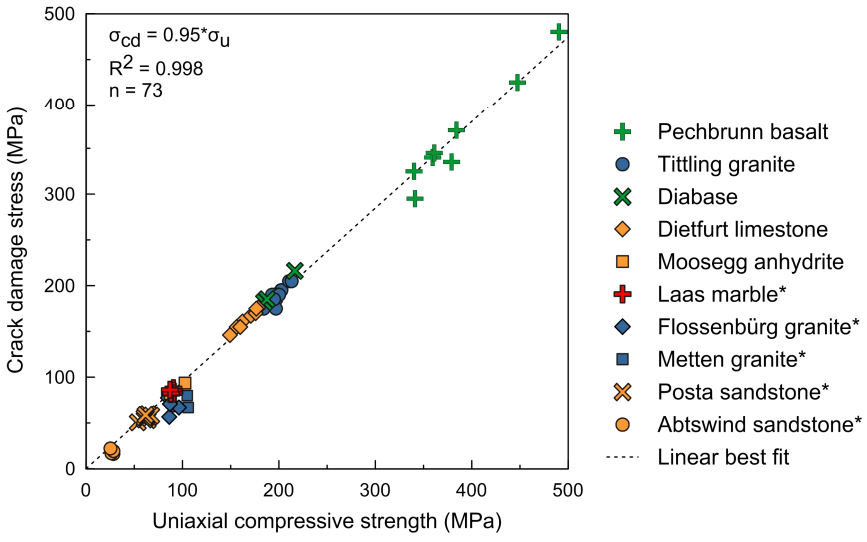

Figure 94: Relation of the crack damage stress to the uniaxial compressive strength. Single values are determined from the number of AE, tagged data could only be determined from the volumetric strain curve (after NICKSIAR & MARTIN 2013).

The crack initiation stress was calculated using the LSR method of NICKSIAR & MARTIN (2012) and is compared with the stress levels determined with the AE method (Figure 95). Compared to the crack damage threshold, the variation in the crack initiation stress is considerably higher and in many cases, the onset of AE does not at all coincide with the calculated crack initiation stress. Only in LAM, MET, and POS, both methods resulted in similar values. In the truly brittle rocks like basalt, limestone, and especially in diabase, the calculated values were considerably lower than the values determined with the AE method, whereas in Tittling granite, a higher threshold was calculated with the LSR method. A reliable calculation from the volumetric strain curve is obviously not possible if a clear reversal of the volumetric strain curve does not exist. In brittle rocks, the onset of the AE activity is thus considered as a more reliable indicator for the crack initiation stress.

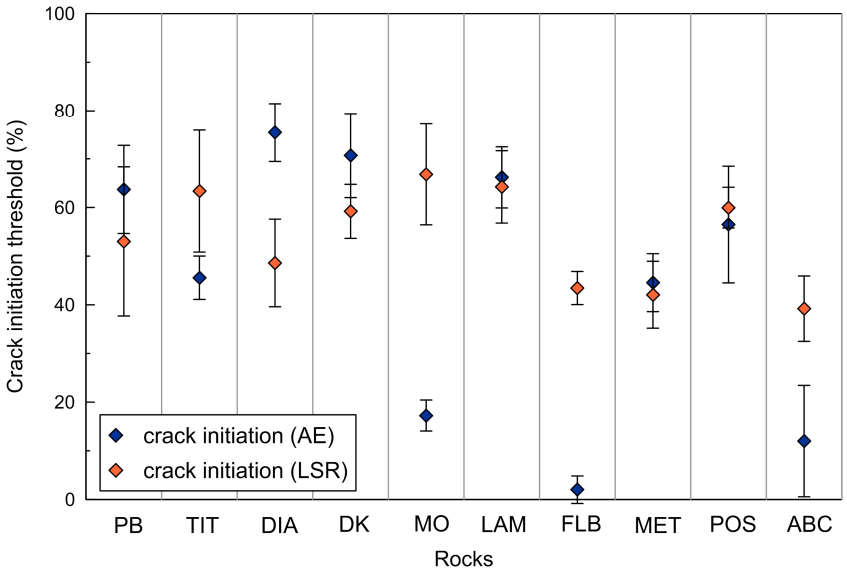

Figure 95: Comparison of the crack initiation thresholds calculated with the LSR method and determined from the onset of the AE activity.

In some of the ductile rock types, a very high difference between LSR and AE method was observed because some of those rocks showed a cracking activity almost from the beginning of loading. Therefore, the AE method revealed low σ_{ci} in anhydrite, Flossenbürg granite and Abtswind sandstone. In contrast, the LSR method resulted in considerably higher stress thresholds. Apparently, the calculated values for crack initiation do not reflect the actual cracking behavior of those rocks and this method can only be applied if the common phases of deformation and cracking occur. In Posta sandstone, a high number of events occurred during the entire loading period. The mechanism responsible for the emission of events is expected to be different in porous sandstones with a granular structure than in low-porosity rocks. The stress level of an increasing number of events is considered as the true crack initiation threshold in Posta sandstone and this stress level almost coincides with the stress threshold determined with the LSR method.

Figure 96 illustrates the ratio of crack initiation to the uniaxial compressive strength. The linear best fit shows a mean crack initiation stress of $0.62\,\sigma_u$ for all tested rock types. For igneous and metamorphic rocks, NICKSIAR & MARTIN (2013) found a ratio of $0.46\,\sigma_u$ and for sedimentary rocks, their results showed a crack initiation level of $0.42\,\sigma_u$. A mean of 0.45 ± 0.06 is presented in NICKSIAR & MARTIN (2014) for all of their tested rock types. Further studies, however, have also shown that higher values for σ_{ci} and σ_{cd} may occur (see Table 1). The higher mean value of crack initiation from this study might

result from the lower number of tested rock types and from the high proportion of rocks with a high crack initiation level.

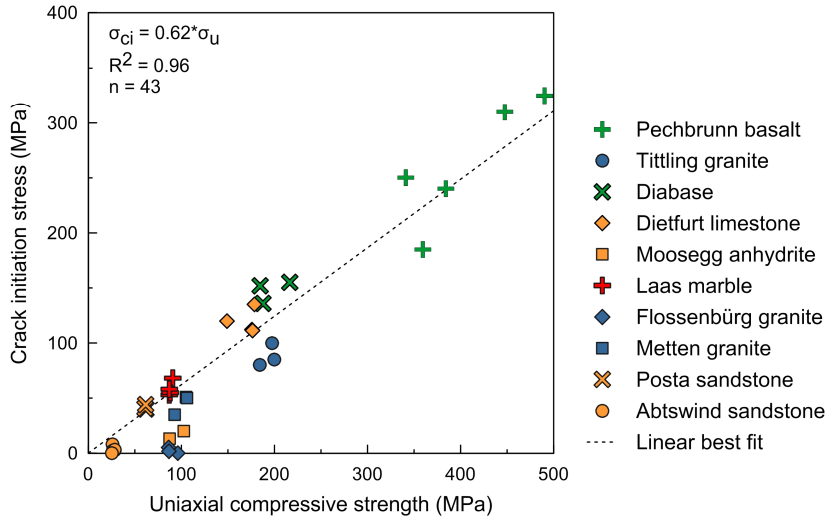

Figure 96: Relation of crack initiation stress to uniaxial compressive strength. The crack initiation stresses for all specimens were determined from the number of AE.

In Figure 97, all stress levels determined with the AE method are summarized. Where a determination of the crack damage stress with the number of AE was not possible, the results from the volumetric strain method are given. In some rock types, a crack closure phase does not exist because microcracking started with the beginning of loading (MO, POS) or because no events were emitted in the initial phase of compression (DK). In the brittle rock types like basalt, Tittling granite, diabase and limestone, the phases of stable crack growth and unstable crack growth were clear from the cracking activity. In the more ductile rock types like anhydrite, marble, weathered granites and the sandstones, the typical phases of deformation and cracking were only partly reflected by the AE activity.

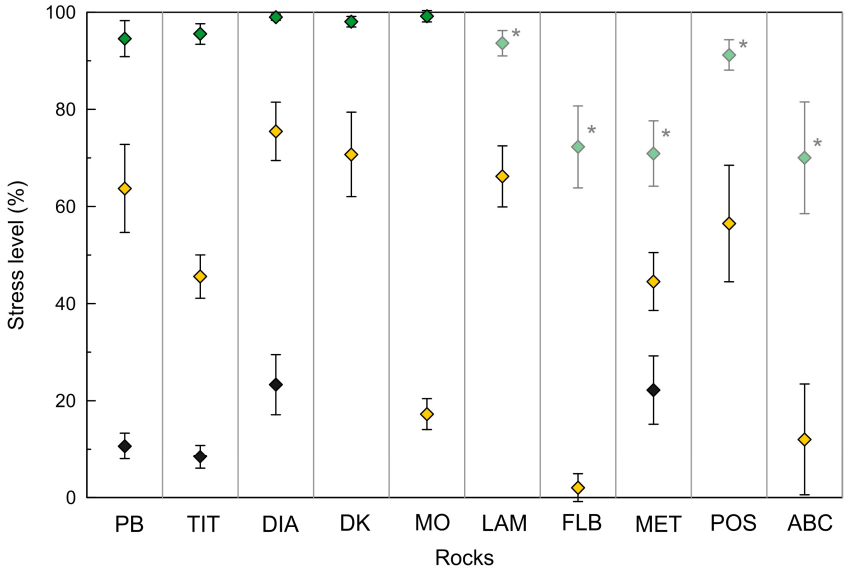

Figure 97: Crack closure (black), crack initiation (yellow) and crack damage threshold (green) determined from the number of AE (in percentage of the uniaxial compressive strength). Light colors indicate crack damage levels determined from the volumetric strain curve.

5.2.3.5 Brazilian tensile strength

The Brazilian tensile strength of the rocks is illustrated in Figure 98 sorted by their uniaxial compressive strength. The results generally show a similar trend as the uniaxial compressive strength. Assuming a linear relation between uniaxial strength and the Brazilian tensile strength, exceptions are basalt, Tittling granite and diabase. Basalt and Tittling granite revealed a relatively low Brazilian tensile strength compared to their extremely high and very high uniaxial compressive strengths, whereas diabase exhibited a relatively high mean tensile strength almost similar to basalt, although its uniaxial compressive strength is considerably lower.

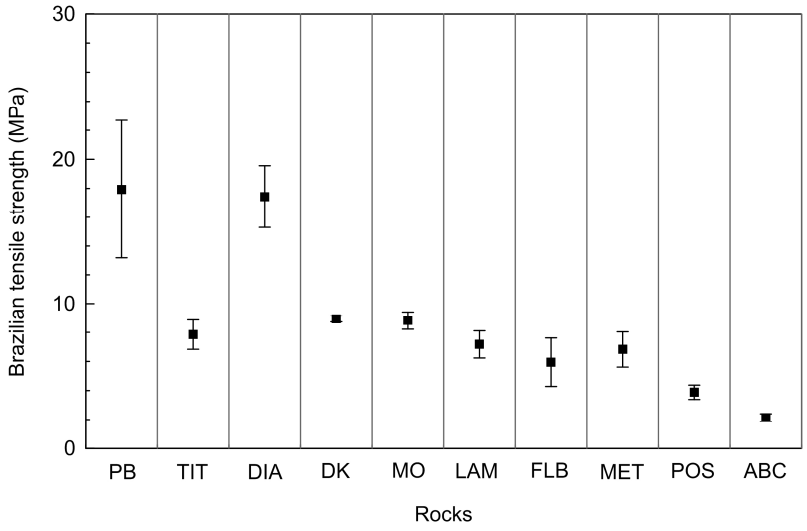

Figure 98: Results of the Brazilian tensile strength test for the tested rock types.

Figure 99 illustrates the relation between uniaxial compressive strength and Brazilian tensile strength, given as the toughness coefficient Z. According to the classification of SCHIMATZEK & KNATZ (1976) and the extension of THURO (1998), a rock with a coefficient Z above 10 defines a brittle failure behavior, whereas rocks with a coefficient lower than 10 show a ductile failure behavior. Although only basalt, Tittling granite, diabase and limestone showed a brittle failure behavior, all of the tested rock types revealed a coefficient Z above 10. Therefore, this method is not able to classify the brittleness of rocks.

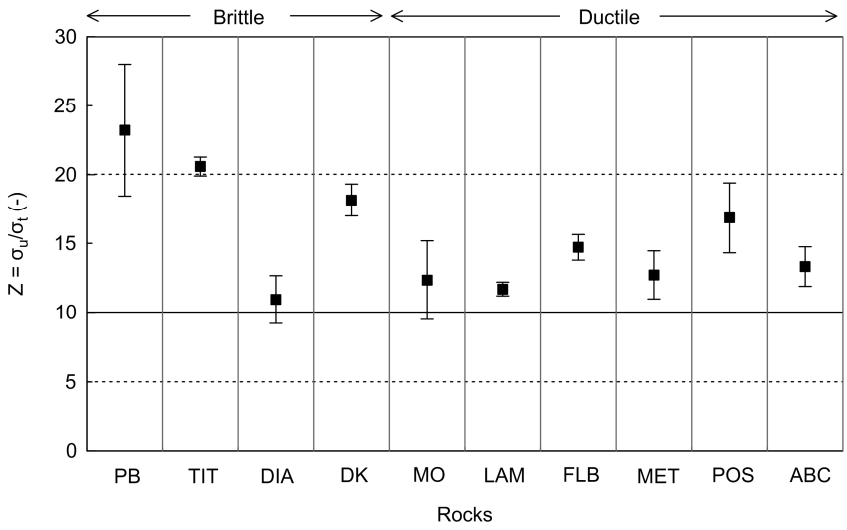

Figure 99: Toughness coefficient Z representing the ratio of uniaxial compressive strength to Brazilian tensile strength for the tested rock types with the classification of THURO (1998).

WILFING (2016) also showed that this classification method does not reflect the actual rock behavior observed in laboratory tests. This becomes clear from the results for the diabase samples, which showed the second highest Brazilian tensile strength but because of a high uniaxial compressive strength the ratio is relatively low, similar to the results obtained for anhydrite and marble. Rock types like Flossenbürg and Metten granite as well as Abtswind sandstone with a distinct phase of plastic deformation showed higher values although they clearly revealed a ductile failure behavior.

5.2.4 Acoustic properties

When approaching the process of damage accumulation during uniaxial compression of rocks, non-destructive testing techniques are the only possibility to obtain information about rock damage without influencing the specimen. In this work, ultrasonic wave measurements and acoustic emission monitoring were used to approach the different failure behavior of rocks. P-wave velocity was measured in axial and radial direction before uniaxial compression testing was carried out. The different measurement directions allowed the detection of a possible velocity anisotropy. Applying the same principles as for ultrasonic testing, the AE technique was applied for monitoring the generation of cracks during uniaxial compression. Since any generation of cracks emits elastic waves, the number of acoustic events gives insight into the process of microcracking and its dependency on the applied stresses. The mean signal energy is a measure for the intensity of an acoustic event and is dependent on the cracking intensity. Table 14 summarizes the acoustic parameters including the number of events until failure ($N_{AE,failure}$) and the mean signal energy E_s. The detailed data is given in Appendix II.

Table 14: Summary of acoustic parameters of the tested rock types. Values are averaged over the samples, which were, in some cases, obtained from different blocks of rock.

Rock type	Blocks	ρ	$v_{p,\,axial}$	$v_{p,\,radial}$	$N_{AE,\,failure}$	E_s
	ID	g/cm³	km/s	km/s	-	V²/s
Pechbrunn basalt	PB-1,2,3,4,5	3.14	6.40	6.76	639 ± 237	1,937
Tittling granite	TIT-1,2,3	2.65	4.41	4.79	12,728 ± 1,726	287
Diabase	DIA-1	2.92	6.24	6.20	916 ± 82	229
Dietfurt limestone	DK-1	2.55	5.29	5.45	288 ± 130	4,775
Moosegg anhydrite	MO-1,2,3,4,6	2.97	4.93	5.90	10,090 ± 1,838	8
Laas marble	LAM-2,4,5	2.71	5.15	5.45	211 ± 167	3
Flossenbürg granite	FLB-1	2.63	3.37	3.42	24,888 ± 529	23
Metten granite	MET-2,4	2.61	3.66	3.85	21,702 ± 2,494	60
Posta sandstone	POS-2,3,4	2.08	3.05	3.21	56,862 ± 1,981	238
Abtswind sandstone	ABC-1	2.03	2.27	2.30	3,315 ± 844	30

5.2.4.1 P-wave velocity

P-wave velocities of all rocks were determined in axial and radial direction in order to detect potential velocity anisotropies within the specimens. The results for the tested rocks are illustrated in Figure 100. Basalt, diabase and marble as well as limestone and anhydrite showed the highest p-wave velocities of over 5 km/s. Tittling granite showed a medium velocity and the weathered granites as well as the siliceous Posta sandstone revealed lower velocities between 3 and 4 km/s. The lowest p-wave velocities with a mean of 2.3 km/s were measured in Abtswind sandstone. The occurrence of clay significantly reduces the p-wave velocities and the elastic moduli of the rock. According to SCHÖN (1996: 176), the

p-wave velocity of clay is lower than that of quartz or carbonate material so that the mean velocity is strongly decreased with increasing clay content. Furthermore, the mechanical properties of clay-rich rocks are highly dependent on the water content and on the distribution of clay within the rock. If clay minerals are present between the grains, they inhibit quartz-quartz contacts and instead of quartz, the clay minerals control the elastic properties of the rock (SCHÖN 1996).

In the tested samples, the measurement error of the p-wave velocity is up to 100 m/s. Several factors have an influence on the accuracy of the determined wave speeds. In general, the error is largely dependent on the measuring distance because the accuracy of arrival time picking is only as precise as the sampling rate. Given a constant sampling rate, the picking accuracy decreases proportionally to a smaller measuring distance. Further influences on the accuracy of p-wave velocity measurement are given in Subsection 3.3.2. Some types of rock showed a relatively high standard deviation indicating heterogeneities within the measuring planes. In basalt, heterogeneities are phenocrysts of olivine that are irregularly distributed in the fine-grained matrix and reach dimensions of up to 1 cm. The tested anhydrite samples showed the highest variability in the velocities, since the tested samples were taken from different blocks of rock, which revealed a high variation in the physical properties. As illustrated in Figure 100, many rocks exhibited a velocity anisotropy in axial compared to radial direction. Only diabase, Flossenbürg granite and Abtswind sandstone resulted in almost similar results for both directions, indicating an isotropic p-wave velocity distribution within the specimens.

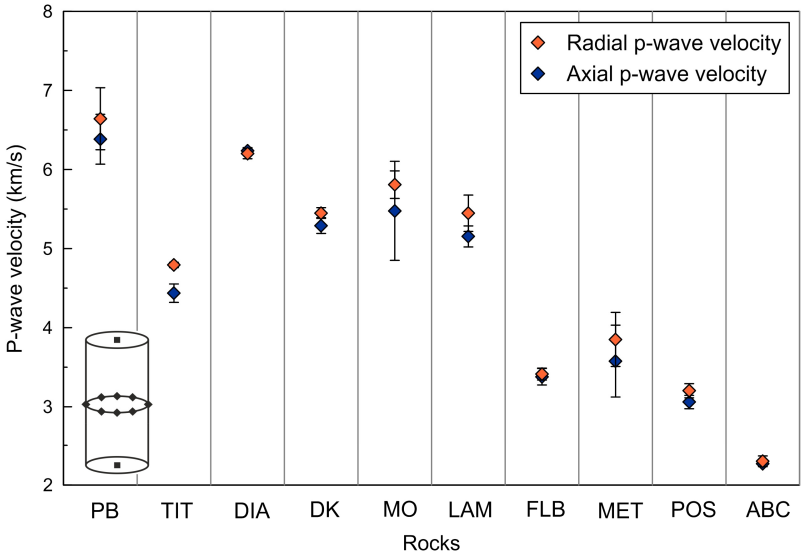

Figure 100: Results of the mean p-wave velocities in radial and axial direction of the tested rocks.

Basalt, limestone, anhydrite, marble, Metten granite and Posta sandstone all resulted in higher radial than axial velocities. Part of this difference might be the result of attenuation and dispersion of the sonic waves, which WINKLER & MURPHY (1995) ascribe to scattering at heterogeneities in the grain or pore scale. Within a longer measuring distance, more grain boundaries, cracks and heterogeneities are available. Thus, it is suggested that scattering is one of the reasons for lower p-wave velocities in the axial compared to the radial directions. In Laas marble, the higher velocities in radial direction might be due to thin bands of mica, which occasionally occur perpendicular to the core axis and increase the wave speed in this direction. Furthermore, a preferred orientation of calcite minerals might cause the anisotropy in marble because of different elastic properties along the crystallographic directions. In Tittling granite, a clear velocity anisotropy was observed within the single specimens although neither macroscopically nor microscopically a structural anisotropy was visible.

In addition to the difference in axial and radial velocities, an anisotropy within the radial measuring planes as well as a variation between the different measuring planes was observed. In Figure 101, examples of different velocity distributions within selected specimens are illustrated. The sample of Dietfurt limestone is an example for isotropic radial velocities throughout all measuring planes (Figure 101a). Within the single planes, the values are similar in all directions so that a circular plot results. In Figure 101b, a specimen of Tittling granite is given as a representative example for radial velocity anisotropy. In all three measurement planes, the velocity anisotropy is similar and results in an oval shaped plot. In all planes, the difference between highest and lowest radial velocities is about 500 m/s ranging from about 4.6 km/s to 5.1 km/s. Posta sandstone is an example for changing velocities over the specimen length. Figure 101c illustrates different velocities in the plane at 2.5 cm height, where considerably higher velocities were measured than in the two other planes. The reason for the difference was a brown-colored streak of iron oxides oriented perpendicular to the core axis. The iron oxides occur in irregular bands throughout the rock and exhibit a strong influence on the p-wave velocities. When ignoring the measuring planes in iron oxide rich bands, the radial velocities are almost similar to the axial velocities.

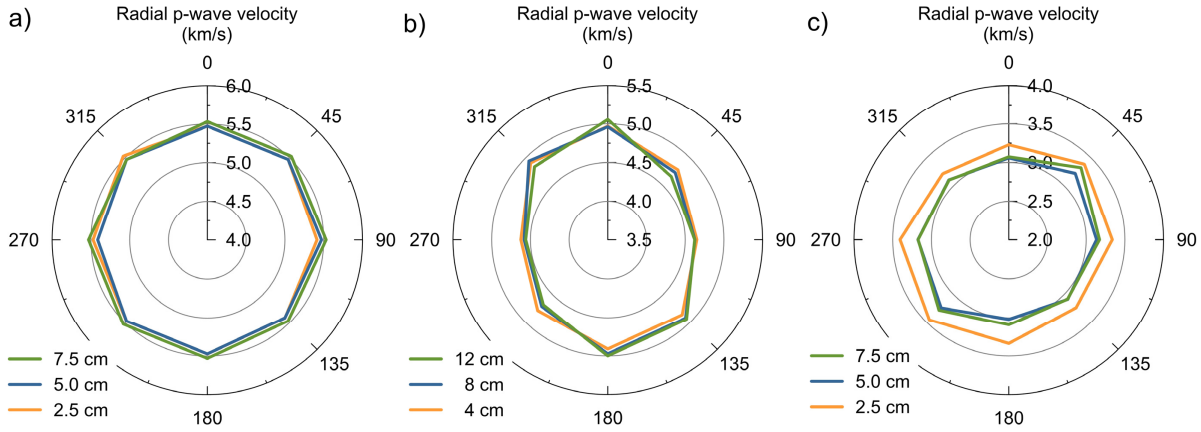

Figure 101: Examples of the p-wave velocity distribution in three radial measuring planes. a) Dietfurt limestone (DK-1-2) shows an isotropic distribution, b) Velocities in Tittling granite (TIT-3-1) are anisotropic and c) in Posta sandstone (POS-4-10), plane 2.5 shows higher velocities because of the accumulation of limonite.

5.2.4.2 Velocity anisotropy of Tittling granite

On an intact cube of Tittling granite, further investigations were performed in order to investigate the differences in the p-wave velocities in all directions. As illustrated in the section above, Tittling granite shows a strong velocity anisotropy throughout the rock. The anisotropic behavior was investigated by measuring the velocities in different direction of an intact cube of rock (BECK 2015). Measurements were performed from center to center of the surfaces and in several measurement planes (Figure 102). The results in Table 15 show a clear difference in the velocities in all three directions of the block although the outward appearance did not indicate an anisotropy or a preferred orientation of the minerals. The horizontal planes at the height of 7 and 21 cm exhibited largely similar results, whereas the middle plane resulted in higher velocities. The results of the cube of rock are consistent with the velocities of the cylindrical specimens, which were later drilled from the block. Since the dimensions of the cube are equal in all directions, a dependency of the measuring distance can be excluded. The differences in the p-wave velocities may have various reasons like variations in the mineral composition, the rock fabric or different porosities. The porosity may not only be the result of open pores but especially in crystalline rock, existing microcracks contribute to a reduced integrity on the microscale.

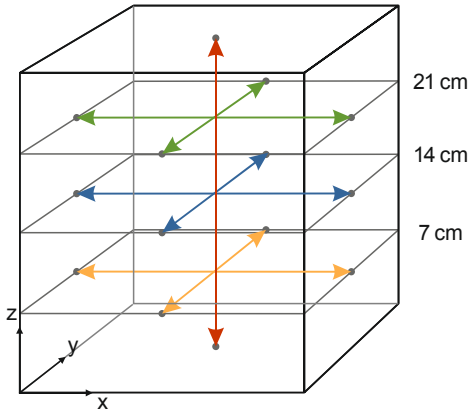

Figure 102: Schematic illustration of p-wave velocity measurements on a block of Tittling granite. Velocities were measured in x and y direction at three measuring planes (yellow, blue, green) and in z-direction (red).

Table 15: P-wave velocities in a block of Tittling granite.

x-y plane	$v_{p,x}$	$v_{p,y}$	$v_{p,z}$
cm	km/s	km/s	km/s
21	4.43	4.53	-
14	4.48	4.54	-
7	4.43	4.52	-
Mean	4.45	4.53	4.90
St.dev.	0.02	0.01	0.03

5.2.4.3 Ultrasonic pulse localization

For AE localization, a bulk p-wave velocity was calculated using different arrival times of ultrasonic pulses at known coordinates (Figure 103). The results of ultrasonic pulse localization are largely consistent with the results from p-wave velocity measurements. Particularly in Dietfurt limestone and Abtswind sandstone, the velocities are almost equal. In basalt, the pulse velocity is in accordance with the slightly higher radial velocity, whereas in Moosegg anhydrite and Laas marble, it corresponds with the mean value of the axial velocity. In diabase and Metten granite, slightly higher values were calculated compared to the measured values, whereas lower values were determined for Tittling and Flossenbürg granite. Only Posta sandstone revealed considerably lower values of about 2 km/s compared to the measured velocities with a mean of 3.1 km/s for the same samples. Therefore, the calculated values could not be used for AE localization.

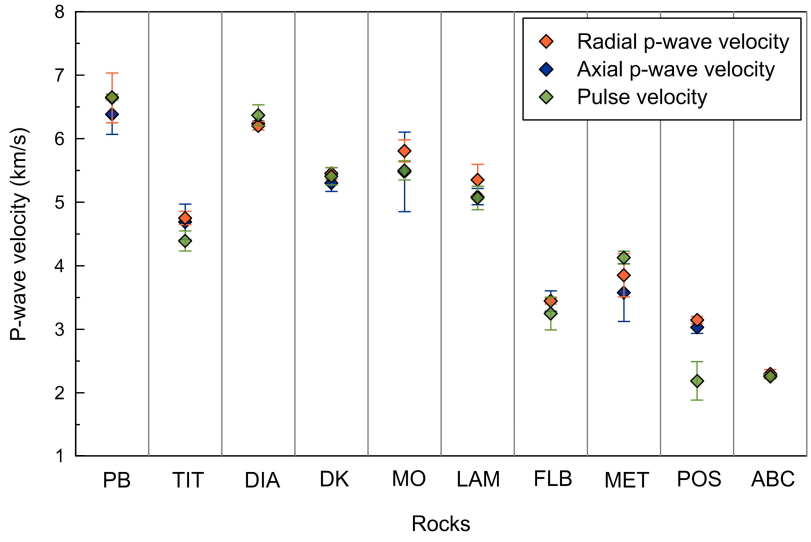

Figure 103: Comparison of the measured p-wave velocities and the calculated velocities from ultrasonic pulse coordinates.

5.2.4.4 Signal energy

An average signal energy of AE events was calculated from the events emitted until the maximum stress (Figure 104). Rocks showing a brittle failure behavior like basalt, Tittling granite, diabase and limestone revealed a high average signal energy. Brittleness means that plastic deformation is small before final collapse occurs. The energy, which is introduced by a compressional load, is thus stored within the rock without being released by the formation of microcracks. Above the crack initiation stress, the formation of single microcracks is marked by a sudden release of stored energy in the form of high-energy events. Consequently, the fine-grained, homogeneous rock types like basalt and limestone showed by far the highest signal energies.

The lowest energies were detected in marble where the applied loading energy is predominantly released by intracrystalline deformation instead of intergranular or transgranular microcracking. The rock types showing a more ductile failure behavior with a pronounced plastic deformation generally revealed lower signal energies. Lower energies also correspond with a higher number of events. This shows that the induced strain energy is partly released by the formation of microcracks in the specimen. In ductile rocks, cracking mostly releases low-energy and only few high-energy events. Only in samples of Posta sandstone, higher energy events similar to those detected in Tittling granite and diabase were detected. In the porous sandstone, high-energy events occurred during the complete loading phase. It is concluded that events emitted in the pre-failure range of loading mainly resulted from a compaction of the grains and the breaking of the siliceous cement between the grains. A distinct increase in the number of high-energy events first occurs when the peak strength was exceeded. This indicates that intragranular microcracking and the formation of major fracture planes began. The events after peak stress are not included in the results given in Figure 104.

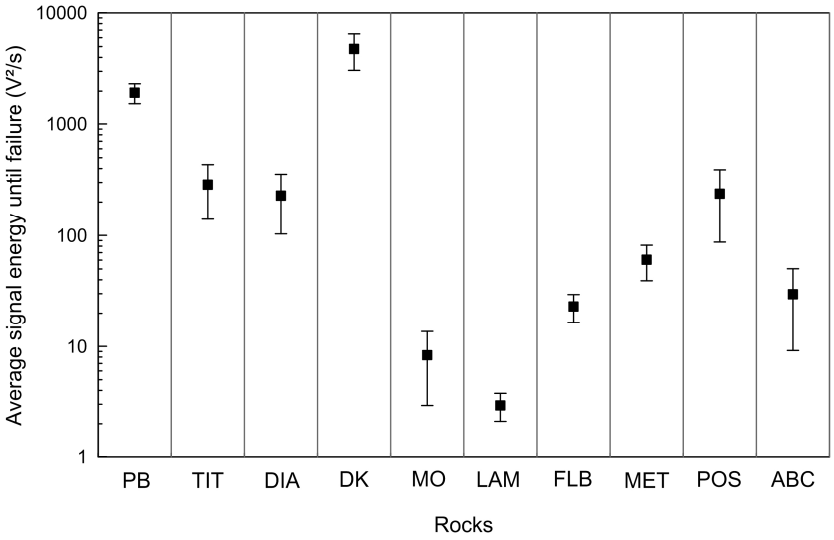

Figure 104: Average signal energy calculated from the events occurring until failure for all tested rock types.

5.2.4.5 Number of acoustic events

During uniaxial compression of the rocks, acoustic event monitoring was performed. In Figure 105, the number of AE normalized to the uniaxial compressive strength is illustrated against the mean number of events for each tested rock type. Within the different rocks, the number of events at maximum stress varied considerably. The results show two clusters of rocks with a different acoustic emission activity. The rocks of Group A showed a low total number of events and a low normalized number of events.

Apart from marble, all of those rocks (basalt, diabase, limestone) are fine-grained, massive rocks with a brittle failure behavior. They did not show a post-failure phase but a pronounced phase of elastic deformation in the pre-failure range. Except from marble, the rock types showed a very high to extremely high uniaxial compressive strength. The low cracking activity of brittle rocks can be the result of the applied strain energy, which is stored within the rocks for a long proportion of loading without the formation of new crack surfaces. As soon as the critical stress for crack initiation is exceeded, only few localized microcracks are generated. Marble is an exception in Group A, since it exhibits a mainly ductile failure behavior with a distinct post-failure phase and a pronounced plastic deformation in the pre-failure phase. At the same time, the marble specimens emitted the lowest number of events and a low normalized number of AE in the pre-failure phase. A reason might be the ability of calcite minerals to take up deformation at the atomic scale so that AE could not be detected with the applied measuring device. Twinning or twin gliding within the crystal lattice may prevent the formation of microcracks.

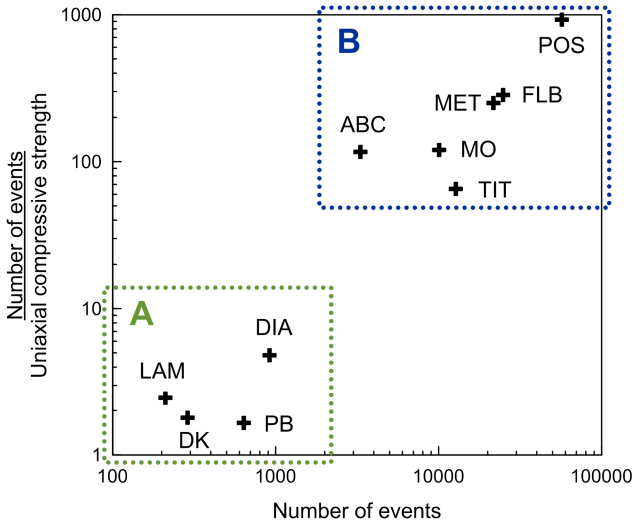

Figure 105: Number of acoustic events until strength failure during uniaxial compression tests. In brittle rocks like basalt, diabase and limestone (Group A), few events occurred, whereas more ductile rocks (Group B) emitted a high number of events. Marble and Tittling granite show an exceptional cracking behavior.

A second group of rocks, Group B, emitted a high number of events as well as a high normalized number of AE. Rocks in this group are anhydrite, sandstones and all tested granites. Except from Tittling granite, the rocks from Group B showed a distinct post-failure phase and a curvilinear stress-strain curve in the pre-failure range indicating a ductile behavior. Since the post-failure phase of the stress-strain curve is not considered in the number of events, the AE rate during pre-failure already provides information about the brittleness of rocks. In the generally ductile rocks, microcracking does not only occur at single localized spots but it is assumed that the high number of events is the result of numerous flaws and planes of weakness where crack propagation takes place. Tittling granite can be considered as an exception in this group. Although the granite does not show a distinct post-failure phase and only a small phase of plastic deformation, a high number of events was measured because of its rock structure. The granite shows larger grain sizes compared to the clearly brittle rocks as well as different elastic properties of the constituent minerals. This shows that Tittling granite is not truly brittle but shows several characteristics of a ductile material behavior.

5.3 Discussion of laboratory rock properties

In this section, the results of the rock mechanical and acoustic emission tests are discussed and a new classification scheme is proposed. The categorization is based on the characteristic rock properties and material behaviors of the analyzed rocks. A suggestion of factors determining the response of rocks to an applied stress is presented.

5.3.1 Qualitative summary of rock characteristics

The results from laboratory investigations on ten rock types allow a characterization of the rocks according to their mechanical and acoustic properties. Five groups of rocks with a similar deformation and cracking behavior were established. A qualitative summary of the characteristic properties is presented in Table 16. Group 1 includes the fine-grained, low-porosity rocks like basalt, diabase and limestone. The unweathered Tittling granite represents Group 2, the crystallized, mono-mineral rocks like marble and anhydrite are summarized in Group 3, the altered granites in Group 4 and the sandstones represent Group 5.

Table 16: Classification scheme of characteristic material behaviors, based on the mechanical and acoustic properties of the analyzed rocks. Green indicates a brittle material behavior, blue indicates a ductile behavior and grey shows an indistinct behavior.

Rock parameter	**Group 1** PB, DIA, DK	**Group 2** TIT	**Group 3** MO, LAM	**Group 4** FLB, MET	**Group 5** POS, ABC
Grain size	fine	medium	fine – medium	medium – coarse	fine – medium
Stress-strain curves	near linear	slightly curved	distinct yield	distinct yield	distinct yield
Post-failure phase	no	short	pronounced	pronounced	pronounced
Uniaxial compressive strength σ_u	extremely high – very high	very high	high	high	high – medium
Axial strain at failure/σ_u	low	low	low	high	POS: high ABC: very high
Radial strain at failure/σ_u	low	low	low	high	POS: low ABC: very high
Δ Strain at failure	high	high	low	low	low
Strain index	low	low	medium	high	POS: medium ABC: high
Crack damage	high	high	medium	low	POS: medium ABC: low
Brazilian tensile strength	high – medium	medium	medium	medium	low
P-wave velocity	high	medium	high	low	low
Average signal energy	high	high	low	medium	ABC: medium POS: high
Total number of AE	low	high	LAM: low MO: high	high	very high – high
Number of AE at failure	low	high	LAM: low MO: high	high	high

Group 1: Brittle behavior (fine-grained, low-porosity rocks)

Group 1 includes the fine-grained, low-porosity rock types PB, DIA and DK, which showed a clearly brittle deformation and failure behavior. The rock types revealed a very high to extremely high uniaxial compressive strength and the final collapse occurred explosively so that a post-failure phase was not present. A minor phase of plastic deformation in the pre-failure range is marked by a high crack damage stress above 95 %, a high difference between axial and radial strain as well as a low strain index. In the pre-failure phase, the induced loading energy is largely stored within the rock without being released by cracking. Only single microcracks occurred in the phase of unstable crack growth but those cracks released high-energy events so that the average signal energy of AE was very high. The total number of AE until failure was low, since only few microcracks initiated during the test. Most of the recorded events occurred during the final collapse of the rocks.

Group 2: Brittle behavior with ductile characteristics (unweathered granite)

Tittling granite shows a transitional behavior regarding the deformation and cracking behavior. The stress-strain curves of the granite exhibit a rather brittle failure behavior with either a short or a missing post-failure phase. Because of its heterogeneity on the grain scale and the different elastic properties of its constituent minerals, the granite revealed a lower p-wave velocity than the rocks from Group 1. Tittling granite does not show a clearly brittle material behavior, since the high normalized number of acoustic events and a high total number of AE until failure indicate the ductile characteristics of the medium-grained, low-porosity rock.

Group 3: Ductile behavior with brittle characteristics (crystallized, mono-mineral rocks)

Group 3 includes the crystallized, mono-mineral rock types anhydrite and calcite marble, with a grain size of fine to medium and a low porosity. Both rock types exhibited a transitional behavior regarding several rock properties. In general, the deformation and cracking behavior of both rocks can be classified as ductile, but there are several properties representing brittle or indistinct rock characteristics. In both rock types, a pronounced post-failure phase with a distinct phase of plastic deformation exists and there is a low ratio of axial to radial strain comparable with the strain ratios of the ductile rocks of Group 4. Furthermore, a high cracking activity and a low signal energy in anhydrite indicates a gradual and non-violent cracking mechanism. The two rock types exhibited a strong difference in the number of acoustic events. Anhydrite showed a high cracking activity during the entire loading phase, whereas marble exhibited the lowest total number of events at maximum stress. Since the stress-strain curves are largely similar in both rocks, it is assumed that plastic deformation also occurs in marble even though it is not detectable with the applied settings. Brittle fracturing with a sufficiently high event amplitude, however, is minimal during the pre-failure phase. In marble, intracrystalline deformation of the crystal structure, like twinning or lattice gliding, is thus expected as the main cracking mechanism during loading. A rock property typical for brittle rocks is the high p-wave velocity, which results from the low porosity of the crystallized rocks as well as the density and the elastic properties of anhydrite and calcite minerals. Other brittle characteristics are a low axial and radial strain at failure as well as a high tangent Young's modulus. Furthermore, the reversal of the volumetric strain curve occurs at a comparably high stress level of over 90 % in both rock types.

Group 4: Ductile behavior (weathered granites)

A pronounced post-failure deformation, low AE signal energies and a high number of acoustic events characterize the two types of altered granite. Rock mechanical and acoustic properties clearly indicate a ductile behavior with a distinct phase of unstable crack growth and a gradual dissipation of energy in the form of microcracking in the pre-failure phase. Although the mineralogy is similar, the deformation and cracking behavior as well as the mechanical properties are strongly different compared to the unweathered Tittling granite. The reduced rock quality in the weathered granites is caused by the beginning alteration and an associated deterioration of the interlocking microstructure. A low bonding strength at grain boundaries and a low strength of the alteration products can facilitate crack growth. Both rocks are characterized by a gradual, non-violent crack growth in the pre-failure and post-failure phase until final rupture.

Group 5: Ductile behavior with exceptions (sandstones)

The two different sandstones with cements of quartz and clay minerals are summarized in Group 5. The reason for a different deformation and failure behavior compared to the previously described rock types is the fabric of the clastic sedimentary rocks and a structure consisting of a framework of grains, a matrix, and an open pore space between the grains as well as the existence of a cement material. Nevertheless, some characteristics of Posta sandstone are more similar to the deformation behavior of brittle rocks like anhydrite than to the behavior of Abtswind sandstone. In accordance with the results of THURO (1998), the sandstones exhibited the lowest uniaxial compressive strength of all tested rocks. The uniaxial compressive strength and the deformation behavior of sandstones is governed by the degree of cementation and the strength of the cementing agent. A lower strength of clay minerals compared to quartz cement caused a significantly lower uniaxial compressive strength of Abtswind sandstone. In general, both rock types revealed a ductile material behavior. They showed a distinct phase of unstable crack growth in the pre-failure phase and a pronounced post-failure phase. The ratio of axial to radial strain is similar in both rocks, but while Posta sandstone exhibited a relatively low total strain, Abtswind sandstone showed an extremely high axial and radial strain.

It is expected that the ductile clay minerals in ABC allow high deformations before cracks can evolve. This becomes clear from the difference in the crack damage stress determined from the volumetric strain curve compared to the onset of a high AE activity. Although an early increase in radial strain causes an early reversal of the volumetric strain curve at about 70 %, a considerable cracking activity only begins shortly before peak stress. This indicates that the clay minerals largely respond elastically without emitting acoustic signals with a sufficiently high energy to be detected. Still, a small number of AE is recorded during compression and the number of events increases with an increasing load. Those events are assumed as cracks resulting from displacements of strong grains against each other. In the siliceous sandstone, the onset of cracking coincides with the beginning of loading and the rupture of the siliceous bonds emits acoustic signals during the whole phase of compression. A high signal energy results from the breaking of the strong and brittle quartz cement. The brittleness of quartz is the reason for some brittle characteristics like a high signal energy and a high crack damage threshold. The generally ductile material behavior of POS, however, is the result of the porous sandstone structure.

5.3.2 Factors influencing the cracking behavior of rocks

The results from uniaxial compression tests showed that every rock type exhibits a different deformation and cracking behavior, dependent on mineralogy and rock fabric. Heterogeneities resulting from variations in grain size, composition or structure are preferred locations for crack propagation. Here, particularly the factors influencing microcrack initiation, coalescence and rock strength are presented.

5.3.2.1 Grain size

The fine-grained rock types with a low porosity exhibited high to extremely high strength values and except granite, they resulted in a high crack initiation threshold above $0.6\sigma_u$. Acoustic emission testing showed only a low cracking activity in the phase of stable crack growth. In that phase, cracks are considered to result from stress concentrations at few existing heterogeneities like fossils in DK or phenocrysts in basalt and diabase. According to the theory of Griffith, the stress level of crack initiation depends on the length of the initial flaws. If only few stress raisers exist, crack growth occurs at isolated locations in the rock and a large part of the specimen needs to be broken for crack coalescence. Therefore, high stresses are necessary for crack coalescence and the onset of unstable crack growth is almost identical with the maximum rock strength. In fine-grained rocks, the existence of initial flaws with a considerable length thus influences the stress level of crack initiation. The quantity of existing and induced cracks as well as their spatial proximity to other flaws, however, strongly affects the stress level of crack damage and the maximum strength of those rocks. HATZOR & PALCHIK (1997) also found that in low-porosity rocks, individual grains that function as initial flaws have a significant influence on the crack initiation stress.

In coarser-grained rocks like Tittling granite, many stress raisers like grain boundaries or intragranular microcracks with a considerable length exist. Since those planes of weakness are expected to function as potential Griffith flaws, an increasing length of initial flaws reduces the crack initiation stress. When comparing the three tested types of granite, the medium-grained granites (TIT, MET) showed an almost similar σ_{ci} of about $0.45\sigma_u$, whereas in the coarser-grained porphyric granite (FLB), the cracking activity started with the beginning of compression. This indicates that the existence of longer grain boundaries and intragranular cracks reduces the required stress for crack initiation because few but longer flaws exist. Those act as preferential planes of weakness where stress concentrations cause crack propagation. An early onset of cracking activity was also detected in the fine to medium-grained anhydrite samples, where the cleavage planes are supposed to act as preferential stress concentrators. Although many initial flaws exist and considerable rock damage is induced during compression, the coalescence of microcracks begins at a relatively high stress level shortly before failure. It is assumed that crack initiation and crack propagation occur at a considerable number of existing flaws but preferential zones of crack interaction and coalescence do not evolve until shortly before failure. A high crack damage threshold was also determined in TIT and its homogeneous grain size distribution with a homogeneous stress distribution is expected as the reason for the late onset of crack coalescence. Without preferential zones of increased stresses, continuous fractures cannot evolve until shortly before failure.

Observations of EBERHARDT et al. (1999b) also showed a minimal influence of the mean grain size on the crack initiation level. An increasing grain size, however, significantly reduces the threshold for crack coalescence and the resulting rock strength because of a more continuous path of weakness that is available for crack propagation.

5.3.2.2 Mineralogy

The influence of the mineralogy on the deformation and cracking behavior can be evaluated when comparing the mono-mineral rock types with the polycrystalline rocks of a similar grain size. The polycrystalline Tittling granite consists of quartz, alkali feldspar, plagioclase and biotite and all minerals are characterized by different elastic properties and strengths. Under compression, the heterogeneity in the elastic mineral properties can create additional tensile stress concentrations at the grain boundaries between minerals with different elastic moduli. In granite, biotite minerals are very flexible and elastic, in contrast to the stiffer feldspar and quartz minerals. The response to an applied stress is thus controlled by the heterogeneous elastic deformations at the contacts between different constituent minerals.

In this thesis, mono-mineral rocks revealed among the highest crack initiation stresses between 0.6 and 0.7 σ_u, whereas rock types with a homogeneous grain size distribution but consisting of different minerals exhibited lower crack initiation stresses. It is supposed that the higher the difference in the elastic constants of adjacent minerals, the higher is the potential for an early onset of microcracking. This assumption can be transferred to the different structure of Posta sandstone that mainly consists of quartz and open pore space. The difference between the solid, brittle quartz and the air in the pores is very high so that an applied load causes a rearrangement of the grains. At an early stage of compression, this results in high shear forces at the grain contacts and a high AE activity. Similar observations on the influence of heterogeneous minerals properties have been obtained by TAPPONIER & BRACE (1976), EBERHARDT & STEAD (1999) and MAHABADI et al. (2014).

For the ductile rock types like anhydrite and marble, a relatively high crack damage threshold of $>0.95\,\sigma_u$ was determined from the volumetric strain curve. A similar deformation behavior of both rocks indicates that the mono-mineral composition might cause the late onset of crack coalescence. The AE activity in anhydrite showed that many low-energy microcracks evolved during loading and considerable damage is induced before crack coalescence begins. In general, unstable crack growth begins as soon as the strength of the constituent minerals is exceeded so that individual microcracks can coalesce to form continuous cracks. In a homogeneous rock mainly consisting of a single mineral species, the necessary stresses to break the mineral bridges are very similar because of the homogeneous mineral properties. Therefore, in both analyzed rocks, the maximum rock strength is reached after a short phase of unstable crack growth because the critical stress for crack coalescence is exceeded within a short stress range.

5.3.2.3 Bonding forces

The strength of the interlocking microstructure in crystalline rocks and the quality of the cementation in clastic sedimentary rocks also have an important influence on the mechanical behavior and the strength of rocks. This becomes clear from the comparison of the almost unaltered Tittling granite with the two weathered types of granite (FLB, MET), where the rock strength and the crack damage stress are considerably lower than in the unweathered granite. Beginning sericitization of feldspar and oxidation of biotite reduces the bonding forces between adjacent minerals of granite. The alteration process does not only reduce the strength of the involved minerals, microscopic analyses showed that intracrystalline cracks of all constituent minerals are widened and are partly filled with alteration products. This shows that weathering reduces the interlocking microstructure of rocks so that the rock strength as well as the onset of microcracking and crack coalescence is reduced. Especially the influence on the crack damage stress is significant. From the volumetric strain curve a low crack damage stress of about $0.7\,\sigma_u$ was determined in the weathered granites (FLB, MET), showing that the weakened bonding forces facilitate crack propagation. The gradual increase in the AE activity without a distinct increase in the number of

events indicates that true crack coalescence as breaking of rock bridges does not occur in the weathered rocks. Therefore, a clear crack damage threshold as an indicator for crack coalescence is not present in the weathered granites. The stress level determined from the volumetric strain curve is not directly followed by rock failure, instead, a disintegration of the rock takes place along existing intracrystalline and grain boundary cracks so that failure is not violent but the rocks crumble along existing cracks.

Tests of sandstone with quartz and clay cement also showed different deformation and strength characteristics resulting from the bonding forces. While cementation in POS results from grain margin dissolution and re-precipitation at the grain contacts, the clay minerals fill the pore spaces in ABC, holding the quartz minerals together. AE testing shows a similar spatial distribution of events in both rocks but still, the deformation phases are different. POS resulted in a high crack damage level over $0.9\,\sigma_u$, whereas the volumetric strain of ABC reversed at a comparably low level of about $0.7\,\sigma_u$. The differences in the crack damage stress determined from volumetric strain reversal can be attributed to the contrasting strengths of the cement material. Furthermore, the high increase in radial and axial strain of ABC indicates a high ductility of the granular sandstone structure. During this phase, the cementation cohesion from the clay minerals is exceeded and the granular structure of solid quartz is compacted without an emission of acoustic events. A major shear fracture begins to evolve as soon as the interlocking strength of neighboring quartz minerals is exceeded.

5.3.2.4 Heterogeneities

Existing flaws, microcracks and voids are well known to act as local stress raisers, where microcracks may nucleate. Minerals with a distinct cleavage or twin planes will preferably break along those planes of weakness. Therefore, the occurrence of minerals like feldspars, calcite or anhydrite will promote crack initiation, whereas a high quartz content will increase the threshold for crack initiation. Petrographic analyses showed that preexisting microcracks affect the crack initiation strength only if they are preferably oriented with respect to the loading direction.

From numerical modelling, NICKSIAR & MARTIN (2014) found that the influence of the grain size on crack initiation and rock strength can be neglected as long as the grain size distribution is uniform and the mineralogy is constant. In general, they showed that the grain size distribution had the most significant influence on crack initiation and uniaxial compressive strength. The findings in this work confirm that a variability in the grain size can reduce the threshold for crack initiation. The example of the porphyric basalt with a strong difference in the grain sizes but an extremely high strength and a high σ_{ci} above $0.6\,\sigma_u$ shows that the grain size distribution is not alone the reason for an early initiation of cracks.

6 The influence of damage and stresses on rock properties

In order to investigate the influence of stress-induced damage on rock mechanical properties, uniaxial constant loading tests were performed. Similar studies with constant compression have been conducted by LIN et al. (2004), THOMPSON et al. (2006), and FABRE & PELLET (2006). The results of constant loading tests and the results of subsequent standard uniaxial compressive tests are presented in the following sections. The detailed data is given in Appendix III.

6.1 Stress-induced damaging of rock

In this thesis, the influence of a previously applied load on different types of rock was analyzed by applying a constant stress with a simultaneous recording of the AE activity. As soon as the stresses exceed the critical tensile strength of a rock, damage in the form of microcracks is created in the rock material. To overcome the critical tensile strength in a rock, a minimum external stress level (σ_{ci}) must be applied. Uniaxial constant loading tests were carried out on five rock types with a different characteristic failure behavior. In order to induce damage, the rocks were loaded with two to four maximum stress levels between crack initiation stress and the uniaxial compressive strength. In Table 17, the applied stress conditions for the constant loading tests as well as the expected deformation and crack growth behavior are summarized. The crack initiation and crack damage stress levels, determined from the number of AE are given (in % of σ_u), except for those rocks, where the results from the volumetric or lateral strain method revealed more reliable results. In the constant loading tests, a constant force rate was applied until the required stress level was reached. The force was kept constant for 30 minutes and was then reduced to zero. During loading, the emission of acoustic events was recorded.

Table 17: Summary of the different stress levels applied in the constant loading tests and the expected deformation and cracking behavior of the tested rocks.

Rock		σ_{ci}	σ_{cd}	Stress level	Stress level	Expected deformation and cracking behavior
		%	%	MPa	%	
Flossenbürg granite	Min	41*	65*	45	51	**stable**
	Mean	**43***	**77***	60	68	**stable** (unstable)
	Max	50*	91*	75	85	**unstable** (stable)
Laas marble	Min	61	91*	60	69	**stable** (linear elastic)
	Mean	**66**	**94***	70	81	**stable**
	Max	75	99*	80	93	**stable** (unstable)
Posta sandstone	Min	38	86*	40	66	**stable** (pore closure/ compaction)
	Mean	**56**	**91***			
	Max	72	95*	50	74	**stable**
Dietfurt limestone	Min	63	97	120	74	**stable** (linear elastic)
	Mean	**71**	**98**	140	86	**stable**
	Max	81	99	160	99	**unstable** (stable)
Tittling granite	Min	43	89	120	61	**stable**
	Mean	**46**	**96**	140	72	**stable**
	Max	51	98	160	82	**stable**
				180	92	**stable, unstable**

*determined from the stress-strain curve

6.1.1 Continuing strain during constant loading

During the phase of constant load, all tested rock types exhibited a small proportion of creep deformation, where axial and radial strain continued to increase. In Figure 106, the example of a granite specimen (TIT) loaded with 180 MPa shows an increase in axial strain $\Delta\varepsilon_a$ of 0.014 and an increase in radial strain $\Delta\varepsilon_r$ of 0.006. The increasing strains during constant load are given in Figure 107 for all tested rocks. The difference between the strains after 30 minutes ($\Delta\varepsilon_{a,max}$, $\Delta\varepsilon_{r,max}$) of constant force and the strains at the beginning of constant force ($\Delta\varepsilon_{a,1}$, $\Delta\varepsilon_{r,1}$) are presented. All specimens exhibited a phase of creep deformation, where the radial strain generally increased more than the axial strain. A distinct increase in the axial strain was observed in those samples loaded beyond the crack damage threshold, like Flossenbürg and Tittling granite.

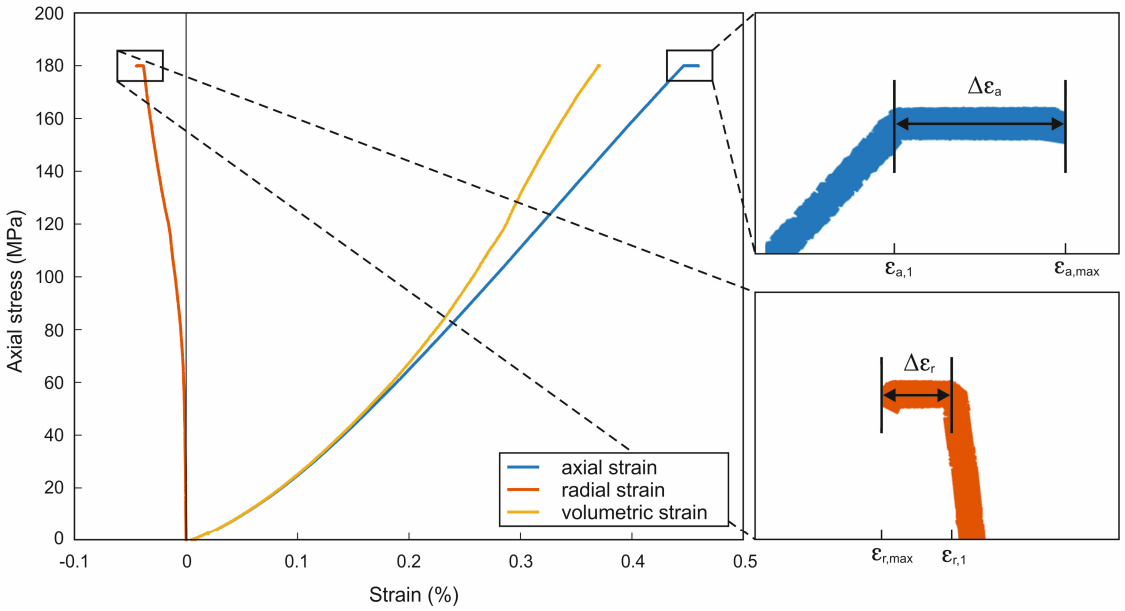

Figure 106: Continuing axial and radial strain during the phase of constant load. Illustrated is a sample of Tittling granite loaded with 180 MPa near the crack damage stress.

The continuing deformation during constant loading can have various reasons in the different rock types. In low-porosity rocks like granite or limestone, the dominant mechanism for continuing strain is proposed by DUSSEAULT & FORDHAM (1993) as the propagation of microcracks and thus an accumulation of rock damage. During the phase of stable crack growth, creep deformation stabilizes and attenuates, whereas in the phase of unstable crack growth, microcrack propagation accelerates, cracks interact and coalesce. This leads to rock failure even if the stresses are kept constant. Large radial creep deformation compared to lower axial deformation demonstrate that cracks open predominantly normal to the direction of compression. The highest radial strains of more than 10 % were recorded in most granite specimens as well as in individual specimens of Posta sandstone and marble. High creep strain in granite might result from the medium to coarse-grained texture of the rocks with long grain boundaries and intragranular cracks acting as planes of weakness, where crack propagation occurs. In Posta sandstone, the radial creep strains vary from below 5 % to above 40 %. In the high-porosity sandstone, uniaxial compression increases the density of grain packing accompanied by microcracking (DUSSEAULT & FORDHAM 1993). The differences in the radial strains might thus result from a lower degree of dense packing but an earlier and more intense formation of axial cracks.

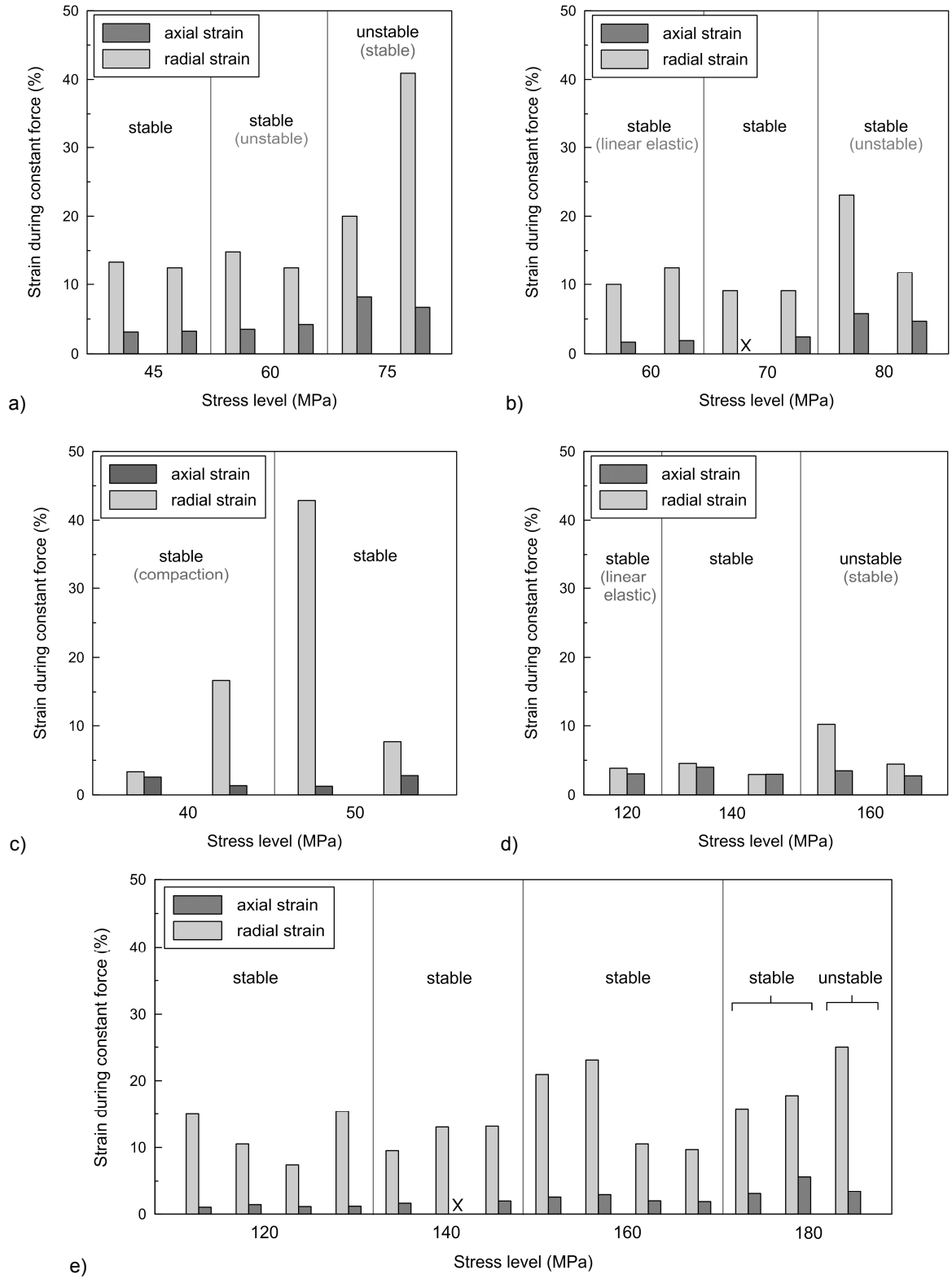

Figure 107: Continuing strain during constant loading given in percentage of the strain at the beginning of constant force. a) Flossenbürg granite, b) Laas marble, c) Posta sandstone, d) Dietfurt limestone, and e) Tittling granite.

In general, an increasing load increases the internal energy of the system. In rocks with high creep rates, the stored energy is partly released by compaction or by propagation of microcracks until a state of equilibrium is achieved. The fine-grained limestone exhibited a low increase in radial strain, which is in the same range as the axial strain. As presented in Chapter 5, the tested limestone shows a brittle material

behavior with a low radial strain and with an abrupt final collapse. During compression of brittle rocks, a large proportion of the strain energy is stored within the rock without being released by the generation of microcracks until shortly before or upon rupture. In brittle rocks, creep can therefore only occur if the stress concentrations at existing flaws and cracks exceed a characteristic stress value so that crack propagation can occur. Therefore, the low creep deformation of limestone must result from the homogeneous, fine-grained texture, where only minor heterogeneities or zones of weakness exist.

6.1.2 Acoustic activity during constant loading

In the constant loading tests, samples were loaded up to the phases of stable or unstable crack growth. According to the theory, in the phase of stable crack growth, crack propagation will stop after a certain period if the applied stresses are kept constant. The cracking behavior of the tested rocks in the phase of stable crack growth is illustrated in Figure 108 for specimens of Tittling granite. Figure 108a shows the AE activity of a specimen loaded with 120 MPa up to the phase of stable crack growth and Figure 108b shows another specimen loaded with 180 MPa near the stress level of crack damage.

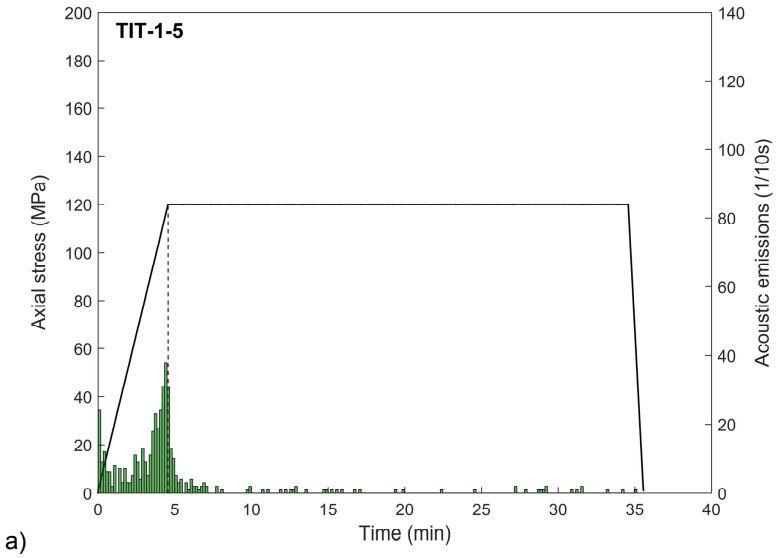

Figure 108: Stress-time curve of TIT a) preloaded with 120 MPa and b) preloaded with 180 MPa (stable crack growth). The ceasing AE activity during constant loading shows that the crack damage threshold was not exceeded in both specimens.

The number of AE versus time shows that the typical stages of crack development are present during the increase of the applied stress. As soon as the maximum stress level is reached, crack propagation and AE slowly cease and only single events occur toward the end of loading. In the specimen loaded with 120 MPa, cracking ceased very fast after the beginning of constant force and only very few events were recorded until the end of loading. In contrast, in the specimen loaded with 180 MPa, the decrease in the number of events took several minutes. After that, some events were still recorded during constant loading. The ceasing cracking activity shows that stable crack growth occurred and the crack damage threshold was not yet exceeded.

Two additional specimens of Tittling granite were loaded with 180 MPa and the results are given in Figure 109 and Figure 110. The emission of AE shows clearly that the crack damage stress was exceeded in both specimens. This is evident because the AE activity did not cease during the phase of constant loading. Both specimens showed the common phases of deformation and cracking during the phase of increasing stress, but during constant loading, the cracking activity did not cease. Instead, after an initial decrease, the number of AE increased again after several minutes. In Figure 109, some smaller peaks indicate several local interactions of cracks. A second maximum peak after about 18 minutes shows an intense propagation and coalescence of major cracks. The maximum number of recordable events was reached shortly after the second peak so that data was not available for the last period of compression. Although a high cracking activity is obvious from the high number of events, the sample did not fail during the measuring period of 30 minutes. It is expected that the sample would have failed if the applied load was held constant for a longer period.

The second specimen failed after several minutes of constant stress (Figure 110). In this specimen, the AE activity remained at a high level with the beginning of constant loading. After a short phase of high AE and cracking activity, a second peak of events occurred. An overall high number of AE was detected until the maximum number of recordable events was reached after about 13 minutes. During constant loading, unstable crack propagation and coalescence lead to the formation of major fractures and to final collapse after about 22 minutes of testing. In both illustrated specimens, the AE activity did not cease but a second increase in the event rate demonstrates that the crack damage threshold was exceeded and unstable crack propagation occurred.

The total number of AE and the number of AE during constant loading are given in Figure 111. Samples like FLB and POS as well as TIT exhibited a large number of events, whereas DK and LAM showed a very low AE activity. This was also observed during standard uniaxial compression tests, where the fine-grained limestone showed a brittle failure behavior with few events before failure. Marble revealed an exceptional cracking behavior with dislocations inside the crystal lattice instead of cracking. In general, the cracking activity and the total number of AE increased with an increasing stress level. According to the results from standard uniaxial compression tests, FLB shows a steady increase in the number of AE with an increasing stress level. In the highest stress level applied to FLB, the total number of recorded events was highest of all tested rocks.

Single specimens of other rock types also emitted a large number of events. One specimen of limestone loaded with 140 MPa, for example, emitted more events than the samples loaded with 160 MPa. This might be caused by the presence of heterogeneities in the specimen where the formation of microcracks is facilitated. A specimen of POS showed a comparatively high total number of events, which occurred mainly during the phase of increasing load when compaction and pore closure occurred. During constant loading, the number of events and thus the cracking activity was similar to the second tested sample. In TIT, there is a clear trend toward a higher number of events during constant loading with an increase of

the applied preloading stress. This is particularly evident from the two specimens loaded beyond the crack damage stress, where both, the total number of AE and the events during constant load, were considerably higher than in the samples loaded below the crack damage stress. In all analyzed rock types, a general trend towards an increasing cracking activity during constant load with an increasing stress level was observed. Although several specimens were loaded near the expected level of crack damage, only in two specimens of TIT a second increase in the cracking activity confirms that the phase of unstable crack growth was actually reached. In FLB, uniaxial compression tests showed that the phase of stable crack growth is not characterized by a distinct increase in the cracking activity but a continuous degradation of the rock structure takes place. Therefore, it is assumed that constant loading above σ_{cd} would not lead to a second increase in the cracking activity in this ductile rock type. Instead, the rock would fail after some time because of an increasing crack volume but without an additional emission of a considerable number of events.

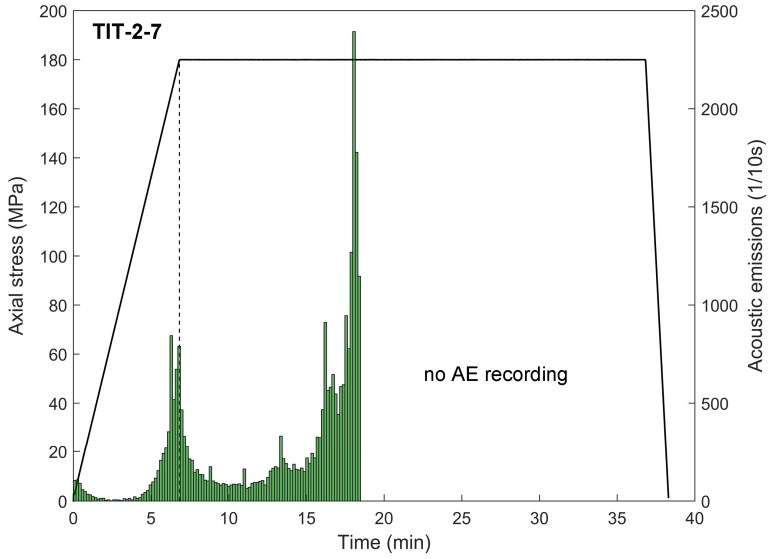

Figure 109: Stress-time curve of a specimen of Tittling granite preloaded with 180 MPa, up to the phase of unstable crack growth. The AE activity increased again after a first decrease but failure did not occur.

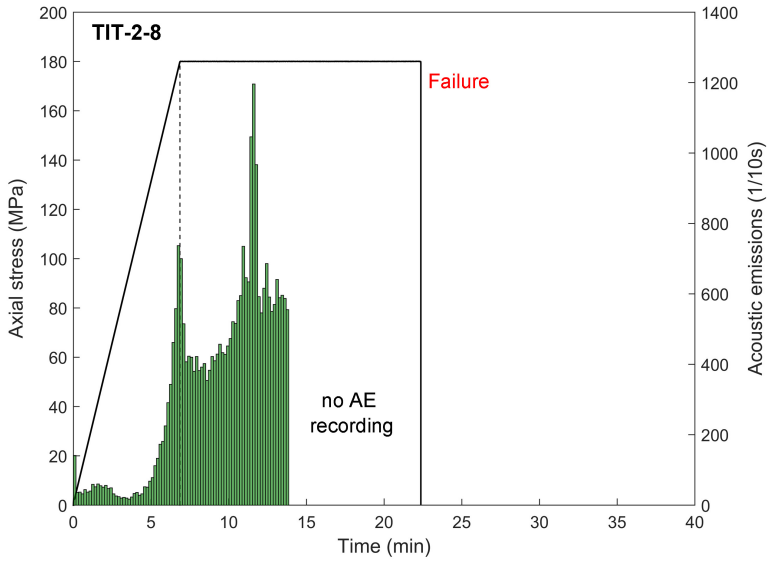

Figure 110: Stress-time curve of a specimen of Tittling granite preloaded with 180 MPa, up to the phase of unstable crack growth. The AE activity increased again after a first decrease and failure occurred after about 15 minutes.

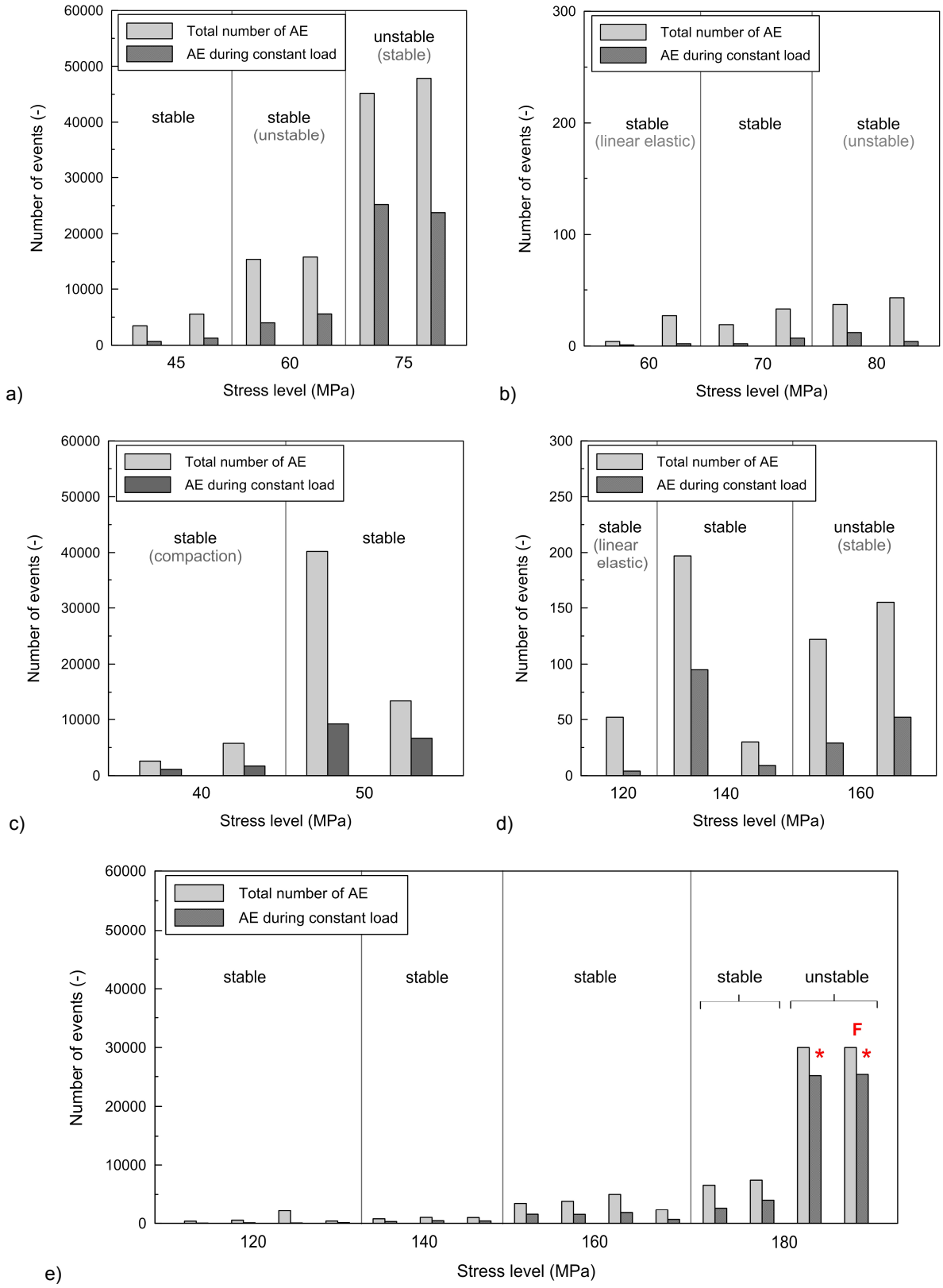

Figure 111: Comparison of the total number of AE with the number of AE during constant loading in a) Flossenbürg granite, b) Laas marble, c) Posta sandstone, d) Dietfurt limestone, and e) Tittling granite. (: the maximum number of recordable events was exceeded, F: failure during constant loading).*

6.2 Rock properties of pre-damaged rock

In this section, the rock properties of the pre-damaged rock samples are presented and the influence of the applied stress level is analyzed. Changes in the mechanical and acoustic properties before and after the application of different stress levels are illustrated for the analyzed rock types.

6.2.1 P-wave velocities

P-wave velocities were measured before and after the constant loading tests. In all types of rock, the p-wave velocities decreased after loading, indicating that damage was induced. In Figure 112, the radial p-wave velocities of two exemplary specimens of Flossenbürg and Tittling granite are illustrated. In both samples, the p-wave velocity decreased considerably after loading. FLB was loaded with 75 MPa beyond the crack damage stress and the velocity was reduced by 19 % compared to the velocity before loading. The example of TIT shows that an anisotropy had been present before loading and it was still present after the preloading test. The sample was loaded up to the phase of stable crack growth with 160 MPa and the velocity was on average reduced by 8 %.

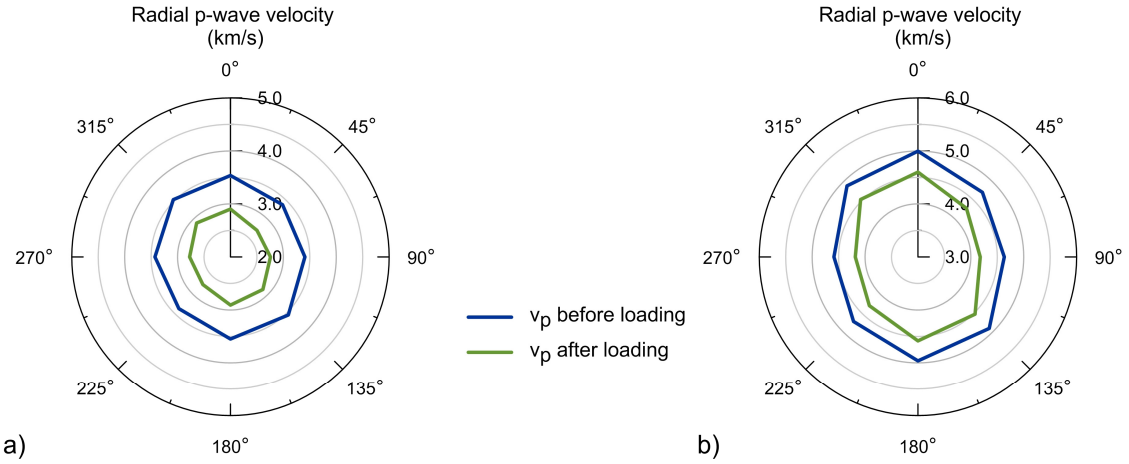

Figure 112: Examples of radial p-wave velocities before and after uniaxial constant loading of a) Flossenbürg granite (FLB-1-3) loaded with 75 MPa (unstable) and b) Tittling granite (TIT-3-1) loaded with 160 MPa (stable).

In most tested rocks, the measurement of the radial p-wave velocities in different planes revealed that the radial velocities showed a stronger decrease in the middle part than near the end planes of the specimens. The reason are the differences in radial dilatation over the length of the specimen. Restraints at the loading plates prevent a dilatation near the end planes, whereas radial strain is highest in the middle of the specimen. In axial direction, the difference in the p-wave velocity is generally lower.

Figure 113 shows the results of the decreasing p-wave velocities in axial and in radial direction for the tested rock types. In all rocks, the decrease in radial direction is higher than the decrease of the axial velocities. Except from one specimen of FLB, the decrease of the axial velocities was less than 5 % of the velocities measured before loading. In general, a relation between axial velocity decrease and the stress level was not noticed, whereas the radial velocities showed a dependency of the stress level in most cases. Specimens loaded with compressive stresses within the phase of stable crack propagation resulted in relatively low radial velocity decreases compared to specimens stressed up to the phase of unstable crack propagation. In those samples, the velocity decrease was significantly higher.

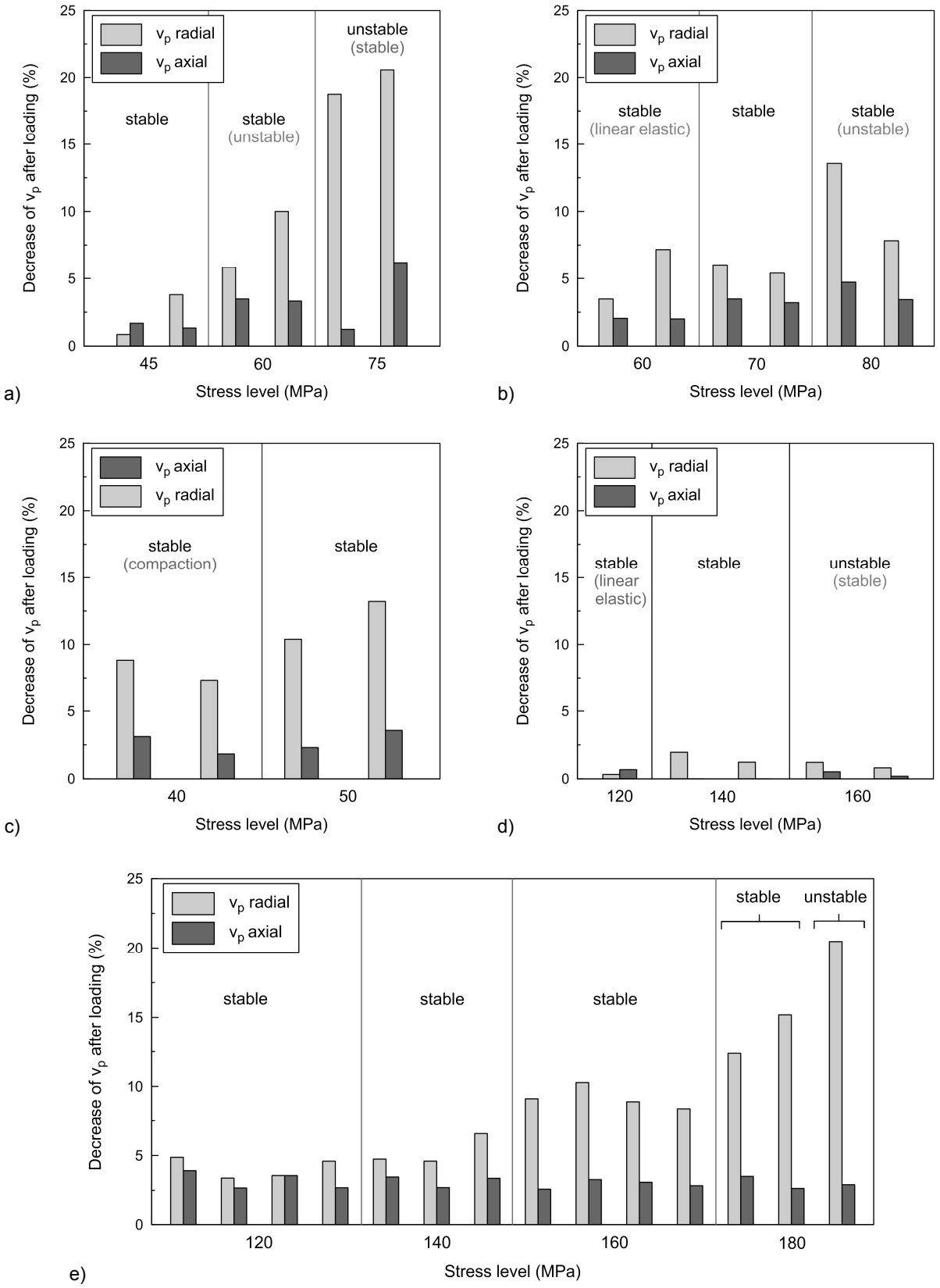

Figure 113: Comparison of the decrease in axial and radial p-wave velocities after constant loading up to different stress levels. Illustrated is the difference in the velocity before and after loading of a) Flossenbürg granite, b) Laas marble, c) Posta sandstone, d) Dietfurt limestone, and e) Tittling granite.

In Flossenbürg granite, one stress level was set below the crack damage stress, a second was set at the transition between stable and unstable crack propagation and the highest stress level was set above the crack damage threshold. The transition between stable and unstable crack propagation is clear from a distinct reduction of the radial velocity in the samples loaded with 75 MPa. The results show that the stress level of 60 MPa did not exceed the crack damage stress but stable crack growth occurred. In Laas marble, two specimens were loaded with 80 MPa near the crack damage threshold. One of the tested samples showed a decrease in the radial velocity of about 14 %, whereas the decrease in the second specimen was almost similar to the changes in the velocity from the lower stress levels. This indicates that the first sample may actually have reached the crack damage stress, whereas the crack damage strength of the second sample was higher than the applied stress level. In Posta sandstone, the applied load was not high enough to reach the crack damage threshold and the decrease in the radial velocity was reduced only little between lower and higher stress level. Compared to the other tested rocks, Dietfurt limestone showed almost no decrease in both measuring directions. The reason might be the brittle failure behavior of the limestone and a crack damage threshold of almost 100 %. Two specimens of limestone were loaded up to about 99 % of the maximum stress but still, the p-wave velocities were nearly unchanged, indicating that almost no cracks were formed until shortly before failure. The samples of Tittling granite were loaded with four different stress levels, where three levels were set in the stage of stable crack propagation and the fourth was set at the transition to unstable crack propagation. The results in Figure 113 show that the radial velocities decreased with an increasing load. The sample loaded beyond the crack damage threshold showed a considerable decrease. In the two additional samples loaded with 180 MPa, the decrease in the velocity was already higher than in the stress level of 160 MPa because of an increasing damage resulting from the progressive propagation of cracks.

The clear influence of a preload on the p-wave velocity is directly associated with the accuracy of acoustic event localization. Particularly the increasing difference between axial and radial velocity has a major influence on the localization accuracy, since a mean p-wave velocity for the whole specimen is used for localization. The localization error is examined by setting sonic pulses with known coordinates and known times of origin before and after the preloading test. From the different arrival times, a back-calculation is performed, resulting in a bulk p-wave velocity for the rock specimen. In Figure 114, the measured p-wave velocities and the velocity determined from the back-calculation of pulse coordinates are illustrated for three samples of Flossenbürg granite. The diagram shows the differences in measured and calculated p-wave velocity before and after loading.

In all intact specimens of Flossenbürg granite, the radial velocity is generally higher than the axial and the calculated velocity. When comparing the velocities before and after compression, the difference between measured and calculated velocity is relatively small for the stress level of 45 MPa. With an increasing load, all velocities are clearly reduced, but in general, the radial velocity decreased more than the axial velocity. When the crack damage stress is exceeded with the stress level of 75 MPa, the difference between axial and radial velocity increases significantly. The calculated velocity is between radial and axial velocity but is more in accordance with the lower radial velocity. With an increasing stress level, the localization accuracy is reduced because of an increasing velocity anisotropy. Together with an overall increase in the microcrack porosity, the localization of microcracks becomes more erroneous with an increasing rock damage. A comparison of localization errors before and after preloading, however, did not reveal a considerable difference, since only the suitable signals were used for localization. Nevertheless, an increasing error with increasing rock damage must be taken into account, if all recorded events are considered.

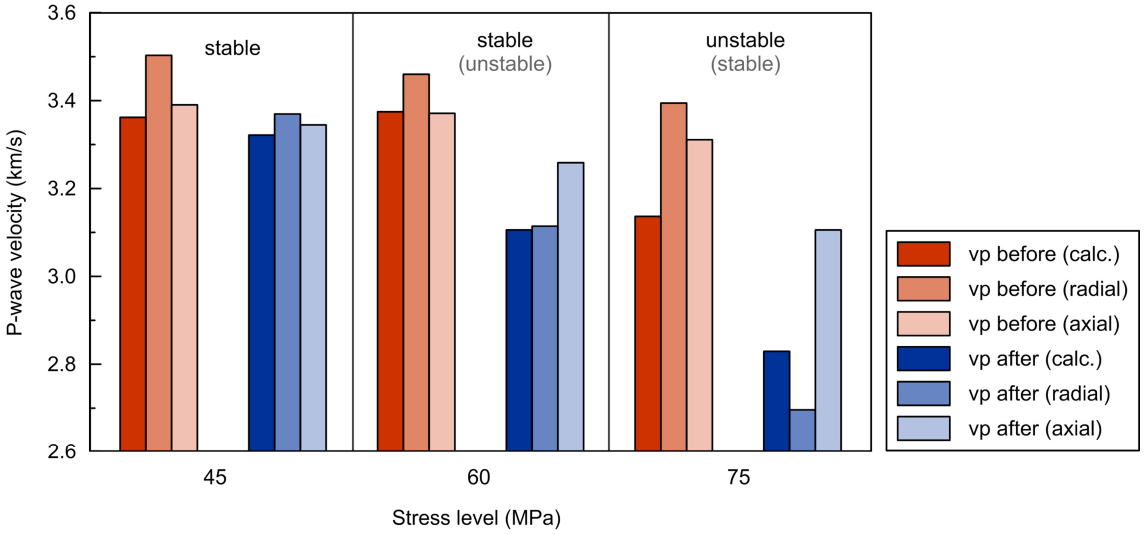

Figure 114: Comparison of back-calculated p-wave velocities and measured radial and axial velocities of three specimens of Flossenbürg granite (FLB-1-4, FLB-1-5 and FLB-1-6) before and after uniaxial constant loading with increasing stress levels.

6.2.2 Tangent Young's modulus

The tangent Young's modulus was determined from the stress-strain curve in the first preloading test and from the second loading test, where the rocks were stressed to final rupture. In Figure 115, the stress-strain curves of the preloading test and the subsequent uniaxial compression test of a Flossenbürg granite are given. The stress-strain curves show that the slopes of both axial and radial strain clearly change after the preloading phase. The axial strain curve becomes steeper, whereas the gradient of the radial strain curve generally decreases. A distinct bend can be observed in the radial strain curve at about 25 MPa, where the radial strain increases considerably. Then, the slope decreases and increases again before an accumulation of major damage again reduces the slope of the curve. A similar deformation behavior was observed in most preloaded specimens.

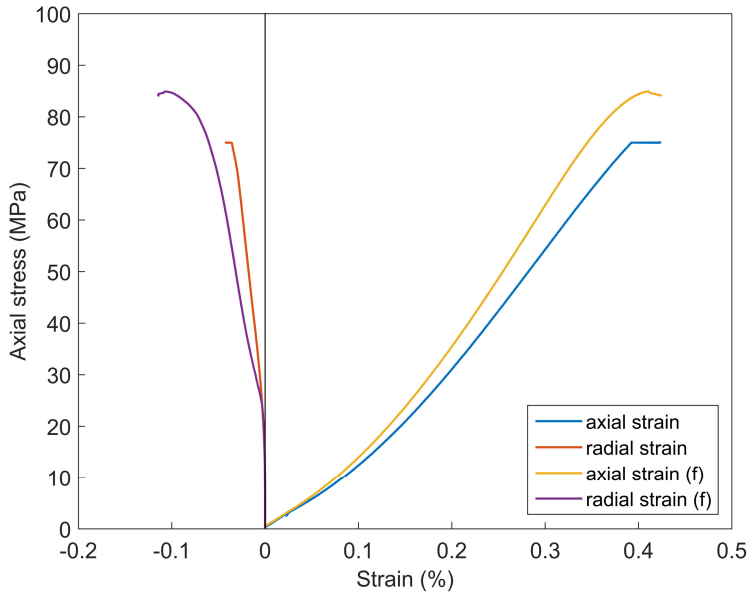

Figure 115: Example of stress-strain curves of Flossenbürg granite (FLB-1-3) from the constant loading tests (blue and orange) and the uniaxial compression tests until failure (yellow and purple, marked with f). The slopes of axial and radial strain change after preloading.

The change in the axial tangent Young's modulus ΔE_T is calculated as the change of the slope of the second loading compared to the preloading phase. The results in Figure 116 show the difference in percentage of the initial tangent Young's modulus. In general, the results show that the axial tangent Young's modulus increases after preloading. Only in the porous Posta sandstone, the axial stiffness did not show a considerable change. Flossenbürg granite revealed the largest increase of up to 22 % in the lowest preloading level. The high increase in the axial stiffness is certainly due to the effect of weathering, which enhances the compaction of the sample because of a loosened rock texture.

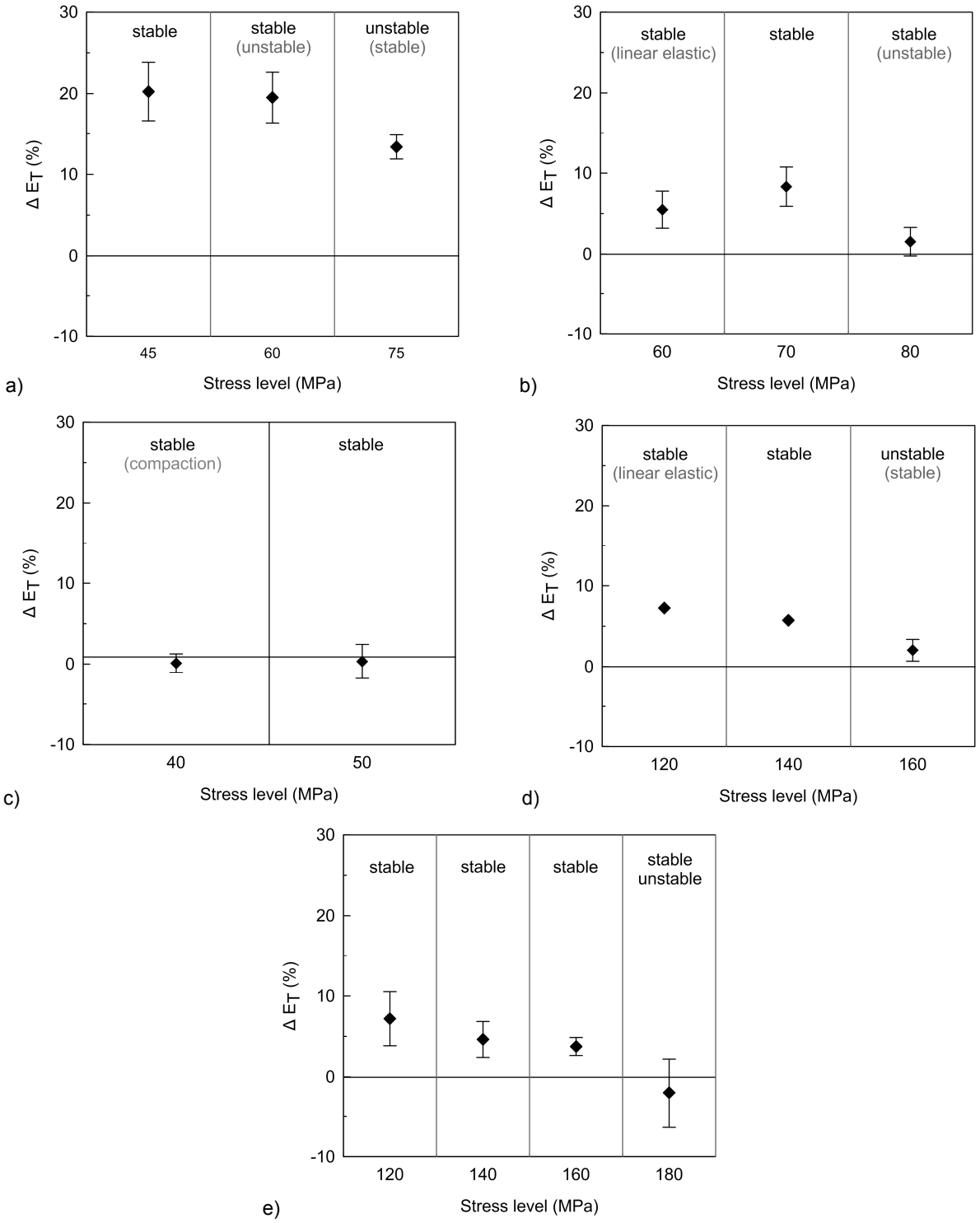

Figure 116: Axial tangent Young's modulus, given as the difference between second and first loading in percentage of the initial modulus. a) FLB, b) LAM, c) POS, d) DK and d) TIT.

The results of marble, limestone and Tittling granite showed a smaller increase with maxima of about 10 %. The increase in tangent Young's modulus is proportional to the stress level of the previously applied stress. This trend becomes particularly clear from the results of Flossenbürg and Tittling granite as well as from Dietfurt limestone. Two samples of Laas marble were loaded with a stress level between elastic deformation and stable crack growth and the lower increase compared to the next stress level indicates that the stress level of at least one of the specimens might not have exceeded the crack initiation stress. As the axial stiffness increases up to the phase of stable crack growth, it decreases because of additionally induced damage. The specimens of Tittling granite, loaded with a stress level above the crack damage threshold even showed a decrease in the axial modulus. This shows that the axial stiffness of samples containing considerable damage is reduced because of a beginning disintegration of the rock.

6.2.3 Uniaxial compressive strength

Standard uniaxial compressive tests were carried out on the preloaded samples and the complete stress-strain curve was recorded. In Figure 117, the uniaxial compressive strength of Tittling granite is illustrated for each stress level. Most samples were loaded up to a stress level where stable crack growth occurs and two of the three specimens loaded with 180 MPa were definitely loaded beyond the crack damage stress. The onset of unstable crack growth in two specimens loaded with 180 MPa was observed from the acoustic event rate (see Subsection 6.2.4). One of the specimens loaded beyond the crack damage stress did not fail during constant loading although a considerable cracking activity was recorded. In the second loading, the sample revealed a uniaxial compressive strength of 195 MPa, which is within the standard deviation for Tittling granite. One specimen failed at 180 MPa after several minutes of constant loading and it is clear that the crack damage threshold was reached with the applied stress level. The average uniaxial compressive strength, given in Figure 117, shows a decrease of the strength in those specimens, where the crack damage stress was exceeded in the constant loading test. The specimens loaded with 180 MPa show a high variation because the crack damage threshold was only reached in two of the three samples. In Tittling granite, the average crack damage level is at about 96 % of the uniaxial compressive strength and is between 177 and 195 MPa, with a mean of 198.6 MPa.

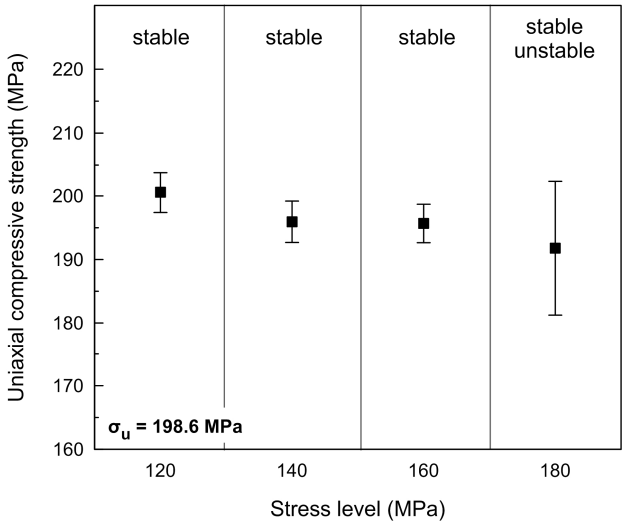

Figure 117: Average uniaxial compressive strength of preloaded samples of Tittling granite. The samples loaded beyond the crack damage stress show a considerable decrease of the rock strength compared to the average uniaxial compressive strength of undamaged samples of 198.6 MPa.

The results show that a clear decrease of the compressive strength in reloading is only observed when the crack damage stress is exceeded before. This is in agreement with the assumption that the crack damage stress corresponds with the long-term laboratory strength of rocks (BIENIAWSKI 1967). The maximum decrease of the ultimate strength resulting from an accumulated damage is thus the stress level of crack damage. In the tested rocks, the maximum reduction of the strength was 9.4 % of the average uniaxial compressive strength. The results from other rock types did not show a significant reduction of the uniaxial compressive strength because the crack damage threshold was not clearly exceeded with the applied stress levels.

6.2.4 Acoustic Emission

When comparing the AE activity during initial and second loading, a significant difference becomes obvious. In the preloading test, the onset of AE marks the crack initiation threshold, whereas in the second loading test, the onset of AE varies considerably. It largely coincides with the previous applied stress level instead of the crack initiation threshold. The delayed onset of AE corresponding with the previously applied load is known as the Kaiser effect (KAISER 1950). In Figure 118, the Kaiser effect is illustrated in samples of Tittling granite that were loaded with different stress levels. With the stress levels of 140 MPa and 160 MPa, stable crack growth occurred during the first loading test, whereas the sample loaded with 180 MPa was loaded near the crack damage stress. The samples with a lower preload show clearly that the emission of acoustic events begins shortly before the previously applied stress level is exceeded.

According to the theory, the onset of AE begins when the previously applied stress is exceeded. YOSHIKAWA & MOGI (1989) also noted the beginning of AE activity below the memorized stress and they suggest that this phenomenon may be caused by frictional sliding along existing crack surfaces. When the previous stress is exceeded, events are emitted because of a renewed crack growth. The sample loaded with 180 MPa does not show a clear match between preload and onset of AE. Instead, crack initiation begins at about 130 MPa and thus at a lower stress levels than in the samples with a lower preloading stress. This shows that the Kaiser effect can mask the first onset of cracking but the beginning of crack interaction is still present in the AE activity. In the samples of Posta sandstone, the Kaiser effect was most clearly observable. In the first loading of the sandstone, AE began right after the beginning of compression and in the preloaded specimens, a distinct delay of the beginning AE activity was present. Also in Flossenbürg granite, the Kaiser effect was clearly observable, whereas in Dietfurt limestone, it could not be determined because, anyway, only few events occur before final failure. The same was observed in Laas marble, where very few events occurred before the samples collapsed and thus, no significant change in the AE activity was recognized between the standard uniaxial compression tests and the test on preloaded samples.

For the samples loaded beyond the crack initiation stress, the occurrence of the Kaiser effect does not allow the determination of the initial crack initiation stress but reveals the previous maximum stress. The Kaiser effect is observable, as soon as a permanent plastic deformation and thus, the formation of microcracks begins. When the crack damage stress is exceeded, the phenomenon of the Kaiser effect can no longer be observed. Similar findings have been made by KURITA & FUJII (1979) and LI & NORDLUND (1993b) who found that the Kaiser effect becomes less pronounced, the closer the previous stress is to the uniaxial compressive strength of the rock. They define the ratio of AE onset stress to the previous maximum stress as the “felicity ratio FR”. Before the formation of microcracks begins, the felicity ratio is 1.0 and it decreases with increasing preload. At a preload similar to the uniaxial compressive stress, it decreases to zero (LAVROV 2003).

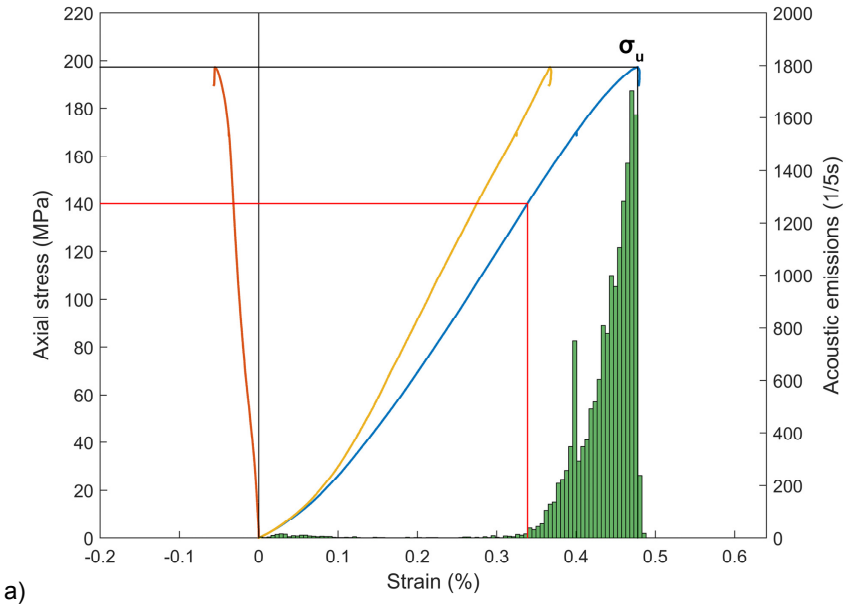

a)

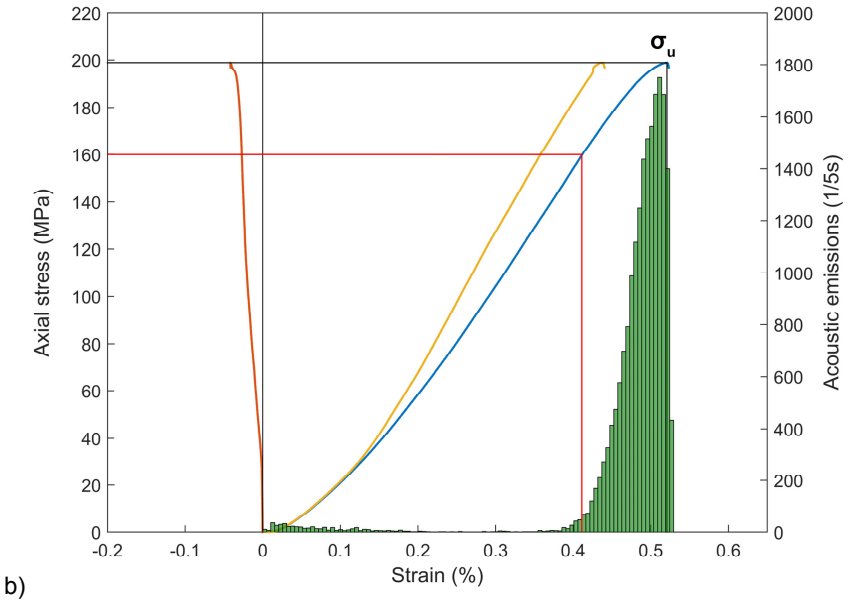

b)

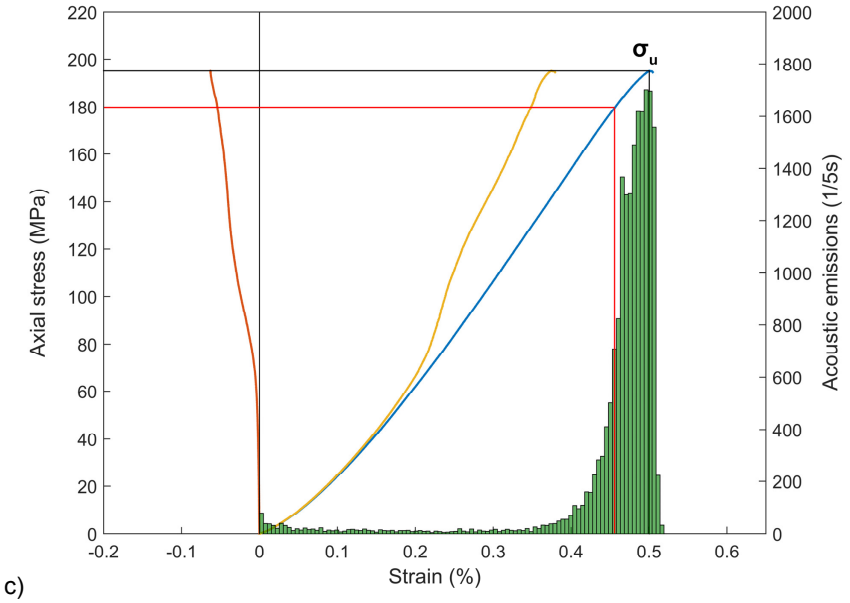

c)

Figure 118: Stress-strain curves of Tittling granite preloaded with a stress level (red line) of a) 140 MPa (TIT-2-1), b) 160 MPa (TIT-2-5) and c) 180 MPa (TIT-2-7). Below the crack damage stress, AE begins when the previous load is exceeded (Kaiser effect).

The felicity ratios determined for Tittling granite, Flossenbürg granite and Posta sandstone for the different stress levels are given in Figure 119. The felicity ratio is a measure for the rock quality, where a flat curve represents a low quality rock and a steep curve represents a high quality rock type. This becomes clear when comparing the steep curve of the fresh Tittling granite and the flat curve of the altered Flossenbürg granite.

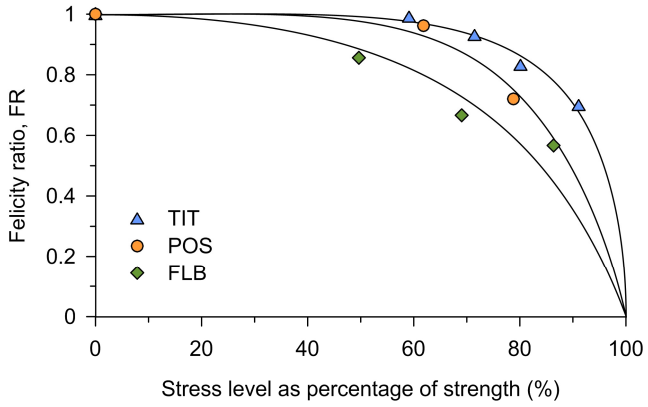

Figure 119: Felicity ratios (AE onset stress/previous maximum stress) of Tittling granite (TIT), Posta sandstone (POS) and Flossenbürg granite (FLB) determined for the different stress levels.

6.2.5 Petrographic analysis of microcracks

Petrographic analysis of microcracks was performed on Tittling granite, Posta sandstone and Pechbrunn basalt. The microcracks were colored with fluorescent resin so that they were visible under UV light. A qualitative crack analysis gives information about a preferred occurrence of cracks in different minerals and a preferred orientation with respect to the loading direction. An overlay of the fluorescent composite image was thus added to the composite image under crossed polarizers allowing a clear assignment of microcracks to minerals or grain boundaries. A quantitative crack analysis was performed with an image processing tool (see Section 0) using sections of fluorescent composite images. For each rock type, a thin section was prepared from an intact sample as reference.

6.2.5.1 Tittling granite

In the untested sample of Tittling granite, microcracks and voids are already present at grain boundaries and within the minerals (Figure 120). In feldspar, a diffuse network of irregular intragranular cracks, following cleavage planes and twin lamellae, as well as grain boundary cracks exists. The twin microcracks are particularly associated with polysynthetic twin lamellae, microcline grid patterns (b) or the suture of Karlsbad twins. Most of the fluorescent resin intruded altered feldspars, where the resin is diffusely distributed within the minerals (a, c). Several healed cracks were observed, which are either intragranular or transgranular in more than one grain (b). Biotite minerals are largely free of any microcracks, whereas in quartz, few localized high aspect ratio cracks as well as healed and closed cracks are present. Closed, inactive cracks were observed in all orientations from horizontal to vertical. A preferred orientation of all preexisting cracks is present at angles between 60 and 120° with respect to the vertical axis (see Figure 121).

Additional samples loaded with 140, 160 and 180 MPa were analyzed using image processing tools. Since many microcracks interact and form complex crack networks instead of individual microcracks, the calculation of length and orientation of the total crack area was not reasonable. From the fluorescent images, the crack network was filtered according to the procedure described in Section 3.5. Only elongated shapes with a high aspect ratio were used for the analysis. Because of those restrictions, not all existing microcracks are included in the analysis. Particularly grain boundary cracks are excluded if they surround a whole grain and thus show a circular shape equivalent to the grain shape.

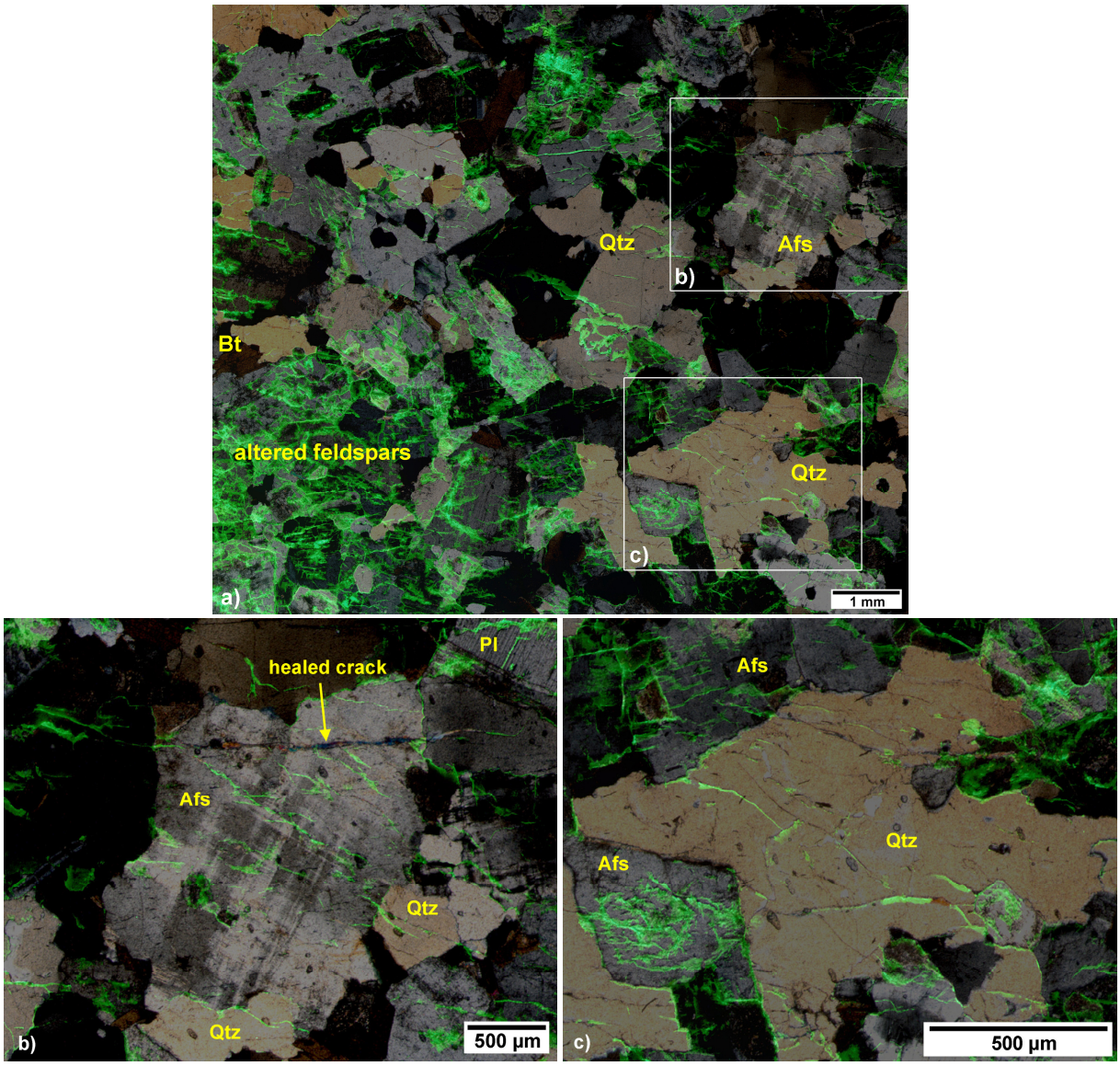

Figure 120: Microcracks in an untested sample of Tittling granite (TIT-1). a) Fluorescent resin mainly intruded altered feldspars. b) Open microcracks following cleavage planes or twin lamellae and healed cracks. c) Few localized high aspect ratio cracks occur in quartz.

In Table 18, the total crack area and the analyzed crack area are given for the applied stress levels. The total crack area is between 4.6 and 22.1 % and the analyzed crack area in percentage of the total crack area is between 4.4 and 28.3 %. The total crack area is strongly dependent on the mineral content in the selected area of the thin section. A higher percentage of feldspar, for example, increases the total crack area because of many intragranular cracks that are present along the cleavage and twin planes. A high percentage of quartz and biotite, however, reduces the total crack area because only few but clearly

localized cracks occur in quartz and almost no cracks were observed in biotite. There is a negative correlation between total crack area and analyzed crack area, indicating that the denser the crack network, the lower is the number of clearly defined microcracks. A clear relationship between total crack area and applied stress level does not exist. The qualitative image analysis showed that only the second sample loaded with 180 MPa exceeded the crack damage threshold and beginning crack coalescence took place. Although the quartz content in the analyzed section is relatively high, image analysis revealed the highest total crack area of all tested samples. An increasing rock damage, thus, also becomes clear from the image analysis.

Table 18: Stress levels applied to samples of Tittling granite and the resulting crack area determined from microcrack analysis of fluorescent thin sections. Q: Quartz, F: Feldspar, B: Biotite

Stress level	Stress level	Expected crack growth behavior	Mineralogy	Total crack area	Analyzed crack area
MPa	%		%	%	%
0	0	none	Q: 38, F: 55, B: 7	20.5	4.4
140	72	stable	Q: 42, F: 49, B: 9	12.6	13.5
			Q: 25, F: 68, B: 7	5.8	19.0
			Q: 29, F: 62, B: 9	19.6	5.6
160	82	stable	Q: 34, F: 57, B: 9	13.6	10.3
			Q: 46, F: 50, B: 4	4.6	28.3
180	92	stable	Q: 20, F: 73, B: 7	17.2	6.4
		unstable	Q: 27, F: 64, B: 9	22.1	5.9

The orientation of the analyzed cracks for the untested and tested sample is given in Figure 121. In the intact sample, only a small number of cracks could be used for image analysis but the preferred horizontal orientation noticed from the qualitative analysis also becomes clear from the rose diagram. Almost no vertical cracks were detected but many cracks are aligned at a high angle with respect to the vertical axis. Two sets of almost horizontal crack orientations dominate, which are aligned at angles of about 10 to 20° and 190 to 200° from the horizontal. Both sets of preexisting cracks can also be found in the preloaded samples. Particularly in samples 3, 6 and 8, the two sets of microcracks prevail. In samples 2, 4, 5 and 7, the two sets of cracks also occur but they do not represent the dominant orientations. Instead, additional cracks oriented at angles of 70 to 80° and 110 to 125° are present. In samples 2 and 5, no dominant crack orientation was noticed, whereas the 70-80° orientation dominates in sample 4. In sample 7, the orientation of 110-125° is most pronounced. Those additional directions are also present in samples 3, 6 and 8.

Figure 122 shows a sample loaded with 180 MPa (Sample 8 in Figure 121), where the phase of unstable crack growth was reached. In the feldspar minerals, the typical crack network exists, where cracks mainly follow cleavage planes and twin lamellae. Both plagioclase and alkali feldspar show beginning alteration, which is present in areas of sericitization in several minerals (Figure 122c). Those altered areas are mostly fully surrounded by cracks but only few intragranular or transgranular cracks were observed in the alteration products. In largely altered feldspar, a large number of indistinct cracks cross the minerals (Figure 122c). Similar to the fine sericite, no intragranular cracks occur in biotite minerals and only few grain boundary cracks are present. When neglecting the low aspect ratio cavities within feldspar minerals, two prevailing sets of microcrack orientations are apparent in the preloaded sample, which coincide with the results from the image analysis.

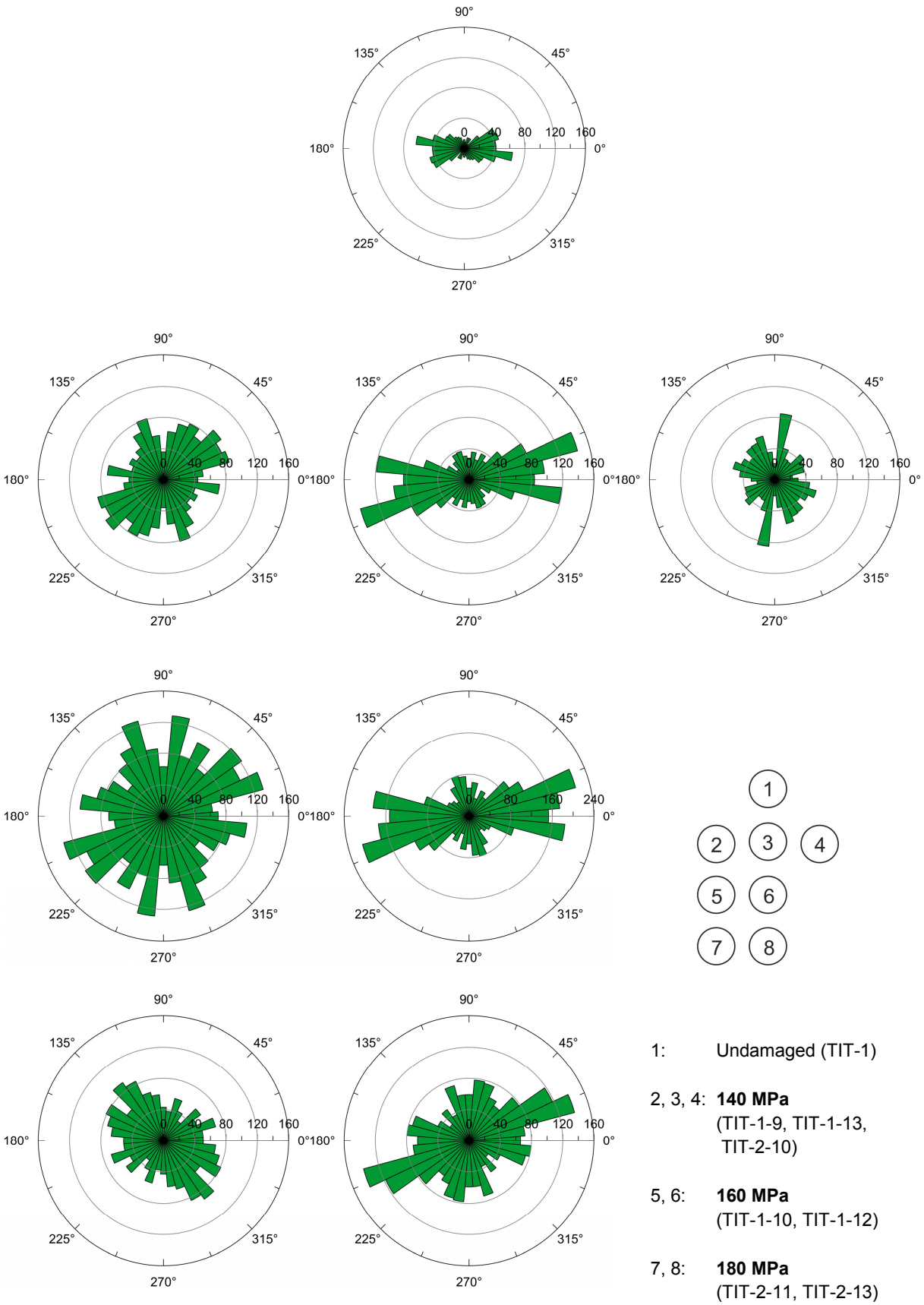

Figure 121: Rose diagrams showing the orientation of microcracks in Tittling granite of one undamaged sample and samples loaded with 140, 160 and 180 MPa. Orientations are given as the inclination of the Feret diameter with respect to the horizontal.

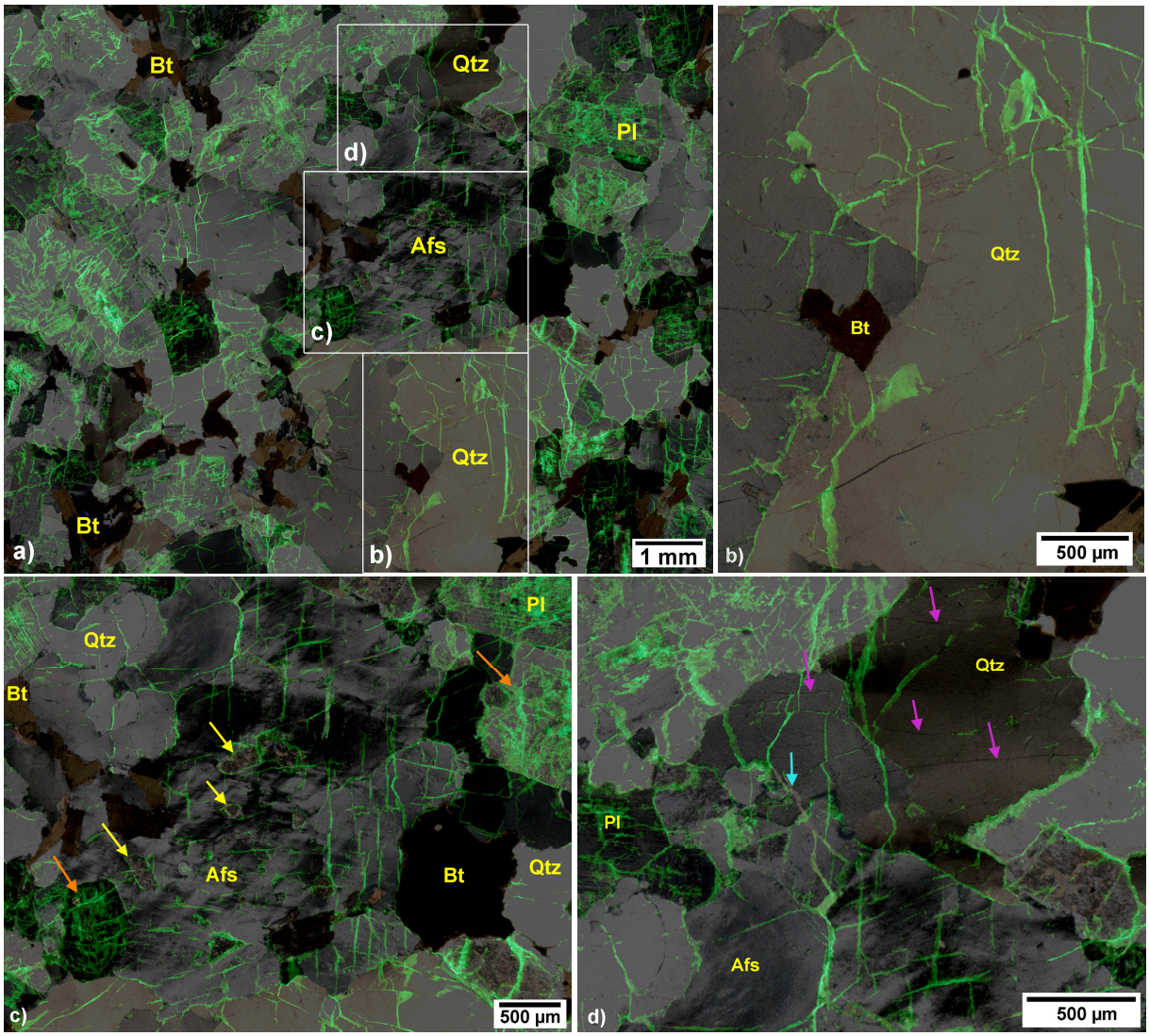

Figure 122: Tittling granite loaded with 180 MPa (TIT-2-13). a) A high total crack area indicates that σ_{cd} was exceeded. b) Vertical stress-induced cracks and biotite acting as stress concentrators for cracks. c) Intergranular cracks surrounding sericite alteration in alkali feldspar (yellow arrows). Fully altered feldspar crossed by a diffuse crack network (orange). d) Horizontal, preexisting cracks are closed (pink), vertical cracks opened or evolved during loading and racks also formed along healed cracks (blue). The applied load was vertical.

In the tested sample of Tittling granite, similar sets of cracks occur, where one group coincides with the preexisting crack orientations in the untested sample. Those cracks are mostly short, some are closed and they are usually associated with an additional set of axial fractures. The cracks with the longest extent are vertical cracks parallel to the loading direction (Figure 122b, c). Those cracks are, however, not apparent in the results from image analysis because most of the axial cracks are connected with cracks of different orientations. The axial cracks mainly occur as intragranular, transgranular fractures or as grain boundary cracks, which extend in adjacent minerals. Only few closed vertical cracks could be found because on the one hand, only few axial cracks existed before loading and on the other hand, it is supposed that the existing axial cracks opened during compression.

The preexisting horizontal cracks are often connected by axial tensile cracks so that the axial cracks represent crack bridges. The combination of both crack sets causes little crack steps so that the compound fractures show the shape of a staircase (Figure 122b, d). The phenomenon of axial cracks and load-normal cracks forming steps was also observed on fault surfaces by PENG & JOHNSON (1972).

Other major tensile cracks show a number of short shear cracks branching from the main tensile fracture (Figure 122). The branching of cracks and the formation of crack bridges demonstrate that the crack damage stress was exceeded in the represented sample because crack coalescence was observed.

In Tittling granite, a general tendency of microcrack initiation at the corners of minerals rather than at their straight boundaries was observed so that in neighboring minerals with different elastic properties, axial tensile cracks and load-normal shear cracks evolve. In Figure 122b, the corners of a biotite mineral act as stress raisers where cracks start to propagate in the adjacent quartz minerals. TAPPONIER & BRACE (1976) also observed that axial cracks initiate from low angle grain boundaries and horizontal cracks initiate from grain boundaries oriented at a high angle with respect to the maximum stress. In uniaxial compression tests on plaster samples, LAJTAI & LAJTAI (1974) found similar sets of orthogonal fractures, extending from the corners of voids independent of their shape and orientation. In their study, tensile fractures extended in the direction of maximum compression and a second set oriented perpendicular to the maximum compression was observed, which is described as a set of load-normal shear fractures. In the loaded sample of Tittling granite, no intragranular cracks were present in biotite but cracks extend in adjacent minerals from the grain boundaries of biotite minerals. This is also in accordance with the findings of TAPPONIER & BRACE (1976), who found that plastic slip in biotite acts as an important source of major cracks in the surrounding quartz and feldspar minerals. They conclude that the occurrence of minerals, which are capable of plastic slip or with an unusually low or unusually high elastic modulus relative to the main constituents may determine the strength of brittle rock.

6.2.5.2 Posta sandstone

Five fluorescent thin sections of Posta sandstone were analyzed, including one undamaged sample as a reference and four samples loaded with different stress levels. From the fluorescent images, the open pore space was calculated and the results are given in Table 19. The calculated pore space of the untested sample is 24.5 % and is thus slightly higher than the porosity of 22 %, which was determined experimentally by SCHALLHAMMER (2014). Since grain size and packing is not uniform within the sandstone, the difference is within the natural variability. The variability can also be observed within the sample loaded with 40 MPa, which revealed the highest open pore space of 35 % (Figure 123). The sample shows a distinct area of densely packed grains in the lower part of the analyzed section and a less densely packed area in the central part.

Table 19: Open pore space determined from fluorescent thin section analysis for samples of Posta sandstone.

Stress level MPa	Stress level % of σ_u	Expected crack growth behavior	Open pore space %
0	0	none	24.5
22	37	pore closure/linear elastic	21.6
35	59	linear elastic/stable	24.6
40	67	stable	35.0
50	87	stable/unstable	26.1

In all of the tested sandstone samples, only a minor occurrence of intragranular cracks was observed so that the fluorescent areas only show open pores and open grain boundaries. Acoustic emission testing showed that most of the compaction displacement in the pre-failure phase of compression occurred at the upper and lower ends of the cylinder, whereas almost no events were localized in the central part of

the sample. In the sandstone, shear planes only start to develop when the peak stress is reached. With the beginning of the post-failure phase, major fractures also form in the central part of the rock. This phenomenon was also observed by BAUD et al. (2004), who noted discrete compaction bands in the lower and upper part of the cylinder of different types of porous sandstone. The compaction bands show a high crack density extending over several grains, where the grains are crushed and axial cracking may occur. Outside the compaction zone, no or only little localized damage was observed (BAUD et al. 2004). The analyzed thin sections of Posta sandstone were taken from the center of the rock specimen, where the formation of distinct shear planes begins in the post-failure phase. Accordingly, the fluorescent images were obtained from an unaffected zone and the stress levels obviously did not exceed the stress required for the generation of major fractures.

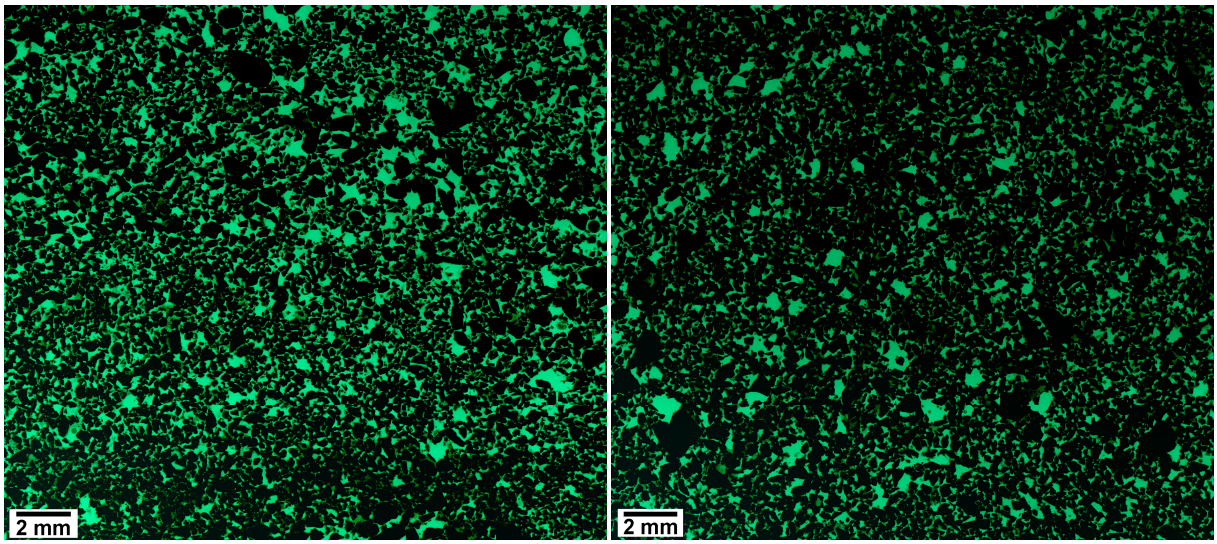

Figure 123: Fluorescent thin sections of Posta sandstone loaded with 40 MPa (POS-3-11, left) and 50 MPa (POS-3-13, right) showing open pore space and open grain boundaries. Intragranular microcracks are not present in the rock. The applied load was vertical.

6.2.5.3 Pechbrunn basalt

Petrographic analysis of Pechbrunn basalt was performed on small specimens with a diameter of 2.5 mm. The specimens were loaded continuously until the first audible cracks occurred. Constant loading could not be performed, since the uniaxial compressive strength of the basalt samples showed a high variability and the crack damage stress was at about 99 % of the peak strength. Thin sections were prepared from the longitudinal sections of the whole specimens. In most samples, only small axial cracks evolved in the external areas near the upper and lower ends of the specimen and only one tested sample showed an internal crack in the analyzed cross section. In Figure 124, the example of an external crack is shown. The crack initiated from an olivine phenocryst, where it mainly followed the intracrystalline cracks, which are typically present in olivine. The created fracture extends into the fine-grained basalt matrix where it forms a straight axial crack. At the boundary between intact rock and the broken off fragment, the fracture split up in several branches. From the fluorescent image, it becomes clear that cracking is associated with larger minerals in the fine-grained matrix. The phenocrysts act as stress concentrators and branching of the crack was only observed associated with those minerals. The major crack split up and was deflected at the existing phenocrysts.

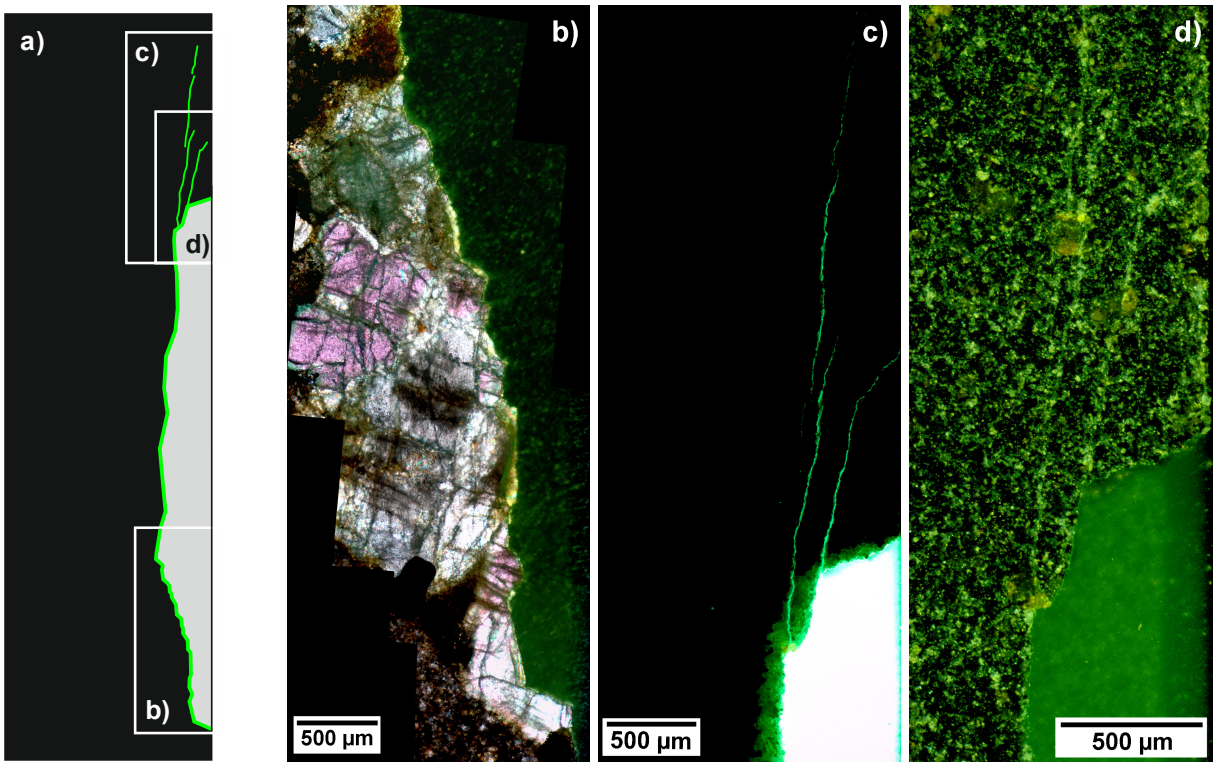

Figure 124: Fluorescent thin section of Pechbrunn basalt (PB-5) loaded until a first fragment split off at the external area. a) Schematic overview of given image locations, b) the final crack initiated from an olivine phenocryst at the surface, c) it further extended into the fine-grained matrix, where it branched at other existing phenocrysts (d). The applied load was vertical.

6.3 Discussion of results

In this section, the experimental results obtained from constant loading tests are summarized and discussed. The conducted preloading tests included the generation of rock damage on cylindrical rock specimens under uniaxial compression. Damage was induced by applying a constant load at different stress levels to some of the previously described and characterized rocks. In a subsequent test, the pre-damaged rocks were reloaded in a standard uniaxial compression test. The deformation and cracking characteristics during the constant loading tests and the influences of a previously induced rock damage on the mechanical and acoustic properties of the different rock types are described in the following. The findings about microcracking in different rock types gained from fluorescence thin section analyses are discussed in a second subsection.

6.3.1 Summary of the preloading tests

For the constant loading tests, different stress levels between stable and unstable crack growth were applied in order to induce controlled damage to the rocks. The constant loading tests showed that brittle rocks like Dietfurt limestone did only exhibit minor continuing creep deformations during constant loading. In contrast, rock types with ductile characteristics like TIT or clearly ductile rock types like FLB and LAM showed a considerable creep deformation during constant loading, especially when the crack damage stress was exceeded with the applied load. The rocks showing a high radial strain during constant loading also resulted in a more pronounced decrease in the radial p-wave velocities. This confirms that a decreasing p-wave velocity is a clear indicator for stress-induced damage.

When loaded up to the phase of stable crack growth, it was observed that the AE activity decreases as soon as the load was held constant and the number of AE ceases shortly after. The specimens, which were loaded above the crack damage stress behaved differently. In Tittling granite, the AE activity decreased as soon as the load was kept constant, but after several minutes, a second increase in the number of events occurred. One of the specimens loaded beyond the crack damage stress failed during the phase of constant load, whereas a second specimen did not fail within this period. Those tests confirmed the theory of unstable crack growth, which states that failure occurs if the load is held constant at a stress level above the crack damage threshold. Specimens of the weathered Flossenbürg granite, however, did not reveal a second increase in the cracking activity during constant loading although they were also loaded above the crack damage stress. Instead, the number of events slowly decreased but it did not totally cease during the period of loading. The lack of a second increase in the cracking activity is assumed to results from the cracking behavior of the ductile Flossenbürg granite. The rock is characterized by a continuous degradation and disintegration of the rock structure during loading until failure instead of a violent generation of major fractures with the beginning of unstable crack growth. It is thus assumed that the sample would have failed if the load was held constant for a sufficiently long period because the continuous degradation of rock quality is supposed finally to lead to failure.

A comparison of rock properties before and after preloading showed an increase in the slope of the axial strain curve, whereas the slope of the radial strain curve decreased in the second loading test. The tested rock types all showed a distinct change in the axial tangent Young's modulus according to their material behavior. In the preloaded specimens of FLB, the highest increase in the axial tangent Young's modulus of about 20 % occurred, whereas in LAM, DK and TIT, a maximum change of about 10 % was observed. Only in POS, the slope of the axial strain curve did not show a marked change. In general, the highest increase was present when the stress level of preloading was set within the phase of stable crack growth and the higher the applied stress level was, the smaller was the observed increase. As soon as the phase of unstable crack growth was reached, a considerably lower increase or even a decrease of the axial tangent Young's modulus occurred.

A decrease in the uniaxial compressive strength resulting from a previously applied stress was only observed in the specimens of Tittling granite, which were loaded beyond the crack damage threshold. The specimens of FLB and DK, however, did not show a reduced uniaxial compressive strength, although it was demonstrated that considerable damage was generated during unstable crack growth.

The existence of rock damage could be shown with AE measurements during the initial and second loading tests. In the reloading test, the onset of AE only started as soon as the previous stress level was exceeded. This phenomenon is known as the Kaiser effect and allows an estimation of the previously applied maximum stress. In the conducted tests, the onset of AE coincided well with the previous stress level, but only if the stress level was set below the crack damage stress. As soon as the crack damage threshold was exceeded during preloading, the cracking activity of the second loading started at a considerably lower stress level. The Kaiser effect is thus obscured as soon as the crack damage threshold is exceeded during preloading. This must be considered when attempting to determine the previous maximum stress level in rock samples from the onset of AE.

6.3.2 Findings of petrographic analyses

The petrographic analysis of fluorescent thin sections showed several crack characteristics, which are important for the understanding of fracturing processes of rock under compression. In Tittling granite, the following features were observed in the undamaged reference sample:

- A high number of preexisting microcracks, which are open, closed, or healed
- In feldspar, grain boundary cracks and a diffuse network of intragranular microcracks along cleavage planes and twins are present. Along the suture of the twin planes in Karlsbad twins, long high aspect ratio cracks exist
- Areas of intensive sericitization are surrounded by cracks but no intragranular cracks occur
- Quartz shows clearly localized high aspect ratio intragranular cracks, grain boundary cracks and few transgranular cracks
- In biotite, no intragranular cracks and only few grain boundary cracks were observed but some cracks initiate from the corners of biotite minerals and extend in neighboring minerals
- The preexisting high aspect ratio cracks show two preferred, almost horizontal orientations of 10-20° and 190-200° with respect to the horizontal. Several subvertical cracks exist but are less pronounced

On additional samples of Tittling granite, constant loading tests were performed using different stress levels between crack initiation stress and crack damage stress. The samples, where stable crack propagation occurred, did not show noticeable differences in the crack characteristics compared to the reference sample. In one sample, which was loaded with 180 MPa, stress-induced fractures developed. Several differences compared to the reference sample and samples with lower stress levels were observed:

- A noticeable increase in load-parallel axial cracks with a high aspect ratio and a considerable extent. They occur in quartz and feldspar as intragranular and transgranular fractures including grain boundary cracks
- The axial cracks are either straight with short branching microcracks along preexisting fractures or they connect preexisting cracks forming the shape of a staircase
- Cracks often initiate at preexisting cracks and at the corners of minerals, particularly at the boundary between biotite and adjacent minerals. Vertical and horizontal cracks initiating from biotite corners were observed
- Horizontal preexisting cracks are often closed, whereas few vertical closed cracks were noticed
- When axial fractures form, subhorizontal branching cracks begin to open

In Posta sandstone, acoustic event localization showed a strong accumulation of events near the ends of the rock specimen. At higher stresses, AE showed beginning cracking in the central part of the rock. The analyzed thin sections, however, did not show any evidence of the applied stress. In none of the thin sections, intragranular microcracks or compaction bands were present. This was on the one hand because in sandstone, damage begins with the breaking of the cement between the grains instead of intragranular cracks and in the porous sandstone, stress-induced breaking of the cement cannot be easily observed in the fluorescent thin sections. On the other hand, the applied stress level might have been insufficient for the generation of compaction bands and intragranular cracks or the thin sections were obtained in an undamaged area of the sample.

A petrographic analysis of Pechbrunn basalt showed that crack initiation starts at the lateral surface of the cylinder in the form of axial fractures. Cracks initiate at phenocrysts and grow preferably between the larger minerals of olivine and pyroxene. Fracturing mainly follows preexisting microcracks in the grains and at the phenocrysts, branching of major cracks can be observed. Beside the stress-induced microcracks at the surface, no further cracks or voids were present in the basalt samples. This might be caused by the fine-grained, dense texture of basalt, which can prevent the fluorescent resin to penetrate the existing microcracks. On the other hand, the petrographic analysis confirms the findings from AE monitoring, which showed a low microcrack activity until shortly before failure of the basalt samples.

7 Transfer of laboratory findings to tunneling

The findings from investigations regarding the time-dependent degradation of rock quality, the characterization of mechanical and acoustic rock properties and the influence of a previously induced rock damage can be transferred to tunneling in high primary stress conditions. This chapter points out the limitations of adopting the outcomes of the conducted tests to tunneling but it also presents the contributions of this research to the current understanding of the deformation and cracking mechanisms in underground tunnel construction under high primary stresses.

7.1 Limitations

For transferring the findings from laboratory tests on core material to the processes and mechanisms at the tunnel face, several limitations must be taken into account. In laboratory tests, intact, isotropic and homogeneous rocks are ideally used for testing. In-situ, however, structural anisotropies and the existence of discontinuities as well as material heterogeneities like changes in composition or existing rock damage can have a major influence on the deformation and fracture behavior of the rock mass. Those heterogeneities can additionally act as stress raisers and result in a reduced crack initiation threshold of the rock mass. For the analysis of the rock mass behavior, the presence of joints and faults needs to be considered, when investigating the influence of high in-situ stresses on the deformation and cracking behavior in the tunnel face. The strength of jointed rock masses can be approximated using the Hoek-Brown failure criterion, which depends on the intact laboratory rock strength and the rock mass quality (HOEK & BROWN 1997).

In massive, unjointed rock masses at depth, the strength of the rock mass is governed by the intact rock strength. In the case of an isotropic, homogeneous and elastic rock, the in-situ rock mass strength is still considered lower than the laboratory rock strength. According to DIEDERICHS (2003: 354 ff.), the lower bound for the in-situ strength is defined as the crack initiation stress. The upper bound corresponds to the crack damage threshold, which is the long-term strength of laboratory samples. The conducted constant-loading tests in this work also demonstrated that the minimum of uniaxial compressive strength corresponds with the crack damage threshold. This stress level is known as the long-term strength of intact rock and the uniaxial compressive strength may be considered as the maximum intact rock strength under unconfined conditions.

As shown by investigations on core material recovered from high primary stresses, sample disturbance is induced during the drilling process and during stress relaxation. Since laboratory tests are usually performed a considerable period after drilling, laboratory rock properties may not reflect the in-situ rock characteristics. This needs to be considered when the uniaxial compressive strength is regarded as the maximum value for the intact rock strength.

Several factors and conditions may further influence the in-situ rock mass behavior but they were neglected in the analysis of the deformation and cracking behavior of rocks:

- For the laboratory program, specimens with a diameter of 5 or 8 cm were used. As was observed by HOEK & BROWN (1980), the uniaxial compressive strength is influenced by the specimen size. With an increasing size, the rock strength decreases because of an increasing number of existing cracks and flaws, which might act as stress raisers where cracks initiate. Additional investigations

of THURO et al. (2001), however, showed that the size effect is minimal in the range of the specimen sizes that are used in geotechnical testing practice. When transferring the laboratory findings to field conditions, the scale effect still needs to be considered.

- The water content of rocks has an additional effect on the rock properties. For the laboratory tests, samples with a minimal moisture content equal to the air humidity were tested. In deep underground excavations, however, water may be present in joints and fractures. Depending on the pore and fracture porosity of the rock, a considerable pore water content may be present in the rock mass, which can influence the cracking characteristics.
- Uniaxial compressive tests were performed to analyze the stress-induced rock damage. When transferring the findings from laboratory tests to the deformation and cracking behavior in the tunnel face, the differences in the stress state need to be considered. The confined conditions in the tunnel face with one free surface strongly influence the rock characteristics, since the deformation behavior of the rock is dependent on the magnitude and the orientation of the principal stresses. At the excavation face, the stresses parallel to the tunnel axis are reduced to zero and the stresses are instead redistributed around the tunnel face. The stress conditions in the tunnel face are thus more complex than the simple uniaxial compression stress in laboratory testing.
- In uniaxial constant loading tests, damage was induced and subsequent tests were performed in the same direction as the previously applied load. During tunnel excavation in high stress conditions, the stresses at the tunnel boundary and in the tunnel face constantly change. This was illustrated by a 3D-finite element analysis of EBERHARDT (2001), which showed changes in stress magnitude and stress rotation ahead of the excavation face. Complex stress paths depending on the orientation of the principal stresses are considered as the major cause for an increased damage and a reduction of the strength in the tunnel face. Magnitude and orientation of the principal stresses affect the orientation of crack propagation and stress rotation may facilitate the interaction of growing cracks.

7.2 Proposed fracture behavior in the tunnel face

Underground excavation in rock masses causes a redistribution of stresses around the opening. Radial stresses decrease to zero at the excavation boundary and the tangential stresses increase. They are at a maximum at the circumference of the excavation and decrease with distance from the tunnel. An inward deformation and a redistribution of stresses can lead to irreversible damage around the excavation boundary. A failed zone (v-shaped notch) or highly damaged zone (HDZ) as well as an excavation damaged zone (EDZ) and an excavation disturbed zone (EdZ) develop with distance from the opening (BÄCKBLOM & MARTIN 1999, SIREN et al. 2015). MARTINO & CHANDLER (2004) summarize the factors affecting the extent of damage around an excavation. These are primarily the in-situ stress magnitudes, the orientation and the stress ratios as well as the orientation of the tunnel relative to the major principal stress axis, the tunnel cross section, the excavation method and the geological conditions.

The accumulation of irreversible damage around the excavation boundary also occurs in the tunnel face, where rock excavation causes stress relaxation parallel to the tunnel axis. The result is an inward deformation of the tunnel face with the highest displacements in the center of the face (HOEK 1998). The effect of stress redistribution varies strongly in the rock mass ahead of and within the tunnel face. Assuming a hydrostatic stress state, the potential for stress-induced damage at the edges of the tunnel face is uniform around the tunnel circumference. If the conditions for crack initiation are met, tensile cracks

develop. An increase in the ratio of σ_1/σ_3 evokes regions of tensile stress concentration at the tunnel boundary perpendicular to the maximum principal stress (CARLSON & YOUNG 1993, READ et al. 1998).

Several authors investigated the complex stress paths ahead of and within an advancing face (MARTIN et al. 1999b, KAISER et al. 2001, EBERHARDT 2001 and DIEDERICHS et al. 2004). Results of BLÜMLING et al. (2007) showed that the increasing principal stresses may exceed the failure envelope of the rock in the external areas of the face. In the center, the confining stresses ahead of the face decrease and are reduced to zero as soon as the excavation surface is reached. In Figure 125, schematic stress paths for different positions in the tunnel face are illustrated for a lithostatic stress field with a maximum vertical stress σ_1 and a minimum principal stress σ_3 oriented parallel to the face. Depending on rock strength and in-situ stresses, the principal stresses at the excavation boundary in the roof may exceed the crack initiation threshold so that damage accumulation takes place. If the failure envelope is reached, shear failure occurs (1). If the upper bound in-situ strength is not exceeded, damage is initiated without evoking failure (2). In this stress regime, irreversible damage is induced and an EDZ develops (PERRAS & DIEDERICHS 2016).

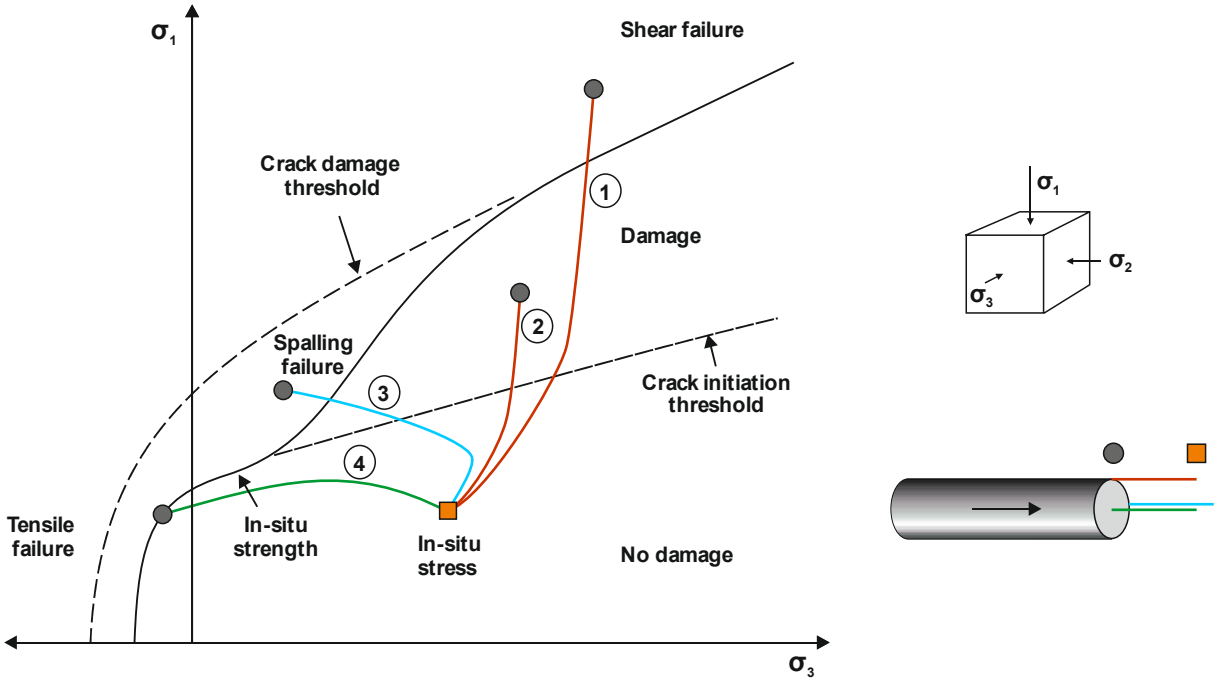

Figure 125: Schematic of failure envelope for brittle failure (after DIEDERICHS 2003) and potential stress paths (1-4) for different positions in the tunnel face. Stress paths are given for the roof (red), the wall (blue) and the center (green) of the advancing face. A lithostatic stress field with σ_3 parallel to the tunnel face is assumed (after BLÜMLING et al. 2007).

Above the crack initiation threshold, stress rotation can promote crack propagation so that the in-situ rock strength may be reduced toward the lower bound in-situ strength. Factors, able to reduce the upper bound strength are scale effects, a reduced local confinement at open cracks or joints, unloading or preexisting damage, damage induced by stress rotation, heterogeneities or local tension (DIEDERICHS et al. 2004). Spalling may occur if the ratio of maximum to minimum principal stress meets the conditions for spalling failure (3). If the spalling limit is exceeded, rock slabs parallel to the tunnel face develop or rock burst failure may occur. Spalling occurs at lower stresses than the failure of laboratory specimens because in-situ, failure is not constrained by the geometry (DIEDERICHS 2003). In the center of a circular tunnel face, the confining stress is reduced to zero or is even negative (4) so that stress relaxation leads to tensile failure (Figure 125).

The potential stress paths show that the stresses resulting from tunnel excavation are strongly different over the diameter of the face so that the processes inducing rock damage are inevitably more complex than the processes observed in laboratory experiments. Nevertheless, the results of the conducted laboratory tests showed that every rock type shows its characteristic deformation and fracturing behavior depending on mineralogy and rock fabric. The characteristic material behavior is thus supposed to have a major influence on the extent of stress-induced damage and the failure behavior around the excavation and in the tunnel face.

Considering the limitations of transferring laboratory results to the in-situ conditions, many observations made in the conducted tests can still be found in the tunnel face. Regardless of the different scales and stress conditions, in many ways, the tunnel face behaves similar to the rock specimens under uniaxial compression. The rock specimens are constrained by an upper and lower loading plate but they can expand laterally equivalent to the free surface of the excavation face that is loaded by the surrounding rock mass. Especially in an anisotropic stress field, the conditions in the tunnel face are in many ways similar to uniaxial compression tests. Under uniaxial compression of brittle rock types like basalt, thin rock fragments split off the sample surface near the end planes after the crack initiation threshold was exceeded. Similarly, the highest stresses in the tunnel face occur in the edges of the face near the excavation boundary. The mechanism of tensile fracturing in basalt specimens can thus be interpreted as a form of spalling on the laboratory scale, similar to the spalling-type failure in the tunnel face. Not all tested rock types, however, were susceptible to brittle rock fracture and spalling. Sudden and violent tensile fractures similar to spalling fractures only occurred in truly brittle rock types, whereas in more ductile rocks, distributed damage accumulated within the specimens. Therefore, it is assumed that spalling failure can only occur in brittle rock types but is unlikely to occur in ductile rocks. This does also mean that the extent of the excavation influenced zones ahead of the face depends on the deformation and cracking behavior of the rock. In ductile rock types, the zones of excavation disturbance and excavation damage are assumed to have a greater extent than in brittle rocks because larger deformations and a greater amount of damage develops before final shear failure occurs. In addition, brittle rock types generally show much higher rock strengths, so that high principal stresses are required to exceed the stress levels of crack initiation and crack damage. In contrast, ductile rocks are generally characterized by a lower rock strength so that comparably low principal stresses are required to exceed the stress thresholds of crack initiation and crack damage.

7.3 The effect of high in-situ stresses on TBM performance

In TBM tunneling, the performance is dependent on the penetration rate, which is the advance per rotation of the cutter head. For a high penetration rate, an efficient rock fragmentation process at the tunnel face is required. The fragmentation of rock with disc cutters includes a zone of crushed material beneath the disc cutters as well as the generation of tensile radial cracks propagating away from the cutting tools (GEHRING 1995, THURO 2002: 44). If the induced tensile cracks parallel to the tunnel face propagate and coalesce with cracks from neighboring cutter tracks, flat rock chips are created between the two disc cutters. For an effective chipping process, the applied thrust needs to exceed the crack initiation stress of the rock in order to induce tensile fractures, but also the crack damage stress needs to be exceeded to promote the interaction and coalescence of cracks in order to cause an effective rock fragmentation. Excavation of rock types with a lower crack initiation and crack damage stress is thus assumed to require a lower thrust than the excavation of rock types with higher stress levels. Only if the crack initiation stress is exceeded, tensile cracks are created under the disc cutters. The coalescence of cracks results in the formation of major fractures and the final release of stresses by the removal of rock chips (GEHRING 1997).

In strong, brittle rock types, the stresses required for crack initiation are generally higher than in weaker, ductile rocks. Furthermore, the crack damage threshold varies strongly between different rock materials. In rocks with a relatively low strength and a high crack damage threshold, like in the tested anhydrite or marble specimens, microcrack initiation occurs during the phase of stable crack growth but comparably high stresses are necessary to exceed the high crack damage threshold for chipping. On the other hand, there are rocks with a similar strength but a relatively low crack damage threshold (FLB, MET). In those rocks, the phase of unstable crack growth and thus the stress level for the generation of shear failure is comparatively low. Those considerations show that not only the rock strength but also, especially the characteristic material behavior including the phases of cracking are important to predict the efficiency of the chipping process and the required thrust force of the cutting tools.

Another important influence on TBM penetration is the stress state in the tunnel face. As is known from triaxial testing, the ratio of the crack initiation and crack damage threshold to the rock strength is largely unaffected by an increasing confinement (NICKSIAR & MARTIN 2013). As a result, the total compressive stress required for crack initiation increases with an increasing ratio of σ_3 to σ_1. Therefore, variable stress magnitudes and stress ratios over the diameter of the face can cause differences in the penetration rate. In the external areas of the face, where the stresses increase after the excavation, a higher thrust force might be required to induce crack propagation and crack coalescence (Figure 126a). In contrast, low confinement or tensile stresses due to stress relaxation in the center of the face may induce tensile fractures parallel to the free excavation face. The flaking of thin rock slabs from the tunnel face was observed in several deep tunnel projects, where high primary stresses were encountered (WEH 2007, GONG et al. 2012, VILLENEUVE 2015).

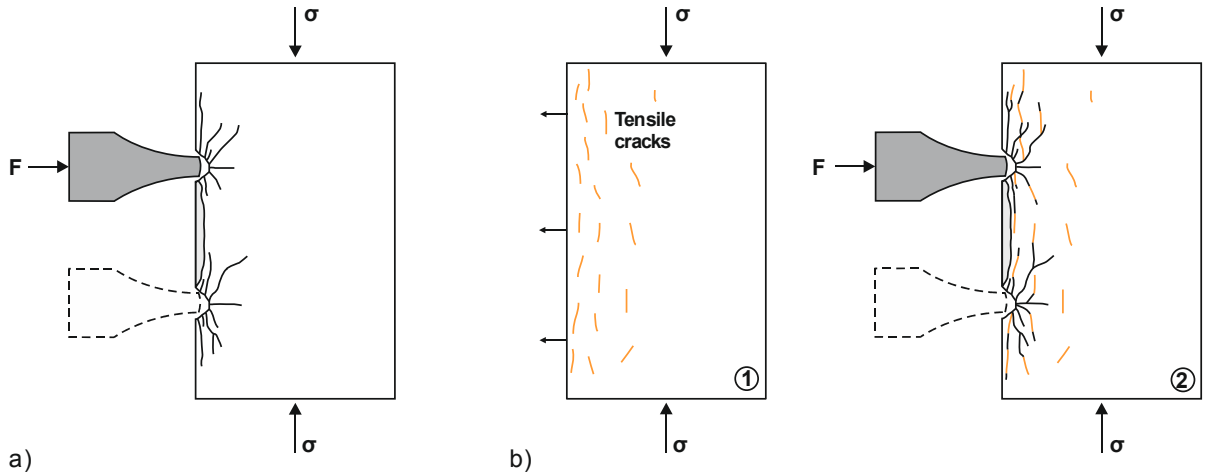

Figure 126: Chipping process under disc cutters for a) high confinement conditions (external area of face) and b) low confinement or tensile conditions (center of face). Damage initiated during stress relaxation (1) can promote crack propagation and enhance the chipping process (2).

Even if the generation of face-parallel microcracks does not lead to spalling failure, tensile microcracks may be created in the excavation face. Existing cracks can act as stress raisers and may thus facilitate crack propagation and crack coalescence, which is necessary for the generation of rock chips (Figure 126b). A pre-damaged rock volume can improve the penetration, but at the same time, the total penetration rate is limited by the lowest excavation progress in the regions of high confinement. The positive effect of a pre-damaged face is consequently restricted and the result is a reduced penetration rate due to high confining stresses in the external areas of the tunnel face. The positive effect of a pre-damaged rock mass is assumed higher in a ductile rock material than in brittle rocks because ductile rocks are

more susceptible to damage even at relatively low stress levels. Furthermore, the development of damage in the tunnel face is a time-dependent process. The longer the face exists, the more damage is induced because of stress redistribution and relaxation. Monitoring of stress relaxation in drill cores showed that this process continues for several days or weeks until an equilibrium is achieved.

Furthermore, in a high stress environment, serious problems may arise as a result of spalling phenomena in the tunnel face (TARKOY & MARCONI 1991). When stress ratio and stress magnitudes exceed the spalling limit, face instabilities may arise and the damaged tunnel face will have a negative effect on the TBM performance. Blocks of rock, generated by spalling or slabbing may accumulate in front of the cutting wheel and the rock material needs to be broken to collect it into the cutterhead. The additional rock breaking process and an irregular excavation face additionally cause an increased cutter wear. The result is a reduced TBM performance because the rock material must be removed before further rock excavation is possible. Furthermore, this leads to downtimes and to increasing construction costs.

In addition to the cutter wear caused by spalling, it has been observed that high primary stresses generally increase the disc cutter wear (FRENZEL 2010, RAUCH 2016). Particularly in the external areas of the excavation face, where the stresses are at a maximum, an increased wear occurs. With Cerchar abrasivity tests on a free surface of confined rock samples, ALBER (2008b) showed that the rock abrasiveness increases with an increasing confinement of the tested samples. Since the abrasiveness of rocks is dependent on the rock strength, a rock volume subject to high confining stresses will exhibit an elevated cutter wear (ALBER 2008a).

8 Conclusions

The excavation of underground openings in high-stress conditions is a major challenge in modern underground construction. In mechanized tunneling using TBM, high stresses may cause delays because of stress-induced face instabilities, a reduced penetration and an increased cutter wear. Until now, little is known about the redistribution of stresses, the resulting stress concentrations and stress relaxation in the tunnel face and especially its influence on rock excavation. In this work, stress relaxation was assessed using acoustic emission techniques to monitor the time-dependent behavior of core samples recovered from their initial stress environment. Additional petrographic analysis of fluorescent thin sections provided information about the development of stress-induced cracks on the microscopic scale. In this thesis, the influence of stress changes on the deformation and cracking behavior of rocks was investigated with an extensive laboratory program. The experimental work included the characterization of acoustic and rock mechanical properties in order to examine the deformation and fracturing behavior of different rock types. Furthermore, constant loading tests were performed in order to evaluate the influence of a previously induced damage on the rock behavior. The experimental study involved representative samples of plutonic, volcanic, sedimentary and metamorphic rocks, which could be considered as nearly homogeneous and isotropic. The following sections contain the major findings and conclusions of this thesis.

8.1 Time-dependent accumulation of rock damage

Monitoring of stress relaxation of core samples recovered from a rock mass at the Pyhäsalmi Mine in Finland showed a considerable microcracking activity in the first hours and days after drilling. From acoustic emission data and p-wave velocity measurements, a continuing formation of stress-relief cracks was observed during a period of days and weeks of monitoring. Beside an elastic component of stress relaxation, which is released during the drilling process, an inelastic, time-dependent relaxation takes place. In the analyzed metavolcanic rocks, a foliation perpendicular to the core axis was present and the major principal stress was parallel to the core axis.

In uniaxial compression tests combined with AE on the core material, the induced damage was also apparent in the stress-strain curves. An evidence for sample disturbance was indicated by the occurrence of a crack closure phase in the otherwise brittle deformation characteristics of the metavolcanic rock. Except from the initial crack closure phase, cracking activity began at a high stress level between 65 and 85 % of the peak strength. The corresponding stress level of 175 to 230 MPa is by far higher than the maximum principal stress (maximum 72 MPa) measured at the Pyhäsalmi Mine. Consequently, the AE activity measured after coring must be the result of microcracking at tensile stress concentrations within the rock structure, preferably at grain boundaries of adjacent minerals. Upon stress relief, the elastic strain energy, which is stored within the minerals, is partly released and significant stress concentrations may arise because of the anisotropic elastic properties of the minerals as well as an anisotropic strain release due to the sample geometry. In addition to stress-relaxation cracks, coring-induced microcracking may occur in rocks recovered from the primary stress state. The phenomenon of core disking is generally supposed to be the result of stress concentrations at the drill bit, which locally exceed the crack initiation stress of the rock. In the tested rocks, core disking was not observed macroscopically but petrographic analysis showed that microcracks formed along the foliation and opened in the direction of the maximum principal stress. Whether the microcracks were generated during the drilling process or during stress relaxation could not be determined.

The opening of microcracks does not only increase the sample disturbance but the preferred crack orientation also increases the anisotropy of the rock. An influence of microcracking on the compressibility and the p-wave velocities of the rock exists, whereas the effect of stress-induced damage on rock properties determined from uniaxial compression tests is supposed to be minimal. When a uniaxial load is applied, the horizontal stress relaxation cracks will be closed. Since loading-induced microcracks will preferentially grow in axial direction, cracks will not be initiated at the horizontal stress relaxation cracks. Instead, crack initiation is supposed to occur at grain boundaries or flaws oriented at a more favorable angle to the loading direction.

8.2 Characterization of laboratory rock properties

For the characterization of laboratory rock properties of ten different rock types, uniaxial compression tests combined with AE monitoring were performed. The four common stages of crack development in the pre-failure range: crack closure, linear elastic deformation, stable crack growth and unstable crack growth (after BIENIAWSKI 1967), have been observed in the brittle rock types like basalt, diabase and limestone as well as in Tittling granite. A different cracking behavior was noticed in Flossenbürg granite, Metten granite, anhydrite, marble, Posta sandstone and Abtswind sandstone. Those rock types show a ductile material behavior with a pronounced phase of plastic deformation and a pronounced post-failure phase. Metten granite showed the phases of crack closure, elastic deformation and the onset of crack initiation but from the number of acoustic events, a phase of unstable crack growth could not be determined. In Flossenbürg granite, anhydrite and Posta sandstone, a high and increasing microcracking activity was detected from the beginning of compression so that a reliable determination of deformation stages was not possible with the AE method. In contrast, marble and Abtswind sandstone revealed an exceptional cracking behavior with only few events during the increasing compression. In Abtswind sandstone, considerable cracking only began shortly before peak strength, although the rock exhibited an exceptionally high deformation. Like the clayey sandstone, marble is characterized by a late onset of AE and a considerable increase in the number of events was first detected in the post-failure phase after the peak stress was exceeded.

In the tested rock types, the stress threshold of crack initiation is between 0.37 and 0.71 σ_u and the crack damage level is between 0.65 and 1.0 σ_u. In general, the tested rocks can be classified in two different types of deformation and cracking behavior. Some rock types exhibit a clearly brittle material behavior, other rock types showed a clearly ductile material behavior. Some of the tested rocks, however, cannot be ultimately classified as brittle or ductile but they showed characteristics of both types.

Rock types with a clearly **brittle material behavior** exhibited the four typical stages of deformation and crack development in the pre-failure phase. In uniaxial compression, brittle rocks showed the following characteristics:

- Absence of a post-failure phase
- High rock strength
- High difference between axial and radial strain at failure
- High crack damage stress (above 95 %)
- Low total number of AE until failure
- High average AE signal energy

In rocks under compression, the kinetic energy applied to the system by loading is stored as potential energy when the rock is deformed. The energy is stored on the atomic scale, since deformation changes the atomic distance and the initial equilibrium position of the atoms is disturbed. Rock types with a brittle failure behavior show a distinct phase of linear elastic deformation where the rock can recover its original shape when removing the applied force. Beyond the elastic limit, plastic deformation begins and irreversible damage occurs because of the initiation of microcracks. The nucleation of microcracks is dependent on the existence of flaws and grain boundaries acting as stress concentrators (GRIFFITH 1920). In fine-grained, homogeneous rock types with equal grain size, few flaws or grain boundaries with a considerable length exist where stress concentrations could arise. In addition, a mineralogical heterogeneity causing elastic mismatch and thus stress concentrations at the mineral contacts does not exist. As a result, the elastic energy is largely stored within the rock sample without being dissipated by the formation of new crack surfaces. Below the peak strength, only few microcracks initiate because the radial deformation of the specimens is restrained, whereas at the same time, the applied load causes axial strain. During compression of brittle rock types, energy is only dissipated by the occurrence of single high-energy cracking events, whereas the major dissipation of energy occurs shortly before or directly upon failure. At failure, an explosive collapse occurs with a rapid development of major fracture planes.

Rock types showing a clearly **ductile material behavior** showed a cracking behavior different from the commonly applied five-stage model. In uniaxial compression, the tested rocks showed the following characteristics:

- Pronounced post-failure phase
- Lower rock strength
- Small difference between axial and radial strain at failure
- Low crack damage stress (below 95 %)
- High total number of AE until failure
- Low average AE signal energy until failure

In rocks with a clearly ductile material behavior, the elastic energy is continuously dissipated by the initiation and propagation of microcracks. The existence of a large number of microcracks, flaws, pores and voids evokes a large number of stress concentrations within the rock specimen. Energy is dissipated by the occurrence of many low-energy cracking events during the whole loading process. Compared to brittle rock types, a lower amount of energy is stored within the rock and the development and growth of microcracks causes a high radial strain. Resulting from the early dissipation of energy, in ductile rock types, the final failure is not a violent collapse but occurs as a continuous disintegration of the rock fabric. Major fracture planes develop in a pronounced post-failure phase so that a residual rock strength is maintained after the peak stress is exceeded. In general, rock types of medium to coarse grain size and rocks with a heterogeneous grain size distribution or mineralogy show a ductile failure behavior. Stress concentrations occur at heterogeneities like existing cracks, flaws or defects and at anisotropies of the textural fabric.

According to their deformation and cracking behavior, the tested rock types were divided in five groups with different mechanical and acoustic characteristics. The fine-grained basalt, diabase and Dietfurt limestone showed a truly brittle material behavior, Tittling granite was classified as brittle with ductile characteristics because of its heterogeneous mineralogy. The mono-mineral, crystallized rocks marble and anhydrite showed a ductile behavior with brittle characteristics and the weathered granites behaved clearly ductile. The sandstones exhibited a ductile material behavior with exceptions because of their granular and porous structure.

Regarding their acoustic properties, Laas marble and Abtswind sandstone showed an exceptional behavior, because the rock deformation is not represented by the detected AE activity. In marble, plastic deformation occurs in the form of intracrystalline deformations, which means that twin gliding takes up the induced stresses. The displacements within the crystal lattice do not produce acoustic events of a sufficiently high amplitude or frequency range to be detected with the applied AE settings. In Abtswind sandstone, a pronounced dilatancy of the rock does not coincide with the emission of a large number of events until shortly before the peak stress. A reason for the late onset of AE is the elastic behavior and a prominent cleavage of clay minerals, which represent the matrix and cement material of the sandstone. Because of the sheet-like structure of clay minerals, it is supposed that deformation mainly occurs by slip along the silicate layers instead of forming new crack surfaces.

The failure behavior of rock is strongly dependent on its mineral composition. According to their bonding forces, minerals like quartz, feldspar or olivine show a brittle failure behavior in contrast to mica, calcite or clay minerals, which behave ductile. Covalent bonds of silicates are characterized by a high strength and high stiffness so that they cause a brittle deformation behavior of the minerals. In phyllosilicates like mica and clay minerals, strong covalent and ionic bonds exist in the tetrahedral layers, whereas the sheets are bonded by weak van-der-Waals, ionic or hydrogen bonds. The bonding forces of calcite are ionic and are thus weaker than in the silicate structure. Furthermore, calcite shows a perfect cleavage, where a smaller number of bonds occurs perpendicular to the cleavage planes. Along those planes of weakness, the ionic bonds can easily be broken. The bonding forces in anhydrite are strong covalent bonds within the SO_4 complex, whereas the bond between SO_4 and the cations is ionic. Cracking can occur at the perfect cleavages similar like in calcite (OKRUSCH & MATTHES 2014: 129). Distinct cleavage planes acting as preferred planes of weakness are also present in feldspar.

The material behavior of rocks, which are mainly composed of ductile minerals with low bonding forces, is controlled by the deformation properties of those minerals. In the tested rock types, this is the case for anhydrite, marble and Abtswind sandstone. The deformation behavior of Abtswind sandstone is dominated by the presence of the ductile clay minerals in the matrix instead of the strong quartz components. In the fine-grained Dietfurt limestone, however, the ductile behavior of calcite is suppressed because of the very small and homogeneous grain size. Short grain boundaries represent a high number of small, uniform planes of weakness, which impede the concentration of local stresses instead of facilitating the formation of microcracks. This demonstrates that the occurrence of ductile minerals controls the deformation and cracking behavior only at a sufficiently large grain size or if heterogeneous grain sizes are present in a rock. If a small amount of ductile minerals exists, the cracking behavior is largely controlled by those minerals. This is the case in the tested granite samples, where microcracks often nucleate at the boundary between mica and adjacent minerals. Stress concentrations preferably occur where the difference between the elastic properties of the minerals is highest. Similar results were obtained in previous studies (DIEDERICHS et al. 2004, VILLENEUVE 2008).

8.3 The influence of damage on rock properties

The influence of stress changes on rock damage and the resulting influence on rock mechanical and acoustic rock properties were investigated with uniaxial constant loading tests. Cylindrical specimens were loaded with different stress levels above the crack initiation stress. The same specimens were used for standard uniaxial compressive tests soon after preloading in order to analyze the effect of the previously induced damage on laboratory rock properties. The tests revealed the following results:

- **P-wave velocity:**

  With an increasing rock damage, the radial p-wave velocities are increasingly reduced. Because of the opening of axial microcracks, the sonic waves are slowed down when travelling through the rock. In contrast, a considerable influence of the applied compressive stress on the axial p-wave velocity could not be observed. A small increase in the velocities was noticed but the velocities remained at a constant value at all stress levels. Existing microcracks, which are aligned at a high angle to the loading direction are closed and the low-angle microcracks open. Therefore, an increasing load does not have a strong effect on the axial travel path of sonic waves.

- **Tangent Young's modulus**:

  A distinct increase was observed in the axial tangent Young's modulus of several samples (FLB, LAM, DK and TIT), which were loaded with a stress level within the phase of stable crack growth. This demonstrates that more stress is required to achieve the same axial strain like in the first loading test. Since rock damage was induced with all applied stress levels, the increase in the Young's modulus must be caused by an irreversible axial deformation. When the applied preload exceeded the crack damage stress, a lower increase in axial Young's modulus was observed. In a specimen of Tittling granite loaded beyond the crack damage stress, it even decreased compared to the first loading cycle. In Posta sandstone, no distinct change was observed. This might be due to an additional compaction of the grains instead of the formation of cracks during the second compression. The tangent Young's modulus determined from the radial strain curve showed an opposite trend. With increasing stress levels, the slope decreased because the existence of permanent damage decreases the stress required for a similar radial strain in unconfined compression.

- **Uniaxial compressive strength**:

  An influence of stress-induced damage on the uniaxial compressive strength was only observed in specimens loaded beyond the crack damage threshold. The crack damage stress is considered as the long-term laboratory strength of rocks and is regarded as a real material property. The uniaxial compressive strength, in contrast, is dependent on the experimental setup and represents the maximum or short-term laboratory strength of rocks (BIENIAWSKI 1967, MARTIN & CHANDLER 1994, READ et al. 1998). This was confirmed by tests of Tittling granite, which were loaded beyond the crack damage stress. One specimen failed during the phase of constantly applied load and a second sample showed clear indications of considerable damage accumulation but without failure during the period of loading.

- **The Kaiser effect**:

  In previously stressed samples, the Kaiser effect describes the delay of the onset of cracking during a second compression (KAISER 1950). The phenomenon of the Kaiser effect was observed in those rock types with a significant cracking activity in the phase of stable crack growth like Posta sandstone, Flossenbürg granite and Tittling granite. When the crack damage stress was exceeded, a

correlation between previous stress and onset of microcracking existed but was no longer clearly identifiable. The Kaiser effect is blurred because additional crack initiation or propagation occurred in the second loading test at a considerably lower stress level near the crack initiation stress. In Laas marble, only minor cracking events occurred in the pre-failure phase and thus the Kaiser effect was not as pronounced as in other rock types. Still, the number of AE until maximum stress decreased with an increasing preload. In the brittle Dietfurt limestone, a delay in the onset of microcracking could not be observed because the formation of microcracks did not occur until shortly before final collapse of the rock.

The results show that an influence on the laboratory rock strength is given only if the previously applied load exceeded the crack damage stress. The deformability, however, is strongly affected as soon as the crack initiation stress is exceeded and a permanent damage is induced. This makes clear that a changing stress magnitude affects the mechanical properties of rocks when the critical stress levels of crack initiation and crack damage are exceeded.

Petrographic thin section analysis showed several characteristics of preexisting and stress-induced microcracks. In granite, a significant number of open, closed and healed microcracks as well as flaws have already existed in the intact samples. In feldspar minerals, flaws are present along cleavage planes, twin planes and along the grain boundaries of alteration products. In quartz, single, localized high aspect ratio cracks are present, whereas biotite is characterized by the lack of intragranular microcracks. At the boundary to adjacent minerals, however, cracks initiate from the corners of mica into the neighboring grains. When loaded beyond the crack damage threshold, an increase in load-parallel intragranular, transgranular and grain boundary cracks was apparent. The initiation of microcracks generally started at preexisting cracks and grain boundaries. In Posta sandstone, the formation of localized cracks could not be observed in the obtained thin sections. It is supposed that the deformation of the porous sandstone largely takes place in the form of grain compaction instead of fracturing. The formation of localized shear planes begins shortly before failure and is supposed to be limited to a narrow area near the final failure planes so that the surrounding material is largely undisturbed. The analysis of Pechbrunn basalt showed that no microcracks existed before loading and cracks only formed shortly before final failure. Crack initiation and propagation occur at heterogeneities in the form of phenocrysts of olivine or pyroxene and preexisting intragranular cracks in the phenocrysts act as stress raisers for crack growth.

9 Outlook

The efficiency of rock excavation in TBM tunneling is strongly dependent on the primary stress state and the redistribution of stresses in the tunnel face. Stress changes may on the one hand induce face-parallel fractures, which can enhance the rock chipping process in areas of reduced in-situ stresses but can also cause cutting tool damage or increased wear. On the other hand, a high confinement in the areas of high principal stresses may impede the rock fragmentation process. Within the excavation face, the mechanisms of rock fracture strongly change from the center towards the outer areas.

In order to improve the TBM performance in high stress environments, it is necessary to understand the effect of stresses and stress changes on rock excavation in different lithologies. The first step are in-situ stress measurements in order to gain information about stress magnitudes and orientation of the principal stresses in the project area. Using the results from stress measurements, three-dimensional numerical modelling of the stresses around the excavation and especially in the tunnel face can reveal areas of high stresses and stress relaxation (READ et al. 1998, EBERHARDT 2001, READ et al. 1998, KAISER et al. 2001). Furthermore, monitoring of microseismic events in the tunnel face can provide quantitative information about the location, the depth and the intensity of stress-induced damage ahead of the tunnel face. During an ongoing tunnel advance, however, conducting microseismic monitoring might be difficult to enforce, since the installation of the sensors is a time-consuming procedure requiring additional drillings near the future excavation.

Another approach are core drillings in the tunnel face at different positions, including the center and outer areas of the face. The drillings and core material from the tunnel face would be useful for the investigation of several aspects:

- Examination of the core material (ultrasonic testing, fluorescent thin sections): Investigation of the extent and intensity of excavation and stress-induced damage like core disking or stress relaxation cracks with a focus on the distribution of damage in the excavation face
- Petrographic fracture analysis on fluorescent thin sections (volume, orientation and length of microcracks, see Section 3.5): Investigation of the mechanisms responsible for crack initiation and of the influence of stress rotation on crack propagation
- Borehole tests in radial drillings in roof, floor and walls (stress measurements, borehole breakouts): Investigation of the depth of failure and estimation of principal stress orientation and stress magnitudes

In tunneling, a number of geological, geotechnical and machine parameters affect the net performance of TBM. The mutual influence and interaction of the parameters is complex and science is far away from fully understanding their correlations and dependencies. At present, a reasonable approach for assessing the net performance of TBM are in-situ penetration tests. A detailed description of the test procedure and the analysis of machine data is given in WILFING (2016). Still, a quantification of the influence of high primary stresses on TBM performance is an important task for future research. For a reasonable prognosis of penetration rate and cutter wear, in-situ penetration tests in an intact, isotropic and homogeneous rock mass could help to assess the influence of the stress state. Further influences like different machine and rock properties or the existence of joints and faults must be excluded for a clear identification of stress effects.

Beside in-situ investigations, laboratory tests are required to approach the influence of stress rotation and changes in the stress magnitude on the rock properties. Stress rotation affects the propagation of microcracks and causes an accumulation of damage in rocks. EBERHARDT (2001, Fig. 20) assumes that stress-induced damage accumulates by rotating the applied stresses. When changing the loading direction, additional damage occurs because of a new propagation of microcracks. In this work, tests on pre-damaged rocks were performed in the same direction as the previous load. In order to approach the influence of stress rotation on rock properties, additional uniaxial compressive tests on cubic rock samples with a change in the applied stress direction are proposed.

10 Bibliography

AKI, K. & RICHARDS, P.G. (2009): Quantitative seismology. – 700 pp., Sausalito (Univ. Science Books).

ALBER, M. (2008a): An integrated approach to penetration, advance rates and disc cutter wear for hard rock TBM drives. – Geomech. Tunnelling, 1 (1): 29–37.

ALBER, M. (2008b): Stress dependency of the Cerchar abrasivity index (CAI) and its effects on wear of selected rock cutting tools. – Tunn. Undergr. Sp. Tech., 23 (4): 351–359.

AMANN, F., BUTTON, E.A., EVANS, K.F., GISCHIG, V.S. & BLÜMEL, M. (2011): Experimental study of the brittle behavior of clay shale in rapid unconfined compression. – Rock Mech. Rock Eng., 44 (4): 415–430.

ASTM E1316-16 (2016): Standard terminology for nondestructive examinations. – 44 pp., West Conshohocken (ASTM International).

ATKINSON, B.K. (ed.) (1987): Fracture mechanics of rock. – 534 pp., London (Academic Press).

AYDIN, A. & JOHNSON, A.M. (1978): Development of faults as zones of deformation bands and as slip surfaces in sandstone. – Pure appl. geophys., 116: 931–942.

BÄCKBLOM, G. & MARTIN, C.D. (1999): Recent experiments in hard rocks to study the excavation response: Implications for the performance of a nuclear waste geological repository. – Tunn. Undergr. Sp. Tech., 14 (3): 377–394.

BANCROFT, S. (1985): An Algebraic Solution of the GPS Equations. – IEEE Transactions on Aerospace and Electronic Systems, AES-21 (7): 56–59.

BARGEL, H.-J. & SCHULZE, G. (2012): Werkstoffkunde. – 545 pp., Berlin (Springer).

BAUD, P., KLEIN, E. & WONG, T.-F. (2004): Compaction localization in porous sandstones: spatial evolution of damage and acoustic emission activity. – J. Struct. Geol., 26 (4): 603–624.

BEATTIE, A.G. (1983): Acoustic emission, principles and instrumentation. – J. AE, 2 (1-2): 95–128.

BECK, C. (2015): The effect of triaxial preloading on the deformation and fracture behavior of the Tittling granite. – 116 pp., unpub. master thesis, Technical University of Munich, Munich.

BELTZER, A.I. (1988): Acoustics of solids. – 245 pp., Berlin (Springer).

BIENIAWSKI, Z.T. (1967): Mechanism of brittle fracture of rock. – Int. J. Rock Mech. Min. Sci., 4: 395–430.

BLÜMLING, P., BERNIER, F., LEBON, P. & DEREK MARTIN, C. (2007): The excavation damaged zone in clay formations time-dependent behaviour and influence on performance assessment. – Phys. Chem. Earth, 32 (8-14): 588–599.

BOLT, B.A. (1982): Inside the earth. Evidence from earthquakes. – 191 pp., San Francisco (W.H. Freeman).

BORCHARDT-OTT, W. (2009): Kristallographie. Eine Einführung für Naturwissenschaftler. – 372 pp., Berlin (Springer).

BOURBIÉ, T., COUSSY, O. & ZINSZNER, B. (1987): Acoustics of porous media. – 334 pp., Paris (Editions Technip).

BRACE, W.F. & BOMBOLAKIS, E.G. (1963): A note on brittle crack growth in compression. – J. Geophys. Res., 68: 3709–3713.

BRACE, W.F., PAULDING, B.W. & SCHOLZ, C. (1966): Dilatancy in the fracture of crystalline rocks. – J. Geophys. Res., 71 (16): 3939–3953.

BRADY, B.H.G. & BROWN, E.T. (2006): Rock mechanics for underground mining. – 645 pp., Dordrecht (Kluwer Academic Publishers).

BROCHER, J. (2014): Qualitative and quantitative evaluation of two new histrogram limiting binarization algorithms. – Int. J. Image Process., 8 (2): 30–48.

BURKHARD, M. (1993): Calcite twins, their geometry, appearance and significance as stress-strain markers and indicators of tectonic regime: a review. – J. Struct. Geol., 15 (3-5): 351–368.

BUTTKUS, B. (2000): Spectral analysis and filter theory in applied geophysics. – 667 pp., Berlin (Springer).

CAI, M., KAISER, P., TASAKA, Y., MAEJIMA, T., MORIOKA, H. & MINAMI, M. (2004): Generalized crack initiation and crack damage stress thresholds of brittle rock masses near underground excavations. – Int. J. Rock Mech. Min. Sci., 41 (5): 833–847.

CARLSON, S.R. & YOUNG, R.P. (1993): Acoustic emission and ultrasonic velocity study of excavation-induced microcrack damage at the Underground Research Laboratory. – Int. J. Rock Mech. Min. Sci. & Geomech. Abstr., 30 (7): 901–907.

COOK, N.G.W. (1965): The failure of rock. – Int. J. Rock Mech. Min. Sci. & Geomech. Abstr., 2 (4): 389–403.

COSTIN, L.S. (1987): Time-dependent deformation and failure. – In: ATKINSON, B.K. (ed.): Fracture mechanics of rock, London (Academic Press): 167–215.

CRAMPIN, S. & LOVELL, J.H. (1991): A decade of shear-wave splitting in the earth's crust: what does it mean? what use can we make of it? and what should we do next? – Geophys. J. Int., 107: 387–407.

CRUDEN, D.M. (1971): The form of the creep law for rock under uniaxial compression. – Int. J. Rock Mech. Min. Sci. & Geomech. Abstr., 8 (2): 105–126.

CRUDEN, D.M. (1974): The static fatigue of brittle rock under uniaxial compression. – Int. J. Rock Mech. Min. Sci. & Geomech. Abstr., 11: 67–73.

DEERE, D.U. & MILLER, R.P. (1966): Engineering classification and index properties for intact rock. Technical Report No. AFWL-TR-65-116. – 300 pp., Urbana.

DIEDERICHS, M., KAISER, P. & EBERHARDT, E. (2004): Damage initiation and propagation in hard rock during tunnelling and the influence of near-face stress rotation. – Int. J. Rock Mech. Min. Sci., 41 (5): 785–812.

DIEDERICHS, M.S. (2003): Rock fracture and collapse under low confinement conditions. – Rock Mech. Rock Eng., 36 (5): 339–381.

DIEDERICHS, M.S. (2007): The 2003 Canadian Geotechnical Colloquium: Mechanistic interpretation and practical application of damage and spalling prediction criteria for deep tunnelling. – Can. Geotech. J., 44 (9): 1082–1116.

DIN EN 14579 (2005): Prüfverfahren für Naturstein - Bestimmung der Geschwindigkeit der Schallausbreitung. – 15 pp., Berlin (Beuth).

DUSSEAULT, M.B. & FORDHAM, C.J. (1993): Time-dependent behavior of rocks. – In: HUDSON, J.A. (ed.): Comprehensive rock engineering, 3 (Pergamon Press): 119–149.

EBERHARDT, E. (1998): Brittle rock fracture and progressive damage in uniaxial compression. – 359 pp., PhD, University of Saskatchewan, Saskatoon.

EBERHARDT, E. (2001): Numerical modelling of three-dimension stress rotation ahead of an advancing tunnel face. – Int. J. Rock Mech. Min. Sci., 38: 499–518.

EBERHARDT, E. & STEAD, D. (1999): The influence of mineralogy on the initiation of microfractures in granite. – In: VOUILLE, G. & BEREST, P. (eds.): Proc. 9th ISRM Congress on Rock Mechanics, Paris, Rotterdam (Balkema): 1007–1010.

EBERHARDT, E., STEAD, D. & STIMPSON, B. (1999a): Quantifying progressive pre-peak brittle fracture damage in rock during uniaxial compression. – Int. J. Rock Mech. Min. Sci., 36: 361–380.

EBERHARDT, E., STEAD, D., STIMPSON, B. & READ, R.S. (1998): Identifying crack initiation and propagation thresholds in brittle rock. – Can. Geotech. J., 35: 222–233.

EBERHARDT, E., STIMPSON, B. & STEAD, D. (1999b): Effects of grain size on the initiation and propagation thresholds of stress-induced brittle fractures. – Rock Mech. Rock Eng., 32 (2): 81–99.

ELLECOSTA, P. (in prep.): Determining abrasivity for mechanical excavation in hard rock, PhD, Technical University of Munich, Munich.

Elsys AG (2014): TranAX 3 User Manual. – 224 pp.

ENGELDER, T. (1984): The time-dependent strain relaxation of Algerie Granite. – Int. J. Rock Mech. Min. Sci. & Geomech. Abstr., 21 (2): 63–73.

ENGELDER, T. (1987): Joints and shear fractures in rock. – In: ATKINSON, B.K. (ed.): Fracture mechanics of rock, London (Academic Press): 27–69.

FABRE, G. & PELLET, F. (2006): Creep and time-dependent damage in argillaceous rocks. – Int. J. Rock Mech. Min. Sci., 43 (6): 950–960.

FAIRHURST, C.E. & HUDSON, J.A. (1999): Draft ISRM suggested method for the complete stress-strain curve for intact rock in uniaxial compression. ISRM Suggested Methods: 2nd Series. – Int. J. Rock Mech. Min. Sci., 36 (3): 279–289.

FINCK, F. (2005): Untersuchung von Bruchprozessen in Beton mit Hilfe von Schallemissionsanalyse. – 147 pp., PhD, University of Stuttgart, Stuttgart.

First Quantum Minerals LTD. (n.d.): Pyhäsalmi Mine Oy - Bringing ore to the surface (Brochure).

FONSEKA, G.M., MURRELL, S. & BARNES, P. (1985): Scanning electron microscope and acoustic emission studies of crack development in rocks. – Int. J. Rock Mech. Min. Sci. & Geomech. Abstr., 22 (5): 273–289.

FORTIN, J., STANCHITS, S., DRESEN, G. & GUEGUEN, Y. (2009): Acoustic emissions monitoring during inelastic deformation of porous sandstone: comparison of three modes of deformation. – Pure appl. geophys., 166 (5-7): 823–841.

FRENZEL, C. (2010): Verschleißkostenprognose für Schneidrollen bei maschinellen Tunnelvortrieben in Festgesteinen. – 64 pp., München (Pfeil).

GEHRING, K. (1995): Leistungs- und Verschleißprognosen im maschinellen Tunnelbau. – Felsbau, 13 (6): 439–448.

GEHRING, K. (1997): Classification of drillability, cuttability, borability and abrasivity in tunnelling. – Felsbau, 15 (3): 183–191.

GEIGER, L. (1910): Herdbestimmung bei Erdbeben aus den Ankunftszeiten. – Kgl. Ges. d. Wiss. Nachrichten Math.-phys. Klasse (4): 231–349.

Geological Survey of Finland (2012): Digital bedrock map of Finland 1: 200 000.

GIGL, L. (2015): Analyse von Mikrorissen mit Hilfe von Fluoreszenzmikroskopie. – 34 pp., unpub. bachelor thesis, Technical University of Munich, Munich.

GONG, Q.M., YIN, L.J., WU, S.Y., ZHAO, J. & TING, Y. (2012): Rock burst and slabbing failure and its influence on TBM excavation at headrace tunnels in Jinping II hydropower station. – Engineering Geology, 124: 98–108.

GORBATSEVICH, F. (2003): Decompaction mechanism of deep crystalline rocks under stress relief. – Tectonophysics, 370 (1-4): 121–128.

GOTTSTEIN, G. (2013): Physikalische Grundlagen der Materialkunde. – 670 pp., Berlin (Springer).

GRIFFITH, A.A. (1920): The phenomena of rupture and flow in solids. – Phil. Trans., 221: 163–198.

GRIFFITH, A.A. (1924): The theory of rupture. – In: BIEZENO, C.B. & BURGERS, J.M. (eds.): Proceedings of the first international congress for applied mechanics, Delft: 55–63.

GROSSE, C.U. (1996): Quantitative zerstörungsfreie Prüfung von Baustoffen mittels Schallemissionsanalyse und Ultraschall. – 168 pp., PhD, University of Stuttgart, Stuttgart.

GROSSE, C.U. & LINZER, L.M. (2010): Signal-based AE analysis. – In: GROSSE, C.U. & OHTSU, M. (eds.): Acoustic Emission Testing, Berlin (Springer): 53–99.

GROSSE, C.U. & OHTSU, M. (eds.) (2010): Acoustic Emission Testing. – 396 pp., Berlin (Springer).

GRUBER, J. (2015): Einfluss der Belastungsgeschwindigkeit beim einaxialen Druckversuch auf das Verformungsverhalten von Gesteinen. – 31 pp., unpub. bachelor thesis, Technical University of Munich, Munich.

GRUNERT, S. (2007): Der Elbsandstein: Vorkommen, Verwendung, Eigenschaften. – Geologica Saxonica - Journal of Central European Geology, 52/53: 3–22.

GUÉGUEN, Y. & PALCIAUSKAS, V. (1994): Introduction to the physics of rocks. – 294 pp., Princeton (Princeton University Press).

HAKALA, M. (2014): State of stress at the depth of planned Laguna Caverns in Pyhäsalmi. – Presentation, LAGUNA-LBNO General Meeting in Helsinki, Finland.

HAKALA, M., KUULA, H., MATINLASSI, M., SOMERVUORI, P., SYRJÄNEN, P. & TOLPPANEN, P. (2002): Analyses of tunnel stress failures at Pyhäsalmi mine. Posiva Working Report 2002-28. – 104 pp., Helsinki (Posiva Oy).

HATZOR, Y.H. & PALCHIK, V. (1997): The influence of grain size and porosity on crack initiation stress and critical flaw length in dolomites. – Int. J. Rock Mech. Min. Sci., 34 (5): 805–816.

HAWKES, I. & MELLOR, M. (1970): Uniaxial testing in rock mechanics laboratories. – Eng. Geol., 4 (3): 179–285.

HEIDBACH, O., TINGAY, M., BARTH, A., REINECKER, J., KURFEß, D. & MÜLLER, B. (2008): The world stress map database release 2008.

HELM, W. (ed.) (2013): Granit. – 264 pp., Hauzenberg (Granitzentrum Bayerischer Wald).

HOEK, E. (1998): Tunnel support in weak rock. Key note address. – Symposium of Sedimentary Rock Engineering, Taipei, Taiwan, November 20-22, 1998.

HOEK, E. & BIENIAWSKI, Z.T. (1965): Brittle rock fracture propagation in rock under compression. – Int. J. Fract. Mech., 1 (3): 137–155.

HOEK, E. & BROWN, E.T. (1980): Underground excavations in rock. – 527 pp., London (Institution of Mining and Metallurgy).

HOEK, E. & BROWN, E.T. (1997): Practical estimates of rock mass strength. – Int. J. Rock Mech. Min. Sci., 34 (8): 1165–1186.

HOLCOMB, D.J. (1993): General theory of the Kaiser Effect. – Int. J. Rock Mech. Min. Sci. & Geomech. Abstr., 30 (7): 929–935.

HOLT, R.M., BRIGNOLI, M. & KENTER, C.J. (2000): Core quality: quantification of coring-induced rock alteration. – Int. J. Rock Mech. Min. Sci., 37: 889–907.

HORNUNG, M. (2015): Untersuchungen zum Deformationsverhalten verschiedener Gesteinstypen mit Hilfe von Querdehnungsmessungen. – 34 pp., unpub. bachelor thesis, Technical University of Munich, Munich.

INSK (n.d.): INSK kompakt: die internationale Naturwerksteinkartei für den aktuellen Markt. Marmor Sandstein Sedimentgesteine fest und weich, 6, Ulm (Ebner Verlag).

IRWIN, G.R. (1957): Analysis of stresses and strains near the end of a crack traversing a plate. – J. Appl. Mech., 24: 361–364.

ISRM (1978): Suggested methods for the quantitative description of discontinuities in rock masses. – Int. J. Rock Mech. Min. Sci. & Geomech. Abstr., 15: 319–368.

JAEGER, J.C., COOK, N.G.W. & ZIMMERMAN, R.W. (2007): Fundamentals of rock mechanics. – 475 pp., Malden (Blackwell Publishing).

JOHNSTON, D.H., TOKSÖZ, M.N. & TIMUR, A. (1979): Attenuation of seismic waves in dry and saturated rocks: II. Mechanisms. – Geophysics, 44/4: 691–711.

KAIM, M. (1990): Geologie und Petrographie der Basalte Hirschentanz/ Grasfurt und vergleichende Untersuchungen an den Basalten des Teichelberges und Zinster Berges in der Oberpfalz. – 117 pp., unpub. Diploma Thesis, Technical University of Munich, Garching.

KAISER, J. (1950): An investigation into the occurrence of noises in tensile tests or a study of acoustic phenomena in tensile tests, PhD, Technical University of Munich, Munich.

KAISER, P.K. (2005): Tunnel stability in highly stressed, brittle ground - rock mechanics considerations for Alpine tunnelling. – In: LÖW, S. (ed.): Geologie und Geotechnik der Basistunnels am Gotthard und am Lötschberg, Zürich (vdf Hochschulverlag AG an der ETH Zürich): 183–202.

KAISER, P.K., YAZICI, S. & MALONEY, S. (2001): Mining-induced stress change and consequences of stress path on excavation stability - a case study. – Int. J. Rock Mech. Min. Sci., 38: 167–180.

KANG, S.S., ISHIGURO, Y. & OBARA, Y. (2006): Evaluation of core disking rock stress and tensile strength via the compact conical-ended borehole overcoring technique. – Int. J. Rock Mech. Min. Sci., 43 (8): 1226–1240.

KNILL, J.L., FRANKLIN, J.A. & MALONE, A.W. (1968): A study of acoustic emission from stressed rock. – Int. J. Rock Mech. Min. Sci., 5: 87–121.

KRANZ, R.L. (1983): Microcracks in rocks: a review. – In: FRIEDMANN, M. & TOKSÖZ, M.N. (eds.): Continental tectonics: Structure, kinematics and dynamics, Amsterdam (Elsevier): 449–480.

KRAUTKRÄMER, J. & KRAUTKRÄMER, H. (1986): Werkstoffprüfung mit Ultraschall. – 722 pp., Berlin (Springer).

KUNIN, I.A. (2012): Elastic media with microstructure II. Three-dimensional models. – 279 pp., Berlin (Springer).

KURITA, F. & FUJII, N. (1979): Stress memory of crystalline rock in acoustic emission. – Geophys. Res. Lett., 6 (1): 9–12.

KURZ, J.H. (2006): Verifikation von Bruchprozessen bei gleichzeitiger Automatisierung der Schallemissionsanalyse an Stahl- und Stahlfaserbeton. – 197 pp., PhD, University of Stuttgart, Stuttgart.

KURZ, J.H., KÖPPEL, S., LINZER, L.M., SCHECHINGER, B. & GROSSE, C.U. (2010): Source localization. – In: GROSSE, C.U. & OHTSU, M. (eds.): Acoustic Emission Testing, Berlin (Springer): 101–147.

LAJTAI, E.Z. (1974): Brittle fracture in compression. – Int. J. Fracture, 10 (4): 525–536.

LAJTAI, E.Z. & LAJTAI, V.N. (1974): The evolution of brittle fracture in rocks. – J. geol. Soc. London, 130: 1–18.

LAVROV, A. (2003): The Kaiser effect in rocks: principles and stress estimation techniques. – Int. J. Rock Mech. Min. Sci., 40 (2): 151–171.

LAWN, B.R. & WILSHAW, T.R. (1975): Fracture of brittle solids. – 204 pp., Cambridge (Cambridge University Press).

LEPIQUE, M. (2008): Empfehlung Nr. 10 des Arbeitskreises 3.3 "Versuchstechnik Fels" der Deutschen Gesellschaft für Geotechnik e. V.: Indirekter Zugversuch an Gesteinsproben - Spaltzugversuch. – Bautechnik, 85 (9): 623–627.

LI, C. & NORDLUND, E. (1993a): Assessment of damage in rock using the Kaiser effect of acoustic emission. – Int. J. Rock Mech. Min. Sci. & Geomech. Abstr., 30 (7): 943–946.

LI, C. & NORDLUND, E. (1993b): Experimental verification of the Kaiser effect in rocks. – Rock Mech. Rock Eng., 26 (4): 333–351.

LI, Y. & SCHMITT, D.R. (1998): Drilling-induced core fractures and in situ stress. – J. Geophys. Res., 103 (B3): 5225–5239.

LIM, S.S. & MARTIN, C.D. (2010): Core disking and its relationship with stress magnitude for Lac du Bonnet granite. – Int. J. Rock Mech. Min. Sci., 47 (2): 254–264.

LIM, S.S., MARTIN, C.D. & ÅKESSON, U. (2012): In-situ stress and microcracking in granite cores with depth. – Eng. Geol., 147-148: 1–13.

LIN, Q., THAM, L., YEUNG, M. & LEE, P. (2004): Failure of granite under constant loading. – Int. J. Rock Mech. Min. Sci., 41 (3): 49–54.

LIN, Q.X., LIU, Y.M., THAM, L.G., TANG, C.A., LEE, P. & WANG, J. (2009): Time-dependent strength degradation of granite. – Int. J. Rock Mech. Min. Sci., 46 (7): 1103–1114.

LOWRIE, W. (2007): Fundamentals of geophysics. – 381 pp., Cambridge (Cambridge University Press).

MAEDA, N. (1985): A method for reading and checking phase time in auto-processing system of seismic wave data. – Zisin (Journal of the Seismological Society of Japan. 2nd ser.), 38 (3): 365–379.

MAHABADI, O.K., Tatone, B. S. A. & GRASSELLI, G. (2014): Influence of microscale heterogeneity and microstructure on the tensile behavior of crystalline rocks. – J. Geophys. Res. Solid Earth, 119 (7): 5324–5341.

MARTIN, C.D. (1993): The strength of massive Lac du Bonnet granite around underground openings. – 278 pp., PhD, University of Manitoba, Winnipeg.

MARTIN, C.D. (1997): The effect of cohesion loss and stress path on brittle rock strength. – Can. Geotech. J., 34: 698–725.

MARTIN, C.D. & CHANDLER, N.A. (1994): The progressive fracture of Lac du Bonnet Granite. – Int. J. Rock Mech. Min. Sci. & Geomech. Abstr., 31 (6): 643–659.

MARTIN, C.D., KAISER, P.K. & MCCREATH, D.R. (1999a): Hoek–Brown parameters for predicting the depth of brittle failure around tunnels. – Can. Geotech. J., 36: 136–151.

MARTIN, C.D. & STIMPSON, B. (1994): The effect of sample disturbance on laboratory properties of Lac du Bonnet granite. – Can. Geotech. J., 31 (5): 692–702.

MARTIN, C.D., TANNANT, D.D., YZICI, S. & KAISER, P.K. (1999b): Stress path and instability around mine openings. – In: VOUILLE, G. & BEREST, P. (eds.): Proc. 9th ISRM Congress on Rock Mechanics, Paris, Rotterdam (Balkema): 311–315.

MARTINO, J.B. & CHANDLER, N.A. (2004): Excavation-induced damage studies at the Underground Research Laboratory. – Int. J. Rock Mech. Min. Sci., 41 (8): 1413–1426.

MAVKO, G., MUKERJI, T. & DVORKIN, J. (2009): The rock physics handbook. Tools for seismic analysis in porous media. – 511 pp., Cambridge (Cambridge University Press).

MCCLINTOCK, F.A. & WALSH, J.B. (1962): Friction of Griffith cracks in rock under pressure. – Proc. Fourth U.S. Congr. Appl. Mech.: 1015–1021.

MEGLIS, I.L., ENGELDER, T. & GRAHAM, E.K. (1991): The effect of stress-relief on ambient microcrack porosity in core samples from the Kent Cliffs (New York) and Moodus (Connecticut) scientific research boreholes. – Tectonophysics, 186: 163–173.

MEIßNER, G. (2015): Untersuchungen zu Verformungsverhalten und Rissbildung unter einaxialer Druckbelastung mittels Schallemissionsanalyse am Beispiel des Tittlinger Granits. – 127 pp., unpub. master thesis, Technical University of Munich, Munich.

MEYER, R.K.F. & SCHMIDT-KALER, H. (1983): Erdgeschichte sichtbar gemacht. Ein geologischer Führer durch die Altmühlalb. – 260 pp., Munich (Bayerisches Geologisches Landesamt).

MOLLEMA, P.N. & ANTONELLINI, M.A. (1996): Compaction bands: a structural analog for anti-mode I cracks in aeolian sandstone. – Tectonophysics, 267 (1-4): 209–228.

MUTSCHLER, T. (2004): Neufassung der Empfehlung Nr. 1 des Arbeitskreises "Versuchstechnik Fels" der Deutschen Gesellschaft für Geotechnik e. V.: Einaxiale Druckversuche an zylindrischen Gesteinsprüfkörpern. – Bautechnik, 81 (10): 825–834.

NÄHER, U. (1989): Geologische Kartierung der näheren Umgebung Kulmain (Oberpfalz) im Maßstab 1:10000 und einer Korrelation von Chemismus und Petrographie nordostbayerischer Basalte mit ihrem gesteinstechnischen Verhalten, am Beispiel der Basalte des Zinster Berges, des Großen Teichelberges, des Hirschentanzes und des Grasfurter Vorkommens. – 85 pp., unpub. Diploma Thesis, Technical University of Munich, Garching.

NICKSIAR, M. & MARTIN, C.D. (2012): Evaluation of Methods for Determining Crack Initiation in Compression Tests on Low-Porosity Rocks. – Rock Mech. Rock Eng., 45 (4): 607–617.

NICKSIAR, M. & MARTIN, C.D. (2013): Crack initiation stress in low porosity crystalline and sedimentary rocks. – Eng. Geol., 154: 64–76.

NICKSIAR, M. & MARTIN, C.D. (2014): Factors affecting crack initiation in low porosity crystalline rocks. – Rock Mech. Rock Eng., 47 (4): 1165–1181.

NUIJTEN, G. & ZITO, M. (2012): Summary Technical Board (WP2+WP3). – Presentation, LAGUNA-LBNO General Meeting at Cern, Geneva.

OHNAKA, M. & MOGI, K. (1982): Frequency characteristics of acoustic emission in rocks under uniaxial compression and its relation to the fracturing process to failure. – J. Geophys. Res., 87 (B5): 3873–3884.

OKRUSCH, M. & MATTHES, S. (2014): Mineralogie. Eine Einführung in die spezielle Mineralogie, Petrologie und Lagerstättenkunde. – 726 pp., Berlin (Springer).

OLSSON, W.A. & PENG, S.S. (1976): Microcrack nucleation in marble. – Int. J. Rock Mech. Min. Sci. & Geomech. Abstr., 13 (2): 53–59.

OLYMPUS (2015): Ultrasonic Transducers - wedges, cables, test blocks. – 51 pp.

PASSCHIER, C.W. & TROUW, R.A.J. (2005): Microtectonics. – 366 pp., Berlin (Springer).

PATERSON, M.S. & WONG, T.-F. (2005): Experimental rock deformation - the brittle field. – 347 pp., Berlin (Springer).

PENG, S. & JOHNSON, A.M. (1972): Crack growth and faulting in cylindrical specimens of Chelmsford Granite. – Int. J. Rock Mech. Min. Sci., 9: 37–86.

PENG, S.S. (1973): Time-dependent aspects of rock behavior as measured by servocontrolled hydraulic testing machine. – Int. J. Rock Mech. Min. Sci. & Geomech. Abstr., 10: 235–246.

PERRAS, M.A. & DIEDERICHS, M.S. (2016): Predicting excavation damage zone depths in brittle rocks. – J. Rock Mech. Geotech. Eng., 8 (1): 60–74.

QUEISSER, A. (1988): Mineralogische Aspekte zur Verwitterungsanfälligkeit des Schilfsandsteins aus dem Raum Bamberg. – Acta Albertina Ratisbonensia, 45: 67–94.

QUESSEL, M. (2014): Bewertung der Schallemissionsanalyse zur Detektion von Mikrorissen beim Einaxialen Druckversuch. – 81 pp., unpub. master thesis, Technical University of Munich, Munich.

RAITH, M. (2013): Schallemissionsanalyse bei Pulloutexperimenten an Verbunddübeln. – 98 pp., unpub. master thesis, Technical University of Munich, München.

RAO, M.V.M.S. & RAMANA, Y.V. (1992): A study of progressive failure of rock under cyclic loading by ultrasonic and AE monitoring techniques. – Rock Mech. Rock Eng., 25 (4): 237–251.

RAUCH, R. (2016): Einfluss des Gebirges auf die Vortriebsleistung und den Diskenverschleiß beim tiefliegenden TBM-Vortrieb am Koralmtunnel (Österreich). – 73 pp., unpub. master thesis, Technical University of Munich, Munich.

READ, R.S., CHANDLER, N.A. & DZIK, E.J. (1998): In situ strength criteria for tunnel design in highly-stressed rock masses. – Int. J. Rock Mech. Min. Sci., 35 (3): 261–278.

REYNOLDS, J.M. (2011): An introduction to applied and environmental geophysics. – 696 pp., Chichester (Wiley-Blackwell).

RICHART, F.E., BRANDTZAEG, A. & BROWN, R.L. (1928): A study of the failure of concrete under combined compressive stresses. – University of Illinois Bulletin, 185 (12): 1–104.

Rocscience Inc. (2014): RS³ Version 1.0 – 3D Finite Element Analysis for Rock and Soil. www.rocscience.com, Toronto.

RUBBIA, A. (2013a): LAGUNA/LBNO: status and plans. – Presentation, ISOUPS 2013 (International Symposium: Opportunities in Underground Physics for Snowmass).

RUBBIA, A. (2013b): LAGUNA-LBNO: design of an underground neutrino observatory coupled to long baseline neutrino beams from CERN. – J. Phys.: Conf. Ser., 408: 12006.

SAYERS, C.M. (1990): Orientation of microcracks formed in rocks during strain relaxation. – Int. J. Rock Mech. Min. Sci. & Geomech. Abstr., 27 (5): 437–439.

SCHALLHAMMER, K. (2014): Felsmechanische und petrographische Untersuchungen der Schäden an Gesteinsproben durch einaxiale Druckbelastung. – 96 pp., unpub. master thesis, Technical University of Munich, Munich.

SCHECHINGER, B. (2005): Schallemissionsanalyse zur Überwachung der Schädigung von Stahlbeton. – 149 pp., PhD, ETH Zurich, Zurich.

SCHIMATZEK, J. & KNATZ, H. (1976): Die Beurteilung der Bearbeitbarkeit von Gesteinen durch Schneid- und Rollenbohrwerkzeuge. – Erzmetall, 29 (3): 113–119.

SCHINDELIN, J., ARGANDA-CARRERAS, I., FRISE, E., KAYNIG, V., LONGAIR, M., PIETZSCH, T., PREIBISCH, S., RUEDEN, C., SAALFELD, S., SCHMID, B., TINEVEZ, J.-Y., WHITE, D.J., HARTENSTEIN, V., ELICEIRI, K., TOMANCAK, P. & CARDONA, A. (2012): Fiji: an open-source platform for biological-image analysis. – Nature methods, 9 (7): 676–682.

SCHNEIDER, C. (2014): Der Einfluss von Dämpfungsmaterialien auf Festigkeit und Verformung von Gesteinen. – 53 pp., unpub. bachelor thesis, Technical University of Munich, Munich.

SCHNEIDER, C.A., RASBAND, W.S. & ELICEIRI, K.W. (2012): NIH Image to ImageJ: 25 years of image analysis. – Nat. Meth., 9 (7): 671–675.

SCHÖN, J. (1996): Physical properties of rocks. Fundamentals and principles of petrophysics. – 583 pp., Oxford (Pergamon).

SHIOTANI, T. (2010): Parameter analysis. – In: GROSSE, C.U. & OHTSU, M. (eds.): Acoustic Emission Testing, Berlin (Springer): 41–51.

SIMMONS, G. & RICHTER, D. (1976): Microcracks in rocks. – In: STRENS, R.G. (ed.): The physics and chemistry of minerals and rocks, New York (Wiley): 105–137.

SIREN, T., KANTIA, P. & RINNE, M. (2015): Considerations and observations of stress-induced and construction-induced excavation damage zone in crystalline rock. – Int. J. Rock Mech. & Min. Sci., 73: 165–174.

SKOČEK, V. & VALEČKA, J. (1983): Paleogeography of the late Cretaceous Quadersandstein of Central Europe. – Palaeogeogr., Palaeoclimatol., Palaeoecol., 44: 71–92.

SPRUNT, E.S. & BRACE, W.F. (1974): Direct observation of microcavities in crystalline rocks. – Int. J. Rock Mech. Min. Sci. & Geomech. Abstr., 11 (4): 139–150.

STACEY, T.R. (1982): Contribution to the mechanism of core discing. – J. South. Afr. Inst. Min. Metall., 9: 269–276.

STANCHITS, S.A., LOCKNER, D.A. & PONOMAREV, A.V. (2003): Anisotropic changes in p-wave velocity and attenuation during deformation and fluid infiltration of granite. – Bull. Seismological Soc. Amer., 93 (4): 1803–1822.

TAPPONIER, P. & BRACE, W.F. (1976): Development of stress-induced microcracks in Westerley Granite. – Int. J. Rock Mech. Min. Sci. & Geomech. Abstr., 13: 103–112.

TAPPONNIER, P. & BRACE, W. (1976): Development of stress-induced microcracks in Westerly Granite. – Int. J. Rock Mech. Min. Sci. & Geomech. Abstr., 13 (4): 103–112.

TARKOY, P.J. & MARCONI, M. (1991): Difficult rock comminution and associated geological conditions. – Tunnelling '91, Sixth International Symposium, 14-18 April 1991, London: 195–207.

TEUFEL, L.W. (1989): Acoustic emissions during anelastic strain recovery of cores from deep boreholes. – In: KHAIR, A.W. (ed.): Rock mechanics as a guide for efficient utilization of natural resources. Proc. of the 30th U.S. Symposium, Morgantown, Rotterdam (Balkema): 269–276.

THOMPSON, B.D., YOUNG, R.P. & LOCKNER, D.A. (2006): Fracture in Westerly Granite under AE feedback and constant strain rate loading: Nucleation, quasi-static propagation, and the transition to unstable fracture propagation. – Pure appl. geophys., 163 (5-6): 995–1019.

THURO, K. (1998): Bohrbarkeit beim konventionellen Sprengvortrieb. Geologisch-felsmechanische Untersuchungen anhand sieben ausgewählter Tunnelprojekte. – 145 pp., Münchner Geologische Hefte, B1, Munich (Verlag Dr. Friedrich Pfeil).

Thuro, K. (2002): Geologisch-felsmechanische Grundlagen der Gebirgslösung im Tunnelbau. – 160 pp., Münchner Geologische Hefte, B18.

THURO, K., PLINNINGER, R.J., ZÄH, S. & SCHÜTZ, S. (2001): Scale effects in rock strength properties. Part I: Unconfined compressive test and Brazilian test. – In: SÄRKKÄ, P. & ELORANTA, P. (eds.): Rock mechanics, Lisse (Swets & Zeitlinger): 169–174.

TOKSÖZ, M.N., JOHNSTON, D.H. & TIMUR, A. (1979): Attenuation of seismic waves in dry and saturated rocks: I. Laboratory measurements. – Geophysics, 44 (4): 681–690.

TROLL, G. (1964): Das Intrusivgebiet von Fürstenstein (Bayerischer Wald). – Geologica Bavarica, 52.

TRZASKA, W.H. (2012): Site selection for the new generation of giant neutrino detectors. – J. Phys.: Conf. Ser., 375: 42060.

UNTERWURZACHER, M. & OBOJES, U. (2012): White marble from Laas (Lasa), South Tyrol - its occurence, use and petrographic-isotopical characterisation. – Austrian J. Earth Sci., 105/3: 26–37.

VILLENEUVE, M.C. (2008): Examination of geological influece on machine excavation of highly stressed tunnels in massive hard rock. – 788 pp., PhD, Queen's University Kingston, Kingston.

VILLENEUVE, M.C. (2015): Geomechanical characterisation of hard rocks for disc cutting in deep tunnels. – In: LOLLINO, G., GIORDAN, D., THURO, K., CARRANZA-TORRES, C., WU, F., MARINOS, P. & DELGADO, C. (eds.): Engineering geology for society and territory - Volume 6. Applied geology for major engineering projects, Cham (Springer): 439–442.

WARPINSKI, N.R., TEUFEL, L.W., LORENZ, J.C. & HOLCOMB, D.J. (1993): Topical report. Core based stress measurements: A guide to their application. – 150 pp., Albuquerque.

WAWERSIK, W.R. & FAIRHURST, C. (1970): A study of brittle rock fracture in laboratory compression experiments. – Int. J. Rock Mech. Min. Sci., 7: 561–575.

WEH, M. (2007): TBM-Hargesteinsvortriebe auf den Abschnitten Raron und Steg am Lötschberg: Erfahrungen und vertragliche Konsequenzen. – Kolloquium "Anspruchsvolle maschinelle Vortrieb im Fels", ETH Zurich, 31.05.2007.

WIESER, C., KÄSLING, H., NUIJTEN, G. & THURO, K. (2015a): Monitoring microcrack evolution during core relaxation from high in-situ stresses by acoustic emission at Pyhäsalmi Mine, Finland. – ISRM Congress 2015 Proceedings, International Symposium on Rock Mechanics, May 10-13, 2015, Montréal. Paper 623.

WIESER, C., KÄSLING, H., RAITH, M., RICHTER, R., MOSER, D., GEMANDER, F., GROSSE, C. & THURO, K. (2015b): Acoustic emission technique to detect micro cracking during uniaxial compression of brittle rocks. – In: LOLLINO, G., GIORDAN, D., THURO, K., CARRANZA-TORRES, C., WU, F., MARINOS, P. & DELGADO, C. (eds.): Engineering geology for society and territory - Volume 6. Applied geology for major engineering projects, Cham (Springer): 465–468.

WILFING, L. (2016): The influence of geotechnical parameters on penetration prediction in TBM tunneling in hard rock. Special focus on the parameter of rock toughness and discontinuity pattern in rock mass. – 168 pp., PhD, Technical University of Munich, Munich.

WINKLER, K.W. & MURPHY, W.F. (1995): Acoustic velocity and attenuation in porous rocks. – In: AHRENS, T.J. (ed.): Rock physics & phase relations, Washington, DC (American Geophysical Union): 20–34.

WOLTER, K.E. & BERCKHEMER, H. (1989): Time dependent strain recovery of cores from the KTB - Deep Drill Hole. – Rock Mech. Rock Eng., 22: 273–287.

WORKMAN, G.L., KISHONI, D. & MOORE, P.O. (eds.) (2007): Nondestructive testing handbook, Ultrasonic Testing, 7. – 600 pp. (American Society for Nondestructive Testing).

XIAO, J.-Q., DING, D.-X., JIANG, F.-L. & XU, G. (2010): Fatigue damage variable and evolution of rock subjected to cyclic loading. – Int. J. Rock Mech. Min. Sci., 47 (3): 461–468.

YOSHIKAWA, S. & MOGI, K. (1989): Experimental studies on the effect of stress history on acoustic emission activity - A possibility for estimation of rock stress. – J. AE, 8 (4): 113–123.

ZAEGE, T. (2012): Untersuchung der Zähigkeit ausgewählter Gesteine. – 48 pp., unpub. bachelor thesis, Technical University of Munich, Munich.

ZANG, A. & BERCKHEMER, H. (1989): Residual stress features in drill cores. – Geophys. J. Int., 99: 621–626.

ZANG, A. & BERCKHEMER, H. (1993): Classification of crystalline drill cores from the KTB deep well based on strain, velocity and fracture Measurements. – Int. J. Rock Mech. Min. Sci. & Geomech. Abstr., 30 (4): 331–342.

ZANG, A., LIENERT, M., ZINKE, J. & BERCKHEMER, H. (1996): Residual strain, wave speed and crack analysis of crystalline cores from the KTB-VB well. – Tectonophysics, 263: 219–234.

ZANG, A. & STEPHANSSON, O. (2010): Stress field of the earth's crust. – 322 pp., Dordrecht (Springer).

URL

www-1 http://www.fracturemechanics.org/fm/griffith.html (last access on March 23, 2016).

www-2 http://imagej.net/BioVoxxel_Toolbox (last access on April 11, 2016).

www-3 http://www.graniteland.de/naturstein/abtswinder-schilfsandstein (last access on March 10, 2016).

Appendix

Appendix I

Table I-1: *Summary of rock mechanical parameters for the characterization of rock properties as mean values with standard deviation and number of tests. σ_u: uniaxial compression strength, E_T: tangent Young's modulus, E_S: secant Young's modulus, v: Poisson's ratio, $\varepsilon_{a,u}$: axial strain at failure, $\varepsilon_{r,u}$: radial strain at failure.*

Rock			**σ_u**	**E_T**	**E_S**	**v**	**$\varepsilon_{a,u}$**	**$\varepsilon_{r,u}$**
			MPa	GPa	GPa	-	%	%
Pechbrunn	PB	Mean	408	75	65	0.05	0.57	0.04
basalt		St.dev.	59	7	11	0.03	0.07	0.01
		No. of tests	22	16	16	7	7	5
Tittling	TIT	Mean	199	47	36	0.13	0.49	0.07
granite		St.dev.	6	2	2	0.02	0.02	0.02
		No. of tests	17	19	19	4	4	4
Diabase	DIA	Mean	190	53	51	0.12	0.39	0.05
		St.dev.	28	1	1	0.01	0.04	0.01
		No. of tests	6	6	6	3	3	3
Dietfurt	DK	Mean	162	37	34	0.10	0.49	0.05
limestone		St.dev.	15	2	3	0.01	0.02	0.01
		No. of tests	7	9	9	9	4	4
Moosegg	MO	Mean	96	57	55	0.08	0.23	0.05
anhydrite		St.dev.	33	18	17	0.05	0.05	0.01
		No. of tests	21	13	13	8	13	5
Laas	LAM	Mean	87	44	36	0.10	0.27	0.06
marble		St.dev.	2	2	5	0.05	0.02	0.02
		No. of tests	10	13	13	7	7	4
Flossenbürg	FLB	Mean	88	23	18	0.19	0.49	0.35
granite		St.dev.	5	1	1	0.06	0.03	0.12
		No. of tests	7	13	13	13	7	7
Metten	MET	Mean	80	22	18	0.34	0.48	0.35
granite		St.dev.	11	5	4	0.21	0.06	0.03
		No. of tests	19	17	17	5	18	18
Posta	POS	Mean	60	22	19	0.09	0.32	0.08
sandstone		St.dev.	5	2	2	0.04	0.02	0.02
		No. of tests	19	21	21	12	11	6
Abtswind	ABC	Mean	28	5.5	5.0	0.27	0.56	0.31
sandstone		St.dev.	3	0.3	0.7	0.06	0.04	0.07
		No. of tests	8	5	5	5	5	5

Table I-2: *Summary of rock mechanical parameters for the characterization of rock properties as mean values with standard deviation and number of tests. σ_{ci}: crack initiation stress, $\sigma_{ci,AE}$: crack initiation stress determined from the AE rate, σ_{cd}: crack damage stress, $\sigma_{cd,AE}$: crack damage stress determined from the AE rate, σ_t: Brazilian tensile strength, σ_u/σ_t: toughness coefficient.*

Rock			σ_{ci}	$\sigma_{ci,AE}$	σ_{cd}	$\sigma_{cd,AE}$	σ_t	σ_u/σ_t
			%	%	%	%	MPa	-
Pechbrunn	PB	Mean	53	64	99	95	18	23
basalt		St.dev.	14	9	3	4	5	5
		No. of tests	7	9	7	11	14	14
Tittling	TIT	Mean	63	46	99	96	9.5	21
granite		St.dev.	11	4	3	2	2.0	1
		No. of tests	4	3	4	16	16	17
Diabase	DIA	Mean	49	75	100	99	17	11
		St.dev.	7	5	0.3	0	2	2
		No. of tests	3	3	3	3	10	6
Dietfurt	DK	Mean	59	71	98	98	9.5	18
limestone		St.dev.	5	8	1	0.1	1.6	1
		No. of tests	4	4	4	4	8	9
Moosegg	MO	Mean	67	-	89	99	8.8	12
anhydrite		St.dev.	10	-	5	1	3.1	5
		No. of tests	8	-	8	2	6	8
Laas	LAM	Mean	64	66	94	116*	7.2	12
marble		St.dev.	7	5	2	3	0.9	0.7
		No. of tests	7	4	7	10	11	13
Flossenbürg	FLB	Mean	43	-	77	-	6.0	15
granite		St.dev.	3	-	10	-	1.6	1
		No. of tests	3	-	3	-	12	13
Metten	MET	Mean	42	45	71	-	6.8	13
granite		St.dev.	6	5	5	-	1.2	2
		No. of tests	4	3	4	-	15	19
Posta	POS	Mean	60	68	90	-	3.9	17
sandstone		St.dev.	4	3	4	-	0.5	2
		No. of tests	8	3	8	-	14	20
Abtswind	ABC	Mean	39	37	70	98	2.1	13
sandstone		St.dev.	6	5	10	1	0.2	1
		No. of tests	5	3	5	5	6	8

* crack damage after peak strength

Appendix II

Table II-1: *Summary of the acoustic parameters of the tested rocks as mean values with standard deviation and number of tests. ρ: density, $v_{p,axial}$: axial p-wave velocity, $v_{p,radial}$: radial p-wave velocity, $N_{AE,\ failure}$: number of AE until failure, E: signal energy.*

Rock			**ρ**	**$v_{p,\ axial}$**	**$v_{p,\ radial}$**	**$N_{AE,\ failure}$**	**E**
			g/cm³	km/s	km/s	-	V²/s
Pechbrunn	PB	Mean	3.15	6.40	6.76	639	1,93.7
basalt		St.dev.	0.02	0.32	0.07	237	276.8
		No. of tests	15	10	10	2	2
Tittling	TIT	Mean	2.65	4.41	4.79	12 728	286.6
granite		St.dev.	0.03	0.08	0.03	1726	126.7
		No. of tests	18	19	19	4	4
Diabase	DIA	Mean	2.92	6.24	6.20	916	229.1
		St.dev.	0.01	0.04	0.06	82	102.9
		No. of tests	6	4	4	3	3
Dietfurt	DK	Mean	2.54	5.29	5.45	288	4,775.2
limestone		St.dev.	0.01	0.09	0.06	130	1,399.5
		No. of tests	12	9	9	4	3
Moosegg	MO	Mean	2.92	5.29	5.85	9,998	8.3
anhydrite		St.dev.	0.01	0.19	0.17	1,711	3.8
		No. of tests	13	7	7	2	2
Laas	LAM	Mean	2.71	5.16	5.57	211	2.9
marble		St.dev.	0.01	0.13	0.10	167	0.7
		No. of tests	13	14	14	3	3
Flossenbürg	FLB	Mean	2.63	3.37	3.40	24 888	23.0
granite		St.dev.	0.01	0.10	0.07	529	5.6
		No. of tests	12	9	9	4	4
Metten	MET	Mean	2.61	3.24	3.45	21,702	60.4
granite		St.dev.	0.01	0.15	0.08	2494	17.4
		No. of tests	24	12	8	3	3
Posta	POS	Mean	2.09	3.00	3.15	56,862	238.0
sandstone		St.dev.	0.00	0.10	0.05	1,981	123
		No. of tests	22	9	8	3	3
Abtswind	ABC	Mean	2.03	2.27	2.30	3,315	29.7
sandstone		St.dev.	0.04	0.02	0.06	844	18.4
		No. of tests	7	6	6	5	5

Appendix III

Table III-1: *Results of the initial constant loading tests and the subsequent uniaxial compression tests. Data is given as mean values of samples tested with a similar stress level. $\Delta\varepsilon_l$, $\Delta\varepsilon_r$: axial and radial strain during constant loading, $N_{AE,total}$: total number of AE, $N_{AE,const.}$: number of AE during constant loading, $\Delta v_{p,axial}$, $\Delta v_{p,radial}$: difference in axial and radial p-wave velocity before and after loading, ΔE_T: difference in tangent Young's modulus, $\sigma_{u,2}$: uniaxial compression strength of preloaded rocks, FR: felicity ratio (AE onset stress/previous max. stress).*

Rock		**Stress level**	**$\Delta\varepsilon_l$**	**$\Delta\varepsilon_r$**	**$N_{AE,total}$**	**$N_{AE,const.}$**	**$\Delta v_{p,axial}$**	**$\Delta v_{p,radial}$**	**ΔE_T**	**$\sigma_{u,2}$**	**FR**
			-	-	-	-	%	%	%	MPa	-
Tittling	TIT	120	0.0035	0.0023	855	777	3.2	4.1	7.5	203.1	0.99
granite		140	0.0062	0.0040	912	533	3.2	5.3	4.6	195.9	0.93
		160	0.0099	0.0063	3,672	2,295	2.9	9.2	4.4	200.0	0.83
		180^-	0.0144	0.0070	6,995	3,649	3.1	13.8	0.9*	200.3*	0.67*
		180^+	0.0245*	0.0080	30,000[m]	4,743	2.9*	20.5*	-5.1*	187.5	0.73*
Dietfurt	DK	120	0.0110	0.0010	52*	48*	0.7	0.3	7.2	162.2*	-
limestone		140	0.0145	0.0010	114	62	0.0	1.6	5.7*	163.6	-
		160	0.0136	0.0035	139	98	0.3	1.0	2.0	173.2	-
Laas	LAM	60	0.0027	0.0007	16	14	2.0	5.3	5.5	91.2	-
marble		70	0.0043*	0.0010	26	22	3.3	5.7	8.3	91.3	-
		80	0.0106	0.0025	40	32	4.1	10.7	1.5	91.7	-
Flossen-	FLB	45	0.0080	0.0015	4,499	3,538	1.5	2.3	20.2	90.7	0.86
bürg		60	0.0120	0.0035	15,646	10,868	3.4	7.9	19.5	87.1	0.67
granite		75	0.0285	0.0080	46,506	22,036	3.7	19.7	13.4	86.9	0.57
Posta	POS	40	0.0033	0.0006	4,163	2,757	2.5	8.1	0.1	64.7	0.96
sandstone		50	0.0051	0.0020	26,759	18,825	2.9	11.8	0.3	63.5	0.72

180^-: below crack damage threshold, 180^+: above crack damage threshold,

[m] maximum number of recorded events, * single value